Accelerated Lifetime Characterization and Development of Test Protocols for Class I/Class II Micro-machined Sensors and Flexible Power Sources

by

Amrit Singh Abrol

A dissertation submitted to the Graduate Faculty of
Auburn University
in partial fulfillment of the
requirements for the Degree of
Doctor of Philosophy

Auburn, Alabama
May 4, 2019

Keywords: Micro-electro-mechanical systems, Reliability testing, Failure analysis, Flexible Lithium-ion power sources, Regression Model

Approved by

Pradeep Lall, Chair, John and Anne Macfarlane Professor of Mechanical Engineering
Dong-Joo Kim, Alumni Professor of Materials Engineering
Robert Dean, McWane Endowed Professor of Electrical and Computer and Engineering
Scott Thompson, Associate Professor of Mechanical Engineering
Jason Clark, Assistant Professor of Electrical and Computer and Engineering

Abstract

Modern day applications have led to extensive miniaturization of consumer electronics along with incorporation of state-of-the-art sensor devices and acceptance of flexible materials within an electronic assembly. With the introduction of portable electronics, given the harsh environments they can be exposed to, reliable and efficient operation is of utmost importance. For harsh environment reliability data, consumer electronic assemblies need to be monitored under conditions mimicking their areas of applications but not much attention has been paid to the incremental shift and degradation in output parameters of the assemblies while under operation. Present day consumer electronics is an amalgamation of Micro-Electro-Mechanical Systems (MEMS) and flexible electronics which allow for the development of thin form-factors with the ability to bend, stretch and fold in electronics applications. The existing electronics ecosystem and supply-chain is geared towards the manufacture of rigid electronics. The manufacturing of thin electronic architecture requires the development of solutions for unique challenges including the integration of thin-chips, flexible encapsulation and compliant interconnects.

Harsh environmental operating conditions have been known to have an impact on the life-time of a MEMS device. Therefore, reliable operation is a quintessential requirement for such devices especially in the areas of military, automotive and space navigation applications. Primarily, the major focus of the current MEMS studies encompasses novel fabrication techniques, effective internal design in order to achieve high quality factors, improved packaging techniques and harsh environmental survivability but in very few works. This section encompasses development of test protocols for MEMS sensors as per their areas of applications, harsh environment life characterization and conducting failure analysis. Harsh environment operating conditions which

the MEMS sensors have been exposed to are drop and shock (1500G), high vibration amplitudes (14G), high relative humidity and temperature (85C/85%RH), low temperature storage (-35C), thermal cyclic stresses and long term aging. The survivability of class I and class II MEMS devices such as gyroscopes, oscillators, microphones, pressure sensors and accelerometers need to be demonstrated as a function of change in their output parameters.

On a very similar note harsh environmental operating conditions present in our daily routines such as varying temperatures and bending loads can affect flexible/wearable electronics such as Li-Ion power sources. The development of electric vehicles (EVs) in the past few years has given rise to the lithium-ion battery technology from a standalone and flexible electronics standpoint. This particular battery chemistry has been the go-to product of the battery community due to its high energy density, long lifetime and high power density but just as in other electronics reliability and safety is still a concern. Combined effects of distinct bending load(s) and operating temperatures (25°C and 50°C) can significantly attenuate the life of flexible Li-Ion batteries in foldable wearable electronics. Present day technologies call for battery applications, which require exposure to bending stresses, human body and varying ambient temperatures. Current health monitoring techniques and test standards for flexible power sources are still in the nascent stages. Flexible power sources such as Li-Ion batteries may undergo multiple charge-discharge cycles during operation, therefore development of a hardware testbed, which mimics the operating conditions in their areas of applications, is needed.

This work comprises of two reliability sections where the first focuses on damage progression in MEMS whereas the other section provides insight into the overall behavior of flexible Li-Ion power sources under harsh operating environments.

Section I

Focuses on obtaining lifetime trend of class I and class II MEMS characteristics when operating within the specified environmental conditions and reporting the evolution of damage progression as a function of MEMS functionalities. This study also analyzes the behavioral trends over multiple cyclic and long term stresses using statistical methods and identifies potential failure sites, if any.

Section II

Shows the combined effects of deep-charge, shallow-charge, distinct bending load(s) and operating temperatures have been characterized for Li-Ion batteries. Thin flexible battery cells were cycled through multiple charge-discharge cycles under simultaneous bending loads plus thermal stresses. Output parameters such as efficiency, power, capacity and charge-discharge time have been analyzed for battery state assessment. The sensitivity of capacity degradation to a number of charge-discharge parameters has been quantified with regression models.

Acknowledgments

I am immensely grateful to many people for their contributions to this dissertation and for the time I spent in the graduate school. This dissertation would not have been completed without their invaluable guidance, support and encouragement.

First, it has been an honor to work with Dr. Pradeep Lall, my mentor and adviser. I cannot express the sheer amount of hard work, determination and patience he has displayed during my doctoral years. He has always provided honest and supportive advice in my research and instilled in me qualities of a successful and a hard-working person. It has been a great privilege to have worked under his supervision. Collaborating with him and having him alongside as a part of my professional career in the future will be an honor. I am truly blessed to have been advised by my committee members, Dr. Robert Dean, Dr. Dong-Joo Kim, Dr. Jason Clark and Dr. Scott Thompson for spending their valuable time in reviewing my proposal and dissertation documents. Their timely feedback and comments have been beneficial in improving the quality of the research work.

On a more personal level I would like to thank Dr. Jason Clark for being my mentor in developing my professional career and helping me with future research areas. It has been rewarding and inspirational to have learned about the MEMS industry, MEMS research and where the sensor market is headed. He has been generous in providing academic and career guidance. All these tough and grueling years would not have been completed without the support of my research fellows. It has been a great journey with a passionate group of researchers, Vikas Yadav, Nakul Kothari, Shantanu Deshpande, Kalyan Dornala, Tony Thomas and Kartik Goyal. I thank each one of them for making graduates school life productive and enjoyable for me.

I would also like to acknowledge the support of my friends, who are like my family, with whom I started the Auburn journey way back in 2010; Mohit Arora, Sarthak Kakkar, Rahul Kumar, Harshit Goyal, Vaibhav Aggarwal, Vaibhav Gupta, Tanuj Puri, Devashish Rawat and Amit Sehrawat. I cannot thank you all enough for being there when I was down and in helping me cross the finish line. Cheers!

Finally, for the most important people in my life, my parents, my fiancé and my little sister. While it has been a proud moment to see your son/fiancé/brother become a doctor, it has been a truly blessed life to have you as a part of it. My mother, Amarpreet Kaur, has always shown how one can be diligent, hard-working and strong-headed whilst facing the life's hardships. My father, Bhupinder Singh, has always asked me to keep going even when the going gets tougher and never lose faith in the almighty because of whom we are here. I owe a special debt to my sister, Noor Kaur, for advising and helping me through the tough decisions of life, although she is six years younger than me, but surely more mature and wise then I can ever be. I would also like to thank my maternal and paternal grandparents, some of them now rest in peace but I know they have always been watching over me. My grandfather, Harpal Grewal, an Indian Army veteran; one of the toughest and the kindest people I have seen, hope your health gets better and that I have made you proud.

My fiancé and soon to be wife, Shubhi, who has been by my side through thick and thin all these years, it has been a privilege to have met you in this life. I cannot express enough gratitude nor can I ever do what you have done for me. Distance cannot do us apart, life will change tides and soon we will be together having our own beautiful life. I would love to thank the almighty for blessing me with this opportunity to undertake my studies in a foreign land; having his grace over me has protected and supported me through tough times.

Finally, I would like to dedicate this dissertation to all the proud mothers who have their brave sons standing tall at the borders while we rest in our homes.

List of Figures

List of Tables

Table of Contents

Chapter 1

1.1 Introduction

Sensors and power source regimes are deeply intertwined in many ways. Firstly, in order to track the performance and safety of power sources a reliable sensor network is required **[3-7]**, secondly both the components are an integral as well as an interactive part of automotive, space navigation and consumer electronics and finally with the recent development of lithium-ion micro batteries, fully batch fabricated, using micro-fluidic Micro-Electro-Mechanical Systems (MEMS) packaging techniques [**4**], has opened up a whole new exploratory dimension where micro-batteries with interdigitated electrodes can compete with the conventional battery architecture comprised of stacked electrode configuration. Miniaturization of sensors and sensor based networks such as in wireless sensor grids, inertial measurement units (IMUs), and membrane/diaphragm based sensors has led to widespread usage of sensor technology but the effective power sources still remain a big issue. The main roadblock is that the reduction in size and cost of the sensors has surpassed the scaling of energy density in power sources, resulting in batteries becoming the biggest and the most expensive component within the assembly [**5**].

1.1.1 MEMS Overview

MEMS is a process technology used to fabricate micro level systems with both electrical and mechanical components. These devices are fabricated using integrated circuit batch processing techniques and have the ability to respond to external stimuli in order to generate effects on the macro scale. MEMS, as an acronym, was originated in the United States and is also referred to as Microsystems Technology (MST) in Europe and micro-machines in Japan. The MEMS device

electronics/circuitry are fabricated using traditional IC technology while on the other hand the mechanical components are fabricated using urbane surface and bulk micromachining techniques. Micromachining processes such as high-aspect-ratio, surface and bulk selectively add or remove silicon layers to form electro-mechanical parts. Conventional ICs are designed in a way that they can make use of the electrical properties of silicon but MEMS design engineers have made it possible to exploit both the electrical and as well as the mechanical properties of silicon.

Micro-sensors	Micro-actuators
MEMS	
Micro-electronics	Micro-structures
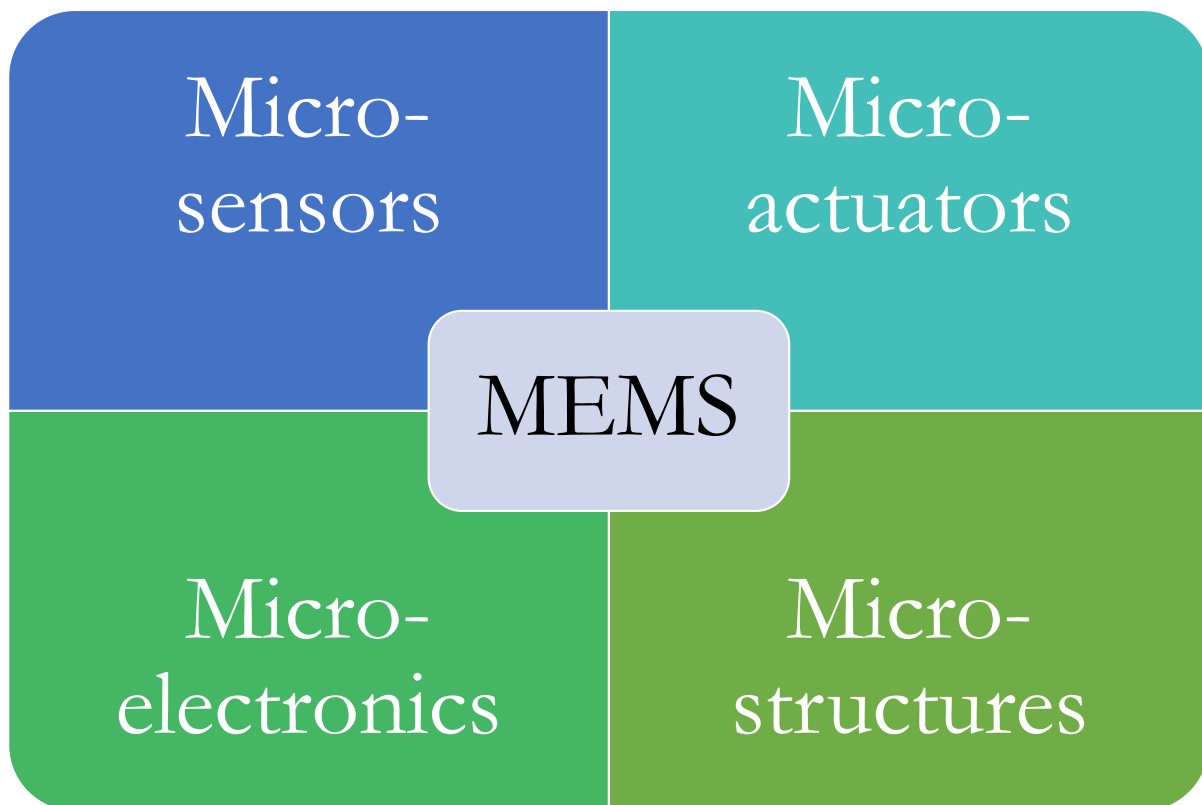
The MEMS regime is comprised of four areas which are micro-sensors, micro-actuators, mechanical micro-structures and microelectronics; where the micro-sensors have the ability to ascertain changes within the local surroundings by gauging thermal, mechanical, magnetic or

chemical data. This data is processed by the micro-electronics which in turn notify the micro-actuators to react to the local changes and generate an electrical signal mostly in terms of a voltage output.
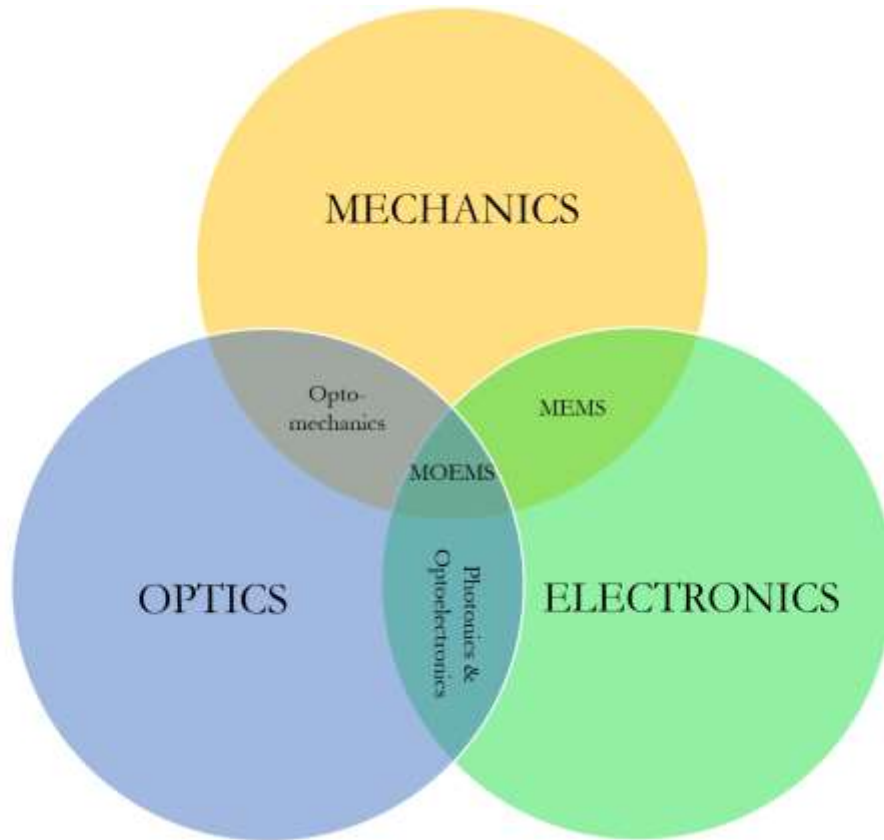
MEMS sensors as mentioned are fully integrated micro-systems which comprise of both electrical and mechanical parts in most cases while some other sensors as per their applications might comprise of magnetic, fluidic or thermal components. These micro-system components are fabricated using the conventional semiconductor batch processing techniques and their dimensions may vary from a few nanometers to microns [**MEMS Reliability 2015**].

The MEMS vision was laid out as early as in the 1950's but it took a long time, almost 30 years, before this technology could be incorporated into consumer electronics. It was only during the mid-1990's that MEMS components could break through and started appearing in commercial

products such as airbags (accelerometers), inkjet printers and medical applications (pressure sensors).

Timeline	MEMS Milestone	Contributor(s)
1948	Invention of Germanium transistor	BELL Labs (William Shockley)
1954	Piezo-resistive effect in Silicon and Germanium	C.S. Smith
1958	First Integrated Circuit	Kilby and Noyce
1959	"There's plenty of room at bottom" lecture	Richard Feynman
1959	First Si-based Pressure sensor demonstration	Kulite
1967	Anisotropic deep Silicon Etching	H.A. Waggener et.al
1968	Gate Transistor (Surface Micromachining)	H.Nathanson et.al
1970	Bulk etched Si wafers used as Pressure sensor	Bulk Micromachining Process
1971	Invention of Microprocessor (4004)	Intel
1979	Micro-machined Ink-jet Nozzle	HP
1982	Silicon used as structural material	K.Petersen
1982	LIGA Process	KFK
1983	Integrated Pressure Sensor	Honeywell
1986	Atomic Force Microscope	IBM
1986	Silicon Wafer Bonding	M.Shimbo
1991	Polysilicon Hinge	Pister et.al
1993	Digital Mirror Display	Texas Instruments
1993	First surface machined accelerometer	Analog devices
1994	Deep Reactive Ion Etching	Bosch
1999	Optical network switch	Lucent
2000s	Optical and Bio MEMS	Many contributors

MEMS Fabrication Process
- Additive
  - Deposition
  - Doping
  - Bonding
- Subtractive
  - Etching
  - Cleaning
  - Wafer Dicing
- Transformative
  - Annealing
  - Radiation

Si wafer deposited with 300 nm Si_3N_4

Deposition and patterning of Cr bottom electrode

Sputtered H_fO_2 film deposition and patterning

PECVD SiO_2 film deposition and patterning

PECVD a-Si:H film deposition and patterning

Sacrificial layer etching and release of cantilever structure

Within the last two decades, research and development of MEMS and surfacing of portable products utilizing MEMS sensors have made exponential strides while realizing the goal of inexpensive, low cost, efficient and complex devices. With the recent developments in automotive, IoT (Internet of things), industrial, military and medical applications MEMS technology has garnered ubiquitous acceptance within multiple regimes. Total value of the current MEMS market stands around $12.5 billion up from $7 billion from 2009 when MEMS market was dominated by pressure sensors, accelerometers, microfluidic sensors and optical devices. One of the current issues faced by the MEMS community is saturation of sensor market due to stagnation in existing motion sensor and conventional end product technologies. Novel technologies and products such as in IoT is helping MEMS market to gain back traction with units deployed in drones, digital economy, self-driven cars and smart things.

As opposed to traditional semiconductor microelectronics, MEMS devices pose a much more difficult as well as challenging problem due to the presence of moving and contact parts. In comparison, MEMS design engineers fabricate 3D structures and complex topologies using different materials. Also the final product functionality is highly dependent on the application therefore fabrication process steps differ resulting in "one process, one product".

7
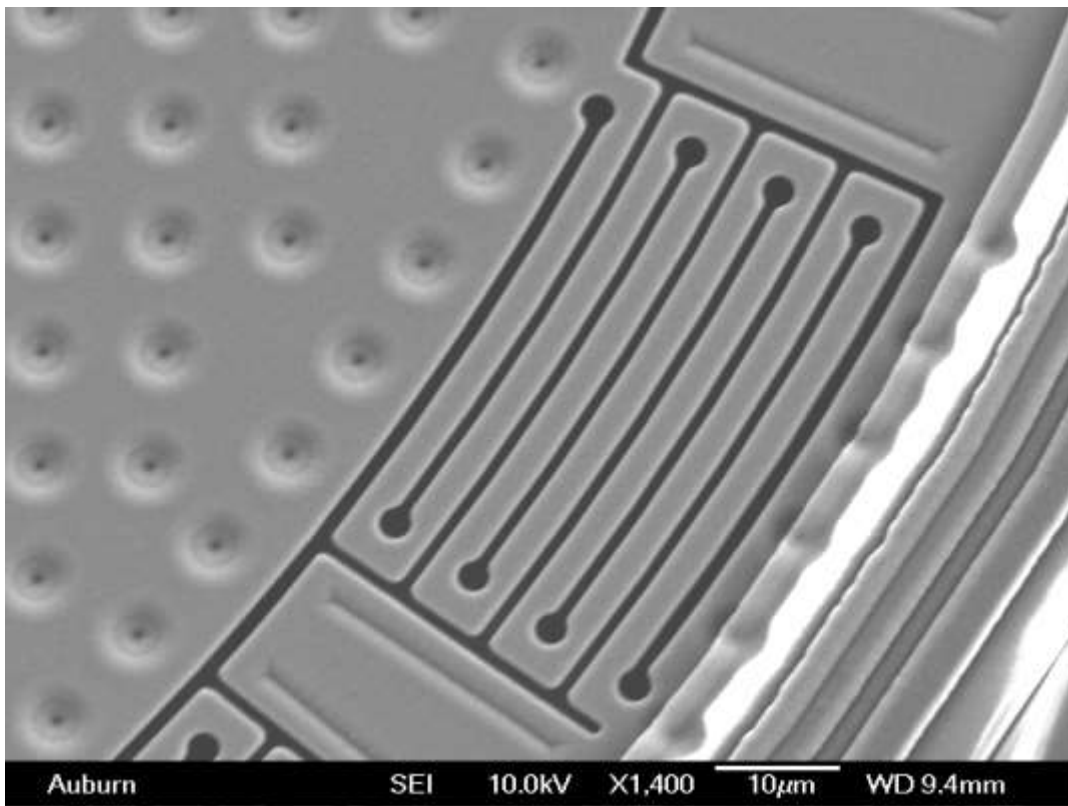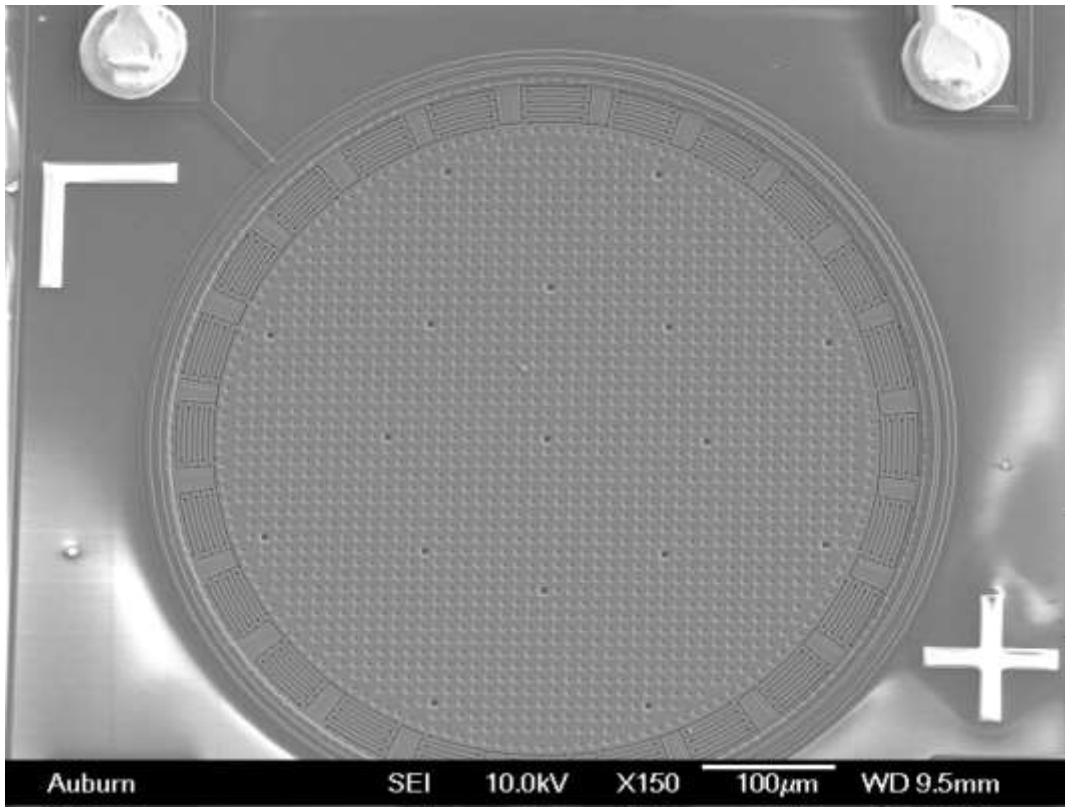
MEMS fabrication technology has seen exponential growth in the past years in order to fabricate at mass levels with different assortment of materials which made it possible for transition into the large-scale volume production from the prototype barrier. Some of the most successful MEMS products are the Freescale pressure sensors (MPX series), Texas Instruments (DLP mirrors) and Analog Devices accelerometers (ADXL series); these products were able to displace rival technologies in terms of successful execution and cost efficiency.

1.1.2 Battery Overview

G.N. Lewis was the frontiersman who began working on the lithium battery in 1912 but it was not until 1970s that the first commercial rechargeable lithium ion battery became available. The idea of lithium ions moving reversibly between the two electrodes was first proposed by Armand in the late 1970s using intercalation materials. This idea was quickly taken over by Scrosati and Lazzari who implemented a tungsten dioxide based electrode packed with a titanium disulfide electrode. The output voltage recorded was a maximum of 2.1 volts and the cell was cycled for 60 cycles. It took some years before Sony in 1991 announced a new product called lithium ion battery, the interest in lithium metal technology was due to its high specific energy and energy density. Corporations such as Exxon and Bell labs had also been working with different lithium battery chemistries but their test samples were plagued with safety issues and were prone to explosion under strong shock conditions. Many studies also utilized large amounts of lithium metal in order to improve the efficiency but when the excess amount of lithium was eaten up the battery capacity dropped drastically. All these works led to considerable amounts of learning about the process and the material requirements.

Timeline	Battery Milestone	Contributor(s)
1600	Establishment of Electrochemical Study	William Gilbert
1745	Invention of Leyden jar	Ewald von Kliest
1800	Invention of Voltaic cell	Alessandro Volta
1820	Andre Ampere	Electricity through Magnetism
1833	Michael Faraday	Faraday's Law
1836	Invention of Daniell cell	John Daniell
1839	Fuel cell	William Grove
1859	Lead acid battery	Gaston Plante
1899	Invention of Nickel Cadmium battery	Waldemar Junger
1901	Invention of Nickel Iron battery	Thomas Edison
1932	Sintered pole plate	Schlecht and Ackermann
1947	Successful sealing of Nickel-Cadmium battery	Georg Neumann
1949	Alkaline Nickel-Manganese battery	Eveready Battery, L. Urry
1970	Valve regulated lead acid battery	Many Contributors
1991	Lithium ion battery	Sony
1994	Commercialization of Li-ion polymer	Bellcore
1995	Pouch cell using Li-ion polymer	Many Contributors
1995	Industry Standard for SMBus	Duracell and Intel
1996	Li-phosphate	University of Texas
2002	Improvements of $LiFePO_4$, commercialization	MIT, Quebec Hydro, UM

One lithium ion technology which has gained huge popularity is the rechargeable Li-ion power source chemistry specifically the Lithium Cobalt Oxide ($LiCoO_2$) cathode with a Carbon based anode and an electrolyte with additive/lithium based salts. From all the metals which fall into the battery chemistry bucket, lithium is regarded as the most effective and promising. Lithium is widely available, light and non-toxic in nature, and chemically electropositive all of which result in higher energy storage. [**Zubi 2015**] The main components of a Li-ion power source are the electrodes (cathode and anode), the electrolyte and separator.

Volumetric Energy Density (Wh/L)

300
250
200
150
100
50
0

Li-Ion

Ni-MH

Ni-Cd

Lead Acid

0   50   100   150   200   250

Specific Energy Density (Wh/kg)

In Lithium-Ion batteries both the electrodes have the capability to intercalate (absorb) Li^+ ions. During the charging phase of flexible power source $LiCoO_2$ oxidizes i.e. loses electrons and in order to maintain the charge balance same number of Li^+ ions are released into the electrolyte. The electrolyte solution which is a mixture of solvents and Lithium salts is already rich in Li^+ ions; therefore the arriving Li^+ ions from the cathode replace the existing Li^+ ions which travel to the anode. The graphite based anode of the flexible power source intercalates the incoming Li^+ ions where are they are attached to the electrons lost by the cathode. This electrochemical reaction is reversible and the direction of Li^+ ions and electrons reverses during the discharging phase [**Battery University 2013**]. Present day commercial power source nomenclature arises from the lithium-ion donator incorporated within the cathode, this is because of the battery properties are determined from the Li-ion donor. The variety of donor materials such lithium iron phosphate (LFP), lithium cobalt oxide (LCO), lithium manganese oxide (LMO) and many more result in significantly distinct battery properties. [**Battery Projections 2014, Battery State of the art 2015**]. Another important aspect of the lithium-ion battery is the anode; graphite has been used as the premium anode material for some time now. Graphite as a material has been undisputedly accepted due to its low volume expansion during repeated charge-discharge phase,

low cost and electrochemical characteristics [**33, 35, 36**].
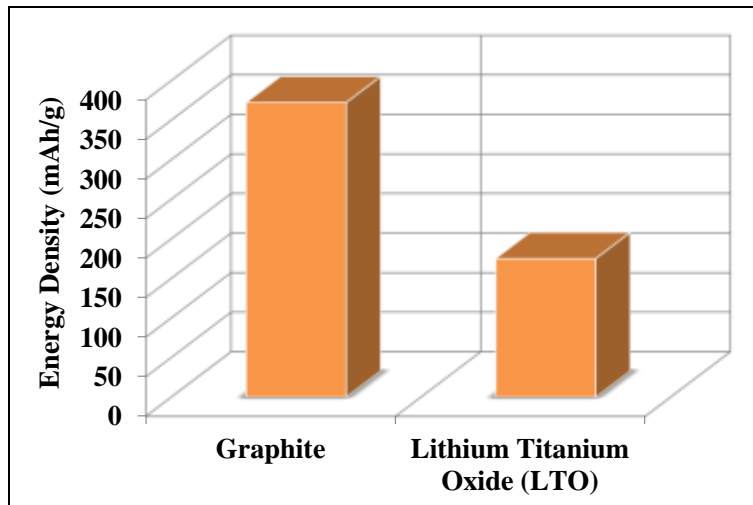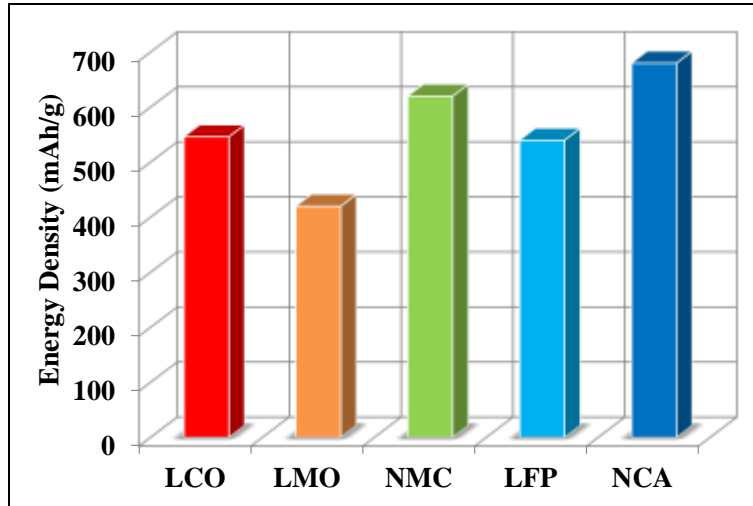
Another material used as anode, only in specific cases, is Lithium Titanium Oxide (LTO) but higher cost and reduced output cell voltage have limited its areas of applications. [**Anode materials 2014**]. Silicon-alloy based anode is being considered as the "anode material" for the future battery market leading up to 2030 because of theoretical capacity of silicon itself. [**Battery Cost Projection 2010**]

The effective cost and performance characteristics of a battery are directly linked with the acclimatization of battery operated vehicles and portable electronics. The adoption of "green

electronics" whether in electric vehicles or consumer electronics largely resides on the fact to willingly pay extra cost for the advanced technology [**Battery cost projection of li-ion battery 2016**]. For a battery operated vehicle, the power source itself accounts for a total of 75% of the EVs powertrain cost [**6**] therefore incorporating a bigger battery will increase the overall cost. Lithium-ion batteries have known to be established power source component within the electronic assemblies such as modern day smart phones, laptops and EVs, with immense potential in off-grid power supply system's [**zubi 2015, Battery University 2016**]. The demand for better and more advanced battery technology is ever increasing and is thrusted by many industries such as consumer electronics, power grids, automotive, energy harvesting units and many more.

1.1.3 Reliability Section

Developing a product on an average lasts several years starting from the initial concept and finally tapering off at the final volume production stage; where the time dwelling factor in each case has been endured usage of conventional manufacturing approaches. The novelty and nuances of the MEMS technology, complex processes, and reliability issues are some of the challenges that fetter the time to market. In the early days of MEMS industry, application of strategies such as Design for Manufacturing (DFM) Total Quality Management (TQM) were not able to fully capture the comprehensive design methodologies[**MEMS Reliability 2015, 2017**] for MEMS devices therefore there was a need for synchronous/parallel strategies for a faster design to volume manufacture cycle. [**Reliability Analysis 2014**]

Exponential growth in many electronic sectors such as MEMS, power sources and portable electronics has led to an increase in development of critical sub-systems; where reliability is one of the critical drivers for their acceptance and overall growth. Novel technologies yearn for market approval in order to leapfrog from the prototype phase to high volume production. Therefore the product's reliability and survivability must be evaluated at the most elementary level when predicting/diagnosing the lifetime of such electronic products. Design and production are two major events during which potential failures can be incorporated into the product; these defects are identified by shortening the time to failure. Reliability testing is performed to accelerate the lifetime of electronic components by applying elevated levels of stresses than what is observed in product use; this impels the failures to occur in significantly lesser time as compared to the average condition. The reliability function is defined as the probability that a product will perform as it is required to under typical operating conditions for its lifetime, and the function can be defined as $R(t) = 1 - F(t)$. Here *F (t)* can be defined as the cumulative distribution function (CDF) i.e. the probability that any randomly chosen part will fail in time t.

Testing techniques such as highly accelerated life testing (HALT) and highly accelerated stress screening (HASS) can help identify issues on the design and production line. The basic idea behind such techniques is that if the manufacturing processes of a product are designed properly then the output units will turn out reliable. Generally, the product population is defined and characterized by the bathtub curve which displays failure rate vs time. The bathtub curve is the distribution of failures over the lifetime of a product where the first region is the infant mortality portion. This section is associated with a decreasing failure rate and is comprised of built-in defects which can be diagnosed by the HALT tests. The width of the infant mortality section

determines the time required for the HASS tests which means that the more extreme the stresses are the faster will be the failures and the width of infant mortality region will be smaller.

This dissertation focuses on consumer electronic devices such as MEMS sensors, flexible power sources and optimization of the respective harsh environmental tests used for testing their survivability. The fundamental behind this study is to observe the behavior of randomly chosen volume production parts and study their response to harsh operating conditions which are not accounted for during the manufacturing and design processes. Exposure to pre-conditioning and harsh operating environments which mimic the actual working surroundings of automotive, space navigation and military, can introduce electrical defects (distortion, drift and thermomechanical noise) and mechanical defects (stiction, fracture, phase change).

Chapter 2

Effect of Simultaneous Vibration and Temperature on MEMS Vibratory Gyroscope

Combined effects of high temperature and vibration can significantly attenuate the life of electronics used in automotive, military and navigation applications. No prior studies exist which examine the simultaneous effects of high temperature plus vibration and analyze failure modes and failure criterion for MEMS based gyros and accelerometers. Accelerometers and gyroscopes make a great complement to one another as the latter is not affected by gravity. Both are used alongside each other in motion-capture, vehicle navigation, missile-control and flight guidance applications. In order to have a reliable harsh environmental reliability data set these MEMS devices need to be monitored under conditions mimicking their areas of applications. In this section a test vehicle with a, MEMS gyroscope, LPY510AL, has been tested under: high temperature exposure at 55°C combined with vibration profile(s) set at 14G. The test boards with gyroscopes were later subjected to rotations between 0°/s and 100°/s. Scale Factor(s) were computed for both the pristine and vibration conditions. This section also showcases the effect of thermal cycling on zero bias stability of LPY510AL. The test boards were subjected to a standard thermal cycling profile, -40°C to 85°C for 250 loops. Shift in output parameters for the gyro has been examined incrementally till failure. The survivability of LPY510AL has been demonstrated as a function of change in the output parameters. Studies conducted previously as in [Szucs 2007] show the effect of vibration and thermal cycling on capacitive MEMS accelerometers. The authors used vibration amplitudes of 1G and temperature cycles from 50°C to 150°C and recorded degradation in 3 of the 5 tested samples. Other studies conducted previously emphasis more on effective internal design and shape optimization such as [Yilmaz

2016] analyzed the change in angular gain, vibration frequency and sensitivity of a solid state wave gyroscope whereas [Chen 2005] used a novel piezo resistive sensing method for Coriolis acceleration detection and stabilization of driving mode vibration amplitude. [Hou 2011] studied the effect of parasitic resistance on a MEMS vibratory gyroscope due to temperature fluctuations. The authors show a 20% dB change in the gain of frequency response over 30°C to 60°C. Our work is primarily focused on providing harsh environmental reliability data which the previous studies don't look into. Survivability of MEMS vibratory gyroscopes at high vibration amplitudes up to 14G combined with elevated temperatures is unknown. Presence of harsh environmental operating conditions affects the quality, reliability and performance of a product thus creating the importance of reliability data for MEMS engineers and designers. MEMS based vibratory gyroscopes make use of a spinning mass and principle of conservation of angular momentum in order to measure angular motion but not translational motion. As per Newton's second law an object in rotational motion continues in that motion unless it is altered by an external torque thereby maintaining conservation of momentum both linear and angular. Similar to a PPA the spinning or the vibrating mass in gyroscope brings back the MEMS device to its original frame of reference by producing an electrostatic force when acted upon by an external force. The virtual force produced by the gyro is known as Coriolis force and consequent acceleration produced is known as Coriolis acceleration. For a standard coordinate system rotating about z axis at $\Omega_z = \theta_z k$ the mass will experience a virtual force in the x-y plane due to the rotation which results in Coriolis acceleration in the x-y plane. Equation 1 is a simplified representation for the Coriolis acceleration $a_c = 2\Omega_z V_{rx} j - 2\Omega_z V_{ry} i$; Where Ω_z is the angular rate produced about the yaw axis, z, V_{ry} and V_{rx} are the velocities along the pitch axis, y, and roll axis, x respectively. Commercially there are many different types of gyroscopes available namely

vibratory gyros, levitated proof mass gyros, Saw based gyros, optical gyros, ring laser gyros and fiber optic gyros. Standalone gyros have been used for space navigation, flight simulation, missile technology and under water navigation but combined with accelerometers they are also used for motion capture and vehicle navigation as Inertial measurement unit (IMU). An IMU is capable of providing 6 DOF which a gyroscope and an accelerometer cannot generate alone. Inertial measurement units can precisely calculate orientation, position and velocity thus making them a viable commercial product. Products such as vibratory gyros are unknowingly subjected to harsh environmental conditions in their fields of applications. Apart from the design and manufacturing issues harsh environments such as high-g shock, vibration, temperature, noise sources and intermode coupling can lead up to a number of error sources in a gyroscope resulting in a bad consumer product thus the importance of reliability data. MEMS technology in commercial gyroscopes is complex and therefore there is a significant lack of reliability data that looks into the impact of simultaneous harsh environment operating conditions. The underlying principle behind this investigation is to analyze the output parameters of a commercial MEMS based vibratory gyroscope and assess the accrued damage. MEMS gyroscope used in this investigation was LPY510AL, a dual axis pitch and yaw analog rate gyroscope, ideal for GPS navigation systems, motion tracking, industrial and robotics. It is manufactured by ST microelectronics. The gyroscope is a combination of one actuator and one accelerometer integrated in a single micro machined structure and has a full scale range of $\pm 100^{\circ}$/s. It comprises of a sensing element and a sensing mass which is kept in continuous oscillating movement. The sensing mass is able to react when an angular rate is applied based on the above explained Coriolis principle. A CMOS IC outputs the measured angular rate to the external user through an analog output voltage. This piece of study is categorized into two different sets of

experiments where in the first set the MEMS test board assemblies were subjected to simultaneous high temperature and vibration, 14G at 55ºC. The MEMS test boards were subjected to a sine sweep 14 G profile ranging from 300 Hz to 330Hz where 323Hz being the natural frequency of the MEMS test board. A total of 20 boards, each with LPY510AL vibratory gyroscope, were selected for the first part of the study.10 boards represent pristine case and the other 10 were subjected to simultaneous high temperature and vibration. The objective of this experiment was to compute and compare the scale factors for both the pristine and 14G samples thereby assessing the accrued damage in the gyroscope. A basic position and rate table was designed using a 12V stepper motor in order to test the gyro samples with specific angular rates between ± 0º/s and ± 100º/s. The analog output voltage of the gyro samples for both pristine and vibration (14G) cases was recorded using a high speed data acquisition system. Another objective of this experiment was to see the effect of vibration on the zero bias stability of LPY510AL. Damage progression was studied until the response of the gyroscope samples had significantly drifted away from the ideal output. For the second set of experimentation the MEMS test board assemblies were subjected to a thermal cycling profile ranging from -40ºC to 85ºC for 250 loops. The motive of this experiment was to observe the effect of extreme temperature change on the zero bias stability of the gyroscope. A total of 5 MEMS test board assemblies were subjected to the above mentioned thermal cycling profile. Zero bias stability spec is of utmost importance to the MEMS design engineers as it best describes the resolution floor of the gyro. Degradation of MEMS gyroscope parameters such as, Zero bias stability, Scale factor and output reference voltage under the influence of high vibration and extreme temperature changes have been observed and documented.

2.1 TEST VEHICLE

The test boards were fabricated and then assembled using the surface mount technology line present at CAVE3 electronics research center. Initially, open source software, Free-PCB was used to design the MEMS test board. The dimensions of the test board are 132mm x 77mm. It is a JEDEC standard double sided FR4 material PCB. PCB pads are solder mask defined with immersion finish.
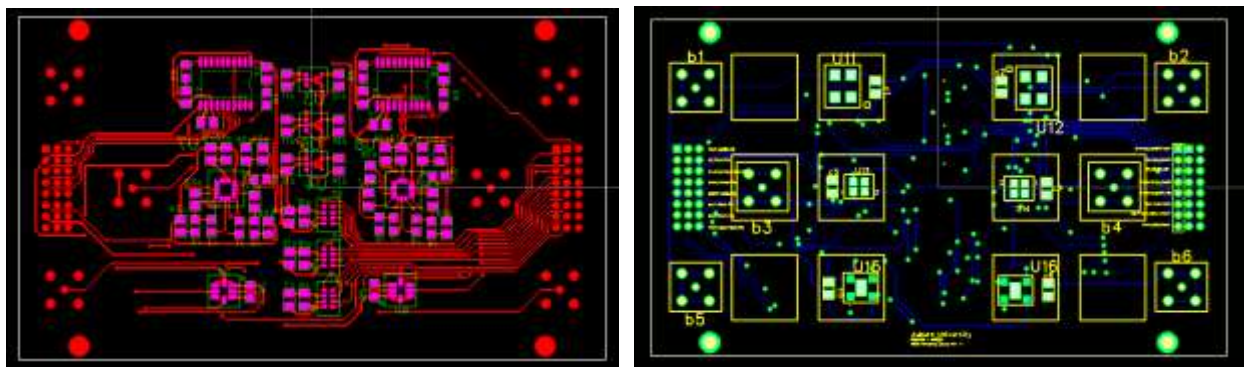
Figure 1:- Test Board Layout
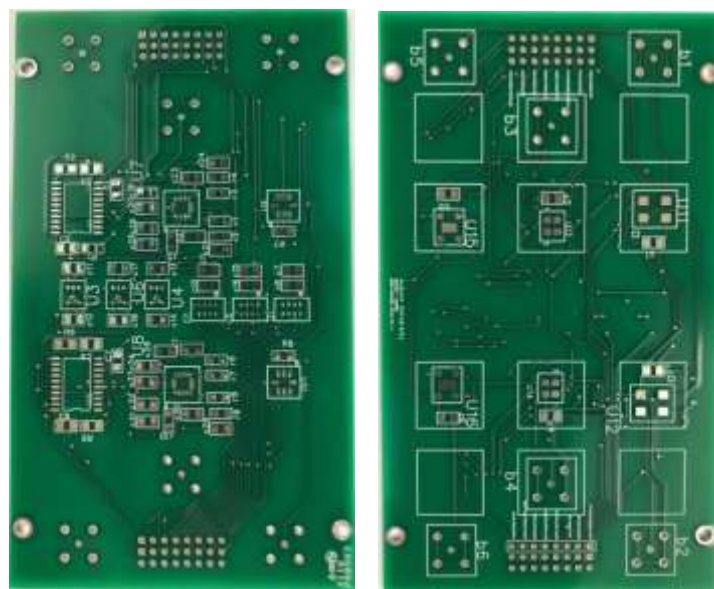
Figure 2:- Test Board Design

The printed circuit board used in this investigation has been fabricated for the testing of Accelerometers, Oscillators, Gyroscopes and Pressure sensors. However this particular study only focusses on LPY510AL, MEMS based vibratory gyroscope.
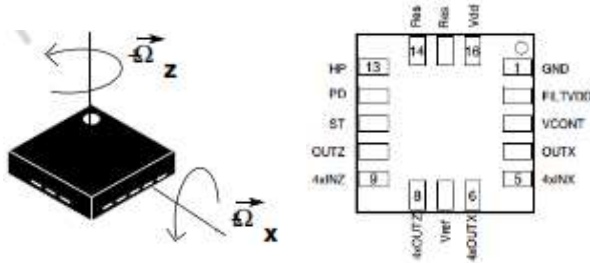
Figure 3:- LPY510AL yaw and pitch axis and Pin Layout
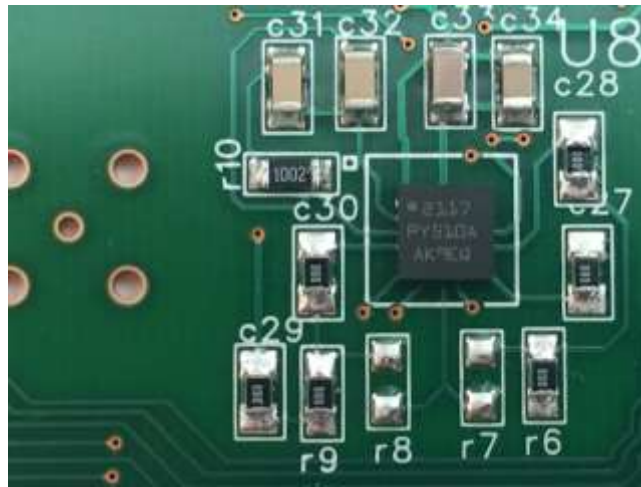
Figure 4:- LPY510AL mounted on MEMS test board

LPY510AL requires a total of 11 passive components, 6 capacitors and 5 resistors, connected to it as seen in **Figure 4.** The LPY510AL IC includes a PLL (phase locked loop) circuit to synchronize driving and sensing interfaces. depicts the different passive components used and their values.

Table 1:- Passive Components and their values

Type	Value	Pin No.
Ceramic Capacitor	0.01μF	2
Ceramic Capacitor	0.47μF	2
Ceramic Capacitor	10μF	1
Ceramic Capacitor	0.1μF	1,9,5
S. Mount Resistor	0 ohm	4,10
S. Mount Resistor	10kohm	3
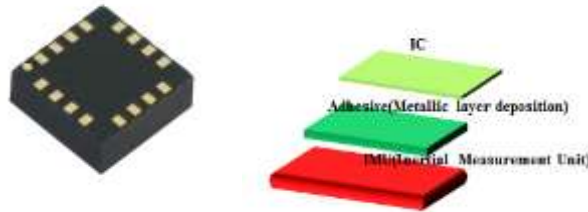
Figure 5:- LPY510AL Gyroscope layer wise structure

The MEMS IMU within the device is fully encapsulated in and boxed within a micro vacuum chamber. The mass and dimensions of the IMU are unknown since it is proprietary to ST microelectronics. LPY510AL package is comprised of a stacked configuration, the top is the CMOS IC die and the bottom die corresponds to the Inertial Measurement Unit die as shown below in **Figure 6**, the x ray images were taken at CAVE3 center at Auburn University.
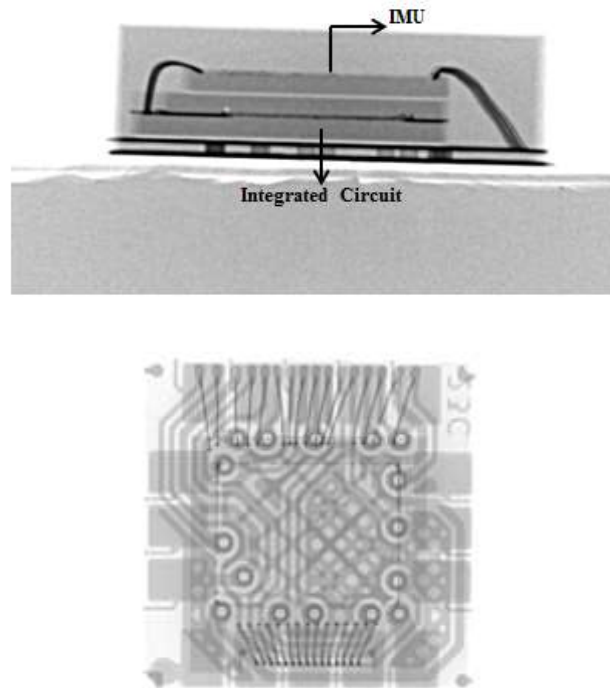
Figure 6:- Cross section view of LPY510AL (top) and front view (bottom)
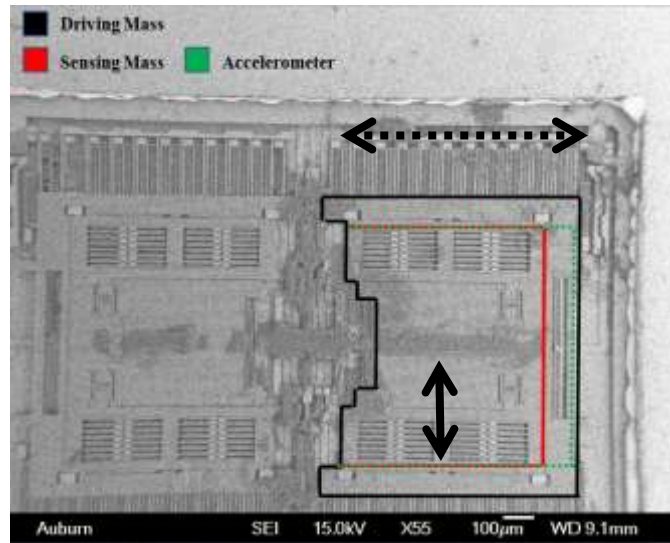
Figure 7:- SEM image of the IMU

Both the drive and the sense mass move out of phase in the x direction and move in phase in the

z axis direction. The driving mass is set into motion in direction of the dashed arrow as shown in

Figure 7.Now this puts the sensing mass into motion which is allowed to move freely in the direction of the single line arrow as shown in **Figure 7**. Any movements in the single line arrow direction caused by Coriolis force are detected by the capacitive plates of the accelerometer shown in **Figure 8**. An inertial measurement unit is generally comprised of an actuator and an accelerometer in order to get exact position, orientation and velocity by using maximum degrees of freedom; in this case a comb drive actuator works in tandem with a capacitive accelerometer shown in **Figure 9**.
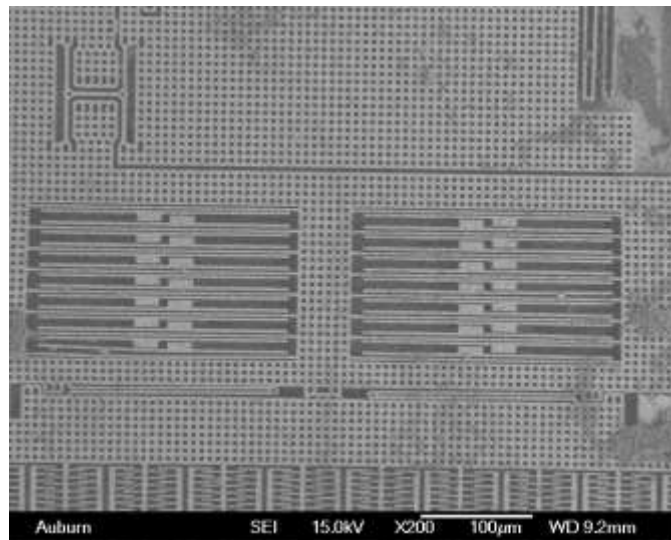
Figure 8:- Capacitive plates of the accelerometer within the IMU

The comb drive actuator (CDA) senses the motion along x axis and the capacitive plates sense the motion along the z axis; assuming a frame of reference where y axis is out of plane.
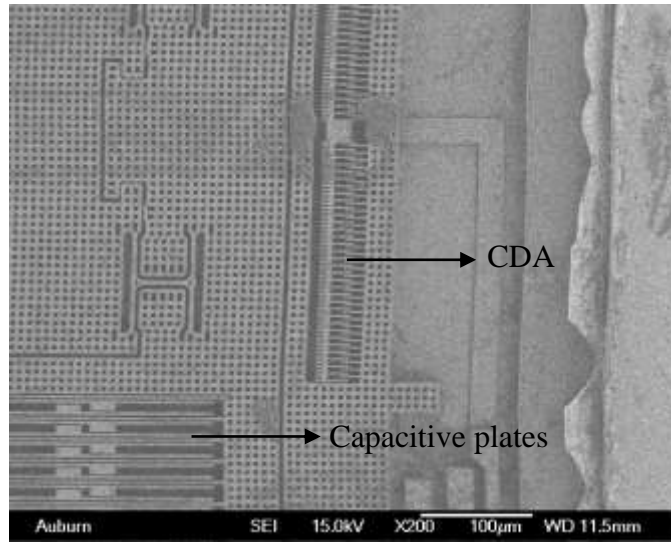
Figure 9:- Comb drive actuator and capacitive plates

2.1.1 De-capping Process

LPY510AL samples were de-capped in order to visualize the internal structure of the MEMS based vibratory gyroscope. The samples were de-capped by placing them on a hot plate set at $100^{o}C$ and then adding a small drop of red fuming Nitric acid (HNO_3) at the center of package. Then they were cleaned with a spray of acetone and later dried with compressed air.

As mentioned before the IMU and ASIC IC blocks are stacked on top of each other. The latter consists of Reference block, Low pass and High pass filters, Trimming circuits, clock, amplified and non-amplified output lines, phase generator block, charge amplifiers, demodulators as shown in **Figure 10**.
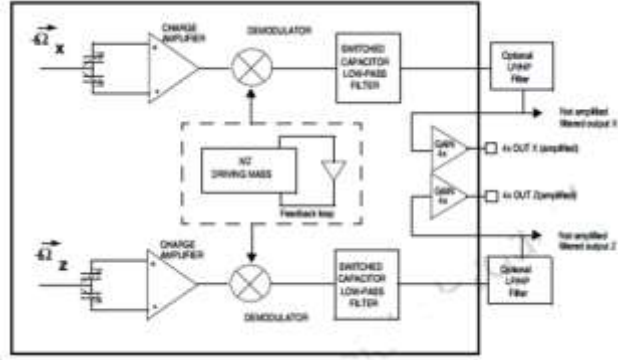
Figure 10:- LPY510AL block diagram as specified in STMicroelectronics Data Sheet

LPY510AL operates anywhere between 2.7-3.3V, for this study it was connected to a 3.3V power supply and 11 other passive components as shown in **Figure 10** and .The 0.1uF capacitor connected between the package and ground acts as the decoupling capacitor, which reduces the noise from power supply line. There are two separate output lines for the yaw/z axis i.e. 1x and 4x, for this investigation we have used 4x amplified output line. The MEMS gyro produces an absolute analog rate output with a zero bias/ DC offset preset at 1.20V. **Table 1**   **Table 2** provides a list of all the pin connections and pin layout for LPY510AL.

Pin No.	Mnemonic	Description
1	GND	Ground
2	FILTVDD	PLL filter pin
3	VCONT	PLL filter pin
4	OUTX	Non amplified out
5	4xINX	Input of 4x amp
6	4xOUTX	Amplified out

25

7	V-ref	Reference Volt
8	4xOUTZ	Amplified out
9	4xINZ	Input of 4x amp
10	OUTZ	Not amplified out
11	ST	Self-Test
12	PD	Power-Down
13	HP	High Pass Filter
14,15	Reserved	Reserved
16	Vdd	Power Supply

Table 2:- LPY510AL Pin Configuration

2.2 RELIABLITY TEST MATRIX

A total of 20 LPY510AL MEMS vibratory gyroscopes were put to test and were divided into two sets of 10 each, Pristine and simultaneous high temperature and vibration. Ten samples of LPY510AL gyroscopes were subjected to 14G at 55°C for 96hrs with gyro zero bias stability data being monitored for the entire length of the test. Each of the 10 MEMS test board assemblies were mounted off the vibration platform every 48hrs and angular rates between $\pm 0°$/s and $\pm 100°$/s were used as input on the gyros in order to record the analog rate outputs. On the other hand the remaining ten samples, Pristine, were tested on angular rates between $\pm 0°$/s and $\pm 100°$/s , all this was done in order to compute and compare the scale factors for the two different sets of pre-conditions. **Table 3** shows the different test parameters applied for the vibration study on LPY510AL gyroscopes.

Test Parameters	LPY510AL	Pre-Condition
Testing Temp.	55°C	Vibration
Stress Level	14G	
Test Condition	0°/s -100°/s	Vibration, Pristine
Test Duration	Till Failure	Vibration

Table 3:- Reliability test matrix for vibration study
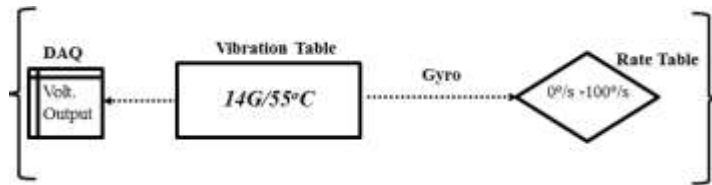
Figure 11:- LPY510AL test flowchart

Figure 11 shows the test flowchart for the vibration study on LPY510AL gyros. Gyroscope analog output voltage has been monitored and recorded using a high speed data acquisition system, Wave-runner Xi series. **Figure 12** shows the data acquisition system used for the experiment.

Figure 12:- Wave-runner Xi series oscilloscope

As mentioned above this piece of study is categorized into two different sets of experiments where one part focusses on analyzing the effect of simultaneous high temperature and vibration on MEMS vibratory gyroscopes; the other part of the investigation analyses the effect of thermal cycling on zero bias stability of LPY510AL. A total of 5 MEMS test board assemblies were selected for this test. **Table 4** shows the reliability test matrix for the thermal cycling experiment.

Table 4:- Reliability test matrix for thermal cycling study

Test Parameters	LPY510AL	Pre-Condition
Testing Temp.	-40°C to 85°C	Pristine
Stress Level	-40°C to 85°C	
Cycling Loops	250	
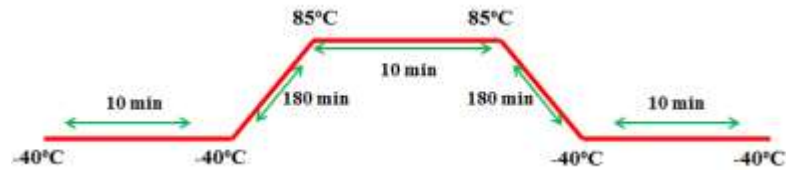
Figure 13:- Thermal cycling profile

Figure 13 shows the thermal cycling profile to which the gyroscope samples were subjected to; the profile temperature ranges from -40°C to 85°C with a 10 min dwell and 180 min ramp time.

2.3 EXPERIMENTAL TEST SETUP

LPY510AL MEMS vibratory gyroscope board assemblies were assembled at the Surface Mount Technology line present on CAVE3 facility. The Surface Mount technology (SMT) line consists of three stages, the Stencil printer, Pick and Place machine and reflow oven as shown in **Figure 14**. SAC305 solder alloy was used for this study and was evenly distributed on MEMS test board assemblies through the Stencil printer. LPY510AL gyroscope and 11 other passive components were placed on the MEMS test board using the Pick and Place machine. Finally, the test boards were baked in the reflow oven. As mentioned before 10 MEMS test board assemblies were subjected to simultaneous high temperature and vibration.

Figure 16 shows the vibration equipment used for testing the MEMS samples. A standard air cooled shaker is used for the vibrating platform. LDS V722 is a lightweight, high performance air cooled vibrator with both vertical and horizontal operation capable of producing a maximum system sine force of 652lbf and a maximum acceleration sine peak of 70G.
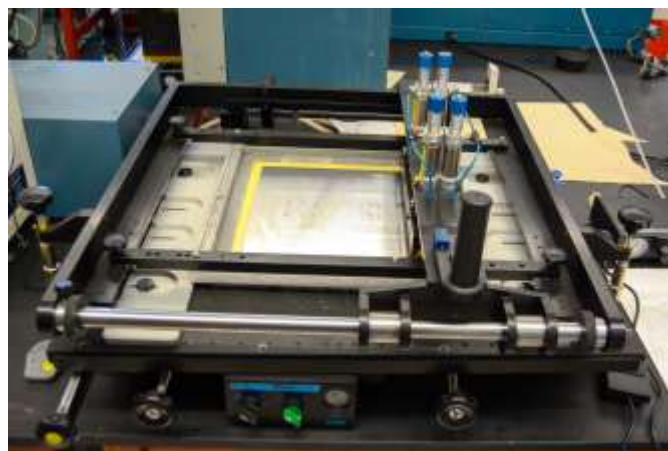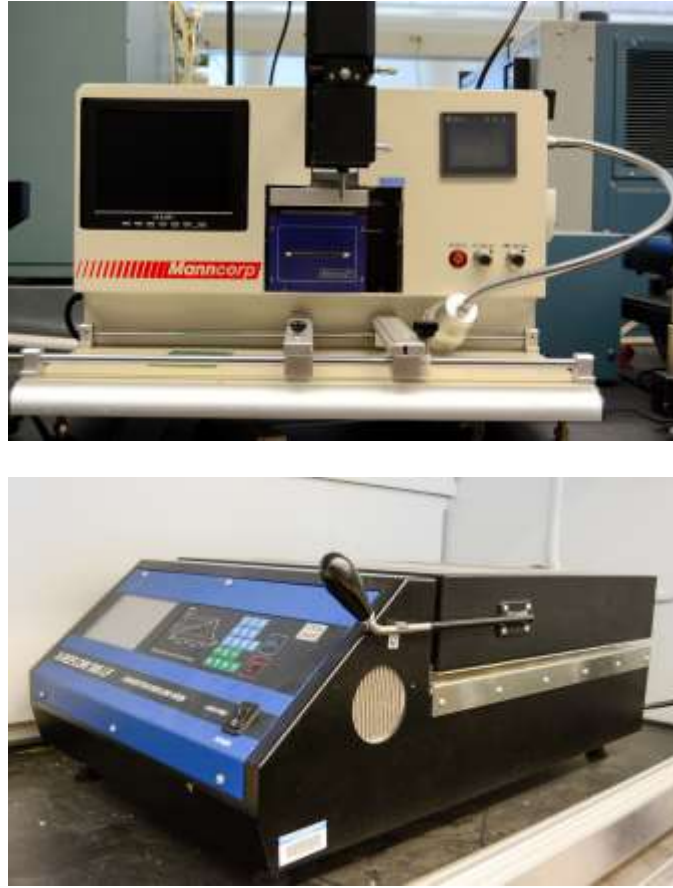
Figure 14:- SMT Line at CAVE3; Stencil Printer (Top), Pick and Place (Middle), Reflow Oven (Bottom)

The vibration platform/shaker system is operated through COMET vibration control system software which provides the flexibility to do random, swept sine and shock testing of electrodynamic shakers.

Figure 15:- COMET-usb vibration control system
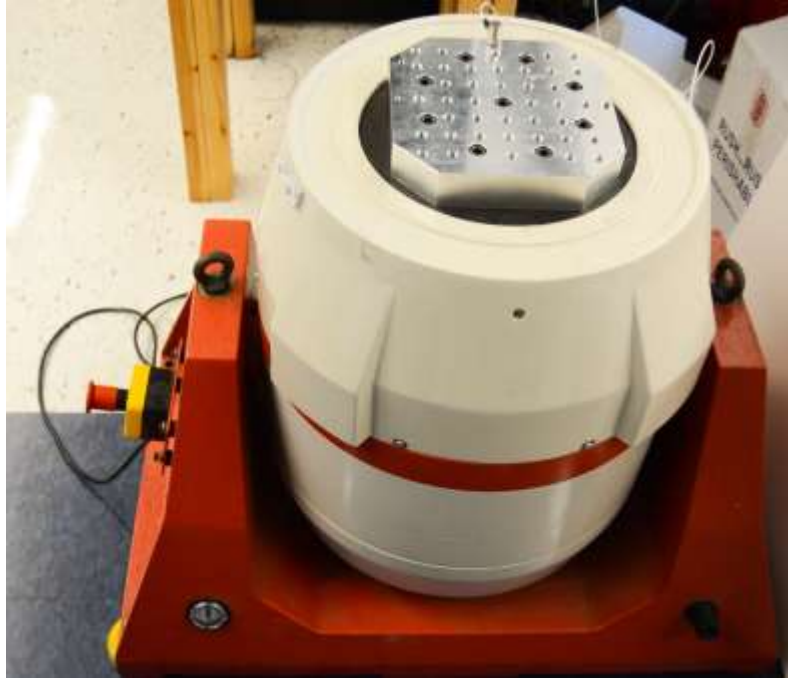
Figure 16:- LDS V722 air cooled shaker

The LDS V722 is connected to a DAQ system which records the data from the MEMS test board assembly every 30 seconds for the entire length of the test period, shown in Error! Reference source not found.. For a single MEMS test board assembly with LPY510AL gyroscope the zero bias is monitored on the vibration platform system and it is mounted off from the system every 48 hours in order to take readings from the gyro off the rate table. An aging oven is mounted on top of the shaker in order to have simultaneous high temperature and vibration as shown in **Figure 17** .

Figure 17:- Data Acquisition System with LDS power supply (left) and Vibration-Temperature setup (right)
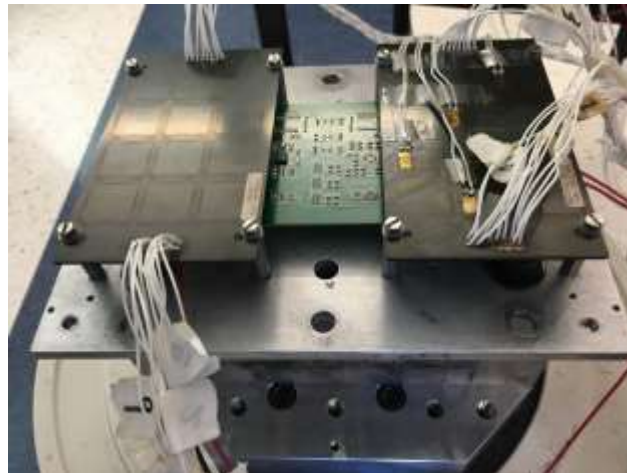
Figure 18:- MEMS test board on Vibration platform

For the vibration analysis the second set comprising of 10 samples which were pristine, did not undergo any aging or high/low temperature or vibration exposure. The methodology applied for this investigation allows us to conduct a constructive comparison among the two sets of samples.

Gyroscope gauge parameters such as scale factor, zero bias stability and reference voltage can demonstrate whether LPY510AL is sensitive to simultaneous high temperature and vibration or not, **Figure 18** shows MEMS test board assembly with the gyroscope mounted on. The testing methodology used in this section follows an incremental approach that allows us to keep a tab whether or not the gyroscope parameters are drifting significantly with respect to the ideal output(s) and by how much; when exposed to harsh environmental conditions.

Figure 19:- Thermal Cycling Chamber

For the thermal cycling portion of the study, zero bias stability was monitored for the MEMS test board assemblies which were kept in a thermal cycling chamber shown in **Figure 19** for 250 loops with the following profile -40ºC to 85ºC. LPY510AL gyroscope samples were connected to a standard Agilent multiplexer to record the data every minute for the entire duration of the test.

2.3.1 Rate/Position Table Setup
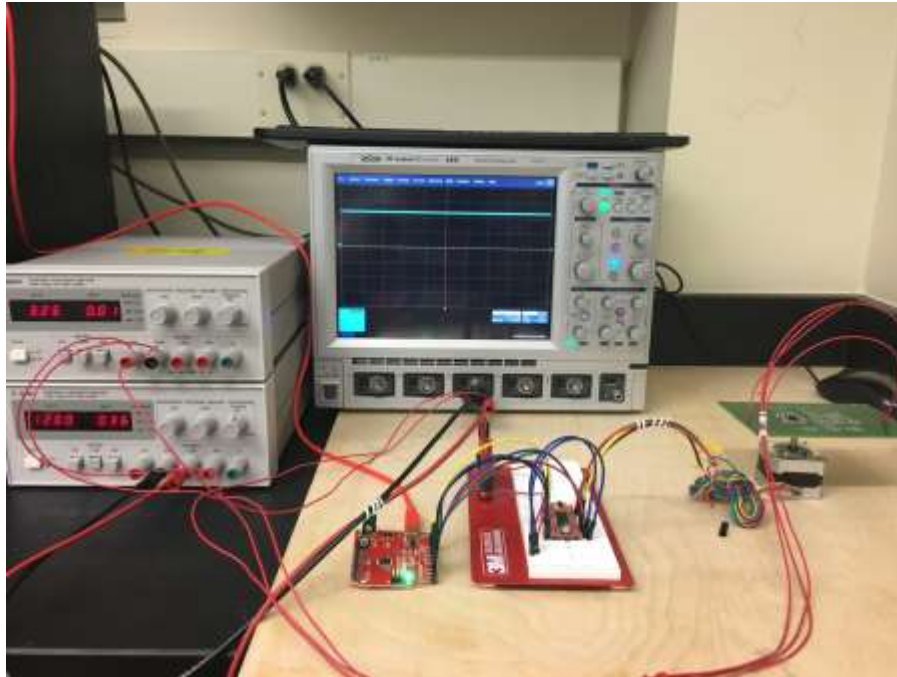
Figure 20:- Rate/Position Table using stepper motor

A standard 12V bipolar stepper motor was used in designing the rate/position table. Since the stepper motor does not have a feedback loop, angular rates were computed first using **Equation 1**

$$\Omega = (Vout - Zero\ rate\ level)/Sensitivity \quad \textbf{(1)}$$

; Where sensitivity of LPY510AL is 10mV/^{o}/s and zero rate level is 1.20V. The obtained angular rates were then applied as a part of experimentation. Different angular rates are obtained by controlling the speed of the motor for which time step or delay is added between the high state and low state of the motor. A delay of 6ms outputs an analog voltage from the gyroscope which corresponds to an angular rate of 100°/s. **Table 5** shows the time steps established for achieving different angular rates. Every voltage output from the gyro was put into **Equation 1** to verify the

angular rates. By changing the state of the direction pin from high to low or vice versa the direction of rotation can be switched for the stepper motor.

CW Rotation	CCW Rotation	Time step(ms)
-100°/s	100°/s	6
-90°/s	90°/s	8
-80°/s	80°/s	10
-70°/s	70°/s	12
-60°/s	60°/s	14
-50°/s	50°/s	16
-40°/s	40°/s	18
-30°/s	30°/s	20
-20°/s	20°/s	22
-10°/s	10°/s	24
0°/s	0°/s	No rotation

Table 5:- Time step/Delay values in milliseconds for different angular rates

The stepper motor is controlled via a standard commercially available motor driver. The driver is connected to a standard microcontroller, ATMEL Mega 328P. The microcontroller is programmed over a USB mini cable through C/C++ functions. The MEMS test board assemblies are mounted on the stepper motor and are connected to a high speed data acquisition system shown in **Figure 20.**

2.4 EXPERIMENTAL RESULTS

MEMS test board assemblies were put to test under conditions mimicking their areas of applications in order to observe and document the incremental damage progression caused by the harsh environments. In this study the term failure does not actually mean that the device is not working at all but is a coined term used to describe the progress of damage i.e. until the gyroscope output parameters go permanently out of the stable operating range or drift significantly with respect to the ideal output(s). The main aim behind exposure of LPY510AL samples to 14G at 55°C environment and also subjecting them to a -40°C to 85°C thermal cyclic stress environment, is to standardize the survivability of LPY510AL, MEMS vibratory gyroscope, for use in automotive, military and navigation applications. LPY510AL gyro samples have been gauged on standard gyroscope metrics such as Scale Factor, Zero Bias, and Reference output voltage.

(a)

36
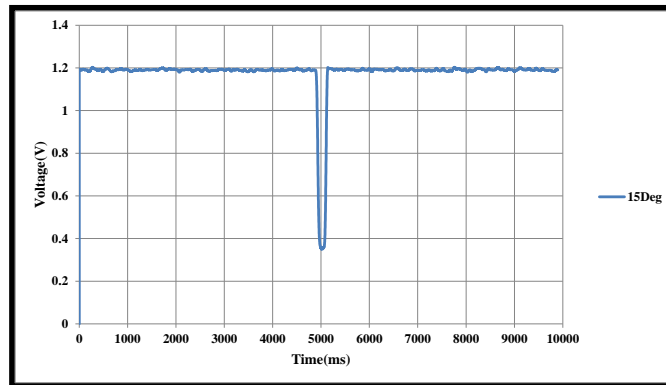
(b)
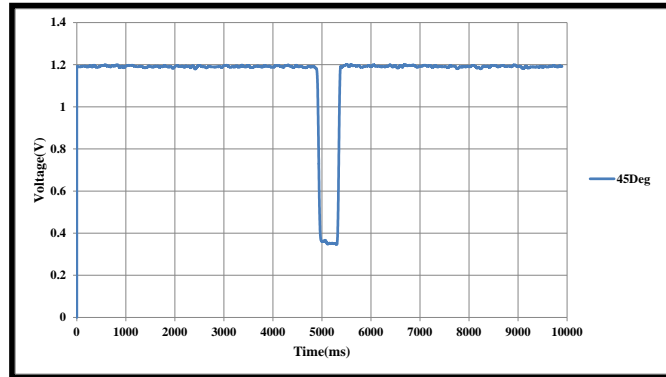
(c)
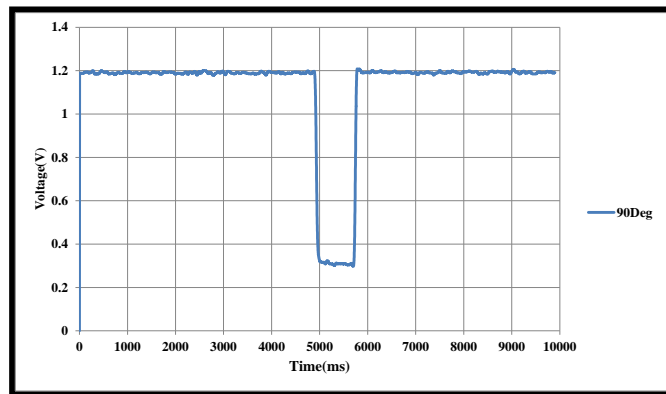
Figure 21:- Sample CW 15º, 45º and 90º (a, b, c) rotation outputs at 90º/s
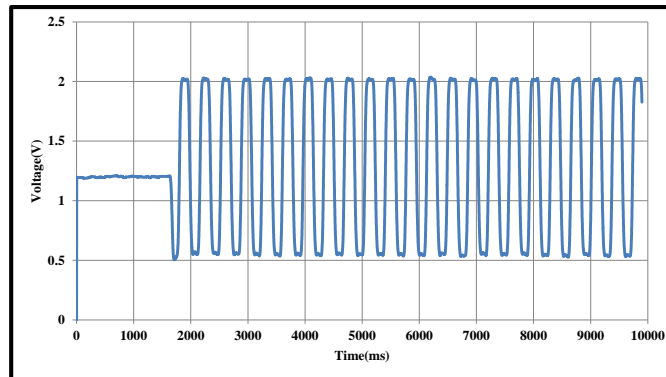
Figure 22:- Sample CW and CCW 15º rotation output at 80º/s
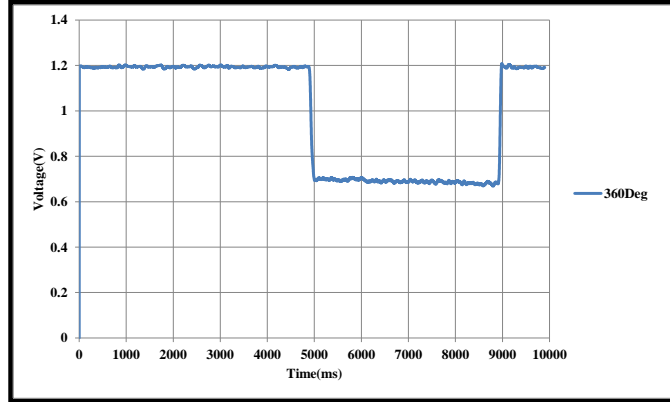
Figure 23:- Sample 360º CW rotation output at 90º/s
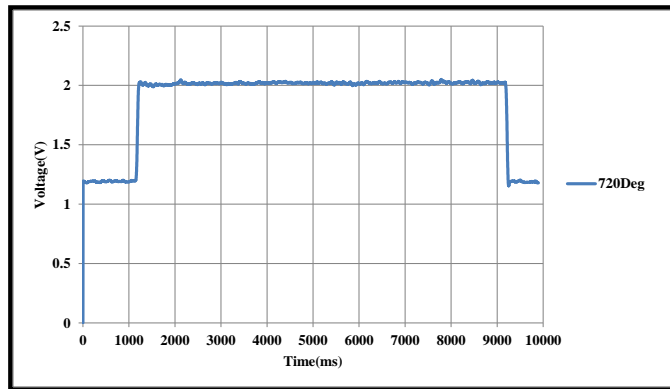
Figure 24:- Sample 720º CCW rotation output at 90º/s

2.4.1 Scale Factor(S) and variation in output voltage w.r.t to Ω

The ratio of change in output to a change in input, units are in mV$^{/o}$/s. It is evaluated as the slope of the least squares straight line fit to the input-output data. LPY510AL, angular rate gyroscope produces a positive-going output voltage for counterclockwise rotation and negative-going output voltage for clockwise rotation. LPY510AL samples show a nonlinearity error i.e. nonlinear deviation from the least squares straight line fit. The MEMS test board assemblies were mounted on the rate/position table and were subjected to angular rates between 0º/s – 100º/s; where 100º/s is the full scale output of LPY510AL. **Figure 25**

Figure 25 demonstrates the output voltages at different angular rates for the ten tested pristine samples. The dotted line is the ideal output of the gyro, which is considered as a reference.
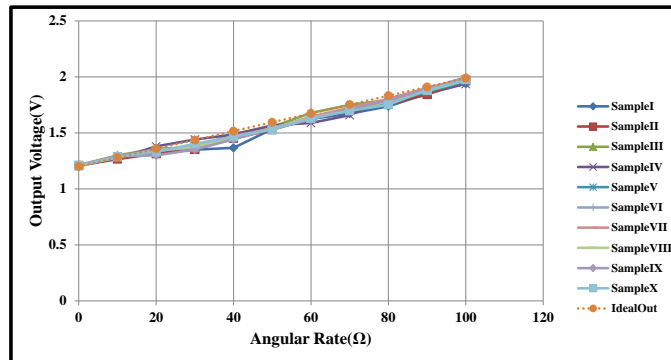
Figure 25:- Output voltages vs Angular rates (Pristine)
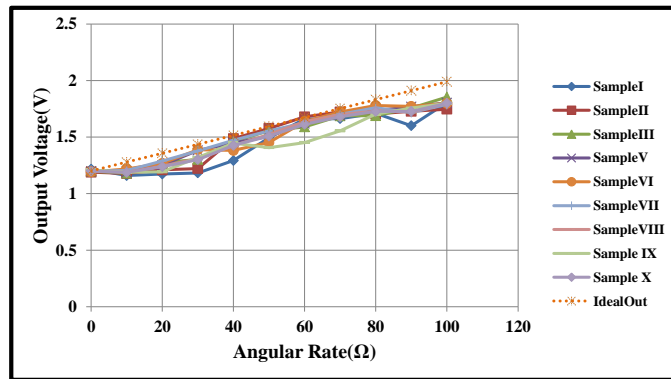
Figure 26:-Output voltages vs Angular rates (14G/55ºC after 48hrs)

In the above plot**, Figure 26,** voltage outputs from the ten tested vibration samples have been shown. As mentioned before after every 48 hours the MEMS test board assemblies were mounted off from the shaker platform and were subjected to rotations between 0°/s – 100°/s. **Figure 27** demonstrates the voltage outputs from the ten tested vibration samples. **Figure 28** shows the voltage output(s) comparison between pristine and the vibration samples. It can be clearly seen that the output voltages drift from the ideal output with increase in vibration exposure time. In **Figure 28** P1 to P10 legends represent the pristine samples and legends 14G_1 to 14G_10 represent the vibration samples at 14G/55ºC for 96hrs.
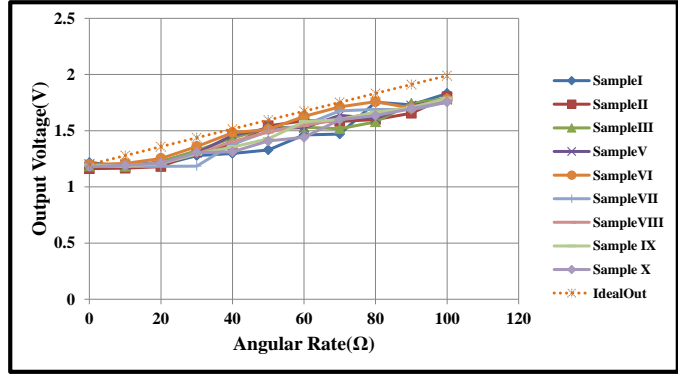
Figure 27:- Output voltages vs Angular rates (14G/55ºC after 96hrs)
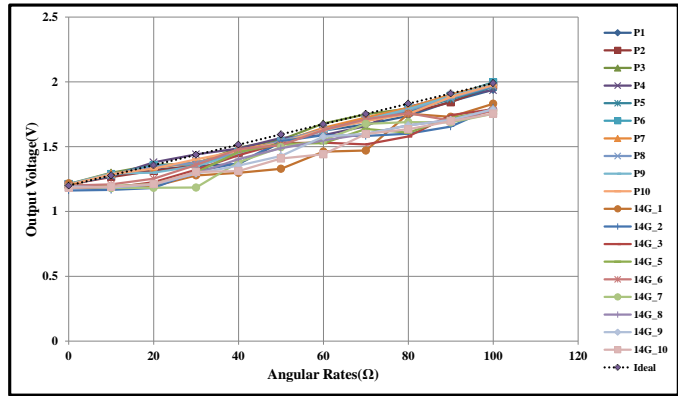
Figure 28:- Output voltages vs Angular rates (Pristine and 14G/55ºC after 96hrs)

From **Figure 25**, **Figure 26** and **Figure 27** for each LPY510AL gyroscope sample the corresponding output voltage response vs angular rate data was fitted with a least square straight line fit in order to obtain the Scale factors. The relation between the input and the output is a Scale factor error i.e. for a 100% input the output should also be 100%. Generally in MEMS based gyroscopes the ideal output which is the result of a linear effect is proportional to the input but is scaled. So ideally it is the slope of the sensor signal. In this part the Scale factors were computed for the following cases Pristine, Vibration at 14G/55ºC for 0 hours, Vibration at 14G/55ºC for 48 hours, Vibration at 14G/55ºC for 96 hours. **Table 6** below shows the scale factors for pristine and vibration samples. The computed scale factors show significant reduction when exposed to harsh

40

environmental operating conditions in comparison to the pristine samples. From the results documented in this section of dissertation it can be clearly established that the scale factor of a MEMS vibratory gyroscope is very sensitive to simultaneous high temperature and vibration. From **Table 6** it can be seen that no scale factors were computed for the fourth vibration sample, as it stopped responding before the 48th hour mark and had continuous flat zero bias at 3.26V as opposed to 1.20V which can be seen in the next section of the chapter.

Pristine	Computed SF	Vibration 14G/55°C	Computed SF		
			0hrs	48hrs	96hrs
I	7.35mV/°/s	I	7.21mV/°/s	6.94mV/°/s	6.80mV/°/s
II	7.58mV/°/s	II	7.55mV/°/s	6.96mV/°/s	6.51mV/°/s
III	7.73mV/°/s	III	7.62mV/°/s	7.02mV/°/s	6.19mV/°/s
IV	7.20mV/°/s	IV	7.44mV/°/s	-	-
V	7.47mV/°/s	V	7.50mV/°/s	6.89mV/°/s	6.28mV/°/s
VI	7.77mV/°/s	VI	7.74mV/°/s	6.99mV/°/s	6.57mV/°/s
VII	7.79mV/°/s	VII	7.27mV/°/s	6.55mV/°/s	6.83mV/°/s
VIII	7.55mV/°/s	VIII	7.67mV/°/s	6.89mV/°/s	6.53mV/°/s
IX	7.82mV/°/s	IX	7.53mV/°/s	6.66mV/°/s	6.60mV/°/s
X	7.50mV/°/s	X	7.66mV/°/s	7.11mV/°/s	6.89mV/°/s

Table 6:- Computed Scale Factors for Pristine and Vibration samples
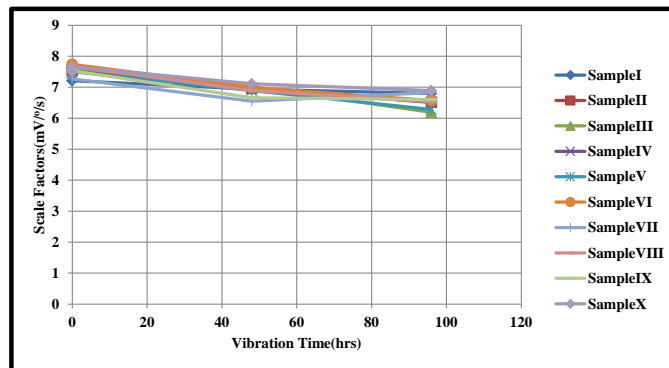
Figure 29:- Scale factor(s) vs Vibration time

Scale factors were computed at 0hours, 48 hours and 96hours for the vibration samples, **Figure 29** shows the decreasing trend in scale factors with increase in exposure time to simultaneous high temperature and vibration.

2.4.2 Effect of simultaneous High temperature and Vibration on Zero-Bias

The average gyroscope output voltage with zero input angular rate, the ideal bias or zero rate level, for LPY510AL MEMS vibratory gyroscope is 1.20V. Although the data sheet promises a zero rate level or zero bias of 1.23V but for all the samples put to test in this section the zero rate output was 1.20V before any harsh environmental tests were conducted. The gyro's output is perturbed by zero-mean thermomechanical noise, which has an effect on the output signal. Generally for MEMS sensors the zero rate level, to some extent, is a result of stress to the sensor. It is believed that this value changes very little over temperature and time [ST microelectronics, 2009], but later in this chapter, in thermal cycling section, we show that zero-bias changes by at least 9% to 11% when exposed to thermal cyclic stress environment.

42
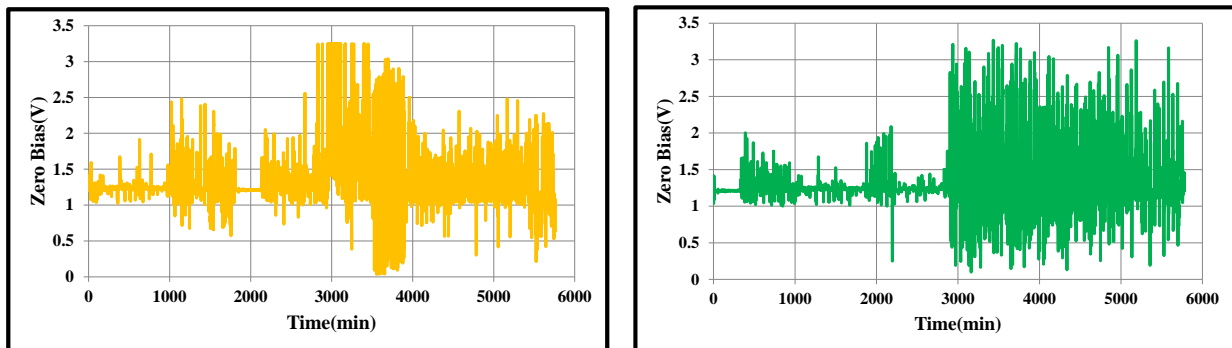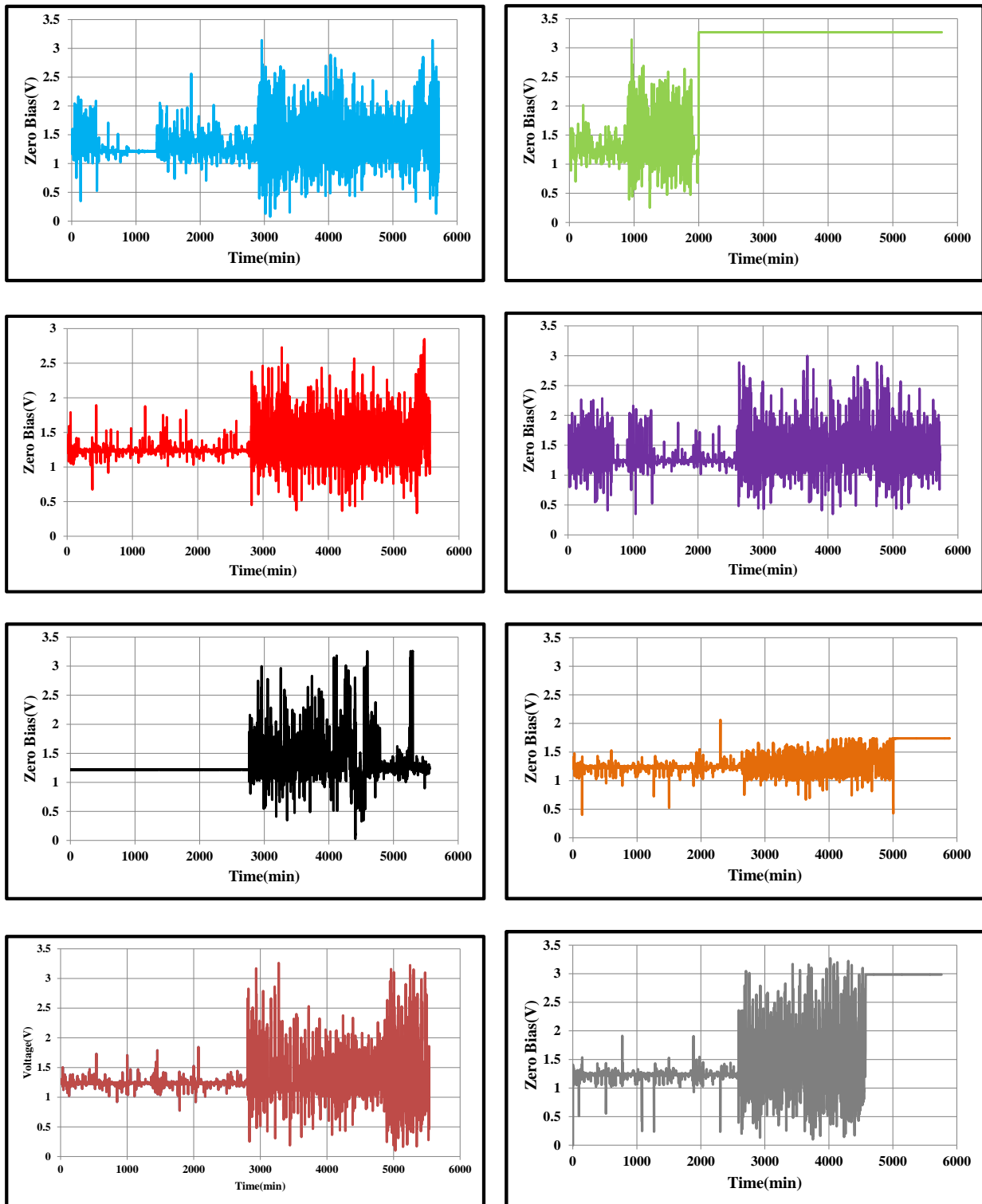
Figure 30:- Zero Bias on exposure to 14G/55°C for Sample I, II , III , IV, V , VI , VII , VIII, IX and X respectively

From the zero-bias plots it can be clearly observed that simultaneous high temperature and vibration has a damaging effect on the zero bias. These plots demonstrate that strong vibration(s) generate a poor solution due to the sensor signal getting saturated and it gets difficult to separate the noise, caused by vibration, from the actual signal. **Figure 30** shows the variation on the zero bias, for entire test duration, when exposed to 14G at 55°C.

As mentioned before after every 48 hours the MEMS test board assemblies were mounted off from the shaker platform and were subjected to rotations between 0°/s – 100°/s. After 48 hours the 14G profile on vibration platform was stopped and before mounting off the MEMS test board assemblies from the vibration platform the zero-bias values were recorded for 15 minutes in order to see whether the zero bias returns back to the original value of 1.20V or not. **Figure 31** shows the zero bias data values at 55°C with no vibration after a period of 48 hours. It can be observed that the zero bias does come back to almost the ideal bias value, apart from sample four which disagrees from the sample set, after completing 48 hours under 14G/55°C. The dotted line in **Figure 31** and **Figure 32** is representing the ideal bias.
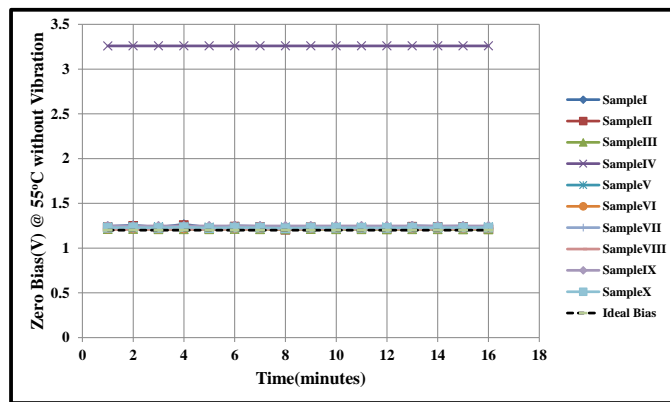
Figure 31:- Zero Bias with no vibration after 48hours
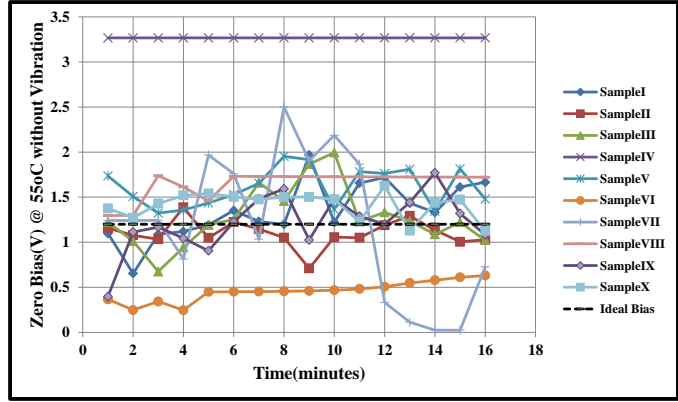
Figure 32:-Zero Bias with no vibration after 96hours

Although this trend of zero bias coming close to its original value is not backed by the plot shown in **Figure 32** which suggests that after completion of 96 hours under 14G/55°C the zero-bias permanently goes awry and does not stay fairly close to its original value of 1.20V.

<table>
<tr><td colspan="2" align="center">**I.**</td><td colspan="2" align="center">**II.**</td></tr>
<tr><td>Mean</td><td>1.223V</td><td>Mean</td><td>1.471V</td></tr>
<tr><td>Error</td><td>.0011</td><td>Error</td><td>.0741</td></tr>
<tr><td>STD.Dev</td><td>.0126</td><td>STD.Dev</td><td>.8386</td></tr>
<tr><td>95%Int</td><td>.0023</td><td>95%Int</td><td>.1466</td></tr>
<tr><td>Max.Vol</td><td>1.266V</td><td>Max.Vol</td><td>2.501V</td></tr>
<tr><td>Min.Vol</td><td>1.203V</td><td>Min.Vol</td><td>0.024V</td></tr>
</table>

Table 7:-Statistical Data for Zero Bias after 48hrs (Table I) and 96hrs (Table II)

As demonstrated in **Table 7** the zero bias mean after 48hrs is close enough to the ideal bias value of 1.20V but not so after the MEMS gyros have experienced 96hrs under the same harsh operating conditions. From the above two tables it can be clearly seen that the statistical mean, standard deviation and standard error for the same samples increase as the exposure time to 14G/55°C increases. The statistical data provided in the two tables within **Table 7** **Table 7** is based on the zero bias data shown in **Figure 31** and **Figure 32** **Figure 31**. The plot below in **Figure 33** helps to better visualize the zero bias but on a single graph

by combining **Figure 31** and **Figure 32**. The zero bias data was recorded for 15 minutes after the 48hr mark and then again for 15minutes after the 96hr mark, note that the data being represented in **Figure 31**, **Figure 32Figure 32 and Figure 33** for zero bias was taken with no vibration but temperature still being at 55ºC.
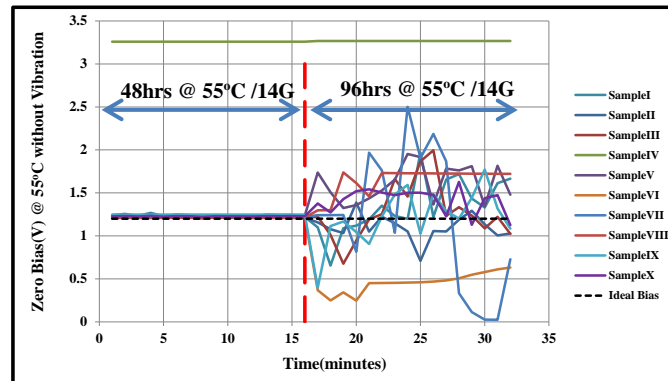
Figure 33:- Zero Bias after 48hrs and 96hrs

Analog Devices [Technical article 2011] show that having g sensitivity compensation cannot entirely be successful as some gyros installed with a compensation scheme vary over a ratio of 12 to 1 from dc to 100Hz when subjected to random vibration. They also show that the error (º/s) due to vibration(s) reduces by half an order of magnitude for some gyros by addition of a g sensitivity compensation scheme. Some gyros which may or may not be optimized for vibration rejection always have unspecified vibration rectification as it is embarrassingly poor or varies greatly from device to device.

2.4.3 Effect of Thermal Cycling on Zero-Bias of a vibratory gyroscope

The effect of thermal cyclic stress environment on the zero rate level of a MEMS gyroscope has been not been studied extensively before and almost no reliability data exists which perfectly describes behavior of MEMS vibratory gyroscope. Although [Wu 2011] describes the sensitivity of a vibratory cylinder gyroscope to temperature changes but the device put to test cannot be deemed as a MEMS gyroscope since its dimensions lie within the macro and meso range. The authors show that varying temperature makes the vibration mode axes unstable which has a significant influence on zero bias stability. In this section we show the incremental drift in the zero bias when exposed to -40°C to 85°C for 250 loops.
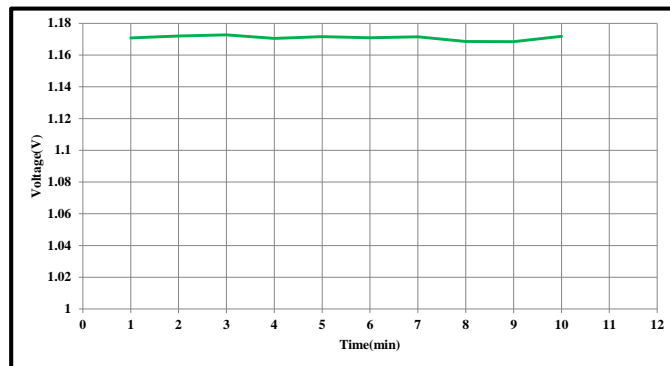
Figure 34:- Zero Bias when profile is dwelling at -40°C
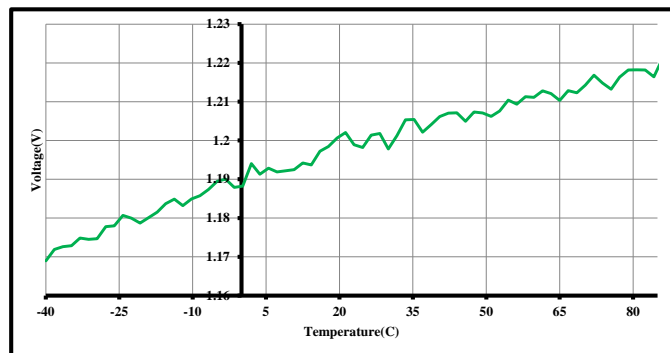
Figure 35:-Zero Bias when profile is ramping up from -40°C to 85°C

47
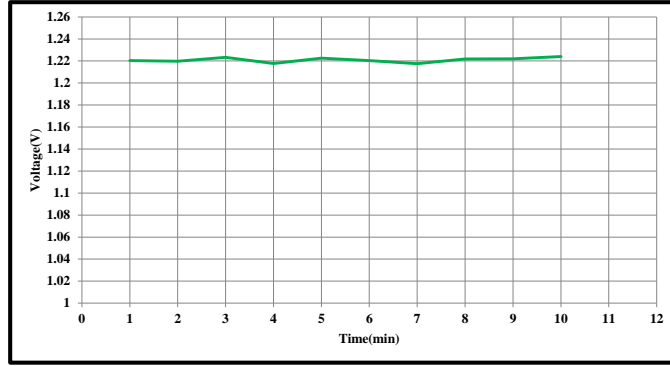
Figure 36:- Zero Bias when profile is dwelling at 85°C
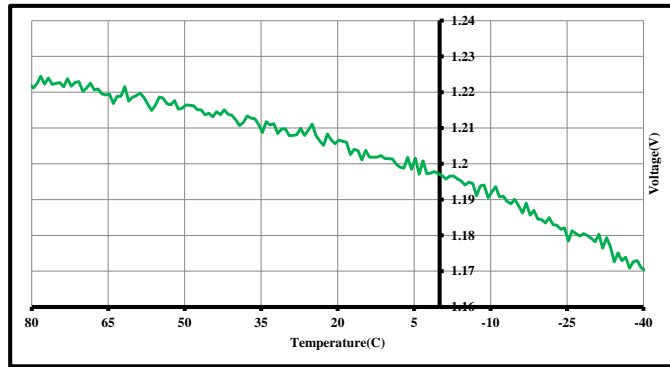
Figure 37:- Zero Bias when profile is ramping down from -40°C to 85°C

Shown above are sample plots in **Figure 34Figure 35, Figure 36, Figure 37 and Figure 34** which demonstrate the behavior of zero bias for LPY510AL for one complete cycle under -40°C to 85°C.

(a)

(b)

(c)

(d)

49
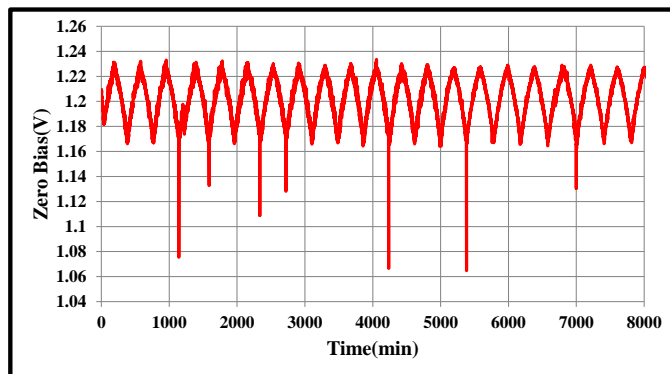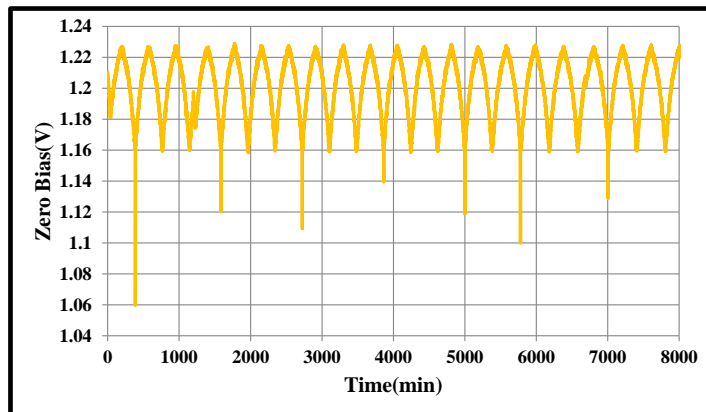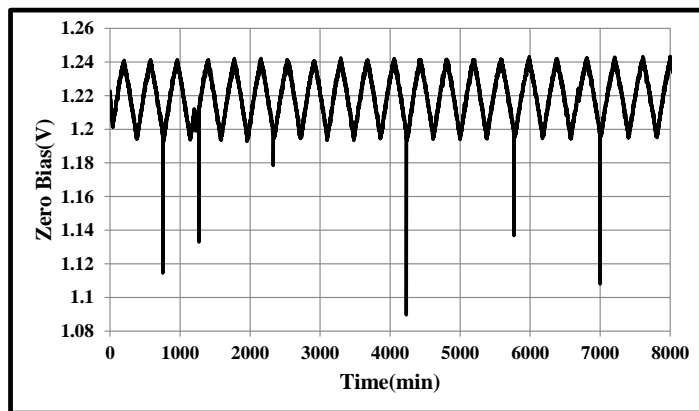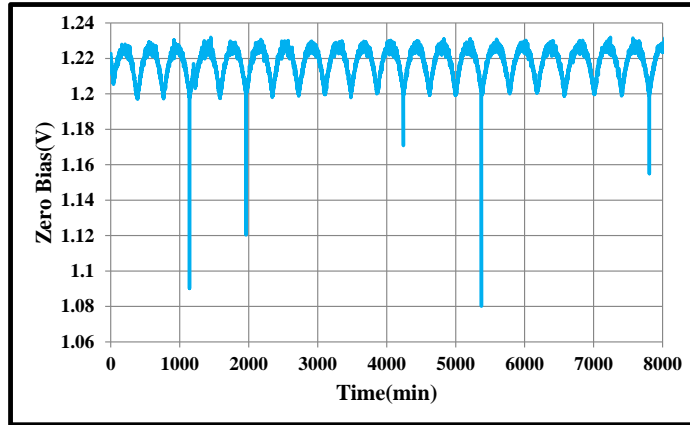
(e)
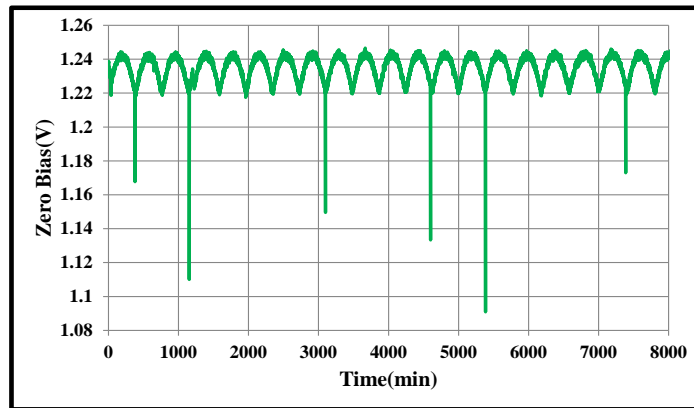
Figure 38:- Zero Bias for Sample one to five (a, b, c, d and e) respectively

The plots shown above represent the behavior of LPY510AL samples under -40°C to 85°C for a period of 8000 minutes. The samples tend to show the same behavior and trend as shown in **Figure 38** (all the sub plots) for the entire 250 thermal cyclic loops. It can be clearly seen from **Figure 34,** **Figure 35Figure 35, Figure 36, Figure 37 and Figure 38** (all the sub plots) that the zero bias for LPY510AL is directly proportional to the change in temperature i.e. for an increasing temperature the zero bias increases and for an decreasing temperature the zero bias goes down. So the minimum recorded voltage or the zero bias value occurs at the lowest temperature (-40°C) and the maximum voltage occurs at the highest temperature (85°C). From all

the plots represented by **Figure 38** it should be noted that there in a sudden plummeting of zero

bias values as the temperature nears -40°C. This trend of values dropping down abruptly at

minimum temperatures is seen for the entire test length and for all the samples. Descriptive

statistics were carried out for all the LPY510AL samples which had been exposed to -40°C to

85°C for 250 cycling loops. **Table 8** shows the statistics such as mean, standard deviation, sample

variance, maximum and minimum voltage for the five samples. Zero Bias difference was

computed for all the samples which is the percentage difference between the lowest or highest,

recorded zero bias value and the ideal zero bias value for LPY510AL which is 1.20V at both the

minimum and the maximum temperature. For example at -40°C the lowest recorded zero bias

voltage, from**,** for sample II is 1.064V; so the percentage difference is

$$\frac{1.20 - 1.064}{1.20} * 100 = 11.33\% \qquad\qquad (2)$$

Similarly zero-bias difference is calculated for all the samples at the two extremes of the thermal

cycling profile. From **Table 9** it can be observed that the zero-bias difference is significantly more

at -40°C as compared to 85°C which states that the zero bias for LPY510AL MEMS vibratory

gyroscopes is more sensitive to lower or subzero temperatures as compared to higher

temperatures.

Stats	Sample I	Sample II	Sample III	Sample IV	Sample V
Mean	1.201V	1.202V	1.219V	1.217V	1.224V
Std.Deviation	.019	.017	.013	.008	.007
Sample Variance	.00036	.00029	.00019	.00039	.00054
Maximum Voltage	1.228V	1.233V	1.243V	1.231V	1.246V
Minimum Voltage	1.059V	1.064V	1.089V	1.080V	1.094V

Table 8:- Descriptive statistics for the 5 LPY510AL samples

Zero-Bias Difference(%)	Sample I	Sample II	Sample III	Sample IV	Sample V
@ -40°C	11.75%	11.33%	9.25%	10%	8.8%
@ 85°C	-2.3%	-2.7%	-3.5%	-2.5%	-3.8%

Table 9:- Zero-Bias difference for all the samples at the two extremes

2.4.4 Effect of simultaneous High temperature and Vibration on Reference Voltage

Reference voltage is a constant DC output voltage produced by the MEMS LPY510AL sensor and its value is 1.23V. This voltage should remain constant irrespective of any loading on the MEMS device, variations in temperature and power supply. Temperature drift or drift due to aging is considered a far more difficult problem than absolute accuracy for reference voltage [Analog Devices, 2009]. Noise is often overlooked in reference voltage but causes an instantaneous change [Analog Devices, 2009]. Therefore vibration induced noise can have a damaging effect on the LPY510AL reference voltage.
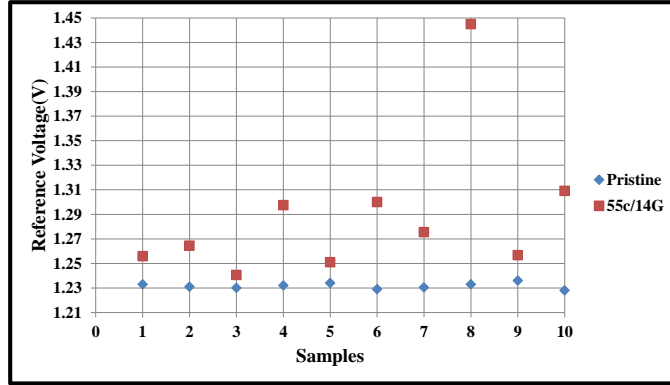
Figure 39:- Reference Voltage for samples after 96hrs of 14G/55ºC and Pristine samples

In **Figure 39** the reference voltages for the LPY510AL samples for both the pristine and the high temperature-vibration cases have been plotted. The red squares represent the high temp-vibration samples and the blue circles represent the pristine voltage samples. The information provided in **Figure 39** agrees with the aforementioned fact that temperature drift and noise can have a damaging effect on the reference voltage for a MEMS vibratory gyroscope. **Table 10** shows that the statistical mean, standard deviation and error of reference voltage(s) for LPY510AL high temp-vibration samples is more than that of pristine samples.

Stats	Pristine	55ºC/14G
Mean	1.231	1.291
Error	.00061	.02321
STD.Dev	.0017	.0656
95%Int	.0014	.0548

Table 10:- Descriptive Statistics for Reference Voltage data for LPY510AL samples

2.5 SUMMARY AND CONCLUSIONS

For this chapter we present a framework to analyze the behavior of a commercially available MEMS vibratory gyroscope on exposure to harsh environmental operating conditions. The dual axis analog rate gyroscope, LPY510AL, was tested under simultaneous high temperature and vibration. The analog rate gyro was also subjected to thermal cyclic stress environment. This methodology investigated and documented incremental damage progression in LPY510AL MEMS vibratory gyroscope and was successful in characterizing the overall behavior of the MEMS device. The evolution of damage was reported in terms of Scale Factor, Zero-Bias and Reference voltage. Drift in the output voltage(s) was observed for samples exposed to a vibration profile of 14G at 55°C. The output voltages drifted more with the increase in exposure time to simultaneous high temp-vibration. Scale factors were computed for both the pristine and high temp-vibration case; a decreasing trend was observed in Scale factors of high temp -vibration samples with the increase in exposure time to simultaneous high temp-vibration. The computed scale factors show significant reduction when exposed to harsh environmental operating conditions in comparison to the pristine samples. From the results documented for Scale factors and variation in output voltage with respect to different angular rates it can be clearly established that the scale factor of a MEMS vibratory gyroscope is very sensitive to simultaneous high temperature and vibration. The effect of simultaneous high temperature and vibration on zero bias was studied and it should be duly noted that the zero bias is greatly affected by the above mentioned harsh operating conditions. With the increase in exposure time to 14G at 55°C the zero bias goes awry and loses its tendency to come back to the original bias value even when there is no vibration present. Plots shown in section II of experimental results demonstrate that strong vibration(s) generate a poor solution due to the sensor signal getting saturated and it gets

difficult to separate the noise, caused by vibration, from the actual signal. A MEMS vibratory gyro whether optimized for vibration rejection or not should always have g sensitivity compensation scheme in order to reduce estimated error due to random vibrations. This chapter also looked into the effect of thermal cycling on the zero bias of LPY510AL; a thermal cyclic stress environment of -40°C to 85°C for 250 loops was subjected to the samples and it was observed that the zero bias or the zero rate level for the MEMS gyro is more sensitive to lower temperatures as compared to higher temperatures. Another key observation reported was that there in a sudden plummeting of zero bias values as the temperature nears -40°C. This trend of zero bias values dropping down abruptly at minimum temperatures is seen for the entire test length and for all the samples. It was also noted that the zero bias for LPY510AL is directly proportional to the change in temperature. Varying temperature, because of thermal cycling, between -40°C to 85°C for 250 loops cause thermal stresses on drive and sense axes of gyro thereby affecting the stability of zero bias. Gyros should be temperature compensated and have an integrated temperature sensor in order to have minimal zero bias variation; Whether the LPY510AL MEMS vibratory gyroscope contains a temperature sensor or is temperature compensated is unknown, since there is no mention of that in the data sheet. A correction factor needs to be added to the gyro when it is subjected to thermal cyclic environment. Simultaneous high temperature and vibration also seem to have an effect on the DC reference voltage of LPY510AL gyro; the reference voltages recorded for high temp-vibration samples were greater than that of the ideal reference voltage value. High temperature aging and noise induced by random vibrations have a deteriorating effect on the DC reference voltage for MEMS vibratory gyroscope.

Chapter 3

Damage Evolution in MEMS Pressure Sensors during High Temperature Operating Life and Prolonged at Sub-Zero Temperature

Harsh environmental operating conditions have been known to have an impact on the life-time of a MEMS device. Therefore, reliable operation is an essential requirement for such devices especially in the areas of military, automotive and space navigation applications. Primarily, the major focus of the current MEMS studies encompasses novel fabrication techniques, effective internal design in order to achieve high quality factors, improved packaging techniques and harsh environmental survivability but in very few works. For harsh environment reliability data MEMS devices need to be monitored under conditions mimicking their areas of applications. Not much attention has been paid to the incremental shift and degradation in output parameters of MEMS devices while under operation. Failure mechanisms and reliability of different classes of MEMS devices are well documented [Fonseca 2011] [Huang 2012] but all together not much effort has been made in assessing the effect of extreme operating environmental stresses on characteristics of MEMS pressure sensors. MEMS pressure sensors are extensively used in high accuracy applications such as barometry, altimetry, wearable technology and weather station equipment. Harsh environment reliability data for such sensors is of utmost importance to MEMS reliability and design engineers. Studies conducted previously as in [Marsi 2015] show the effectiveness of a Silicon Carbide based pressure sensor diaphragm and its ability to sustain and support device operation at temperatures of up to 500°C. Silicon Carbide has stellar material properties which can make it front-runner in harsh environmental applications [Chang 2013]. Due to the material properties possessed by Silicon, electronics based on Si are not able to operate at temperatures beyond 150°C [Yang 2013]. Overall not much effort has been made to study and observe the

incremental evolution of damage progression in MEMS pressure sensors. Reliability data for analyzing the characteristics of MEMS pressure sensors under low temperature storage (LTS) and high temperature operating life (HTOL) conditions is not available especially LTS data sets. In the past [Lall 2017] has shown that diaphragm based devices operating at harsh temperatures lose their ability to respond to the external stimuli with increasing aging time. The authors also show that how oxide formation and metal degradation can cause overall IC instability. Quality, grade, reliability and performance of a MEMS device get affected due to the presence of harsh environmental operating conditions. Survivability of commercial MEMS pressure sensors at high operating temperatures and prolonged storage at sub-zero temperatures is unknown. MEMS pressure sensors make use of a capacitive sensing technique to measure the pressure. It would either have a diaphragm or a membrane as per the requirement of the real world. In most cases the diaphragm or the membrane is constructed using a bossed structure in order to generate a linear capacitance change. During microfabrication of the pressure sensor, the reference cavity is sealed at a certain pressure relative to which the diaphragm/membrane which deflects and creates a change in capacitance. There is another set of pressure sensors which make use of the piezo-resistive technique to measure the change in resistance. To maintain the linearity of the system, when the diaphragm/membrane is bent due to change in pressure, a force-feedback loop or a PPA brings the diaphragm back to its original rest position. As mentioned pressure sensors are categorized in two groups when defining the techniques used to measure the change in capacitance or resistance but commercially there are many different types of MEMS pressure sensors available namely Absolute pressure sensors which measure pressure with respect to full vacuum , Vacuum pressure sensors which measure pressure with respect to 1 atm i.e. negative output for pressure above 1 atm and positive output for pressure less than 1 atm, Gauge pressure

sensors which respond exactly the opposite of Vacuum pressure sensors and finally Differential pressure sensors which measure pressure with respect to the difference in pressure at two points (mostly in fluids). Modern day portable electronics which mostly comprised of pressure sensors are unknowingly subjected to harsh environmental conditions in their fields of applications. Harsh environments such as subzero storage temperatures, high operating temperatures, high-g shock, noise sources and inter-mode coupling result in a significant number of error sources in a pressure sensor, let alone the design and manufacturing issues, resulting in a bad consumer product thus the importance of reliability data. This investigation has been carried out to analyze the output parameters of a commercial MEMS based pressure sensor and assess the accrued damage. In this chapter, a commercially available piezo-resistive, absolute MEMS pressure sensor, MPL3115A2, has been used and the effects of prolonged storage at subzero temperatures and high temperature operating life has been studied. It is manufactured by NXP semiconductors. It has a wide operating range between 20kPa to 110kPa and for this investigation the pressure sensor samples were tested at 85.32kPa or 640mmhg relative to atmospheric pressure. MPL3115A2 makes use of an I^2C digital output interface to communicate with the user. The digital interface has two serial interface communication pins namely serial clock, SCL, and serial data, SDA. Advantage of using an I^2C digital output interface is that it can support large number of slave devices and allows for more than one master device to communicate with the other devices on the bus. MEMS pressure sensors test samples measure external pressure relative to a zero pressure reference (vacuum) sealed inside the reference chamber. This allows for comparison to a standard value of 101325 Pa. The MEMS pressure sensor test samples also utilize an on-chip temperature sensor. The pressure and temperature data is converted to the digital form using a high resolution ADC and the output is in terms of pascals

and °C respectively. For this study the investigation was categorized into three different sets. Each category was comprised of 5 test samples, where in the first set the MEMS test board assemblies were subjected to prolonged storage at -35°C for 120 days. The test samples were taken out from the low temperature storage chamber at a regular interval of 30 days and tested in a vacuum desiccator at 640mmhg. The second set comprised of other 5 test samples which were subjected to 125°C for 120 days, the test samples were powered on at 3.3V during the entire duration of 120 days. Similar to the first test group these test samples were also taken out from the high temperature aging oven at a regular interval of 30 days and tested in a vacuum desiccator at 640mmhg. The remaining 5 MEMS test board assemblies were also tested in a vacuum desiccator at 640mmhg but without any pre-conditioning/aging, this set was considered as pristine. A hardware test-bed was designed to test the MEMS pressure sensors which comprised of a microcontroller unit, a RN-42 based Bluetooth module, 9V battery, vacuum desiccator, vacuum pump, Bluetooth dongle, data acquisition system and passive circuit components. The microcontroller was programmed in a way that it was recording the pressure and temperature readings and sending it to the Bluetooth module via the TX and RX ports. The Bluetooth module was paired with a dongle connected to a data acquisition system which was outside the vacuum desiccator. The data acquisition port was paired with the dongle and a baud rate of 9600 bits was set. Damage evolution in terms of pressure and temperature recorded was studied until the response of the pressure sensor samples had significantly drifted away from the ideal output. Degradation of MEMS pressure sensor parameters such as, absolute pressure and offset under the influence of extreme temperature changes have been observed and documented.

3.1 TEST VEHICLE

MEMS test board assemblies were fabricated and assembled using the surface mount technology line at CAVE3 electronics research center. The test board assemblies have been designed using Free-PCB software. It is a 132mm x 77mm JEDEC standard double sided FR4 material printed circuit board. PCB pads are solder mask defined with immersion finish.
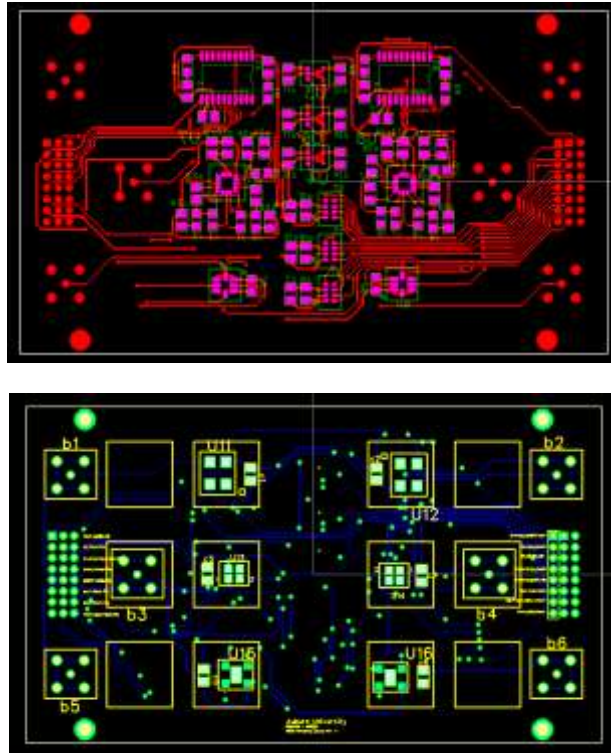
Figure 40:- Test Board Layout
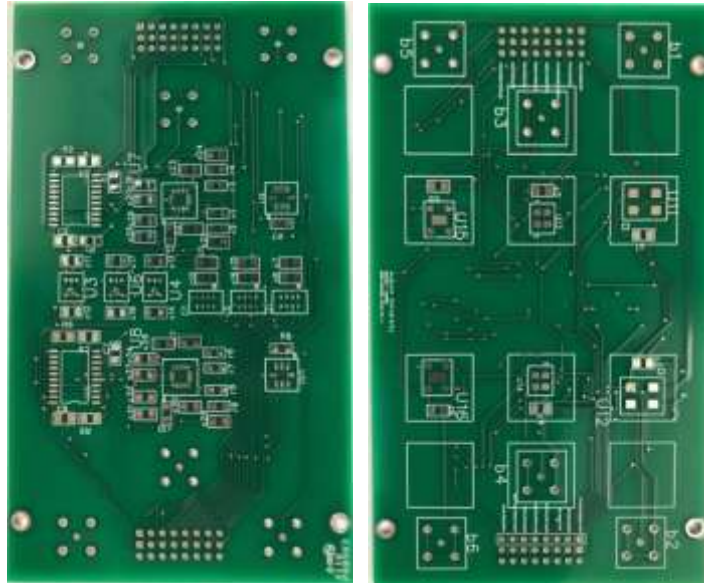
Figure 41:- Test Board Design

The printed circuit board used in this investigation has been fabricated for the testing of Accelerometers, Oscillators, Gyroscopes and Pressure sensors. However this particular study only focusses on MPL3115A2, MEMS piezo-resistive pressure sensor. **Figure 42,** courtesy of NXP semiconductors, shows the test sample inner and outer view.
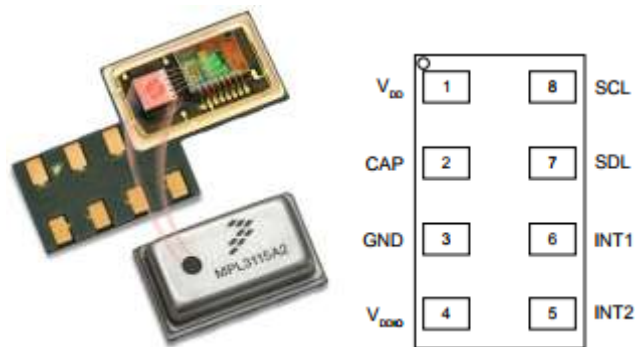
Figure 42:- MPL3115A2 zoomed view and Pin Layout
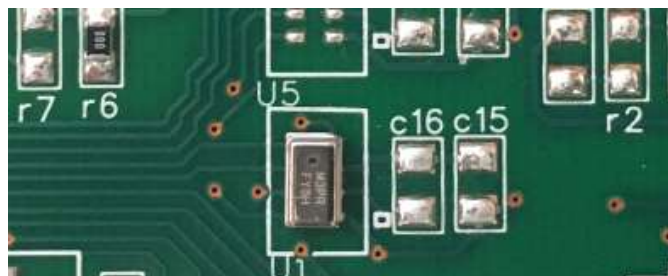
Figure 43:- MPL3115A2 mounted on MEMS test board

MPL3115A2 requires a total of 5 passive components, 3 capacitors and 2 resistors, connected to it. The VDD line supplies the power; decoupling capacitors are put close to pin 1 in order to reduce the noise on the power supply line as seen in **Figure 44** Another 100nF capacitor is used to bypass the internal regulator. Two 330Ω resistors are used between the I^{2}C communication ports on the MCU and SCL and SDA pins of the MEMS device. This was done since the pressure sensor was operating at 3.3V and the MCU was at 5V. **Table 11** demonstrates the different passive components used and their values.

Type	Value	Pin No.
Ceramic Capacitor	100nF	1,3
Ceramic Capacitor	10µF	1,3
Ceramic Capacitor	100nF	2,3
Resistor	330 ohm	SDA, SDA(MCU)
Resistor	330ohm	SCL, SCL (MCU)

Table 11:- Passive Components and their values
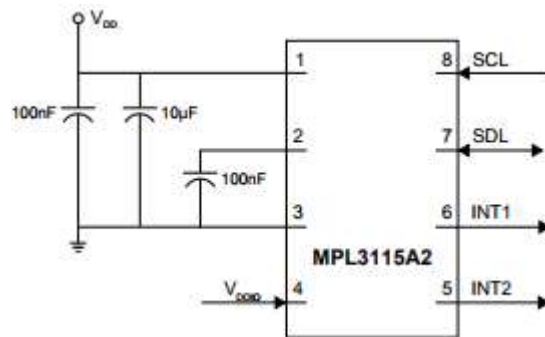
Figure 44:- MPL3115A2 Schematic and pin connections

The MEMS piezo-resistive pressure sensor comprises of a cavity which is filled at a certain pressure and the membrane deflects with respect to that reference pressure. Since it is piezo-resistive in nature it has four micro-fabricated piezo resistors/strain gauges two of which are responsible for measuring compressive strain and the other two measure tensile strain. The

spring constant, k, mass and precise dimensions of the sensing element are unknown since it is proprietary to NXP semiconductors.ST microelectronics. The CMOS IC die sits adjacent to the sensing element and is comprised of the following elements, MUX, ADC, Digital Signal Processing unit, Clock generators, Output data registers and I^2C digital interface unit as shown in **Figure** 45.
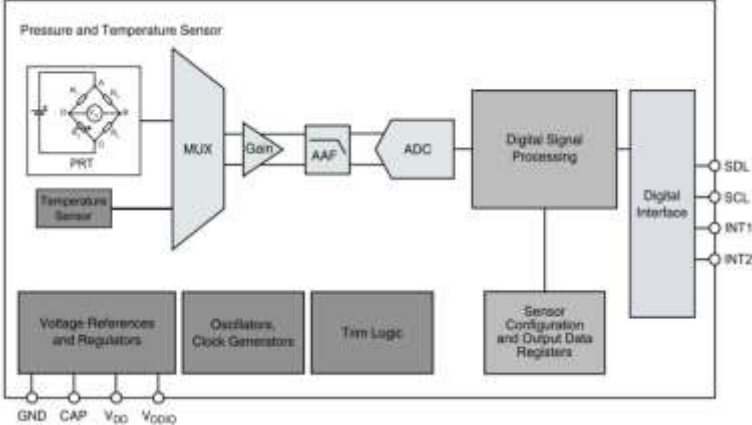
Figure 45:- Block diagram of MPL3115A2 MEMS sensor
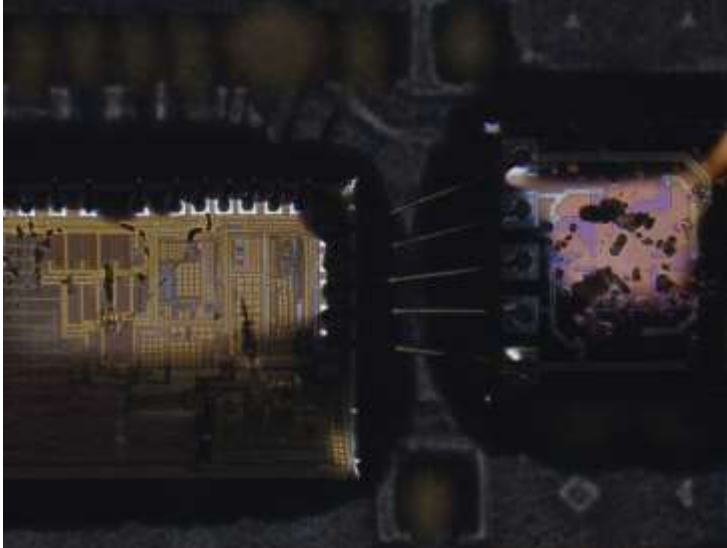
Figure 46:- Microscopic image of the IC die and Sensing element

Figure 46 shows a high resolution microscopic image of the IC control unit along with the sensing element. Figure 47 demonstrates the internal structure of the sensing element along with

the piezo-resistors. **Figure 48** portrays the x-ray image of the MEMS pressure sensor where the membrane and the IC die can be clearly seen. X-ray images were captures using the YXLON CT/X-ray scanner at CAVE3.
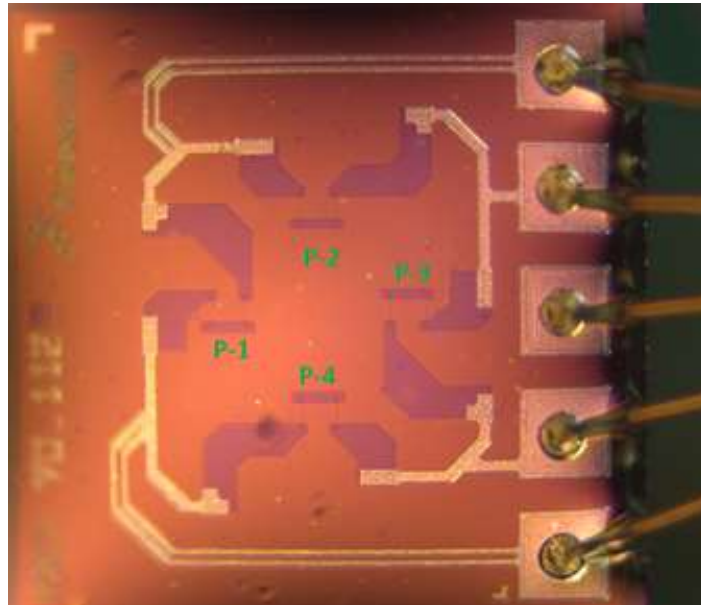
Figure 47:- Internal structure of the sensing element
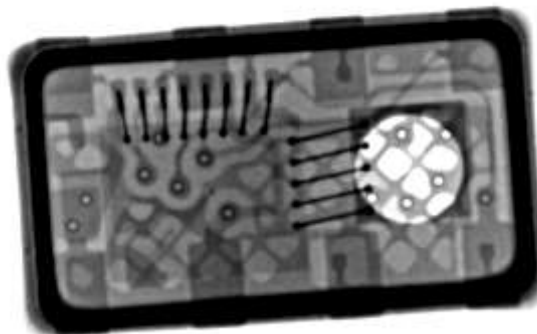
Figure 48:- X-ray image of the piezo-resistive test sample

3.1.1 De-capping Process

A De-capping process which had been applied to MEMS devices in the past [Lall 2017], developed at CAVE3 center, was undertaken in order to view the internal structure of the MEMS pressure sensor. The test board assemblies were de-capped by placing them at 100°C on a hot

plate and adding a small drop of red fuming Nitric acid (HNO_3) at the center of package. Then they were cleaned with a spray of acetone and later dried with compressed air.

MPL3115A2 operates anywhere between 1.62-3.6V, for this investigation it was powered up using the MCU which was operating at 5V; two 330Ω resistors have been used between them since both devices operate at different voltages. **Table 12** provides a list of all the pin connections and pin configurations for MPL3115A2.

Pin No.	Mnemonic	Description
1	Vdd	Power Supply
2	CAP	Ex. Capacitor
3	GND	Ground
4	Vdd-IO	Interface Supply
5	INT2	Pressure Interrupt
6	INT1	Pressure Interrupt
7	SDL	I^2C serial data
8	SCL	I^2C serial clock

Table 12:-MPL3115a2 Pin Configuration
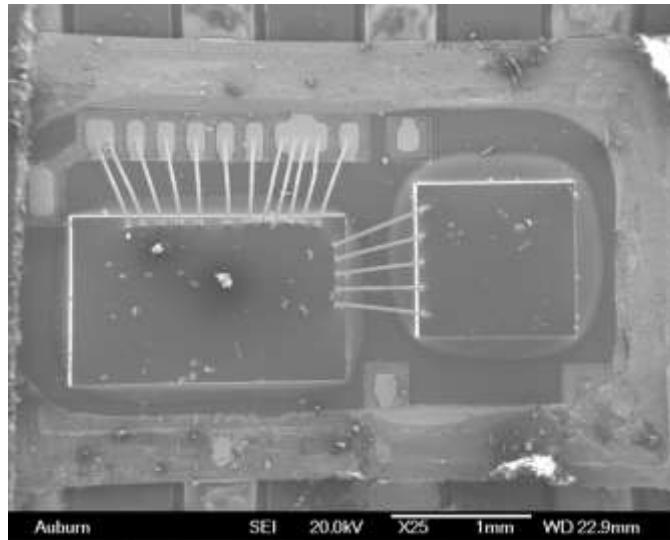
Figure 49:- SEM Image of the MEMS Pressure Sensor

3.2 RELIABLITY TEST MATRIX

A total of 10 MPL3115A2 MEMS piezo-resistive pressure sensors were put to test. For this study the investigation was categorized into three different sets. Each category was comprised of 5 test samples, where in the first set the MEMS test board assemblies were subjected to prolonged storage at -35°C for 120 days. The test samples were taken out from the low temperature storage chamber at a regular interval of 30 days and tested in a vacuum desiccator at 640mmhg. The second set comprised of other 5 test samples which were subjected to 125°C for 120 days, the test samples were powered on at 3.3V during the entire duration of 120 days. Similar to the first test group these test samples were also taken out from the high temperature aging oven at a regular interval of 30 days and tested in a vacuum desiccator at 640mmhg. The remaining 5 MEMS test board assemblies were also tested in a vacuum desiccator at 640mmhg but without any pre-conditioning/aging, this set was considered as pristine. **Table** 13 shows the different test conditions and test parameters applied for this study on MPL3115A2 pressure sensors.

Test Group	Test Condition	Test Parameters	Data Acquisition
1	HTOL	3.3V, 125°C	30,60,90,120…Days
2	LTS	-35°C	30,60,90,120…Days
3	Pristine	3.3V	Start of the test

Table 13:- Reliability test matrix for vibration study

Figure 50 shows the test flowchart used for this investigation The SDL and SCL lines from the pressure sensor are connected to MCU via 330Ω resistors, the MEMS sensor is powered up and grounded from the respective ports on the MCU.
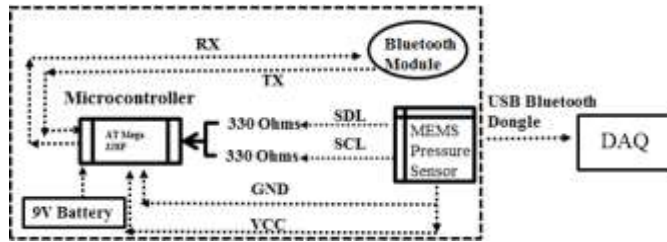
Figure 50:- MPL3115A2 test flowchart

A portable 9V battery is used to power up the AT Mega 328P microcontroller unit which is further connected to a RN-42 Bluetooth module communicating via RX and TX ports. **Figure 51** shows the hardware test bed inside the vacuum desiccator, the Bluetooth module is paired to a USB-Bluetooth dongle which is connected to the data acquisition system.

Figure 51:- Hardware test bed with MEMS test board assembly in the vacuum desiccator

Figure 52:- Bluetooth module and USB-Bluetooth dongle connected to DAQ

A test protocol was written in ARM KEIL software which comprised functions to fetch the digital recorded output pressure in Pascals and temperature in °C. The MCU was loaded, via a mini USB, with this protocol. A specific serial port, which supports communication at a baud rate of 9600 bits, is opened on the DAQ before data is recorded.

3.3 EXPERIMENTAL TEST SETUP

The Surface Mount Technology (SMT) line present at CAVE3 facility has been used for assembling the MPL3115A2 test board assemblies. The SMT line consists of consists of three stages, the Stencil printer, Pick and Place machine and reflow oven as shown in **Figure 54**. For this investigation SAC305 solder alloy has been utilized and evenly distributed on MEMS test board assemblies through the Stencil printer. MPL3115A2 piezo-resistive pressure sensors and 3 surface mount passive components were placed on the MEMS test board assemblies using the Pick and Place machine. After component placement was successfully completed the test board assemblies were baked in the reflow oven. This study is divided into three categories with all the categories being tested inside the desiccator/bell-jar at 640mmhg. This test pressure was selected since it falls between the two extremes of the full scale pressure range of the MEMS device.

Figure 53:- Vacuum Pump and Desiccator

Figure 53 shows the vacuum pump and the desiccator, which has the hardware test-bed, used for this investigation. The vacuum pump has the ability to create vacuum between 0-760mmhg. The vacuum desiccator used for this investigation has a polypropylene bottom and a polycarbonate lid and has the ability to hold a full vacuum of 29.9inhg for 24 hours. It is equipped with a polypropylene stopcock with a PTFE-TFR plug which when turned allows for a gentle, slow entrance of air preventing any unwarranted turbulence and crucible damage. To secure an air-lock a Neoprene O-ring is used between the top lid and the bottom section.
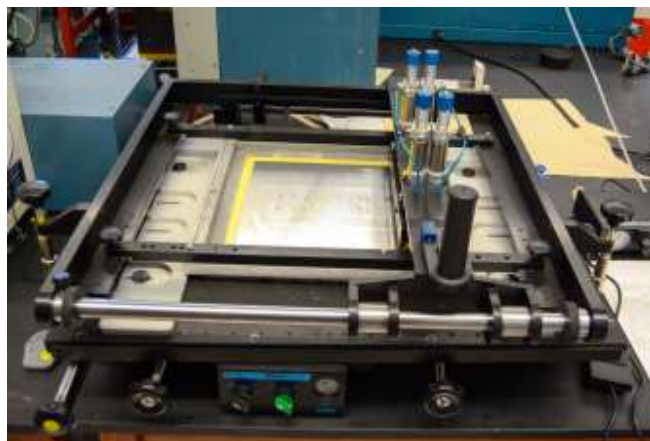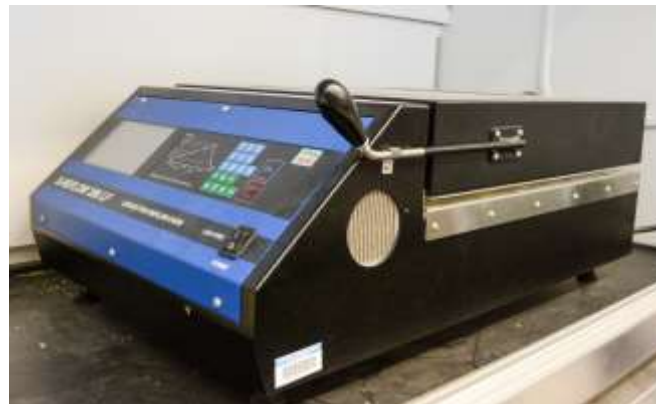
Figure 54:- SMT Line at CAVE3; Stencil Printer (Top), Pick and Place (Middle), Reflow Oven (Bottom)

Test group three which comprised of pristine samples did not undergo any high temperature aging or low temperature storage pre-conditioning; this methodology allows us to administer a productive comparison within the three test groups considering pristine samples as the benchmark.

Figure 55:- HTOL Aging Oven

Figure 56:- LTS Chamber

MPL3115A2 output parameters can be used to calculate the offset and linearity which further can demonstrate whether the pressure sensor test samples are sensitive to high temperature operating life and prolonged storage at sub-zero temperatures or not.

In this investigation the testing methodology is based on an incremental damage evolution approach, which tracks the damage progression by exposing the MEMS test samples to a specific

71

pressure at regular intervals and thereby keeping a tab on the evolution of output parameters. It is a key aspect of this study to analyze whether or not the sensor parameters are drifting significantly with respect to the ideal output(s) and by how much; when exposed to harsh environmental conditions.

3.4 EXPERIMENTAL RESULTS

In this section, a commercially available piezo-resistive, absolute MEMS pressure sensor, MPL3115A2, has been used and the effects of prolonged storage at subzero temperatures and high temperature operating life has been studied. MEMS test board assemblies were put to test under conditions similar to their areas of applications in order to analyze the evolution of stepwise damage progression. For the purpose of this investigation the term failure does not necessarily mean that the device is not working or has suffered a catastrophic failure but rather serves as a pseudonym used to describe the evolution of damage i.e. until the piezo-resistive sensor output parameters drift permanently out of the stable operating range with respect to the ideal output(s). The defining goal behind this incremental investigation, where exposing the MPL3115A2 samples to harsh environments, is to standardize the survivability and reliability for a commercial piezo-resistive pressure sensor for usage in its areas of applications.

3.4.1 Effect of High temperature operating life (HTOL)

MPL3115A2 pressure sensor test board assemblies were subjected to 125°C operating at 3.3V. This test condition surrounds the test samples in a worst case scenario where the stresses act dynamically and approach the maximum absolute in terms various operating parameters such as junction temperature, load current and internal power dissipation [ST microelectronics AN4428].

The main idea behind having the device operate in a biased condition is to study and analyze the presence of failure modes such as wire-bond aging, ASIC oxide faults and metal degradation, if any. **Figure 57** demonstrates the effect of aging at 125°C with increasing duration. As mentioned before five MPL3115A2 test samples were used for this study, the incremental damage evolution can be clearly seen in **Figure 57** which captures the average pressure recorded in Pascals for five samples when exposed to a pressure of 640mmhg each time. The test samples were taken out of the HTOL chamber every 30 days and exposed to the above mentioned pressure in a vacuum desiccator and output pressure was recorded. The inverted triangles in Figure 57 **Figure 57** represent the data points for pristine samples. Since no pre-conditioning is done on the pristine samples the average pressure recorded should not change for them, therefore they can be considered as the benchmark for comparison. HTOL test results indicate that as the test duration increases the average pressure recorded also drifts away significantly from the value of 16000Pa/640mmhg (with respect to atmospheric pressure). As per the manufacturer's specification sheet for MPL3115A2 the allowable resolution for absolute pressure accuracy is +/- 400Pa; all the test samples go beyond this threshold. 4 out of the 5 tested samples drift beyond the threshold value after 90 days of exposure to 125°C at 3.3V; whereas the one remaining sample does go beyond this threshold value but only after 120 days. The initial effect after just 30 days of aging is almost negligible but soon after the trend increases in all the samples.

Figure 57:- Average Pressure Recorded against Aging Time

3.4.2 Effect of Low Temperature Storage (LTS)

MPL3115A2 pressure sensor test board assemblies were subjected to -35°C. This test condition surrounds the test samples in a harsh environment where the device is stored in an unbiased condition at sub-zero temperatures for prolonged time. Not many studies exist which analyze the effects of minimum allowable temperatures for package materials in commercial piezo-resistive MEMS pressure sensors and the failure mechanisms which get activated by extreme cold environments [ST microelectronics AN4428].

Figure 58 demonstrates the effect of prolonged storage at subzero temperature of -35°C with increasing duration. As mentioned before five MPL3115A2 test samples were used for this study, the incremental damage evolution can be clearly seen in **Figure 58** which captures the average pressure recorded in Pascals for five samples when exposed to a pressure of 640mmhg each time. The test samples were taken out of the LTS chamber every 30 days and exposed to the above mentioned pressure in a vacuum desiccator and output pressure was recorded. The inverted triangles in **Figure 58** represent the data points for pristine samples. Since no pre-

conditioning is done on the pristine samples the average pressure recorded should not change for them, therefore they can be considered as the benchmark for comparison. LTS test results indicate that as the test duration increases the average pressure recorded also drifts away significantly from the value of 16000Pa/640mmhg (with respect to atmospheric pressure). As per the manufacturer's specification sheet for MPL3115A2 the allowable resolution for absolute pressure accuracy is +/- 400Pa; all the test samples go beyond this threshold. The drift in LTS test case is much more severe as compared to HTOL test condition; the initial data points, after 30 days at -35°C, for all the five samples are very much consistent to the pristine benchmark but drift significantly as the LTS duration increases. All the test samples go beyond the threshold value after 60 days of LTS storage as opposed to 90 days for the HTOL test case; also the overall average pressure recorded by MPL3115A2 samples is much more during the LTS test case.
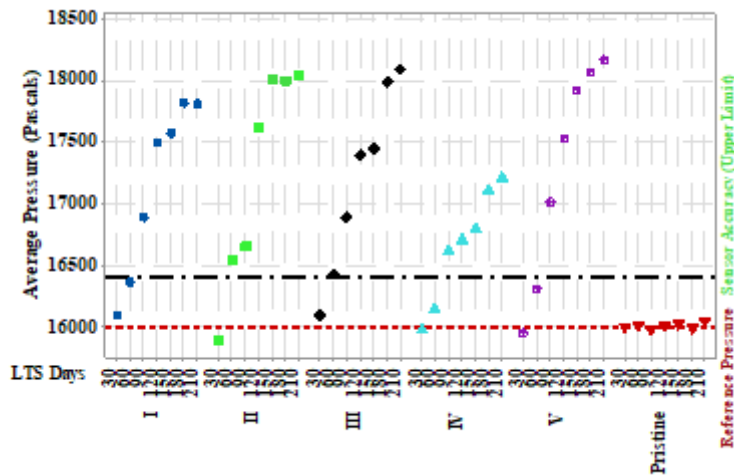
Figure 58:- Average Pressure Recorded against LTS Time

After exposure to 120 days of high temperature operating life and low temperature storage the MPL3115A2 test samples were also subjected to the ambient atmospheric pressure in order to analyze how the pressure sensor behaved when treated to a pressure value which is close to the reference pressure, 101325Pa, sealed within the cavity of the MEMS device instead of a vacuum.

75

Before taking the pressure readings from the test samples, the ambient atmospheric pressure was obtained using a commercial reference pressure sensor and a pristine MPL3115A2 piezo-resistive pressure sensor. **Figure 59** demonstrates the average ATM pressure recordings after subjection to 120 days of LTS and HTOL environments. The reference and the pristine ATM pressure recordings were 99260Pa and 99281Pa respectively; the atmospheric pressure at sea level was 101325Pa and since all the data was captured at 210m above the sea level therefore we see a pressure difference when comparing pressure readings from reference sensor/pristine sensor to the pressure at sea level.
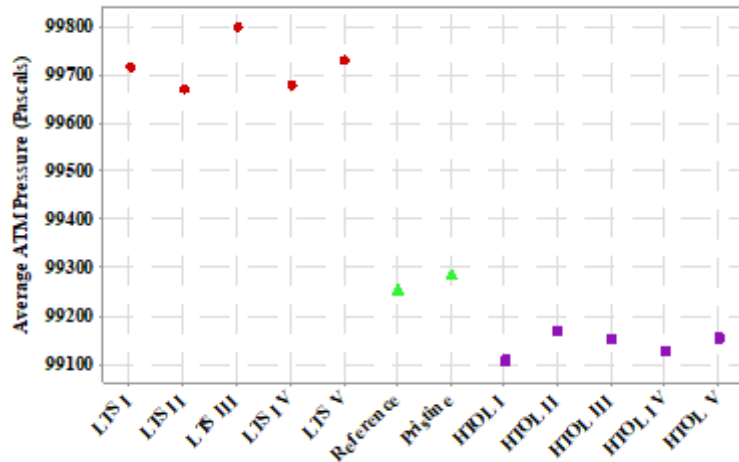
Figure 59:- Average ATM Pressure after 120 Days of LTS and HTOL

It can be clearly visualized from **Figure 59** and **Figure 60** that the LTS test samples have much severe damage after prolonged storage at sub-zero temperatures as compared to HTOL test samples. MPL3115A2 high temperature operating life test samples seem to perform much better as they fall within the manufacturer's specification of +/- 400Pa at ambient pressure close to the reference pressure sealed within the cavity of the MEMS device which is not the case for LTS test samples.
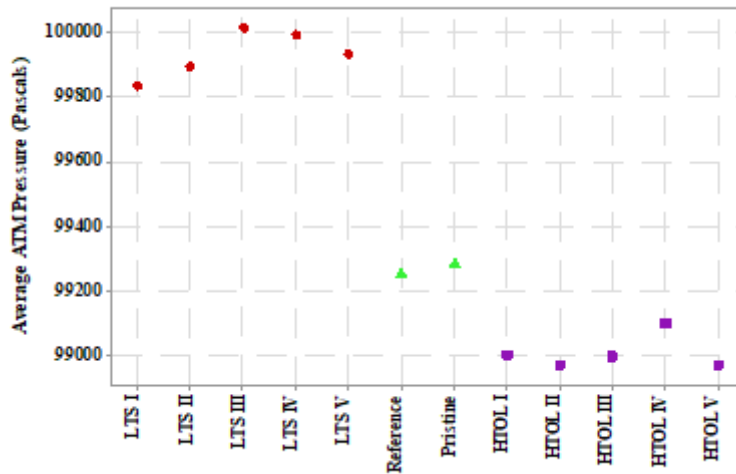
Figure 60:- Average ATM Pressure after 180 Days of LTS and HTOL

However both test board assemblies from both the test conditions seem to fall apart and drift significantly away from the ideal output(s) when subjected to pressure(s) within the vacuum range as shown before.

3.4.3 Effect of Pressure Change

The responsiveness of the MEMS pressure sensors was gauged through a sudden change in pressure from vacuum at 640mmhg to the atmospheric pressure. **Figure 61** demonstrates the pressure change curve(s) for all the tested MEMS samples. The average pristine curve, combined average of ten pristine samples, displays almost the same characteristic as that of the reference curve while LTS and HTOL samples behave in a different manner. This characteristic of the MEMS sensor helps in understanding how the pressure detection and change in pressure is perceived by the piezo-resistive mechanism within the pressure sensor. Both LTS and HTOL samples are impacted as they seem to be less responsive to the pressure change as compared to pristine and reference test cases. Ideally the LTS and HTOL pressure change curves should be as close as possible to the pristine and reference cases but due to long-term exposure to harsh
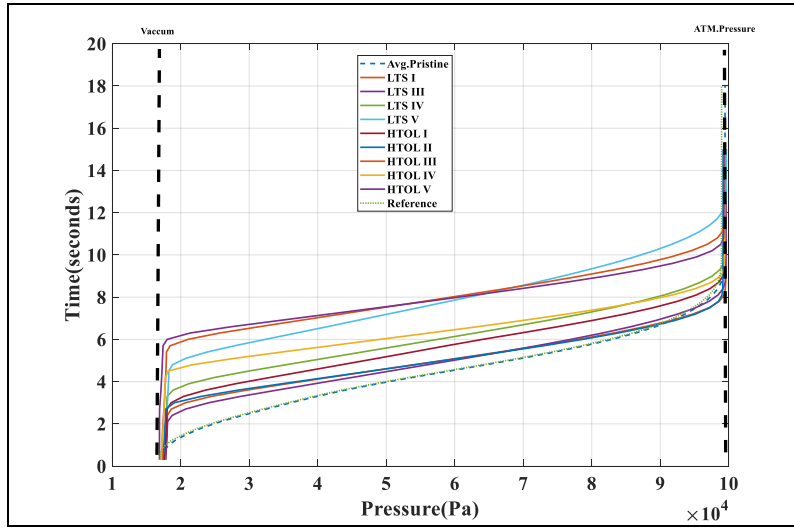
Figure 61:- MEMS pressure sensor response to the change in pressure

environments there is a significant delay in the response characteristic of these curves which affect the effectiveness and efficiency of the sensor system.

3.4.4 Effect on Temperature Sensor

MPL3115a2 pressure sensor is temperature compensated and utilizes an on-chip temperature sensor. Shown in **Figure 62** are the recorded temperatures in °C under a vacuum of 640mmhg from five pristine samples where the number of observations for each sample is 301. Total number of histogram bars denote the different temperatures observed by the on-chip temperature sensor, ideally the less temperatures observed the more accurate is the on-chip temperature sensor.
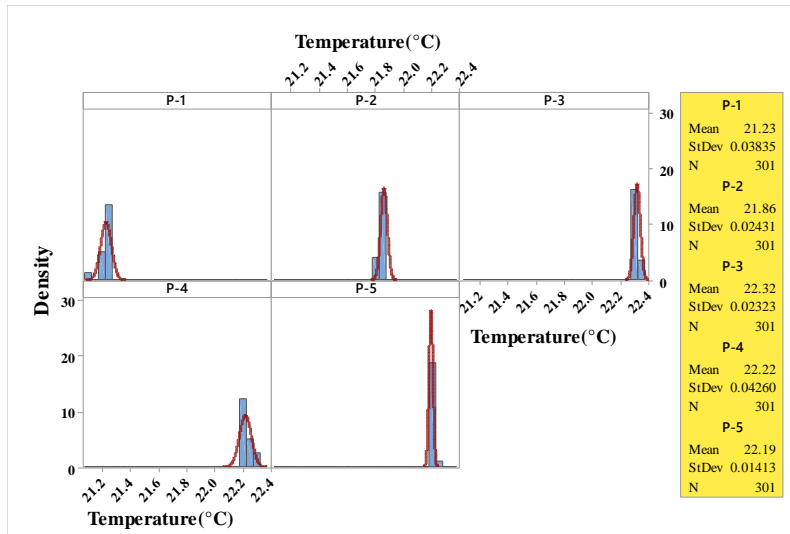
Figure 62:- Temperature recordings for five pristine samples

The ideal temperature range measured using a reference temperature sensor within the vacuum desiccator at 640mmhg was between 21.8°C and 22.2°C. The temperature recordings from all the pristine samples fall within that range, except pristine sample I.
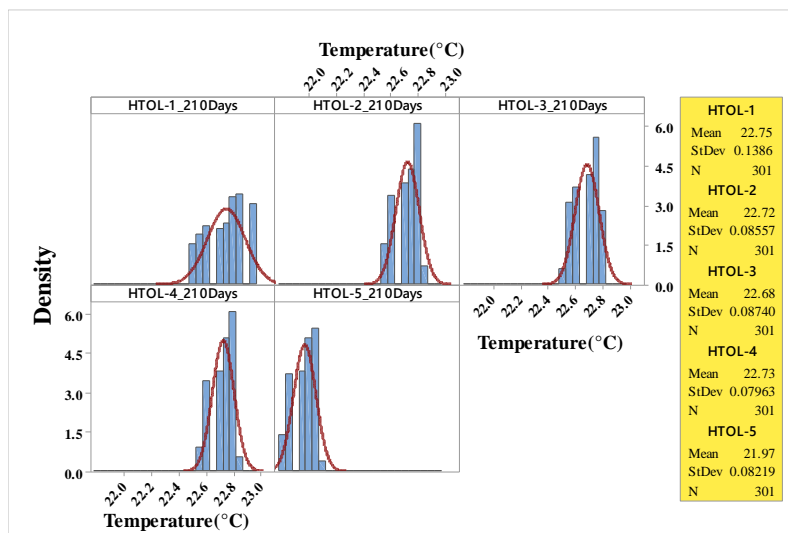
Figure 63:- Temperature recordings for five HTOL samples, under vacuum, after 210 Days of exposure to 125°C at 3.3V

It can be clearly visualized when comparing **Figure 62, Figure 63** and **Figure 64**, that prolonged storage at -35°C and prolonged exposure to 125°C at 3.3V for well over 6months can induce multiple false temperature recordings. Although the temperature recordings after 210 days of

LTS and HTOL exposures don't result in drastic differences when compared to the pristine and reference benchmarks. The HTOL samples show a temperature offset of 0.75°C whereas the LTS samples which have been more affected by their respective harsh environment, as demonstrated in section II, show a temperature offset of 1.13°C.Also the computed statistical data portrays that HTOL and LTS samples show much more variance in temperature recordings after 210 days. As indicated by the results below there is much more variance in temperature readings for LTS samples as compared to their HTOL counterparts.
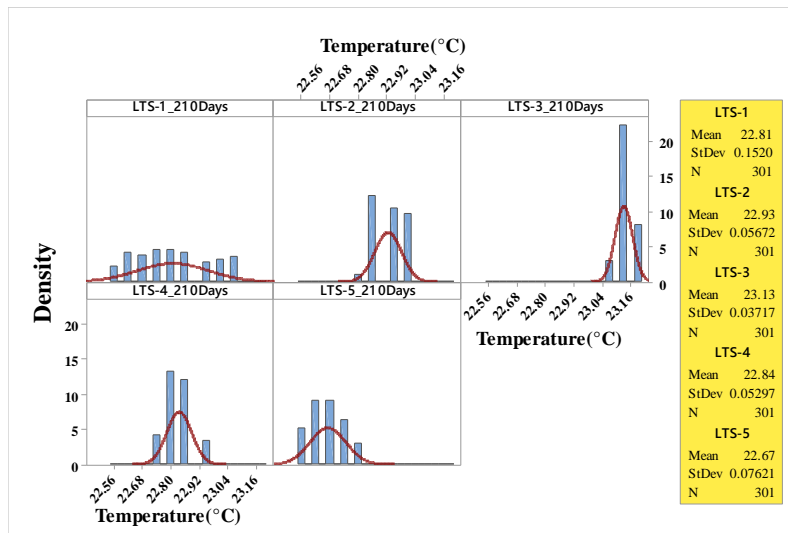
Figure 64:-Temperature recordings for five LTS samples, under vacuum, after 210 Days of storage at 35°C

3.5 FAILURE ANALYSIS

MEMS failure mechanisms and modes for harsh environments involving space, radiation, vacuum and thermal-vibration shocks have been previously studied [Shea 2006] but identifying failure modes and sites for membrane based sensors subjected to long-term exposure to high operating temperatures and low temperature storage have yet to be demonstrated.
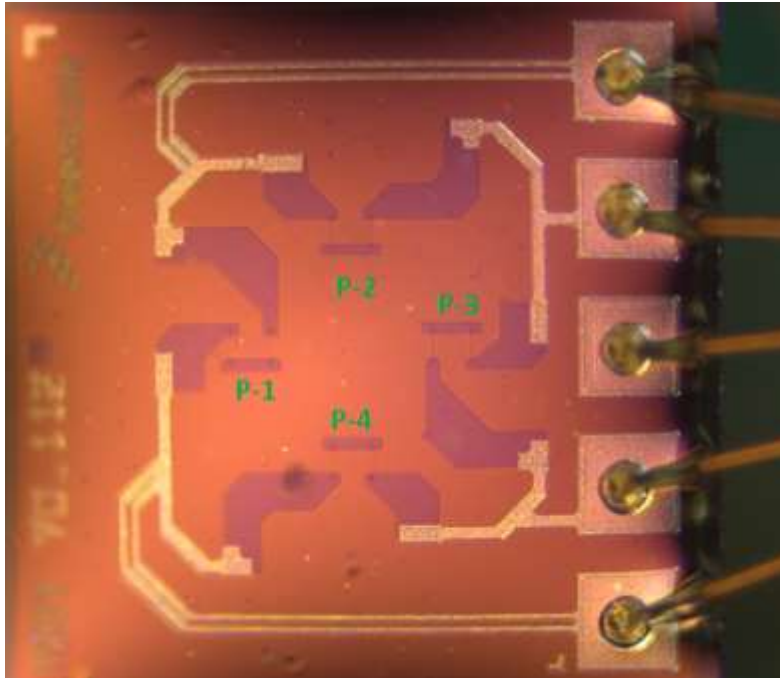
Figure 65:- MEMS pressure sensing element with four piezo-resistors

MPL3115a2 has an adjacent configuration where both the MEMS sensing element, piezo-resistors in wheat stone bridge arrangement, and application specific integrated circuit (ASIC) lie adjacent to each other connected through wire-bonds as shown in **Figure 65**.
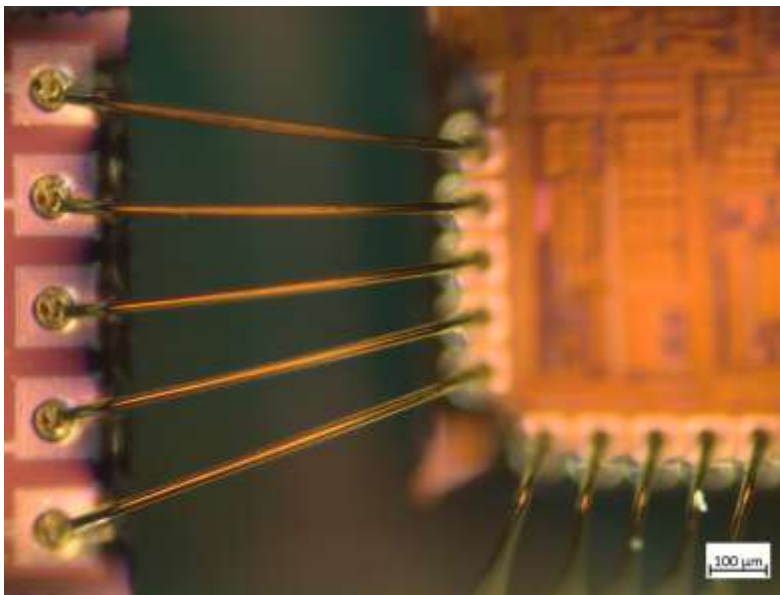
Figure 66:- Wire bonds connecting ASIC die to sensing element
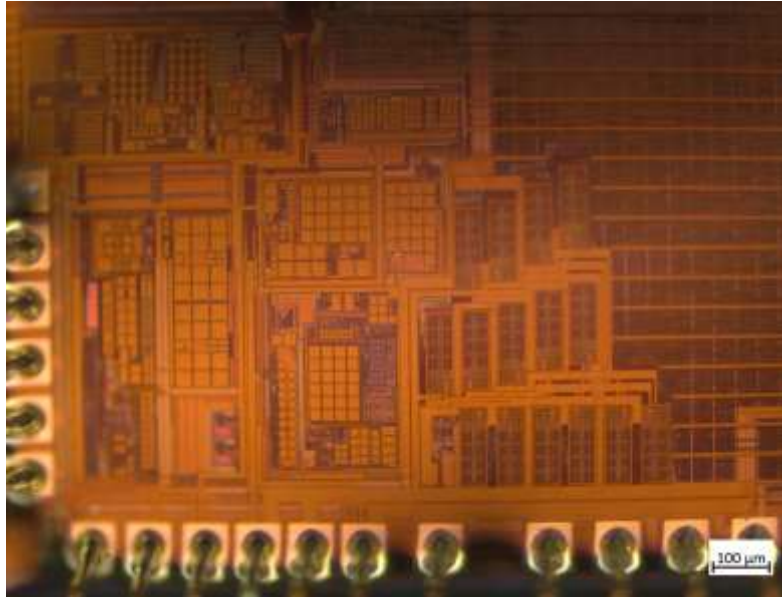
Figure 67:- ASIC die on MPL3115a2

3.5.1 FAILURE MODES

After intensive exposure to the above mentioned harsh environmental conditions, the MPL3115a2 test samples were de-capped and analyzed for potential failure modes and sites. Since the pressure sensor is a commercial product, manufactured by NXP semiconductors, no prior information regarding the internal structure was known.

It was observed that no visual or physical damage was accrued by the MEMS sensing element for both the HTOL and LTS test cases apart from one HTOL sample shown in **Figure 69**. **Figure 65 - Figure 67** represent a pristine sample and how the internal structure looks like. As depicted in **Table 14** most of the damage circumscribed the ASIC die with localized burn-sites and crack sites. It should be noted that only 3 out of the 5 tested HTOL samples had burn/crack-sites and only 1 out of 5 test LTS samples had potential crack-site on the ASIC die. The overall damage reported in above sections, in terms of drift in the pressure and temperature recordings, can be attributed to long-term aging and usage of a product.

Table 14 demonstrates the different failure modes observed on long-term exposure to HTOL and LTS.

Pre-Condition	Failure-Modes	Test Condition	Test Duration
HTOL 125°C	Localized burn-sites and cracks	Low-Vacuum @ 640mmhg	7months/210 days
LTS -35°C	Crack on the ASIC die		

<div align="center">Table 14:- Failure Modes</div>
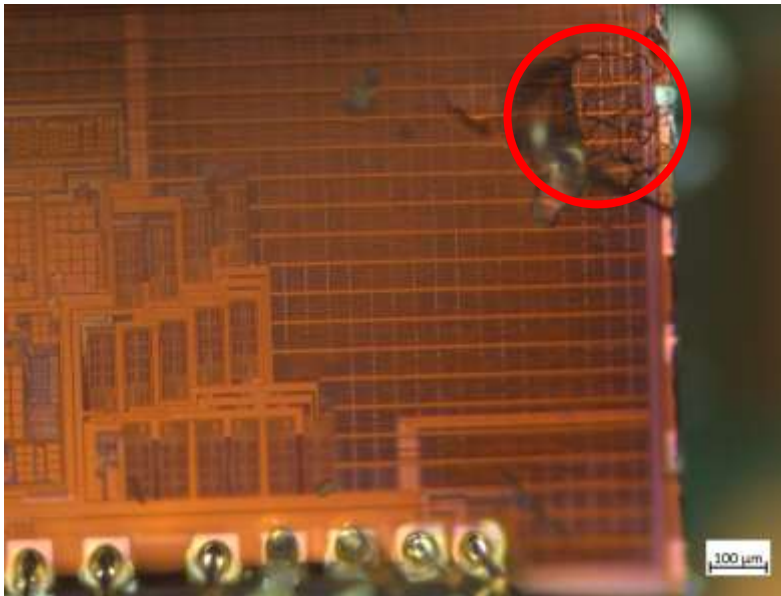
Figure 68:- HTOL sample with burn-crack site on ASIC after 210 days of aging at 125°C/3.3Volts
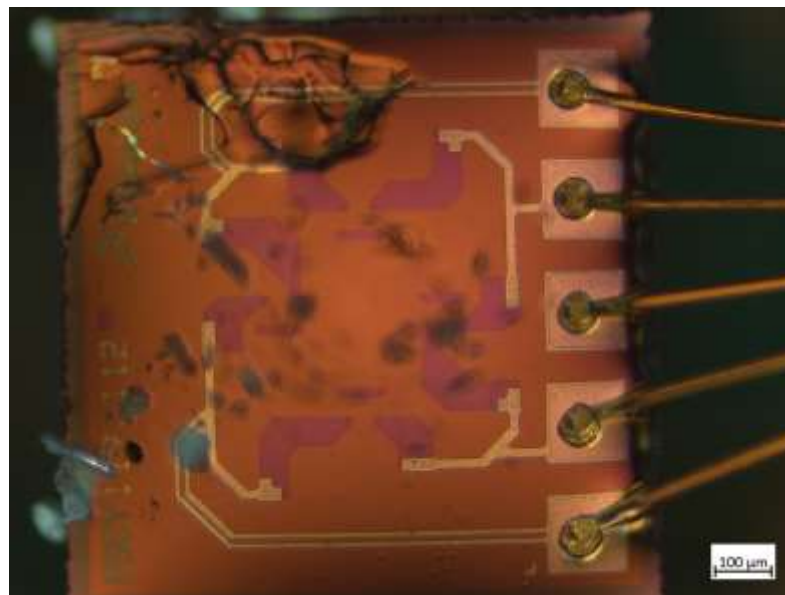
Figure 69:- HTOL sample with burn-site on MEMS sensing element after 210 days of aging at 125°C/3.3Volts
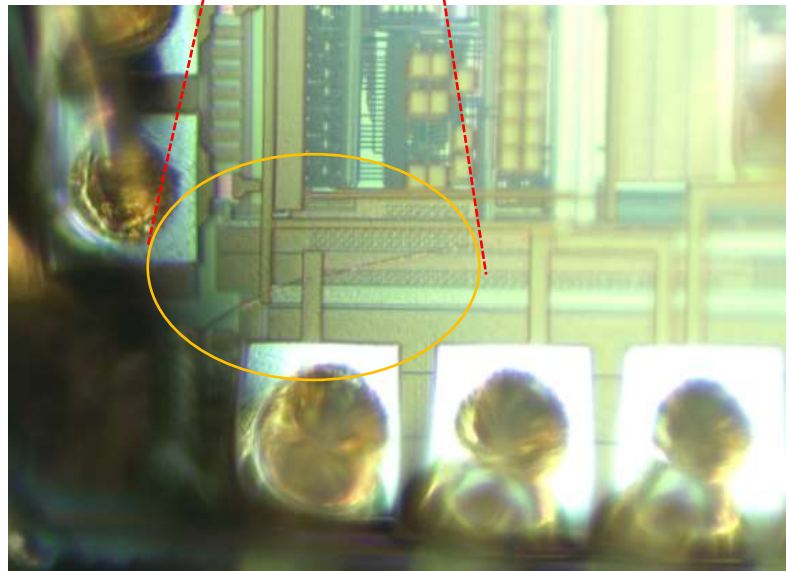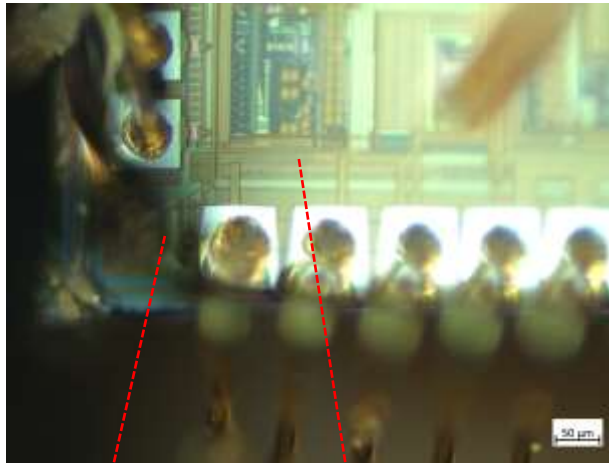
Figure 70:- LTS sample with crack running through the ASIC die after 210 days of aging at -35°C

3.6 SUMMARY AND CONCLUSIONS

In this chapter we present a test protocol for analyzing the characteristics of a commercially available MEMS pressure sensor on exposure to harsh environmental operating conditions. The piezo-resistive pressure sensor, MPL3115A2, was tested under two different harsh environments; high temperature operating life and prolonged storage at sub-zero temperatures. This test protocol helped in investigating and documenting the incremental damage evolution in MPL3115A2 MEMS pressure sensor and was successfully able to characterize and capture the

overall behavior of the MEMS device. The defining goal behind this incremental investigation is to standardize the survivability and reliability for a commercial piezo-resistive pressure sensor for usage in its areas of applications. HTOL test results indicate that as the test duration increases the average pressure recorded drifts away significantly from the value of 16000Pa/640mmhg (with respect to atmospheric pressure) which is the vacuum level during testing. As per the manufacturer's specification sheet for MPL3115A2 the allowable resolution for absolute pressure accuracy is +/- 400Pa; all the test samples go beyond this threshold. 4 out of the 5 tested samples drift beyond the threshold value after 90 days of exposure to 125°C at 3.3V; whereas the one remaining sample does go beyond this threshold value but only after 120 days. The initial effect after just 30 days of aging is almost negligible but soon after the trend increases in all the samples. LTS test results also indicate that as the test duration increases the average pressure recorded also drifts away significantly from the value of 16000Pa/640mmhg. The drift in LTS test case is much more severe as compared to HTOL test condition; the initial data points, after 30 days at -35°C, for all the five samples are very much consistent to the pristine benchmark but drift significantly as the LTS duration increases. All the test samples go beyond the threshold value after 60 days of LTS storage as opposed to 90 days for the HTOL test case; also the overall average pressure recorded by MPL3115A2 samples is much more during the LTS test case. Results from the HTOL and LTS test samples subjected to ambient atmospheric pressure at 210m above sea level show that the LTS test samples have much severe damage after prolonged storage at sub-zero temperatures as compared to HTOL test samples. MPL3115A2 high temperature operating life test samples seem to perform much better as they fall within the manufacturer's specification of +/- 400Pa at ambient pressure close to the reference pressure sealed within the cavity of the MEMS device which is not the case for LTS test samples.

85

However both test board assemblies from both the test conditions seem to fall apart and drift significantly away from the ideal output(s) when subjected to pressure(s) within the vacuum range as shown before. Results from the effect on temperature sensor indicate that due to long-term exposure to harsh environmental conditions for well over 6months can induce multiple false temperature recordings. Although the temperature recordings after 210 days of LTS and HTOL exposures don't result in drastic differences when compared to the pristine and reference benchmarks. The HTOL samples show a temperature offset of 0.75°C whereas the LTS samples which have been more affected by their respective harsh environment, as demonstrated in section II, show a temperature offset of 1.13°C. 3 out of the 5 tested HTOL samples had burn/crack-sites and only 1 out of 5 test LTS samples had potential crack-site on the ASIC die. The overall damage reported in above sections, in terms of drift in the pressure and temperature recordings, can be attributed to long-term aging and usage of a product.

Chapter 4

Effects of Sustained Exposure to Temperature and Humidity on the Reliability and Performance of MEMS Microphone

MEMS microphones are extensively used in almost all applications that require reliability, small size, and high sound quality. For harsh environment reliability data MEMS microphones need to be monitored under conditions mimicking their areas of applications. MEMS microphones have an opening/sound port in order to interact with the environment, therefore cannot be sealed completely since the sensing mechanism requires interaction between sound waves and the sensing element. Little to no information exists on reliability data for MEMS microphones under low/high temperature operating life and temperature humidity bias condition. Our work is primarily focused on providing harsh environmental reliability data which can be useful to MEMS designers and engineers. In this chapter the test vehicles with MEMS Microphones have been tested under three different harsh environmental conditions: high temperature operating life (HTOL) at 125°C at 3.3V, low temperature storage (LTS) at -35°C and temperature humidity 85°C/85%RH at 3.3V. The main motive of this study is to document the incremental shift and degradation in output parameters namely distortion, frequency response, power supply rejection capability of IC, frequency vs pressure characteristics and analog output voltage of the MEMS microphone. The survivability of MEMS microphone, ADMP401, has been demonstrated as a function of change in the output parameters. Failure analysis has been conducted on the microphone samples to study failure modes and sites using analytical methods such as SEM, EDS and X-ray. In past only few studies have been conducted regarding reliability of MEMS microphones, of which some demonstrate the effect of high impact loading [Fang 2013], authors

87

studied the mechanical reliability of MEMS microphones subjected to very high g shocks and demonstrated the characteristics of diaphragm under shock loadings of up to 30000G. Finite element simulations have also been used to study the shock impact loading on a MEMS microphone and study the potential failure sites [Li 2013]. The effect of airborne impurities and humidity on MEMS microphone has been also been studied [Broas 2015], who observed galvanic corrosion in thin film Silicon MEMS. Overall Failure mechanisms and reliability of different classes of MEMS devices are well documented [Fonseca 2011] [Huang 2012] but all together not much effort has been made in assessing the effect of extreme operating environmental stresses on characteristics of MEMS microphones. Previous studies and research areas do not study and observe the incremental evolution of damage progression in MEMS microphones. Also, reliability data for analyzing and understanding the characteristics of MEMS microphones under low temperature storage (LTS), high temperature operating life (HTOL) and temperature humidity bias (THB) conditions is not available. Importance of reliability data for MEMS designers and engineers is of the utmost priority since extreme environmental operating conditions affect the grade, reliability and performance of a MEMS device. MEMS microphones have a similar detection scheme as MEMS pressure sensors which comprises of capacitive sensing using the technique of PPA. Depending upon the application of the sensor it would either have a diaphragm or a membrane. Generally the diaphragm or the membrane will have a bossed structure in order to generate a linear capacitance change. MEMS microphone used in this investigation was ADMP401, an omnidirectional microphone with bottom port and analog output, ideal for smartphones, digital video cameras, video phones and tablets. The sensor is a simple silicon capacitor consisting of two silicon surfaces where one surface is fixed and the other is movable. The fixed surface/plate is conductive in nature and is comprised of acoustic

holes. The movable plate/surface has ventilation holes which allow the membrane/diaphragm to move back and forth. An application specific integrated circuit is connected via wire bonds to the MEMS structure which converts the polarized capacitance into analog voltage output. The IC is comprised of an impedance converter and an output amplifier. The MEMS structure and the IC are housed in a 4.72mm x 3.76mm x 1mm surface mount package which encloses all the components. For ADMP401, the sound port is constructed by drilling the substrate as per the location of MEMS sensing structure. In this architecture the front chamber is the cavity of the MEMS sensor and the back chamber is created by the package. Resonant chambers are distinguished depending on the location of respective chambers in reference to the progressing sound wave. The MEMS sensor is right under the sound port and the two components, MEMS sensor and IC, are attached onto the substrate. MEMS microphones such as ADMP401 and its internal circuitry are unintentionally exposed to harsh environmental conditions when operating in their fields of applications. Extreme environments such as high-g shock, vibration, thermal stresses, noise sources, humidity and intermode coupling can lead up to a number of error sources in a MEMS microphone resulting in a bad consumer product thus the importance of reliability data. Presence of sophisticated and intricate MEMS technology in microphones generates a significant lack of reliability data that looks into the impact of low temperature storage (LTS), high temperature operating life (HTOL) and temperature humidity bias (THB) on characteristics of MEMS microphones. The fundamental objective behind this research work is to observe and anatomize the output parameters of a commercial MEMS microphone and assess the accrued damage. The reliability data shown in this dissertation represents damage progression in MEMS microphones till failure. Three different sets of experiments where conducted in this piece of study where in the first set the MEMS test board assemblies, MEMS

microphone mounted on a FR4 layer PCB, were subjected to high temperature operating life 125°C at 3.3V. The MEMS test boards were put in a thermal aging oven set at the above mentioned parameter and a total of 10 test board assemblies were subjected to harsh environment operating condition. For the second test the MEMS test board assemblies were subjected to temperature-humidity bias environment, 85°C/85%RH at 3.3V. A total of 10 test board assemblies were subjected to THB operating environment. Lastly, for the third test the MEMS test board assemblies were subjected to low temperature storage, -35°C. A total of 5 test board assemblies were subjected to LTS operating environment. MEMS test board assemblies from all the three sets where taken out from their respective chambers after an interval of every 100 hours and put to test in a reverberation chamber. A sine sweep sound ranging from 100Hz to 15KHz is played as the test sound since this range falls in the full scale band of the MEMS microphone. Room equalizer wizard (REW), an open source acoustics software has been used to capture the frequency response of the MEMS microphone samples with respect to sound pressure level. Further this frequency response from the microphone samples has been used to compute the distortion over the entire audio band. Another parameter which was monitored for damage progression is Power supply rejection ratio in order to analyze the degradation in the capability of the ASIC to reject noise added to the supply voltage. The raw output voltage from ADMP401 has also been recorded for all the samples on which Fast Fourier analysis has been performed in order to see damage progression in the amplitude of the voltage output. The objective of this experiment was to compute and compare the frequency response, distortion, PSRR and voltage outputs for pristine and HTOL, LTS and THB samples thereby assessing the accrued damage in the microphone. Degradation of MEMS microphone parameters has been observed and documented.

4.1 TEST VEHICLE

Free-PCB, open source software was used to design the MEMS test board. The dimensions of test board are 132mm x 77mm. It is a JEDEC standard double sided FR4 material PCB. PCB pads are solder mask defined with immersion finish. The test boards were fabricated and then assembled using the surface mount technology line present at CAVE3 electronics research center.
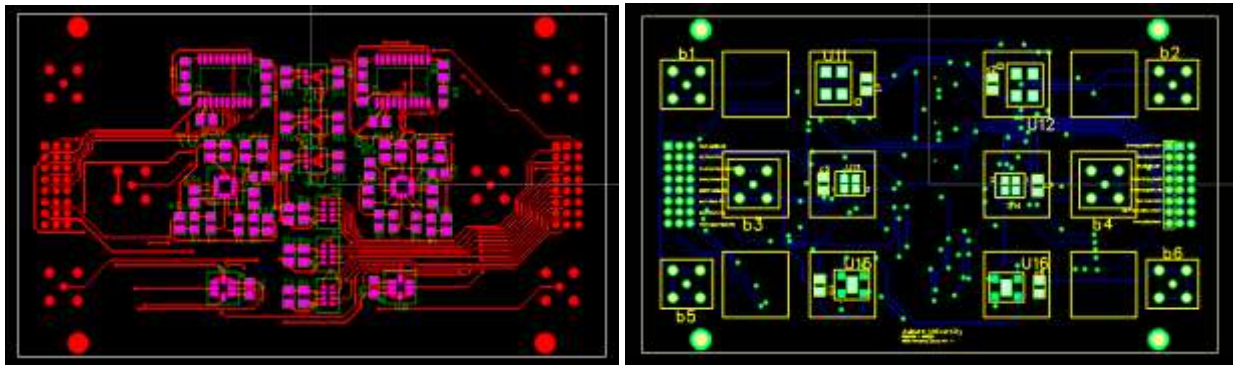
Figure 71: - Test Board Layout
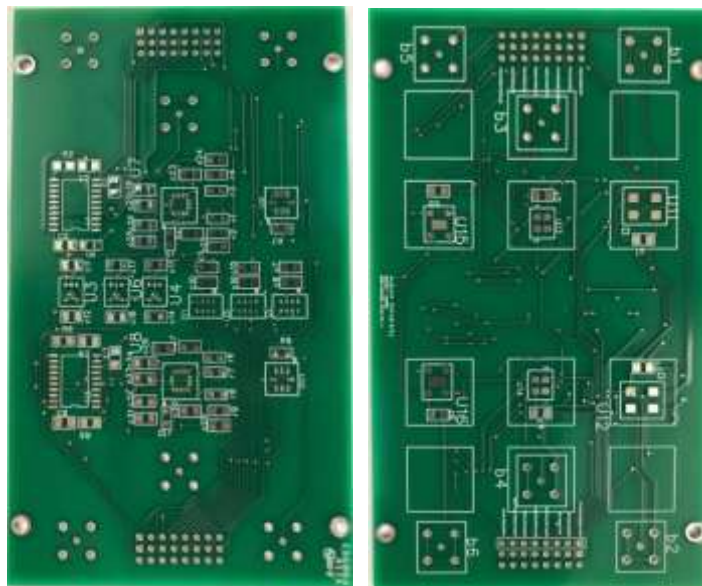
Figure 72:- Test Board Design

The printed circuit board used in this investigation has been fabricated for the testing of Accelerometers, Oscillators, Gyroscopes and Pressure sensors. However this particular study only focusses on ADMP401, MEMS bottom ported analog microphone.
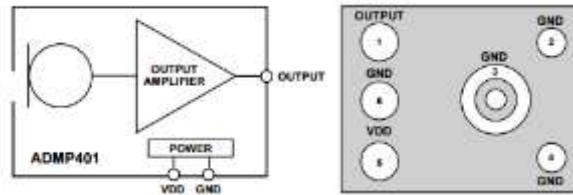
Figure 73: - ADMP401 block diagram and Pin Layout
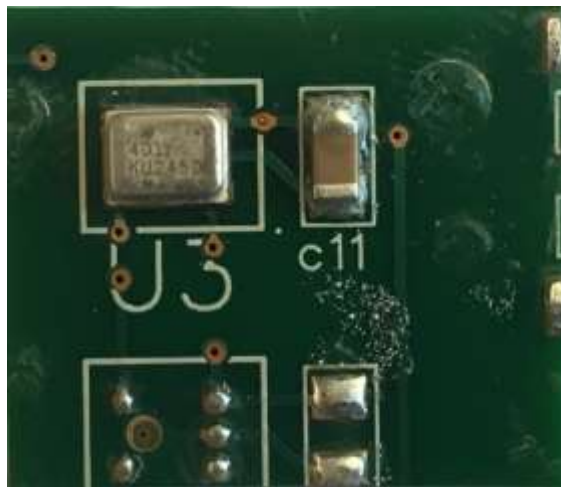
Figure 74:- ADMP401 mounted on MEMS test board

ADMP401 has an internal output amplifier, an impedance converter and requires a single 4.7μF ceramic capacitor serving as the decoupling capacitor. Externally the ADMP 401 sensor is connected to an operational non inverting amplifier, OPA344. Figure shows the external circuitry which was connected between the ADMP401 and the op amp gain stage.
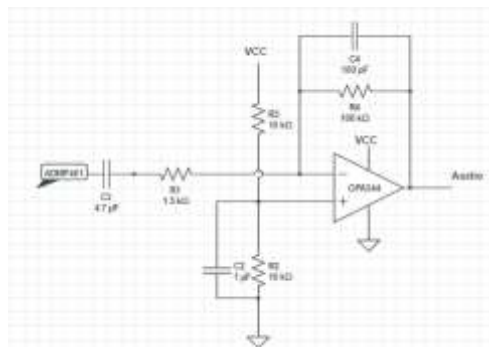
Figure 75:- ADMP401 connections to the op amp gain stage

The MEMS structure and the IC are housed in a 4.72mm x 3.76mm x 1mm surface mount package which encloses all the components. In this architecture the front chamber is the cavity of the MEMS sensor and the back chamber is created by the package. Internal structure properties of the MEMS microphone are unknown since it is proprietary to Analog devices. The MEMS sensor is right on top of the sound port and the IC is located in the back chamber as discussed before. The X-ray images were taken at CAVE3 center at Auburn University.
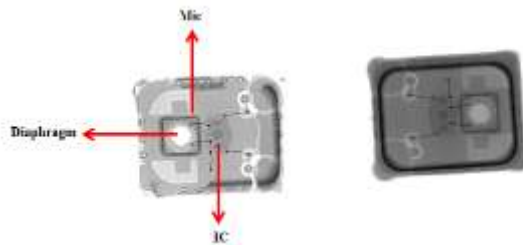
Figure 76:- X ray images of the internal structure
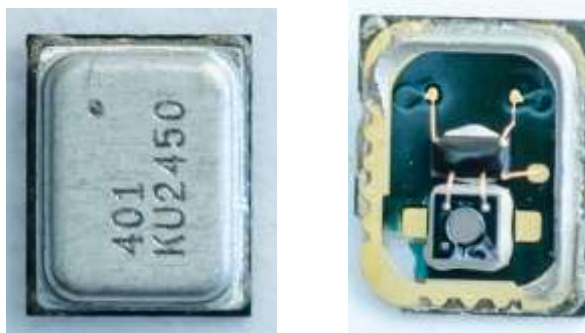
Figure 77:- ADMP 401 with the metallic casing and decapped

ADMP401 samples were decapped in order to visualize the internal structure of the Microphone. The samples were decapped by placing them on a hot plate set at 100ºC and then applying a small amount of shearing force with a sharp metallic tool so as to remove the lid/casing. Scanning electron microscopy was performed on the decapped MEMS samples in order to closely observe the internal structure. Again, since this device is proprietary to Analog devices no information was available regarding the interior edifice and its properties. Below is a set of SEM images which clearly demonstrate the diaphragm shape, IC and diaphragm wire bond sites,

acoustic holes, folded spring elements and the fixed plate which is on the opposite side to the diaphragm.
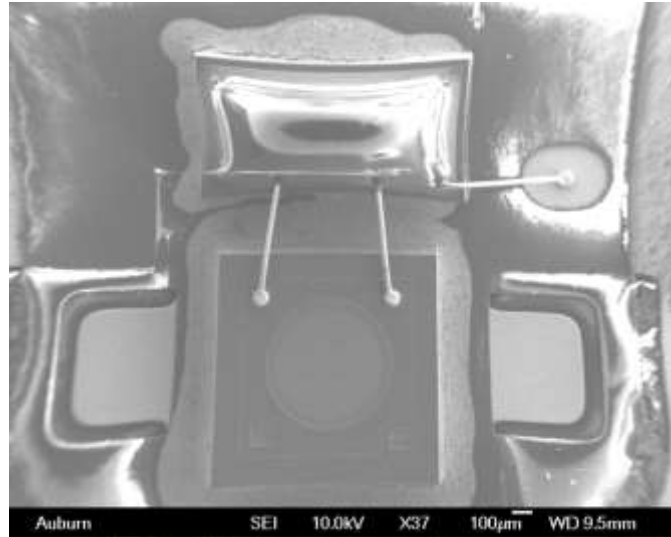
Figure 78:- Top view of MEMS sensor and IC
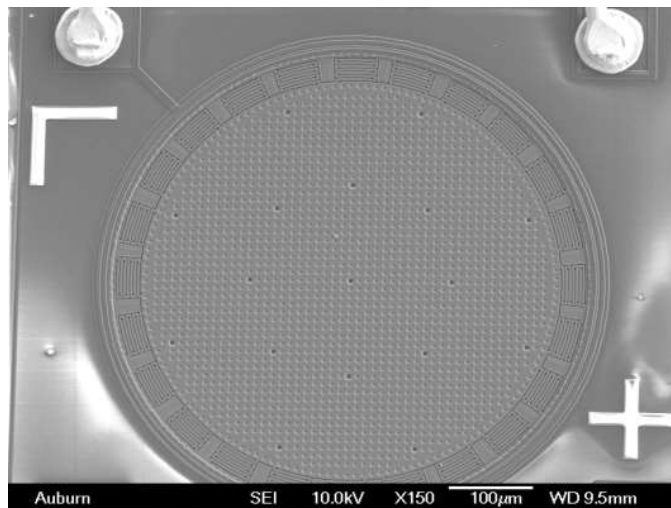
Figure 79:- Zoomed in view of the Diaphragm

ADMP401 uses the capacitive sensing MEMS technology. The diaphragm and the fixed plate comprise to make the variable capacitor, where the diaphragm is movable. The fixed plate, shown in **Figure 82,** has acoustic holes and is conductive which allows sound waves to propagate through. The movable diaphragm is connected to silicon spring element, **Figure 81**, which helps in deflection. The movable surface is full of ventilation holes which allow the air

compressed in the back chamber to disperse out and support in the back and forth motion of the diaphragm. Internal structure properties of the MEMS microphone such as spring constant, k, and mass, m are unknown for analysis since it is proprietary to STMicroelectronics.
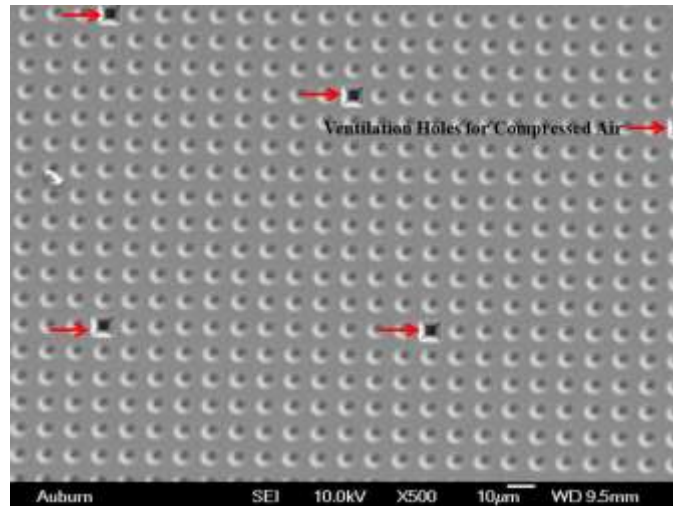
Figure 80:- Ventilation holes for compressed air

ADMP401 operates anywhere between 1.5-3.3V, for this study it was connected to a 3.3V power supply and 6 other passive components listed in **Table 15** referred from **Figure 75**. It is also connected to a standard commercially available low power single supply CMOS operational amplifier, OPA344. The op amp is unity gain stable. The MEMS microphone sensor has a flat frequency response between 100 Hz-15 kHz and a low current consumption value of 250µA.
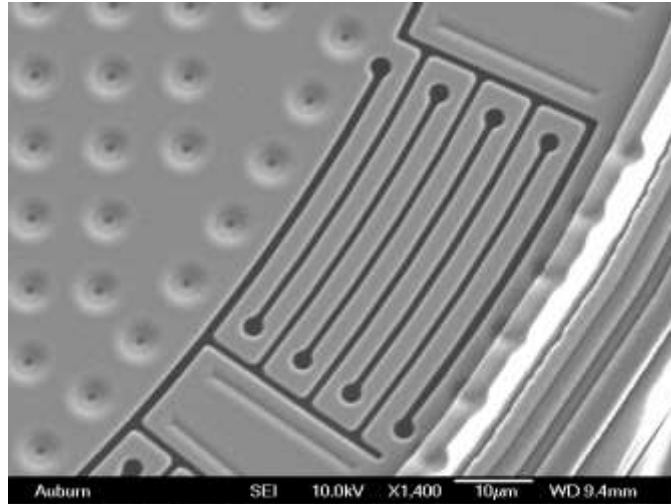
Figure 81:- Spring connected to the diaphragm
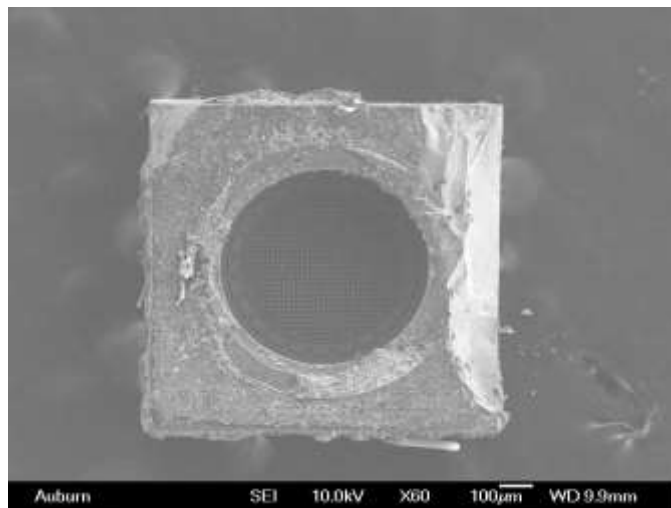
Figure 82:- Fixed plate on backside of ADMP401
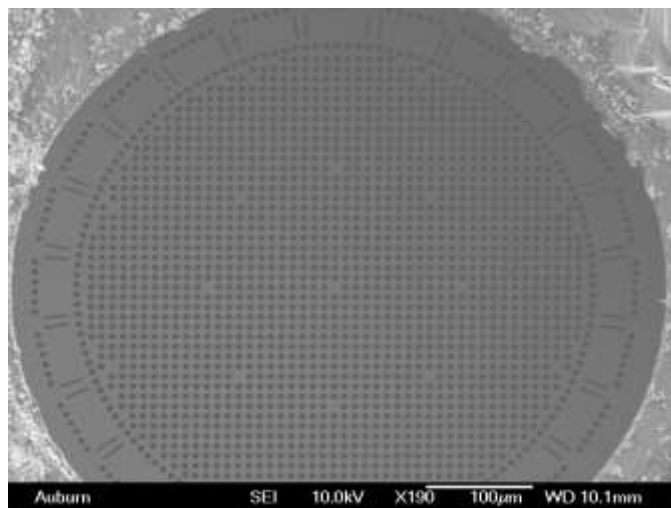
Figure 83:- Zoomed in view of acoustic holes on fixed plate

It is an Omni-directional bottom ported analog sensor with a typical sensitivity of -42dBV and a maximum acoustic input of 120dB SPL (sound pressure level).

Table 16 provides a list of all the pin connections and pin layout for ADMP401 microphone sensor, refer to **Figure** 73.

Type	Value	Pin No.
Ceramic Capacitor	4.7μF (C3)	1 , ADMP401
Ceramic Capacitor	1μF (C2)	2, OP-Amp
Ceramic Capacitor	100pF (C4)	4, OP-Amp
S. Mount Resistor	1.5kΩ (R1)	1, ADMP401
S. Mount Resistor	10kΩ (R2)	GND
S. Mount Resistor	10kΩ (R3)	GND
S. Mount Resistor	100kΩ (R4)	4, OP-Amp, Out

Table 15:- Passive Components and their values

Pin No.	Mnemonic	Description, Pin No.
1	OUTPUT	Analog output, 1
2	GND	Ground, 2
3	GND	Ground, 3
4	GND	Ground, 4
5	Vdd	Power Supply, 5
6	GND	Ground, 6

Table 16:- LPY510AL Pin Configuration

4.2 RELIABILITY TEST MATRIX

A total of 15 ADMP401 microphone sensors were put to test in this study which is further divided into three sub studies each comprising of 5 sensors each. The three different harsh environmental conditions are high temperature operating life (HTOL) 125°C at 3.3V, temperature humidity bias (THB) 85°C/85%RH at 3.3V and low temperature storage (LTS) -35°C. The main objective of this research study is to put forward the progressive evolution of damage in MEMS microphone sensor while monitoring the distortion, frequency response, power supply rejection of IC and frequency vs pressure characteristics. In each sub study the ADMP401 samples were taken out from their respective chambers, operating at different harsh

conditions mentioned above, at a regular interval of 100 hours and put to test in a reverberation chamber. A sine sweep sound ranging from 0Hz-15kHz was used to excite the MEMS acoustic sensor. **Table 17** shows the different test parameters used for the harsh environmental study on ADMP401 MEMS microphones.

Test Condition	Test Parameters	Data Acquisition	Test Samples
HTOL 3.3V	125ºC	100hrs.	5
THB 3.3V	85ºC/85%RH	100hrs.	5
LTS	-35ºC	100hrs.	5
Pristine	------------	-----------	5

Table 17:- Reliability test matrix for harsh environmental study
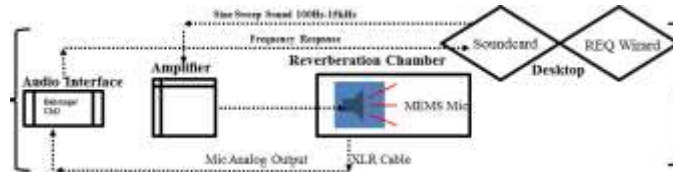
Figure 84:- ADMP401 test flowchart

Figure 84 shows the test flowchart for the harsh environmental study on ADMP401 sensors. The source speaker is connected to a power amplifier and the amplifier is connected to a computer with an operational soundcard. Room equalizer wizard is an open source software which has been used in this study, the software is used to generate a sine sweep sound ranging from 0Hz-15kHz played via the soundcard on the connected computer. The output of the microphone is fed into an audio interface, Behringer UM2, via a XLR cable, which is further connected to the soundcard on the operating computer. Microphone analog output voltage has been monitored and recorded using a high speed data acquisition system, Waverunner Xi series. **Figure 85** shows the data acquisition system used for the experiment.

Figure 85:- Waverunner Xi series oscilloscope

4.3 EXPERIMENTAL TEST SETUP

ADMP401 MEMS microphone sensor test board assemblies were assembled at the Surface Mount Technology line present on CAVE3 facility. The Surface Mount technology (SMT) line consists of three stages, the Stencil printer, Pick and Place machine and reflow oven as shown in **Figure 86** . SAC305 solder alloy was used for this study and was evenly distributed on MEMS test board assemblies through the Stencil printer. ADMP401 and other 6 passive components were placed on the MEMS test board using the Pick and Place machine. Finally, the test boards were baked in the reflow oven. **Figure 87** shows the three different chambers used for this this study.

Figure 86:- SMT Line at CAVE3; Stencil Printer (Top), Pick and Place (Middle), Reflow Oven (Bottom)

Figure 87:- HTOL chamber (TOP), THB chamber (Middle) and LTS chamber (Bottom)

The 5 samples which were pristine did not undergo any aging or high/low temperature or humidity exposure. Our approach for this research study supports for a constructive comparison among the four sets of samples. Microphone gauge parameters such as distortion, frequency response, power supply rejection of IC and frequency vs pressure characteristics can demonstrate on how sensitive the ADMP401 samples are to the four above mentioned harsh environmental.

Figure 89 and **Figure 90** show the inside view of the reverberation room where the samples were put to test.

Figure 88:- YXLON CT and X-ray machine

One of the main objectives behind this investigation is to quantify whether or not the microphone sensor parameters are drifting significantly with respect to the pristine benchmark values and by how much; when exposed to harsh environmental conditions. The X-ray images shown in **Figure 76** were taken at Auburn University, CAVE3 facility, using the state-of-the-art YXLON computed tomography and X-ray machine in **Figure 88.**

4.3.1 Reverberation Chamber Setup

Figure 89:- Inside View of Reverberation room

Figure 90:- Inside View of Reverberation room

Figure 91:- Source speaker on top of MEMS test board assembly

The reverberation chamber/room helps is achieving an even state of acoustic energy. Acoustic impedances offered by the surface of this chamber to the propagating sound waves are very large thereby reflecting most of the acoustic energy back within the room. The chamber comprises of a two layer hardwood and timber setup in order to maximize the reverberation time, also no cavities are present within the walls or the roof which help in avoiding unwanted resonances.

The source speaker was carefully mounted on a wooden rack as shown in **Figure 91** and the MEMS test board assemblies were kept on a small circular table top which was at a fixed distance of 20cm from the speaker, see **Figure 90** and **Figure 91 .** Again as mentioned above the MEMS microphone test board assemblies were taken out after every 50hrs from their respective harsh environmental chambers and then put to test in the reverberation room.
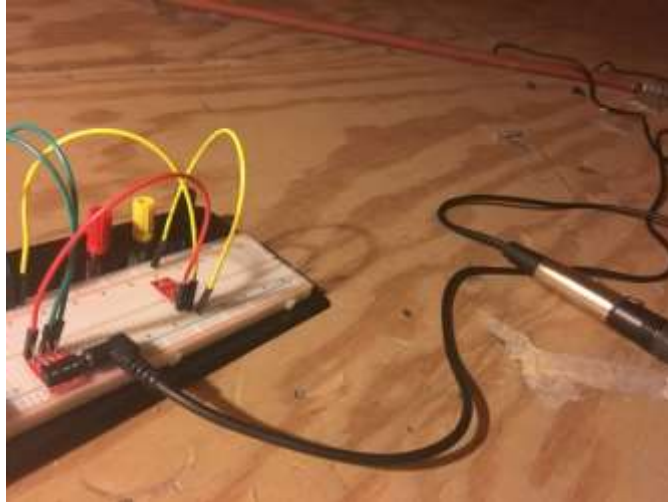
Figure 92:- XLR cable and TRSS connector

Since the ADMP401 is an analog sensor, the output signal cannot be directly fed into the audio interface, Behringer UM2. A commercially available of the shelf TRSS connector, manufactured by Spark fun, was used which takes in the analog output signal and transports it to the audio interface via a XLR cable with an audio jack end as shown in **Figure 92**.

Figure 93:- Power amplifier and audio interface.

The other end of the XLR cable is connected to the audio interface powered through a standard USB cable which is connected to the computer with soundcard. **Figure 93** demonstrates the XLR cable output into the mic/line of the audio interface and the output of the audio interface into the source speaker.

Figure 94:- Behringer UM2 2 x 2 audio interface

The amount of time is takes for a sound wave to fade away is an enclosed space or area is referred to as the reverberation time. Surfaces in the room, reflective in nature, will help in repeated bouncing of sound waves and when these reflections fuse together reverberation is produced. Highly bibulous surfaces reduce the reverberation when hit by reflections. The acoustic status of a room is mostly characterized by the reverberation. RT60 (60dB decay) reverberation time measurement is an ISO 3382-1 standard for performance spaces and is measured as soon as the source signal is abruptly ended [NTI Audio 2017]. In experimental phase we generally measure 20dB or the 30dB decay and since the decay is linear, one can extrapolate for 60dB decay.
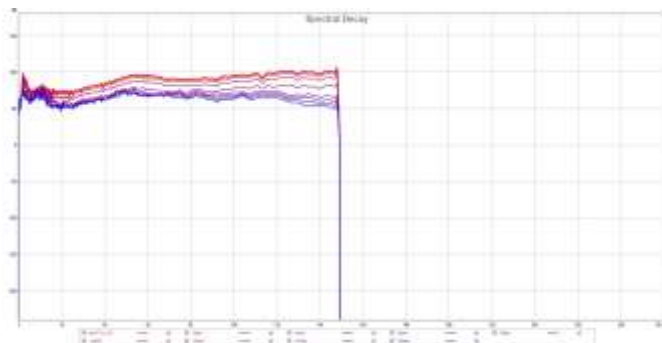
Figure 95:- RT60 decay for reverberation chamber

RT60 plot for the reverberation chamber, shown in **Figure 95**, was generated before every test so in order to maintain the continuity of the experiment.

4.4 EXPERIMENTAL RESULTS

The fundamental objective behind this research work is to observe and anatomize the output parameters of a commercial MEMS microphone and assess the accrued damage. The reliability data shown in this study represents damage progression in MEMS microphones till failure. In this study the term failure does not actually mean that the device is not working at all but is a coined term used to describe the progress of damage i.e. until the Microphone output parameters go permanently out of the stable operating range or drift significantly with respect to the ideal output(s). In order to normalize the survivability of ADMP401, MEMS analog microphone, for smartphones, digital video cameras, video phones and tablets, it has been subjected to the aforementioned harsh environments. ADMP401 microphone sensors have been gauged on standard microphone metrics such as distortion, frequency response, power supply rejection capability of IC, frequency vs pressure characteristics and output voltage.
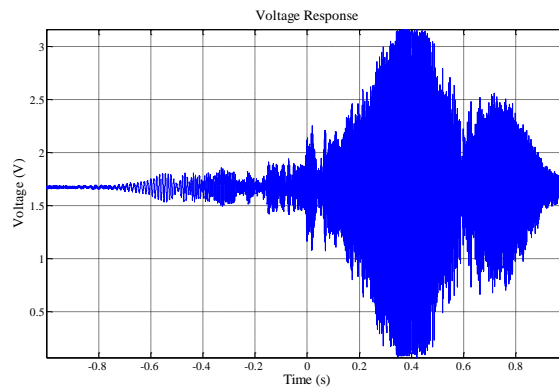
Figure 96:- Voltage response of ADMP401 for a sine sweep sound from 0 Hz-15 KHz

Room equalizer wizard is an open source software which has been used in this study, the software is used to generate a sine sweep sound ranging from 0 Hz-15 kHz played via the soundcard on the connected computer. **Figure 96** shows a typical output voltage response signal for a pristine microphone sample.
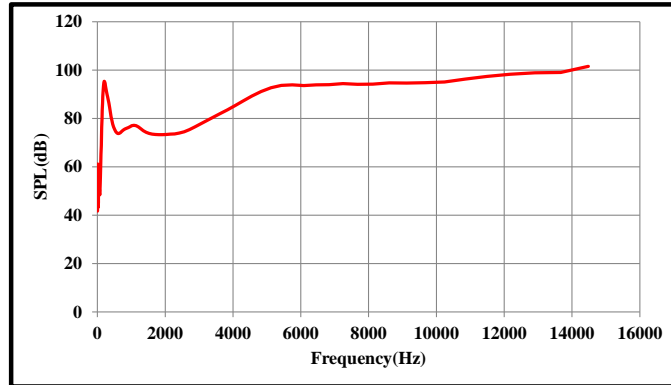
Figure 97:- Frequency response vs Sound Pressure Level for ADMP401

I. *Effect of High temperature operating life (HTOL)*

As mentioned before five MEMS test board assemblies were subjected to 125°C operating at 3.3V. High temperature operating life provides a harsh environment for the microphone sensor where the stresses act dynamically and approach the max absolute ratings in terms of junction temperature, load current and internal power dissipation [ST microelectronics AN4428]. The main idea behind including HTOL test in our test matrix is that this test simulates the worst case application harsh conditions. Since the device operates in a biased condition typical failure modes such as wire-bond aging, ASIC oxide faults and metal degradation have been investigated.

A) **Distortion**

The ratio of output pressure to the input sound pressure when sweeping from 0Hz - 15 kHz, where the reference sound pressure in air is 20µPa, is referred as distortion.
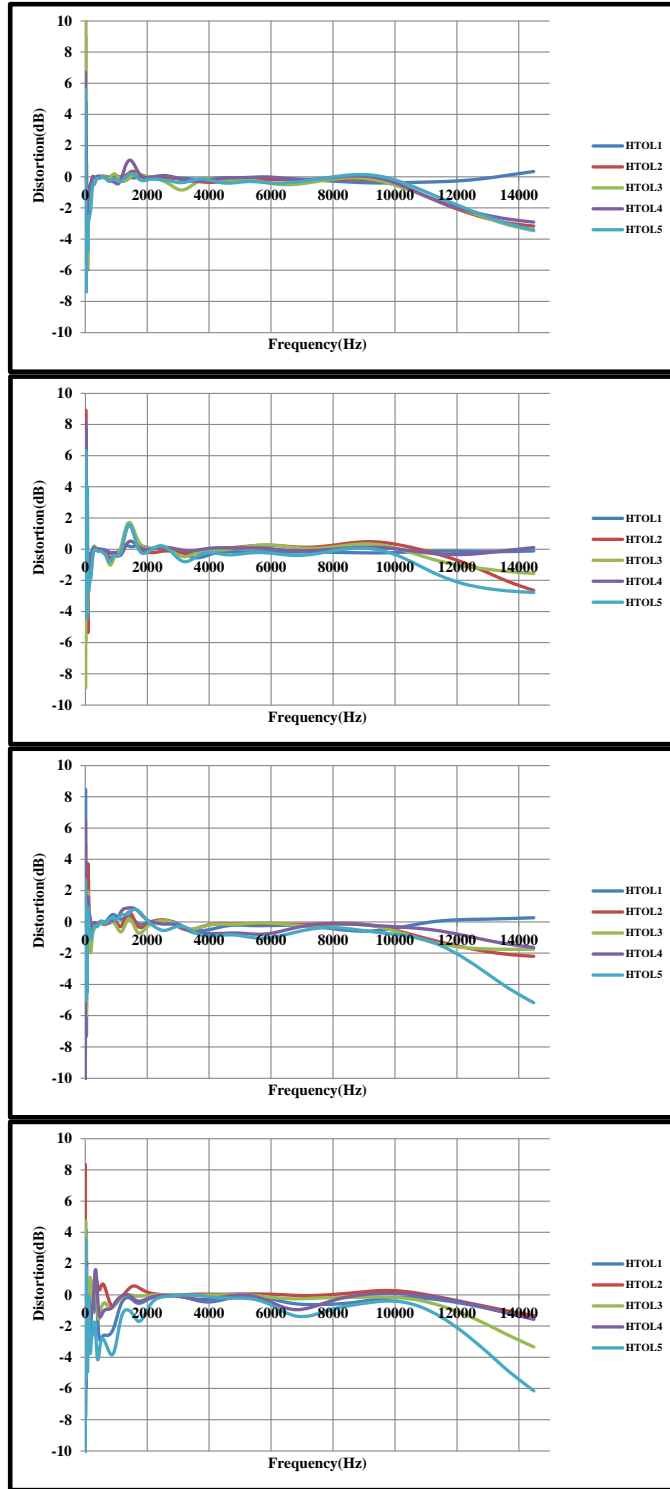
Figure 98:- Distortion after 300 hours, 400 hours, 500 hours and 600 hours of HTOL respectively

Figure 98 shows the distortion in five HTOL samples after 300, 400, 500 and 600 hours of

125°C at 3.3V. It can be clearly seen that while most of the distortion between 2000Hz and

8000Hz is not significant, the major frequencies contributing to distortion are the higher and the lower end of the frequency sweep band and this behavior is portrayed by all the HTOL samples. Also the distortion peaks are as high as 10dB at 0Hz which is due to the fact that ADMP401 has a flat frequency response from 100Hz – 15kHz and the sine sweep frequency band lies between 0Hz – 15kHz, therefore these peaks are neglected and do not contribute to the distortion analysis. Progression of HTOL with time yields higher distortion in all the samples especially at lower (100Hz-200Hz) and higher frequencies (10 kHz- 15 kHz). Also the distortion at the intermediate frequencies (2000Hz – 8000Hz) does not tend to remain flat.

B) **Power Supply Rejection**

The ability of ASIC to reject the noise or a spurious signal added to the supply voltage [ST microelectronics AN4426]. A sine tone at 100mV pk-pk at 217Hz (GSM switching frequency in phone applications) is added to the power supply and the amplitude of output signal is measured. PSR is typically expressed in decibels (dB). It is a gauge factor of how much noise on the power supply will squeeze through to the output signal. For complete power supply rejection the microphone would have PSR equal to the A-weighted noise floor.

$$PSR = 20 \times log_{10}(V_{out} @ 217Hz)$$
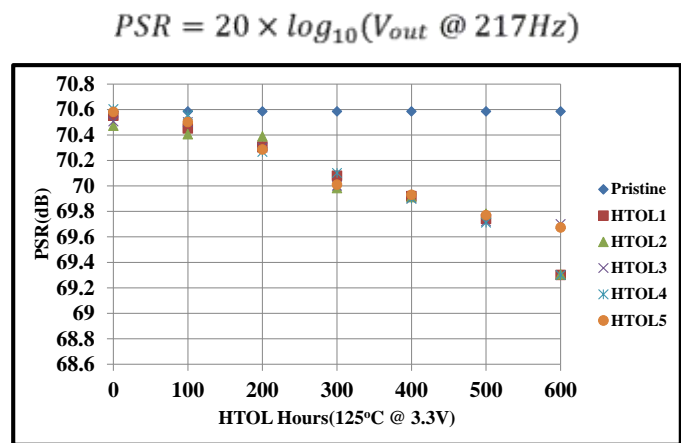
Figure 99:- PSR for HTOL samples

Five pristine samples were evaluated and the computed PSR values were around 70.584dB for all of them. **Figure 99** shows the degradation in the PSR computed values for HTOL samples as the HTOL operating time progresses. The deterioration of ASIC over time reduces its capability to reject the noise added to the supply voltage and also loses the IC parametric stability. Average PSR decay is 0.63dB.

Power supply rejection ratio (PSRR) is the residual noise amplitude at microphone output to the added spurious signal on the supply voltage [10]. PSRR is typically expressed in decibels (dB) as

$$PSRR = 20 \times log_{10}(\frac{V_{out}}{V_{in}} @ 217Hz)$$
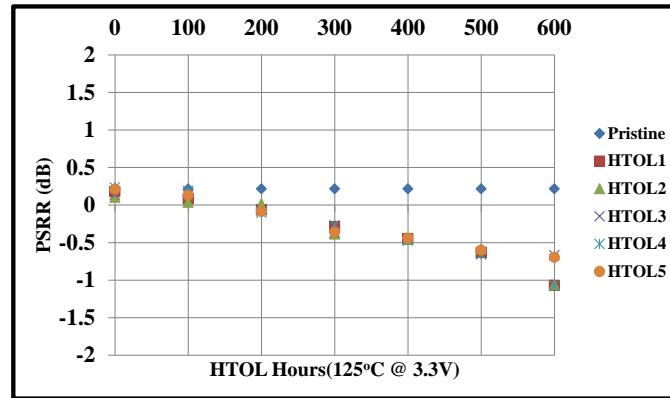
Figure 100:- PSRR for HTOL samples

Figure 100 shows the deterioration in the PSRR computed values for HTOL samples till 600 hours. As mentioned before both the PSR and PSRR parameters were evaluated using a 100mV pk-pk sine tone at 217Hz (GSM switching frequency in phone applications) which is added to the power supply and the amplitude of output signal is measured.

C) Frequency vs Pressure

The diaphragm of the ADMP401 sensor is disturbed by the sound pressure deviations which is a sound field quantity. This analysis can help us determine how the sound pressure is detected by

the diaphragm for a pristine case and a harsh stress environment case. Since the same sine-sweep signal is used for all the test cases and the distance of the MEMS test board assemblies from the source speaker is kept same so ideally the pressure detected by the diaphragm should be similar irrespective of the test conditions.

With the increase in exposure time to HTOL test condition the diaphragm expands thereby changing the dimensions of the ventilation holes, on the micro scale, which in turn results in change in the pressure detection by the diaphragm. It can be observed from **Figure 101** that the pressure detected by the diaphragm for pristine ADMP401 sample is higher than the HTOL samples especially at higher frequencies.
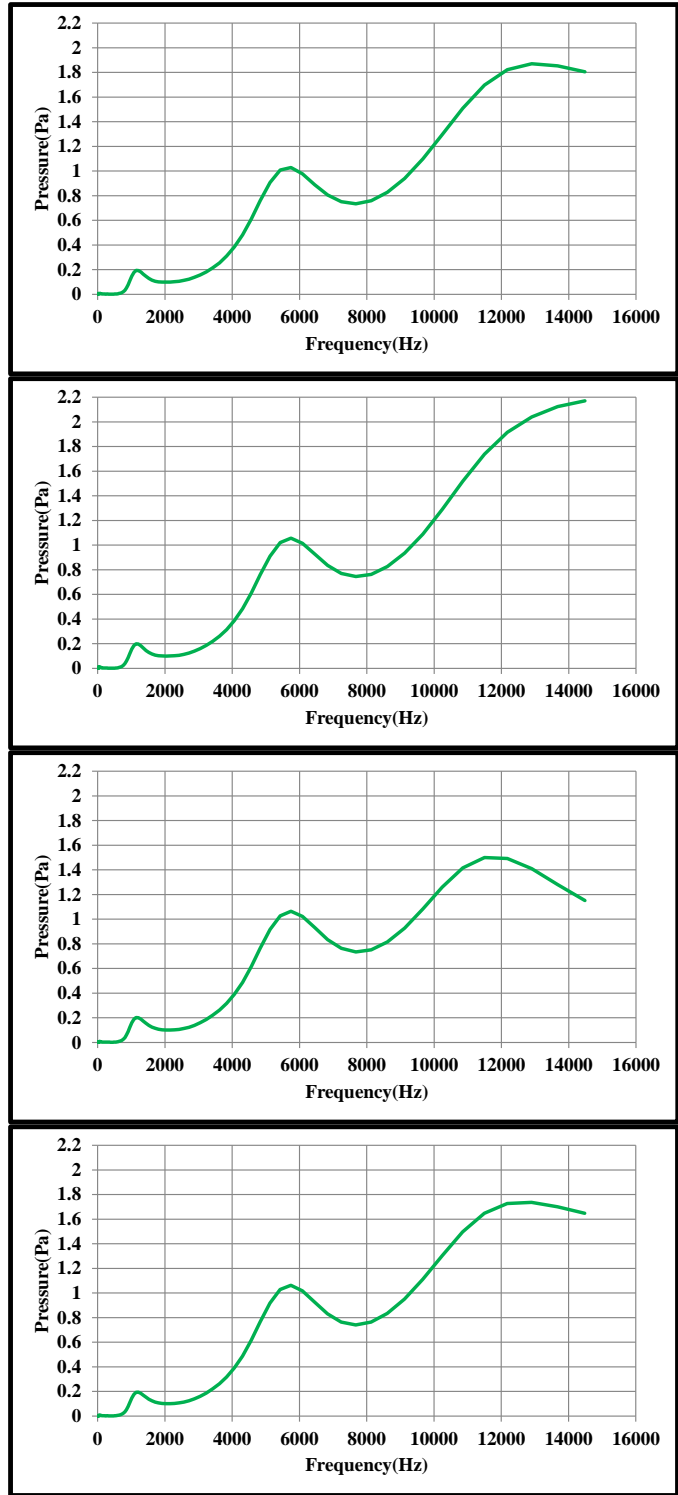
Figure 101:- Pressure detected by diaphragm vs Frequency for Pristine (Top), HTOL test samples

113

D) <u>Interval Plot for HTOL</u>

Interval plot is a graphical representation for a sample distribution which focuses on the sample's tendency and variability. **Figure 102** compares the means of pristine and HTOL test cases, sample 3 and sample 5 do not show any significant difference as their respective interval bars easily overlap with the pristine interval bar. On the other hand samples 1, 2 and 4 show different means and are also significantly different from the pristine test case.
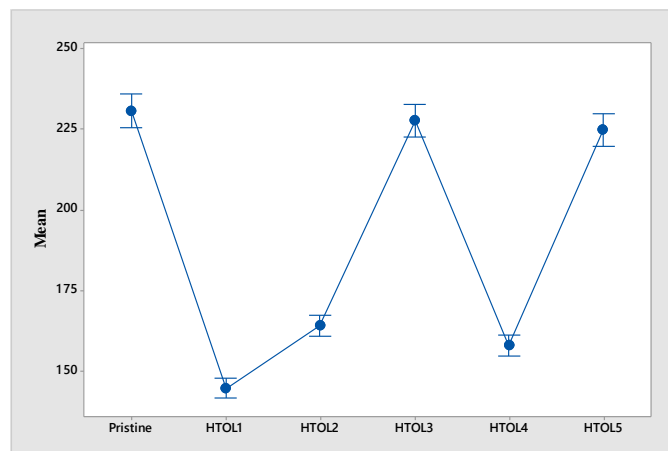
Figure 102:- Interval Plot for HTOL samples after 600 hours

E) <u>FFT analysis of output voltage</u>

Fast Fourier transform allows us to analyze the voltage signal, which is in time domain, in frequency domain and study the overall signal content in terms of energy and spectral density. FFT techniques have been used in the past [Lall 2015] to analyze the incremental deterioration in energy of the MEMS output voltage signal.
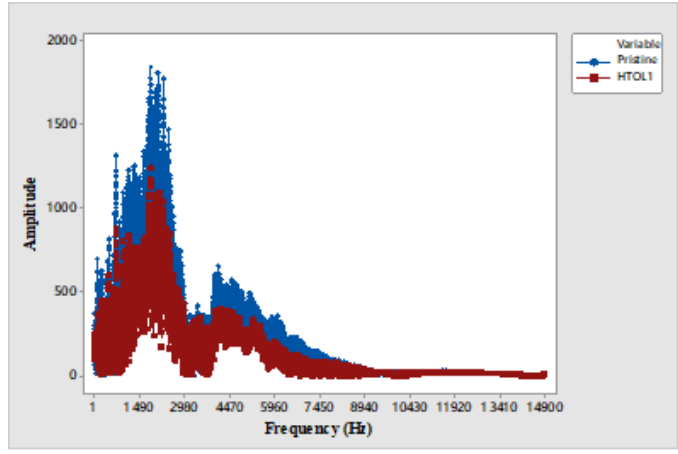
FFT analysis shows a significant reduction in the amplitude of the output voltage signals in HTOL test samples. Samples 1, 2 and 4 show significant reduction in peak amplitude and overall signal energy of the output signal. A drift in the peak frequency has also been observed for the harsh environment test cases when compared to pristine.
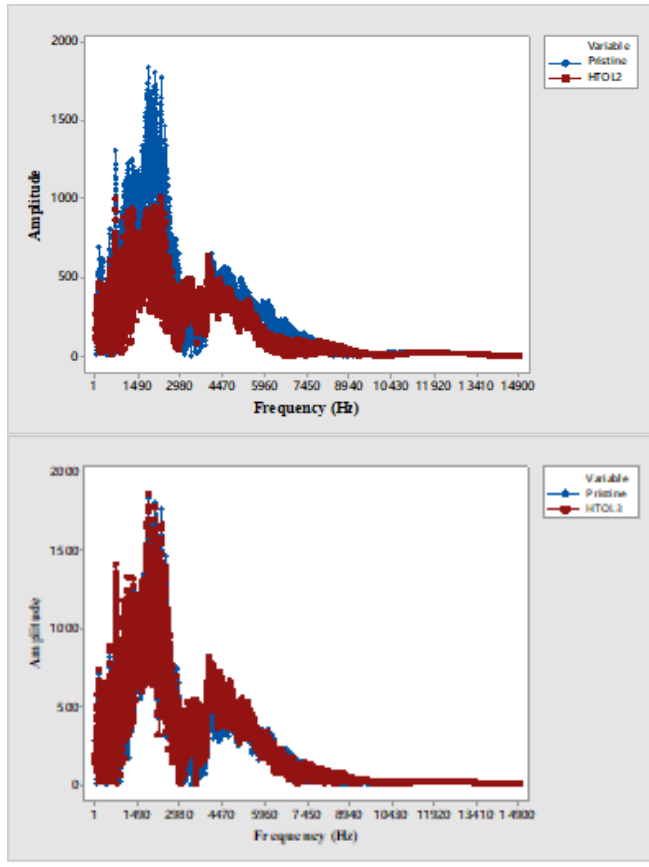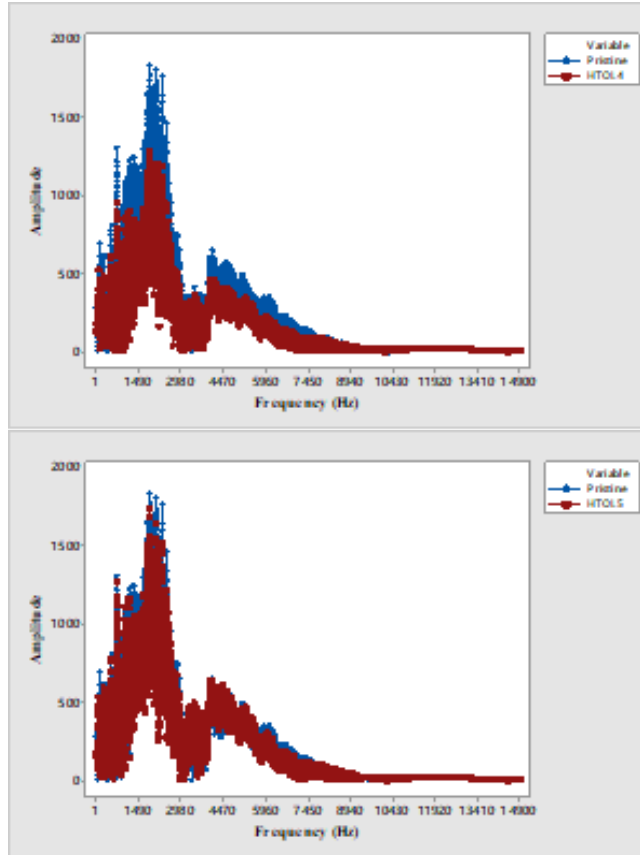
Figure 103:- FFT overlays for Pristine, HTOL1, HTOL2, HTOL3, HTOL4 and HTOL5 after 600 hours

II. Effect of Low Temperature Storage (LTS)

As mentioned before five MEMS test board assemblies were subjected to -35°C. Low

temperature storage provides a harsh environment for the microphone sensor where the device is

stored in an unbiased condition at the minimum temperature allowed by the package materials,

this harsh environment is useful for investigating the failure mechanisms activated by extremely

cold environments for prolonged time [ST microelectronics AN4428].

A) Power Supply Rejection

The ability of ASIC to reject the noise or a spurious signal added to the supply voltage [ST

microelectronics AN4426]. A sine tone at 100mV pk-pk at 217Hz (GSM switching frequency in

phone applications) is added to the power supply and the amplitude of output signal is measured.

PSR is typically expressed in decibels (dB). For complete power supply rejection the microphone would have PSR equal to the A-weighted noise floor.

$$PSR = 20 \times log_{10}(V_{out} \ @ \ 217Hz)$$

Five pristine samples were evaluated and the computed PSR values were around 70.584dB for all of them. **Figure 104** and **Figure 105** show the deterioration in the PSRR and PSR computed values for LTS samples till 300 hours. It can be clearly seen that in the LTS test case the drift in the PSR and PSRR values is almost negligible (about 0.2 dB) as compared to HTOL test case up until the 300th hour mark.
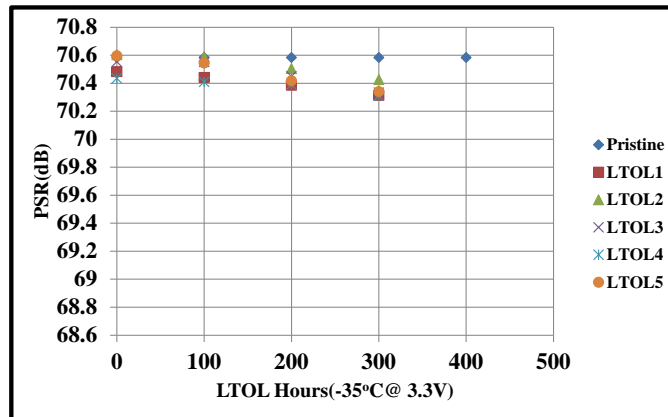
Figure 104: - PSR for LTS samples
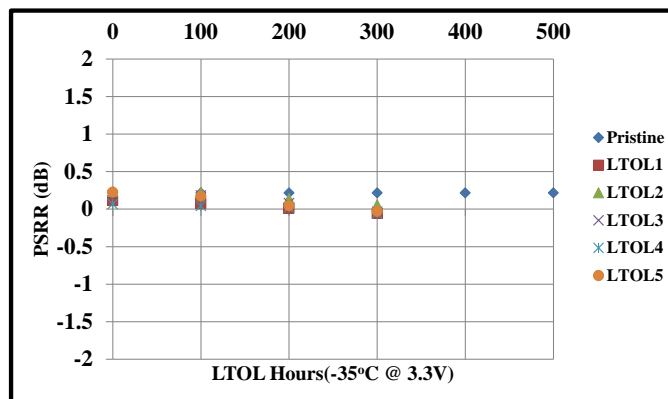
Figure 105:- PSRR for LTS samples

117

B) Interval Plot for LTS

Interval plot is a graphical representation for a sample distribution which focuses on the sample's tendency and variability. **Figure 106** compares the means of pristine and LTS test cases, it can be clearly seen that since the interval bars for all of the samples easily overlap with the pristine test case therefore there is no significant difference or drift between the pristine and LTS samples.
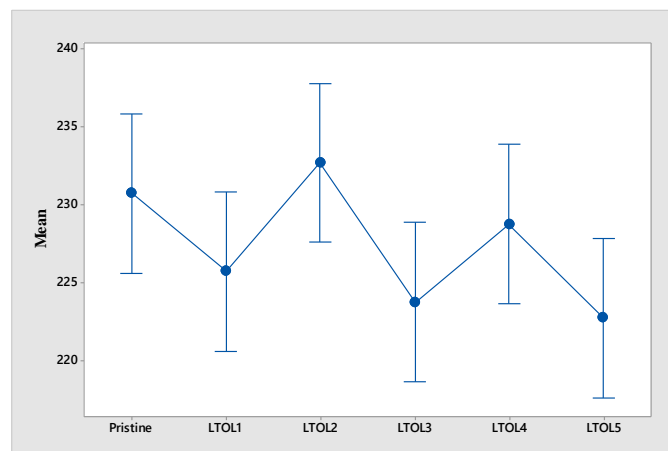
Figure 106:- Interval Plot for LTS samples after 300 hours

C) FFT analysis of output voltage

Fast Fourier transform allows us to analyze the voltage signal, which is in time domain, in frequency domain and study the overall signal content in terms of energy and spectral density. FFT techniques have been used in the past [Lall 2015] to analyze the incremental deterioration in energy of the MEMS output voltage signal.
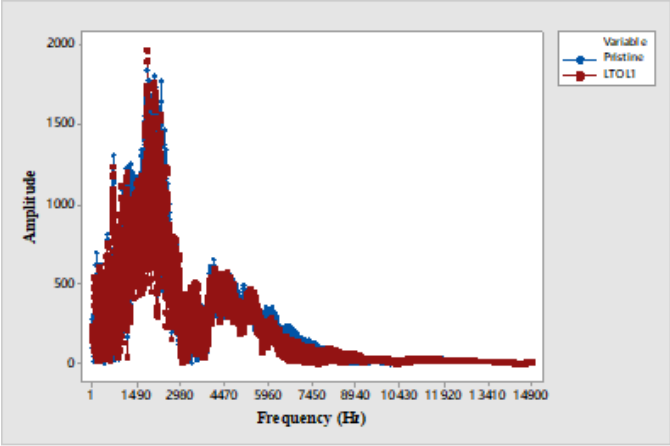
FFT analysis shows that there is no significant reduction in the amplitude of the output voltage signals in LTS test samples. Samples 1, 2, 3, 4 and 5 show insignificant reduction in peak amplitude and overall signal energy of the output signal. A drift in the peak frequency has not been observed for the harsh environment test cases when compared to pristine. **Figure 107** shows the FFT overlays for pristine and LTS test cases after 300 hours.
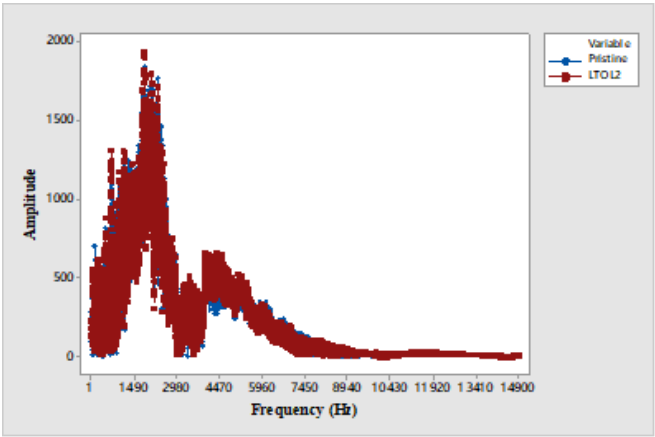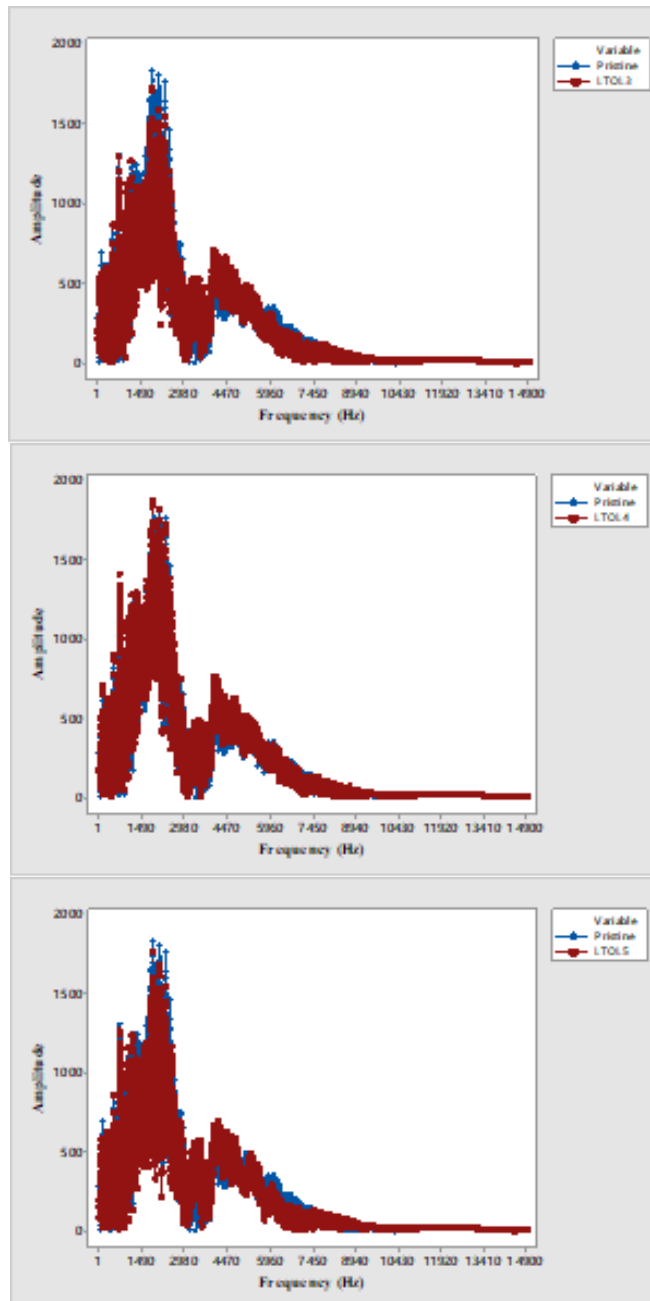
Figure 107:- FFT overlays for LTS test case after 300 hours

III. Effect of Temperature Humidity Bias

As mentioned before five MEMS test board assemblies were subjected to 85°C/85%RH

operating at 3.3V. Temperature humidity bias test aims at examining failure mechanisms

especially in the die-package surroundings caused by harsh wet conditions and electric potential .Since the device operates in a biased condition typical failure modes such as electro-chemical corrosion have been investigated. EDS analysis shown in section III below demonstrate high oxygen content found in THB samples especially in the back chamber which constitutes the ASIC.

A) <u>Distortion</u>

The ratio of output pressure to the input sound pressure when sweeping from 0Hz - 15 kHz, where the reference sound pressure in air is 20μPa, is referred as distortion.
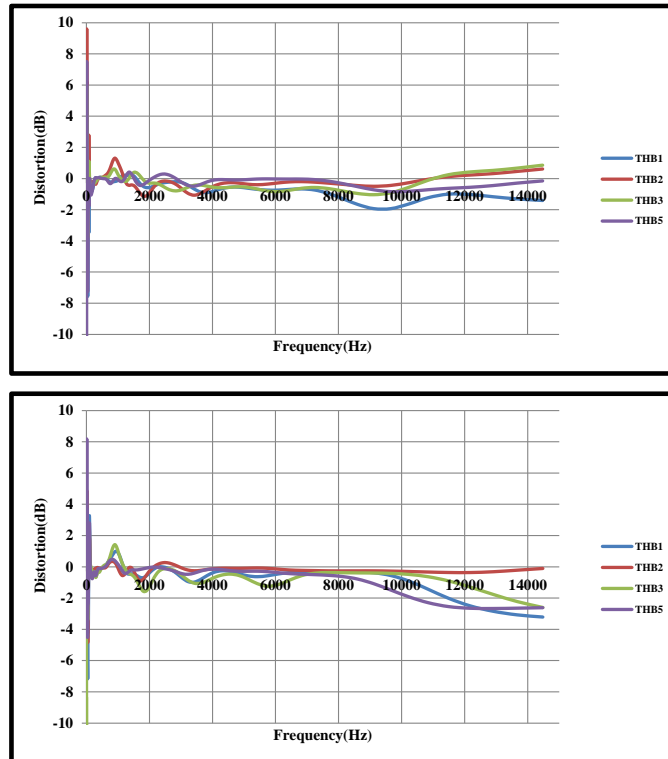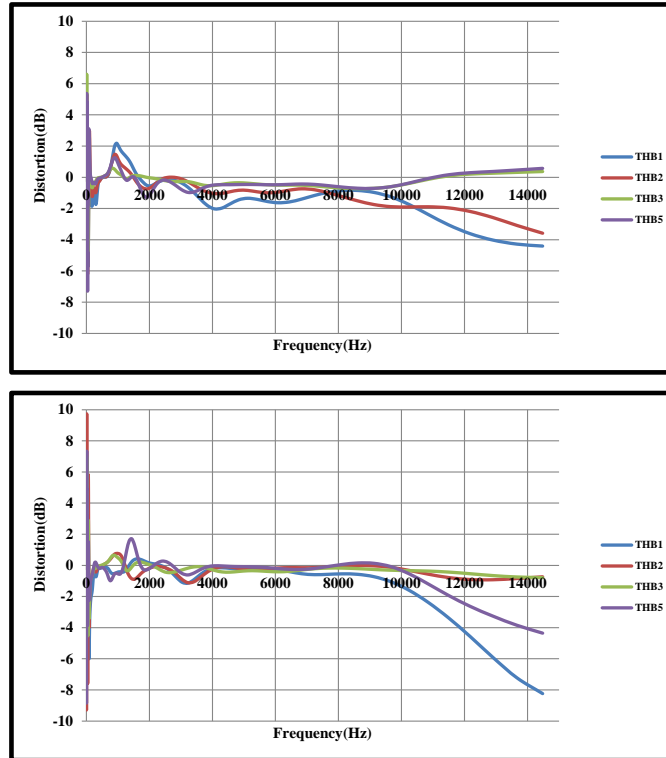
Figure 108:- Distortion after 100 hours, 200 hours, 300 hours and 400 hours of THB respectively

Figure 108 shows the distortion in five THB samples after 100, 200, 300 and 400 hours of 85ºC/85%RH at 3.3V. Unlike HTOL test case for THB the distortion between 2000Hz and 8000Hz is significant and more than what is observed for HTOL. Similar to high temperature operating life the major frequencies contributing to distortion are the higher and the lower end of the frequency sweep band and this behavior is portrayed by all the THB samples. Also the distortion peaks are as high as 10dB at 0Hz which is due to the fact that ADMP401 has a flat frequency response from 100Hz – 15kHz and the sine sweep frequency band lies between 0Hz – 15kHz, therefore these peaks are neglected and do not contribute to the distortion analysis. Progression of THB with time yields higher distortion in all the samples especially at lower (100Hz-200Hz) and higher frequencies (10 kHz- 15 kHz) and is as high as -8dB. One of five tested THB samples did not show any output signal even before the completion of 100 hours of THB test, which mainly can be because of an electrical overstress subjected to the ASIC.

Electrical overstress which is an unexpected phenomenon causes irreversible damage to ASIC such as burned areas or voids in Silicon [ST microelectronics AN4428]

B) <u>Power Supply Rejection</u>

The ability of ASIC to reject the noise or a spurious signal added to the supply voltage [ST microelectronics AN4426]. A sine tone at 100mV pk-pk at 217Hz (GSM switching frequency in phone applications) is added to the power supply and the amplitude of output signal is measured. PSR is typically expressed in decibels (dB). It is a gauge factor of how much noise on the power supply will squeeze through to the output signal. For complete power supply rejection the microphone would have PSR equal to the A-weighted noise floor.

$$PSR = 20 \times log_{10}(V_{out} \ @ \ 217Hz)$$

Five pristine samples were evaluated and the computed PSR values were around 70.584dB for all of them. **Figure 109** and **Figure 110** show the degradation in the PSR and PSRR computed values for Temperature-humidity biased samples as the THB operating time progresses. The deterioration of ASIC over time in this case is more than as in HTOL test case. Average PSR decay was 1.8dB.
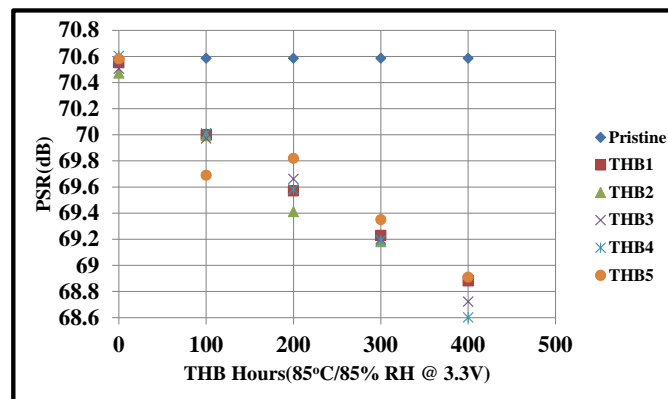
Figure 109:- PSR for THB samples
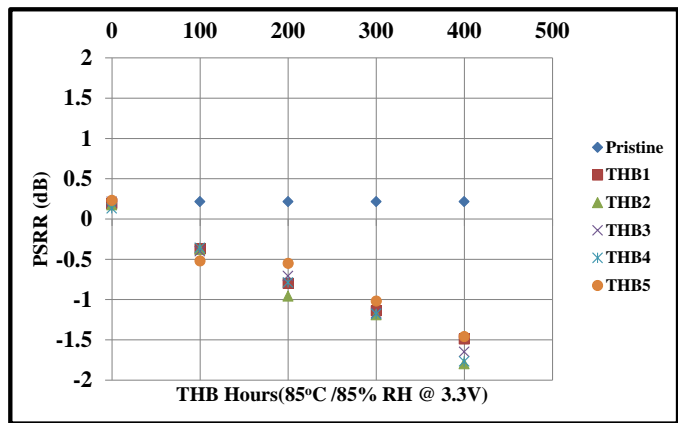
Figure 110:- PSRR for THB samples

III. Energy Dispersive X-ray Spectroscopy Analysis (EDS)

Temperature Humidity Bias

Sample I
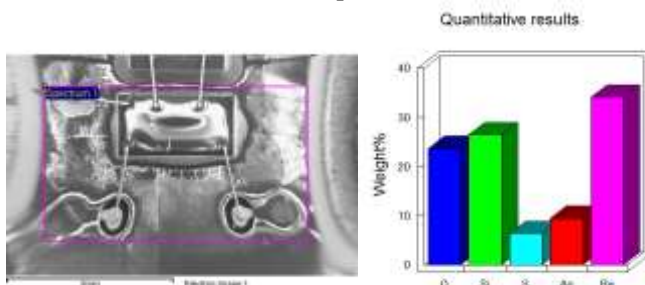
Sample II
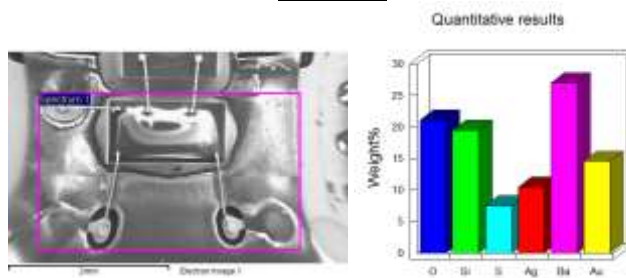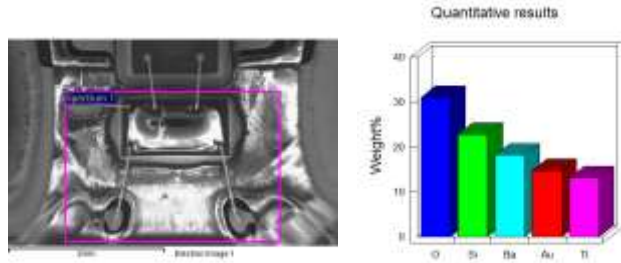
Energy dispersive X-ray spectroscopy analysis shown in **Figure 111** demonstrate high oxygen content found in THB samples especially in the back chamber which constitutes the ASIC. Oxygen rich content as high as 25-40% has been discovered which makes oxidation a big possibility and metal degradation and oxide faults at the ASIC site are very much likely.

Sample IV
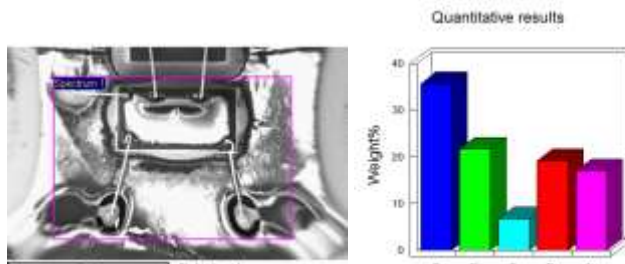
Sample V
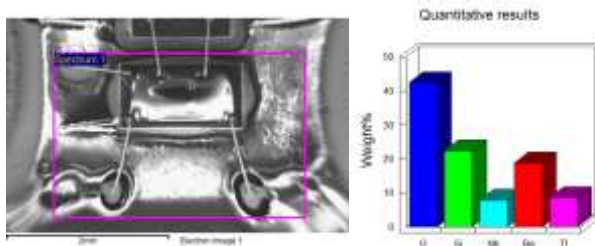
Figure 111:- EDS scan results for THB samples I, II, III, IV and V respectively after 400hours of 85ºC/85%RH at 3.3V
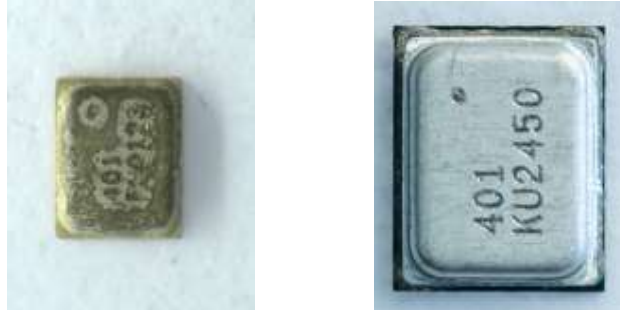
Figure 112:- ADMP401 THB sample after 400hrs (Left) and Pristine sample (Right)

<u>Pristine</u>
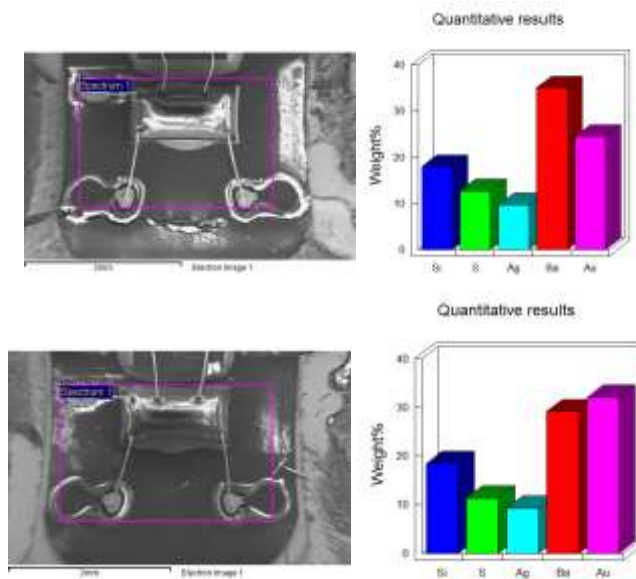
Figure 113:- EDS scan results for pristine samples

For the same ASIC site Pristine samples do not show any traces of Oxygen thereby indicating to the fact that ADMP401 samples subjected to THB test condition have Oxygen presence within the MEMS package which causes the deterioration of the MEMS assembly.

4.5 SUMMARY AND CONCLUSIONS

This research study presents a reliability and defect detection technique to analyze the behavior and characteristics of a commercially available MEMS microphone when exposed to high temperature operating life and biased temperature-humidity test conditions. This approach allows MEMS designers and engineers to investigate and document the evolution of damage in ADMP401 MEMS bottom ported microphone. Through reliability and defect detection analysis this methodology was successful in characterizing the overall behavior of the MEMS device. The incremental damage progression was reported in terms of distortion, frequency response, power supply rejection capability of IC, frequency vs pressure characteristics and output voltage. On comparing the pristine and harsh environment test case samples, FFT analysis show a significant reduction in the amplitude of the output voltage signals in THB and HTOL test samples especially samples from THB test condition. Power supply rejection values were computed for all the test cases; a decreasing trend was observed in the PSR values of HTOL and THB samples with the increase in exposure time. The computed PSR values show significant reduction, especially for biased temperature-humidity samples where reduction is almost 2dB, when exposed to harsh environmental operating conditions in comparison to the pristine sample. Results put forward for power supply rejection clearly established that the IC connected to the MEMS device is very sensitive to high humidity and high temperature exposure when in a biased condition. This is also supported by the EDS scan results which show significant amount of Oxygen presence, 25-40% by weight, in and around the IC site within the MEMS package. Oxide formation and metal degradation are very likely to have caused the overall IC parametric instability. The diaphragm of the ADMP401 sensor is disturbed by the sound pressure deviations which is a sound field quantity. In this research study pressure detection by the diaphragm for a

127

pristine case and a harsh stress environment case vs frequency was also analyzed. Since the same sine-sweep signal was used for all the test cases and the distance of the MEMS test board assemblies from the source speaker is kept same so ideally the pressure detected by the diaphragm should be similar irrespective of the test conditions. It was observed that the pressure detected by the diaphragm for pristine ADMP401 sample is higher than the HTOL samples especially at higher frequencies. This can be due to the fact that the compressed air in the back chamber is not being properly vented out through the ventilation holes present on the diaphragm for its proper back and forth motion. The Silicon diaphragm within the MEMS device operating at 125ºC at 3.3V undergoes thermal expansion thereby changing the dimensions of the ventilation holes present on the diaphragm. Distortion or the ratio of output pressure to the input pressure was also observed and the results have been documented. The results shown above in the study demonstrate that for HTOL samples most of the distortion between 2000Hz and 8000Hz was not significant, the major frequencies contributing to distortion were the higher and the lower end of the frequency sweep band and this behavior was portrayed by all the HTOL samples. Progression of HTOL test condition with time yields higher distortion in all the samples especially at lower (100Hz-200Hz) and higher frequencies (10 kHz- 15 kHz). Also the distortion at the intermediate frequencies (2000Hz – 8000Hz) does not tend to remain flat. For the THB test samples unlike HTOL test case the distortion between 2000Hz and 8000Hz was significant and more than what was observed for HTOL cases. Similar to high temperature operating life the major frequencies contributing to distortion were the higher and the lower end of the frequency sweep band and this behavior was demonstrated by all the THB test samples. Progression of THB with time yields higher distortion in all the samples especially at lower (100Hz-200Hz) and higher frequencies (10 kHz- 15 kHz) and was as high as -8dB. Also the distortion peaks in both

HTOL and THB test conditions were as high as 10dB at 0Hz which was due to the fact that ADMP401 has a flat frequency response from 100Hz – 15 kHz and the sine sweep frequency band lies between 0Hz – 15 kHz, therefore these peaks were neglected and did not contribute to the distortion analysis.

Chapter 5

A Study on Damage Progression in MEMS Based Silicon Oscillators Subjected to High-G Harsh Environments

Traditional Quartz based oscillators still outnumber their MEMS counterparts in the industry therefore no extensive prior studies exist which provide harsh environment reliability data for Silicon oscillators. MEMS based oscillators serve as clocks which control the timing in electronics, a better clock signal ensures higher performance, more consistent behavior and reliable operation. Harsh environment applications such as under the hood automotive, military, space navigation all make use of MEMS oscillators. None of the previous studies look into the impact of sequential harsh environment operating conditions. Survivability of MEMS oscillators at high relative humidity and high G environments is unknown. The effects of these pre-conditions along with the drop test conditions have been studied and analyzed. Anomalies in the oscillator behavior due to the presence of harsh environments lead to mismatch in the electronic timing of the circuit resulting in a bad consumer product, thus the importance of reliability data. In this study a test vehicle with a MEMS oscillator, SiT 8103, has been tested under: high relative temperature humidity exposure and then followed by subjection to high-g shock loading environments. The test boards have been subjected to mechanical shocks using the method 2002.5, condition G, under the standard MIL-STD-883H test. The effect of temperature, humidity and shock on the oscillator has been studied. The survivability of SiT 8103 has been demonstrated as a function of change in the output frequency, rise/fall time(s) and duty cycle. Later the deterioration in oscillator output parameters has been characterized using the techniques of Fast Fourier Transform and Principal Component Analysis. The results obtained show that exposure to sequential high relative temperature-humidity and high-g shock affects the

working of Silicon MEMS oscillators more than just the high-g shock environment. Rise and fall times, Output frequency and Duty cycle show more deterioration and drift in the 85°C/85%RH cases on comparison with their pristine counterparts. The energy spectrum data obtained after conducting the FFT analysis demonstrate that 85°C/85%RH samples have lower peak amplitudes/signal energy than the pristine samples especially during the first 50 drops.

MEMS based oscillators are essentially clocks that control the timing in electronics. A resonator combined with an oscillation circuitry makes an oscillator. MEMS oscillators have made their presence felt in the commercial market since 2006 and are now being widely used in consumer electronics, automotive, military applications, networking, GPS systems, telecom and broadband. MEMS counterpart, Quartz based oscillators are more established and still considered as the benchmark. However Quartz oscillators are much less resilient in environments involving vibration, shock, temperature variation and noise. Thus, making MEMS oscillators more popular and viable in modern day applications. Structurally almost all MEMS based sensors act as a spring mass damper, where the proof mass does not bend and moves in the direction of force. MEMS oscillators which are nothing but MEMS resonators put together with an oscillation circuitry can have different resonating structures such as tuning fork based, interdigitated or a simple cantilever shaped. MEMS technology in commercial oscillators is relatively new and therefore there is a significant lack of reliability data that looks into the impact of sequential harsh environment operating conditions. Studies conducted previously focus more on an effective internal design in order to achieve high quality factor and the change in resonant frequency as a function of temperature [Azevedo 2007]. Silicon Time [Si-Time 2015], Discera are some of the oscillator manufacturers who are analyzing the oscillator behavior in different operating conditions and have shown peak frequency deviation of Silicon based oscillators under

131

500g shock/vibration environments. [Knobloch 2013] developed an acoustically driven silicon comb resonator for usage in high temperature wireless applications. [Azevedo 2009] demonstrates a 10 fold improvement in temperature sensitivity of resonators by building a poly-Silicon Carbide DETF resonator on a SCS substrate whose sensitivity is reduced to 0.7 Hz/°C. The objective of this investigation is to analyze the output parameters of a commercial MEMS based oscillator and assess the accrued damage. For this study, MEMS test board assemblies were subjected to sequential high relative temperature humidity, 85°C/85%RH for 500hrs and then followed by high-g shock loading environments, method 2002.5, condition G; under the standard MIL-STD-883H test. This is equivalent of a 1500G stress environment. Deterioration mechanisms in MEMS oscillator have been documented for the above mentioned temperature-humidity and shock environments. MEMS oscillator used in this investigation was SiT8103, a high performance LVCMOS oscillator, ideal for consumer electronics. It is manufactured by Silicon Time. Some of the key components that make up the SiT8103 are, a tuned silicon MEMS resonator, oscillator sustaining circuit, high precision fractional-N phase locked loop i.e. frequency multiplier, temperature sensor and drivers with fully differential circuits. Oscillator output parameters namely, Rise/Fall time(s), output frequency and duty cycle were recorded using a high speed data acquisition system. Damage progression in the aforementioned parameters was studied until the response of the oscillator was permanently outside the stable operating range as specified by SiTime. A total of 10 MEMS board assemblies were put to test with 5 of them being exposed to sequential temperature-humidity and then followed by high g-shock environments and the other 5 exposed to just high g-shock environment.

5.1 TEST VEHICLE

Open source software, Free-PCB was used to design the MEMS test board. Later, the test board was fabricated and then assembled using the surface mount technology line present at CAVE3 electronics research center. The dimensions of the test board are 132mm x 77mm. It is a JEDEC standard double sided FR4 material PCB. PCB pads are solder mask defined with immersion finish.
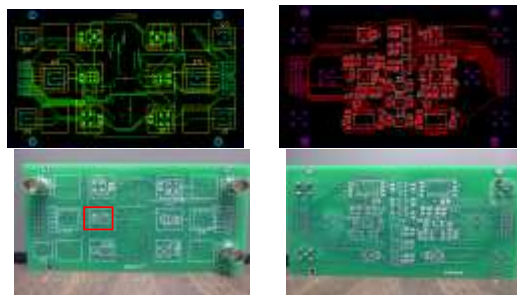
Figure 114:- Test Board Design

The printed circuit board used in this investigation has been fabricated for the testing of Accelerometers, Oscillators, Gyroscope and Pressure sensor. However this particular study only focusses on SiT8103 high performance oscillator.
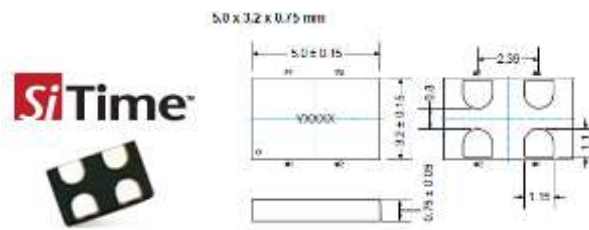
Figure 115:- SiT8103 Layout

The MEMS resonator within the device is fully encapsulated in Silicon and boxed within a micro vacuum chamber. The resonator whose mass is very small, unknown as proprietary to Silicon Time, has a stiff Silicon crystal structure. SiT8103 package is comprised of two stacked die, the top die is the resonator die and the bottom die corresponds to the oscillator die as shown below in Figure 116, the x ray images were taken at CAVE3 center at Auburn University.

133
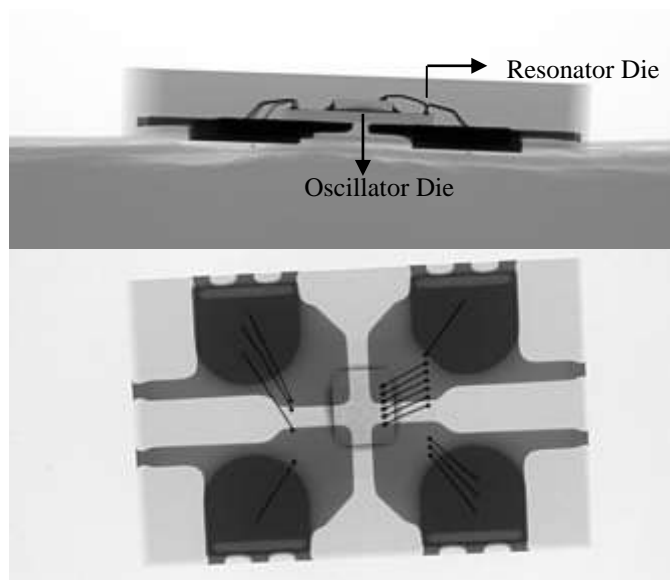
Figure 116:- X-ray images for side and top view of SiT8103

De-capping Process

Silicon Time uses a MEMS first fabrication process for making resonators. Resonator is formed by using Deep Reactive Ion Etching Process. Later these free standing resonator beams are covered with SiO_2 and then thin layers of Silicon are grown on top of SiO_2 and vents are patterned as shown in Figure 118.
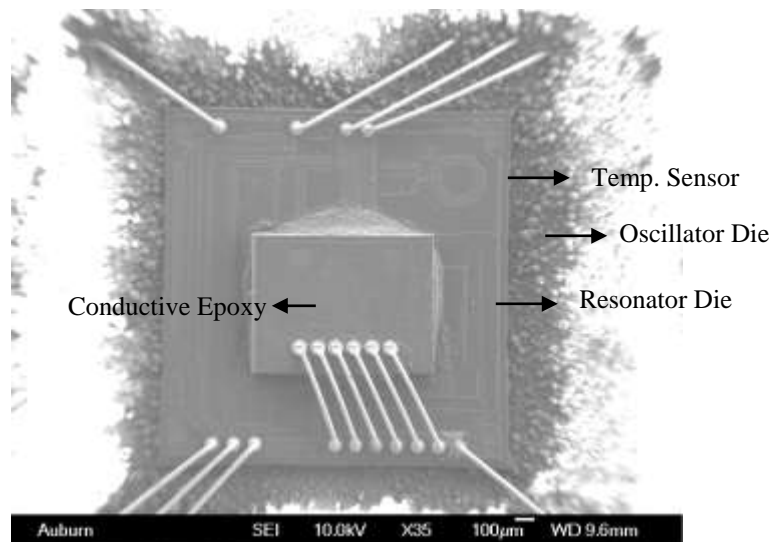
Figure 117:- SEM image of the stacked resonator die on oscillator die
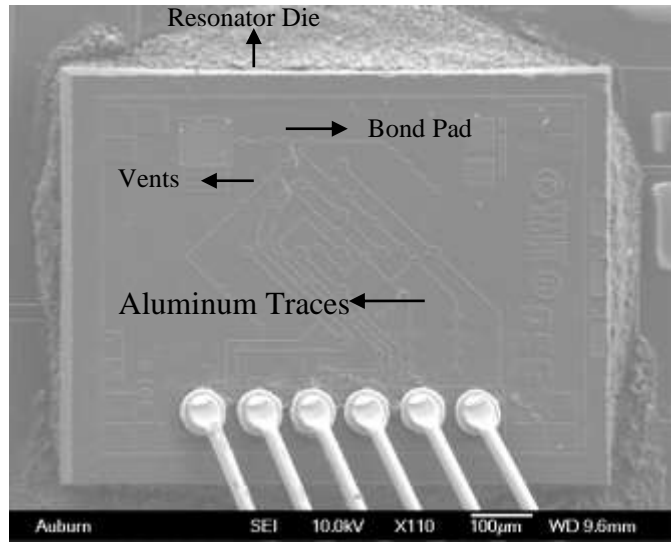
Figure 118:- SEM image of resonator die

SiT 8103 packages were decapped in order to visualize the internal structure of the MEMS oscillator before being taken for SEM. The packages were placed on a hot plate set at $100^{\circ}C$ and then a small drop of red fuming Nitric acid (HNO_3) was dropped at the center of package. After which they were cleaned with a spray of acetone and then dried with compressed air.

As mentioned above the resonator and oscillator die are stacked on top of each other. The latter consists of Resonator sustaining circuit, frequency multiplier, temperature sensor, OTP memory, charge pump for voltage bias and A/D convertor. Figure 119 below demonstrates the SiT8103 architecture block.
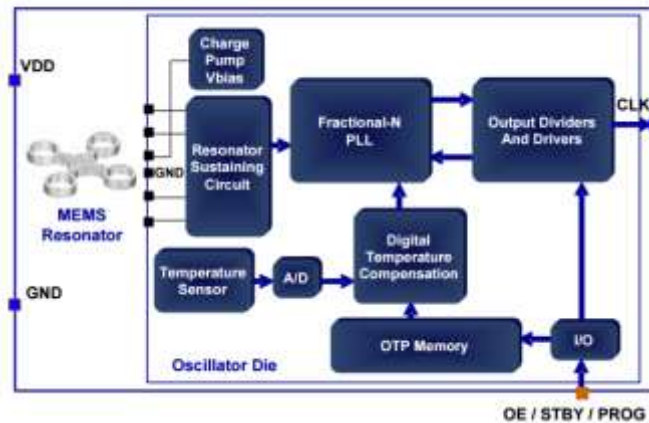
Figure 119:- Architectural block for SiT8103

135

SiT8103 operates anywhere between 1.8-3.3V, for this investigation it was connected to a 2.5V power supply and a 0.1uF capacitor was connected between the package and ground. This acts as the decoupling capacitor, which reduces the noise from power supply line. The resonant frequency of the MEMS resonator is 5MHz but due to the presence of the fractional-N PLL loop, frequency multiplier, the output frequency of the device is 25MHz.

Table 18:- Pin Configurations

Pin No.	Mnemonic	Description
1	OE	Output Enable
2	GND	Ground
3	CLK	Clock Output
4	VDD	Input Voltage

5.2 RELIABLITY TEST MATRIX

Table 19 lists the two sets of pre-conditions along with the test condition. A total of 10 SiT8103 MEMS oscillators were put to test and were divided into two sets, Pristine and Temperature-Humidity depending on the pre-condition they were exposed to. Five samples of SiT8103 high performance oscillator were exposed to 85ºC/85%RH for 500hrs and then subjected to a 1500G stress environment using method 2002.5, condition G, under MIL-STD-883H test standard. On the other hand the remaining five samples, Pristine, were just exposed to the above mentioned shock condition.

Table 19:- Test Matrix

Pre-Condition	Test Condition
Pristine	1500g
85ºC/85%RH for 500 hrs.	1500g

A capacitive shock accelerometer was mounted on the Lansmont drop tower to achieve a stress environment of 1500G. Figure 120 shows the required shock pulse attained from a drop height of 12.5" on the drop tower.
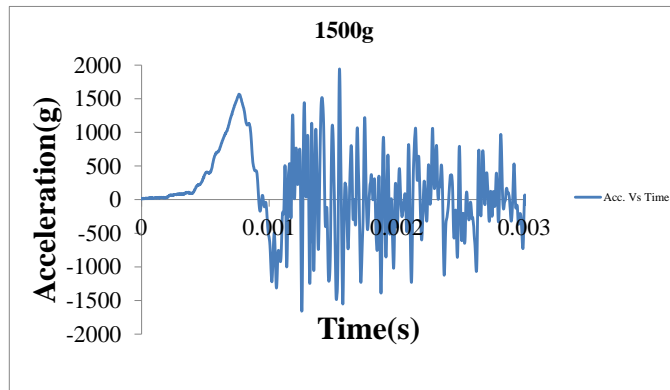
Figure 120:- Shock pulse for 1500G test environment

The MEMS oscillator, SiT8103, was subjected to sequential drops at 1500G using method 2002.5 under the MIL-STD-883H test standard. The oscillator output parameters namely rise time, fall time, duty cycle and output frequencies were recorded after an interval of every 10 drops until 350 drops were conducted on each sample. Damage progression in the aforementioned parameters was studied until the response of the oscillator was permanently outside the stable operating range as specified by Silicon Time. Figure 121 explains the clock basics; SiT8103 has a clock output which was recorded in order to measure the output parameters.
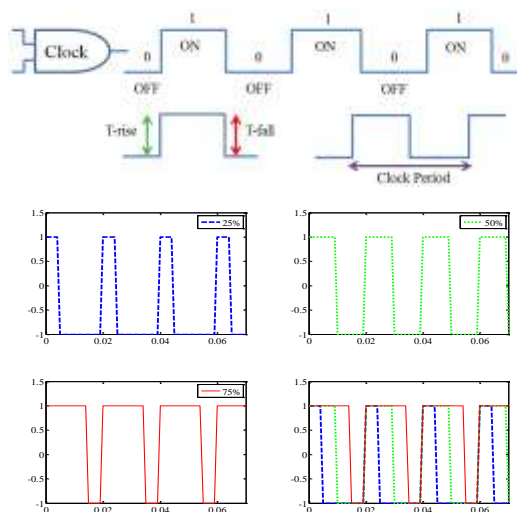
Figure 121:- Clock basics

Rise time is the time it takes for the square wave signal or the clock output to go from logic 0 to logic 1. Similarly the fall time is the time it takes for the clock output to go from logic 1 to logic 0.Logic 1 is referred to as the high state when the system is on and logic 0 is the low state when the system is off. Duty cycle is the percentage of time period a signal is active i.e. in high state. Figure 121 shows 25%, 50% and 75% duty cycles for a clock .A 50 % duty cycle means that the clock output is active or in high state for 50 % of the time and 50% of the time in low state similarly a 25% duty cycle means that the signal is in high state 25% of the time. The maximum value of rise/fall time(s) for SiT8103 is 6.8ns, as specified by Silicon Time [3] for a 2.5V power supply. The duty cycle range for SiT8103 has been specified between 45%-55%.

5.3 EXPERIMENTAL TEST SETUP

SiT8103 MEMS oscillator board assemblies were put together on the Surface Mount Technology line present at CAVE3 facility. The SMT line consists of three stages, the Stencil printer, Pick and Place machine and reflow oven (Figure 122). SAC305 solder alloy was used for this study and was evenly distributed on MEMS test board assemblies through the Stencil printer. SiT8103 oscillator and 0.1uF capacitor were placed on the board assemblies using the Pick and Place machine. Finally, the test boards were baked in the reflow oven. Figure 122 shows the three components of the SMT line.

Figure 122:- Stencil printer, Reflow oven and Pick & Place machine (CW direction)

Figure 123:- Temperature and Humidity chamber

After the MEMS test boards were assembled, first set of 5 samples were put in the temperature-humidity chamber at 85°C/85%RH for 500hrs. Figure 123 above shows the temperature-humidity chamber used for this study. The second set also comprising of 5 samples was pristine, no aging or high/low temperature exposure was done. The methodology used in this study allows us to conduct a constructive comparison among the two sets of samples. Oscillator output parameters can demonstrate whether SiT8103 is sensitive to temperature and humidity changes or not. This methodology also allows us to check whether sequential temperature humidity and high G cause more deterioration as compared to just high G environment or not. Drift in the output parameters of MEMS oscillator during 350 drops has also been monitored for all the samples (Figure 124). The next step in this investigation was to conduct sequential drops on the MEMS test board assemblies. MIL-STD-883H, method 2002.5, condition G, was the drop condition and the shock pulse had an amplitude of 1500G. For the data evaluation phase we used the technique of Principal component analysis in order to see how the output parameters of the MEMS oscillator are correlated to each other. Later Fast Fourier Transform analysis has been used to study the damage progression in the peak amplitude of the oscillator output.
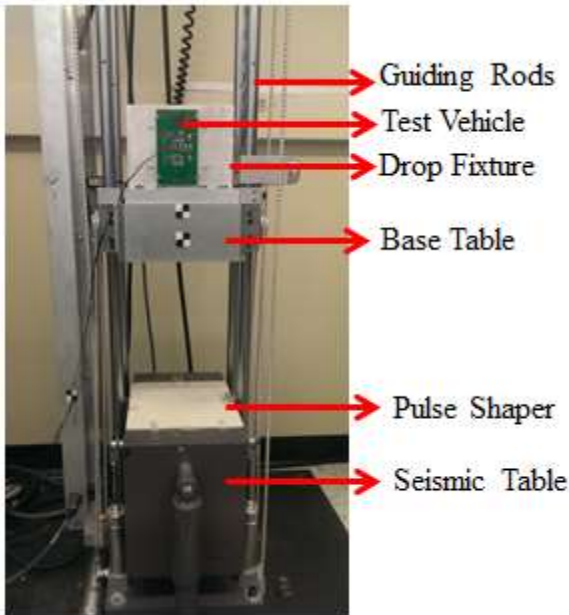
Figure 124:- Lansmont Drop Tower

5.4 EXPERIMENTAL RESULTS

MEMS test board assemblies were tested to failure i.e. until the oscillator output parameters go permanently out of the stable operating range. The motive behind exposure of SiT8103 samples to 85°C/85%RH environment for 500hrs and also subjecting them to a 1500G stress environment, is to gauge the survivability of SiT8103, Silicon based oscillator, for use in modern day consumer electronics, military applications and automotive. Oscillator output parameters such as rise time, fall time, output frequency and duty cycle have been monitored and recorded using a high speed data acquisition system, Waverunner Xi series (Figure 125).

Figure 125:- Waverunner Xi series oscilloscope

A total of 350 drops were conducted on each of the 10 samples used for this study. Data for the four output parameters was recorded after an interval of every 10 drops, so there are a total of 35 data points for each sample till the last recorded drop event. The four ports of the SiT8103 were connected to namely voltage source, 2.5V, output enable, 2.5V, ground and clock output. A LeCroy passive probe was used in this investigation to capture the data from the clock. Output data from the oscillator was captured at two different sampling rates 5MS/s and 10GS/s. The data recorded at 5MS/s showcases the output square wave and a plot of Time vs Voltage. The sampling rate was increased to 10GS/s from 5MS/s in order to correctly measure the rise time, fall time, duty cycle and output frequency. By doing so the number of data points increased on the slope of the output wave and no anomalies would be recorded while measuring the four output parameters. Figure 126 shows the oscillator square wave output at 5MS/s. The four oscillator output parameters were recorded at 10GS/s as discussed before.
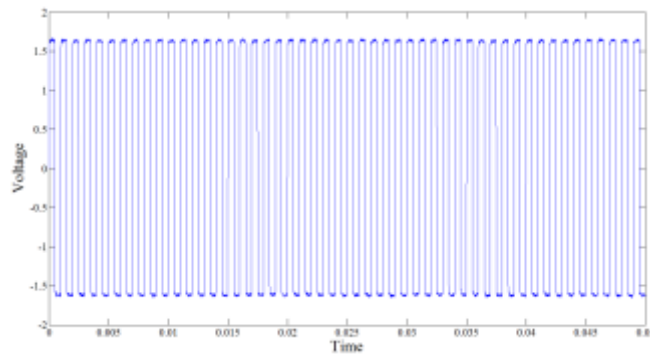
Figure 126:- Sample output plot of voltage vs time for SiT8103, a typical square wave

141

Rise Time vs Drops

As discussed earlier rise time in electronics is defined as the time it takes for the clock output from logic 0 to logic 1 i.e. from low state to high state. Figure 127 shows how the rise time is evolving for all the samples with the number of drops.
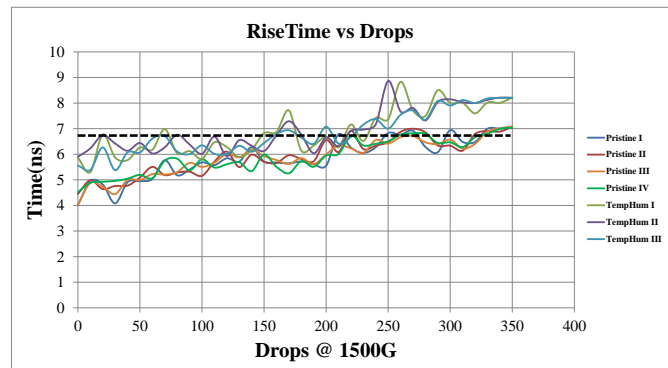
Figure 127:- Rise Time for 7 test board assemblies' w.r.t number of drops

The black dashed line represents the maximum value for rise time i.e. 6.8 ns as specified by Silicon Time Corporation [3] for a 45pF load at 2.5V. For pristine samples the lower end of the rise time starts from 4ns, increases gradually with the number of drops and crosses the maximum threshold value in the region between 270-350 drops and remains permanently outside the stable operating range. The last recorded drop event results in a rise time of more than 7ns for all the pristine samples. On the other hand, for the 85ºC/85%RH samples the lower end of the rise time data starts from 5.5 ns and stays permanently outside the maximum threshold value after the 250th drop mark with 8.8 ns being the highest recorded rise time, which is well above the specified threshold value.

Fall Time vs Drops

The time it takes for the system to go from an active stage to a non-active stage i.e. from logic 1 to logic 0. Figure 128 shows how the fall time is evolving for all the samples with the number of drops.
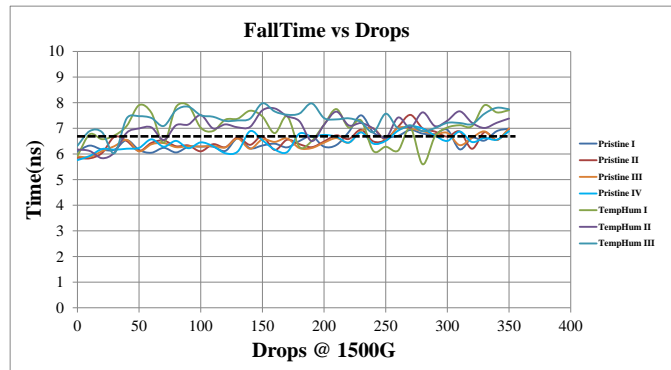
Figure 128:- Fall Time for 7 test board assemblies' w.r.t number of drops

The black dashed line represents the maximum value for rise time i.e. 6.8 ns as specified by Silicon Time Corporation [3]. For pristine samples the lower end of the fall time starts from 5.6ns, stays consistent and then goes permanently out of the maximum threshold value between the 270th -350thdrops. In this process the maximum value of fall time recorded was 7ns. For the 85°C/85%RH samples the lower end of the fall time data starts from 5.9ns and goes permanently out of the stable operating range as early as the 50th drop mark. The maximum value recorded for fall time was 7.9 ns.

Output Frequency vs Drops

The finely tuned Silicon based MEMS resonator inside the SiT8103 has a resonant frequency of 5MHz. The presence of a fractional PLL phase lock loop, a frequency multiplier, results in an output frequency of 25MHz for this device. The frequency stability is specified as +/-20PPM. So the stable frequency range becomes 24.9995MHz-25.0005MHz. Figure 129 shows the evolution of output frequency with the number of drops.
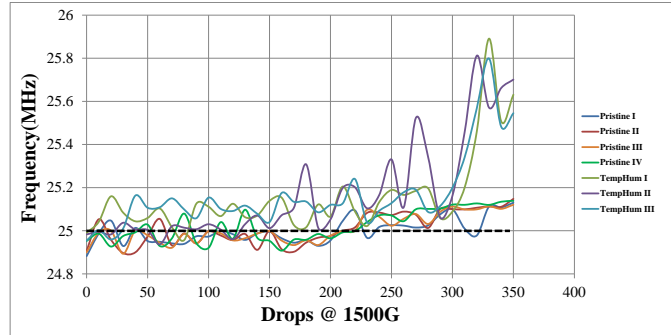
Figure 129:- Output frequency of 7 test board assemblies' w.r.t number of drops

The black dashed line represents the typical output frequency value for SiT8103 i.e. 25MHz as specified by Silicon Time Corporation. The output frequency behavior for all the pristine samples tends to remain consistent within the stable operating range but increases rapidly after the 230th drop mark and touches 25.1MHz. For the 85°C/85%RH samples the output frequency goes beyond the upper end of the stable range as early as the 20th drop mark. This behavior of 85°C/85%RH samples only tends to increase with the number of drops and the highest recorded value for output frequency is 25.85MHz.

Duty Cycle vs Drops

Duty cycle is defined as the proportion of time in which the system is active or is being operated. It can be expressed as a ratio or a percentage. Figure 130 demonstrates the duty cycle in percentage for all the SiT8103 MEMS oscillator samples. The evolvement of duty cycle with the increasing number of drops has been represented. The stable operating range for this oscillator has been specified as 45%-55% by Silicon Time Corporation.

144
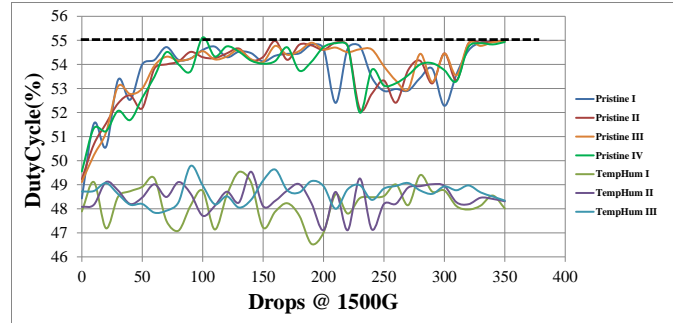
Figure 130:- Duty cycle for 7 test board assemblies' w.r.t number of drops

Pristine samples showcase a trend where the duty cycle percentage remains within the upper and the lower limit of stable operating range. For most period of the time the duty cycle percentage for pristine samples operates within 52% -55%. Similar trend is observed for the 85°C/85%RH samples, duty cycle percentage lies within the upper and lower bounds. Another key observation from the duty cycle data for 85°C/85%RH samples is that the duty cycle percentage in this case lies only within 47%-49% which states that the 85°C/85%RH systems are responding less frequently as compared to the pristine samples and .i.e. the pristine samples are active 52%-55% of the time while 85°C/85%RH samples are only active 47-49% of time. From the above explained data sets for oscillator output parameters, some of the key observations are (1) oscillator is more sensitive to temperature and humidity changes. The SiT8103 MEMS oscillators have plastic packaging and might not be hermetically sealed which is why (2) sequential temperature humidity and high G cause much more deterioration as compared to just high G environment. (3) Key output parameters such as rise/fall time(s), output frequency and duty cycle show significant drift more so in 85°C/85%RH samples.

FFT Analysis for Amplitude Degradation

The objective behind carrying out a Fast Fourier analysis is to (1) study the behavior of peak amplitude of the oscillator output (2) along with the evolution of 2nd, 3rd and 4th harmonics. FFT analysis converts the time vs voltage data (in time domain) to frequency vs amplitude data (in

145

frequency domain) where the amplitude degradation can be observed, if there is any. Computing

FFT evaluates the energy content of the oscillator output signal. Thus the energy of the signal or

the output waveform can be studied over the number of drops.

Table 20:- Peak amplitudes for representative samples

Drops	PI	PIV	THI
0	0.9477	0.926	0.906
50	0.9101	0.9003	0.8644
100	0.8722	0.8773	0.8366
200	0.807	0.8264	0.8048
300	0.7813	0.7212	0.7102
350	0.7441	0.6865	0.7026

Sample I Pristine

Pristine Drop 0

Pristine Drop 200

Pristine Drop 350
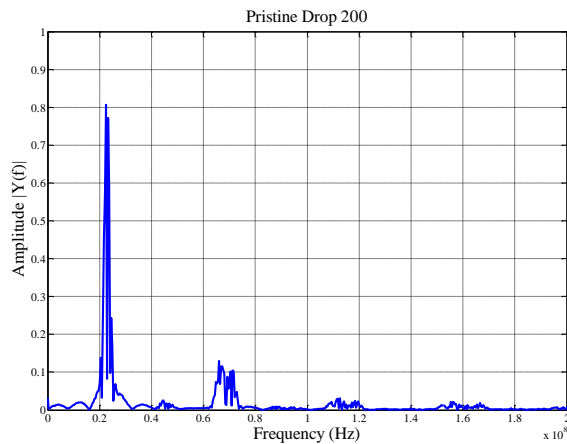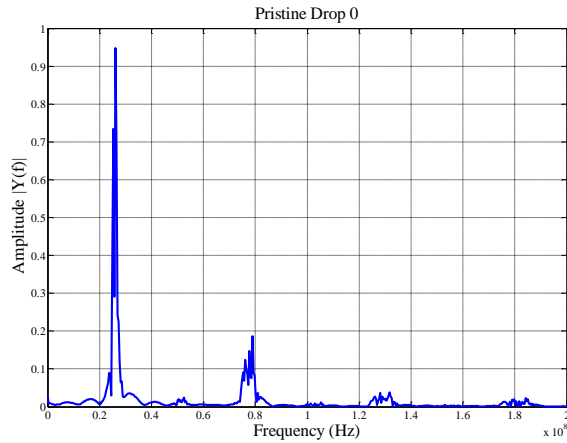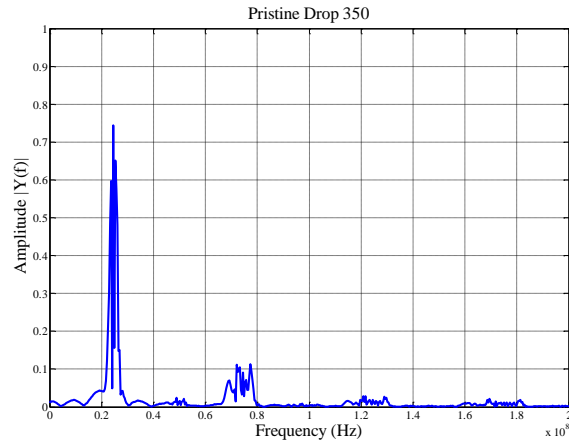
Figure 131:- FFT analysis at 0th, 200th and 350th drop for first pristine sample

Figure 131 shows the FFT plots for a pristine sample after 0,200 and 350 drops respectively. The peak amplitude reduces from 0.9477 at 0th drop to 0.7441 at 350th drop. Significant reductions can also be seen in the 2nd, 3rd and 4th harmonics from the 0th drop to the last recorded drop event. The FFT plots demonstrated above also show that the energy of the, SiT8103, oscillator output signal reduces with the increasing number of drops.

Sample II Pristine

Pristine Drop 0

147
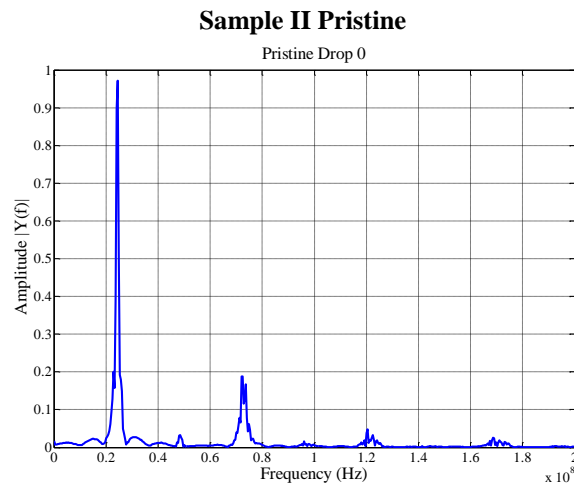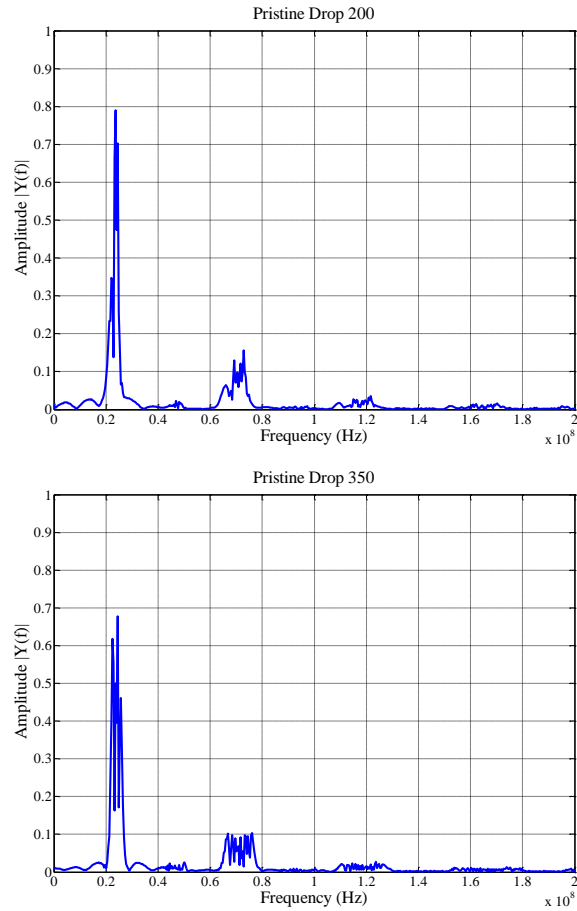
Figure 132:- FFT analysis at 0th, 200th and 350th drop for second pristine sample

Figure 132 shows the FFT plots for the second pristine sample after 0, 200 and 350 drops respectively. The peak amplitude reduces from 0.9611 at the 0th drop to 0.6896 at the 350th drop. Significant reductions can also be seen in the 2nd, 3rd and 4th harmonics from the 0th drop to the last recorded drop event.

Sample III Pristine

Pristine Drop 0

Pristine Drop 200

Pristine Drop 350
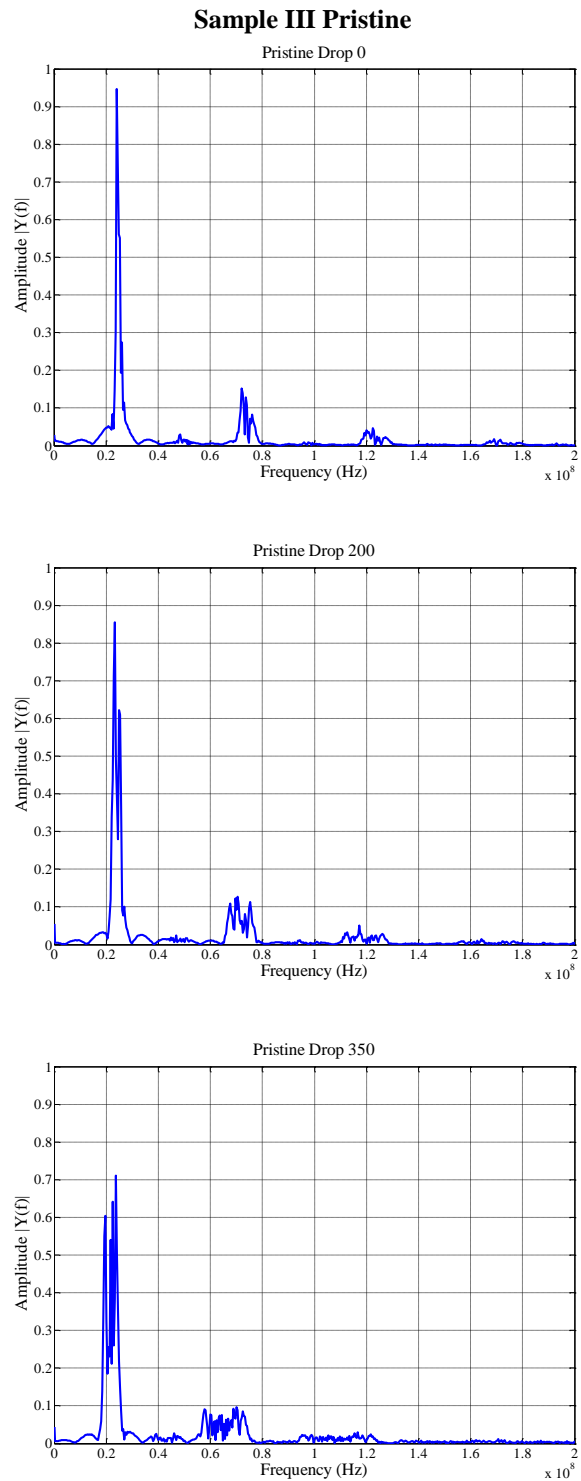
Figure 133:- FFT analysis at 0th, 200th and 350th drop for third pristine sample

Figure 133 shows the FFT plots for the third pristine sample after 0, 200 and 350 drops respectively. The peak amplitude reduces from 0.9468 at 0th drop to 0.7108 at 350th drop.

149

Significant reductions can also be seen in the 2nd, 3rd and 4th harmonics from the 0th drop to the

last recorded drop event.

Sample IV Pristine

Pristine Drop 0

Pristine Drop 200

Pristine Drop 350
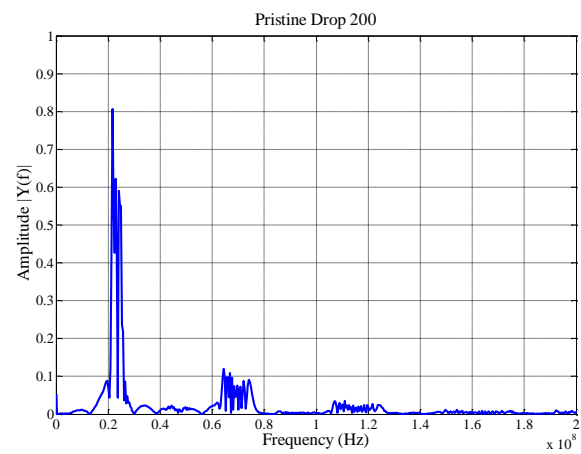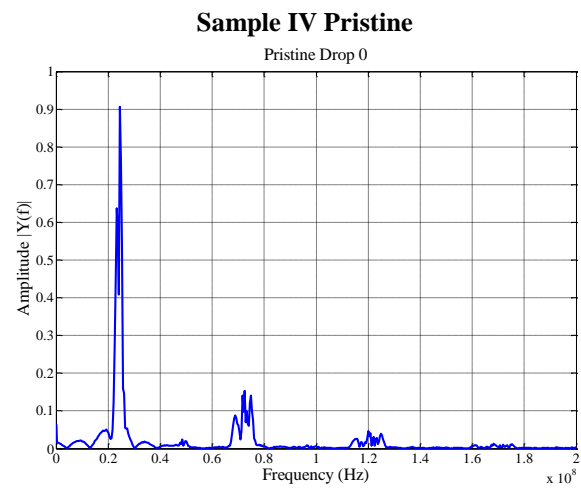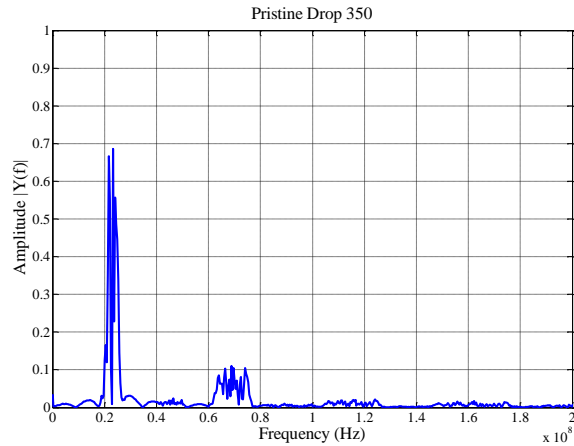
Figure 134:- FFT analysis at 0th, 200th and 350th drop for fourth pristine sample

Figure 134 shows the FFT plots for the fourth pristine sample after 0, 200 and 350 drops respectively. The peak amplitude reduces from 0.926 at 0th drop to 0.6865 at 350th drop. Significant reductions can also be seen in the 2nd, 3rd and 4th harmonics from the 0th drop to the last recorded drop event.

Temp-Humidity 85°C/85%RH Sample I

TH85c/85%RH Drop 0
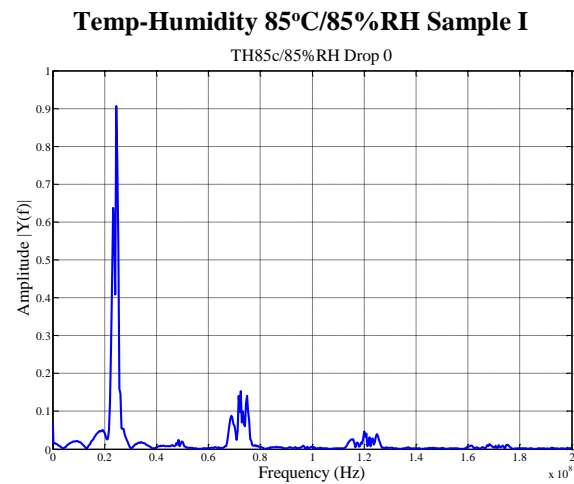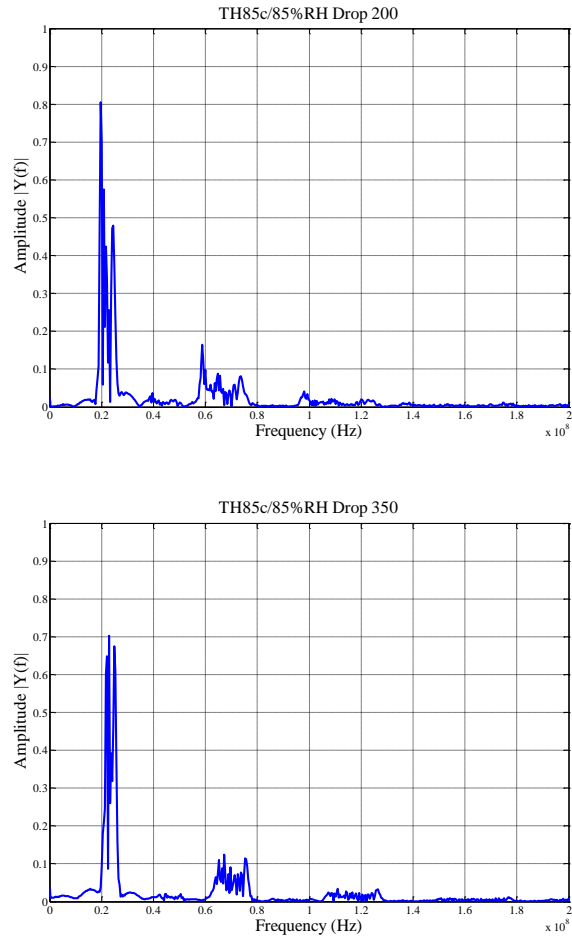
Figure 135:- FFT analysis at 0th, 200th and 350th drop for the first TH sample

Figure 135 shows the FFT plots for first $85^{\circ}C/85\%RH$ sample after 0,200 and 350 drops respectively. The peak amplitude reduces from 0.906 at 0th drop to 0.7026 at 350th drop. Significant reductions can also be seen in the 2nd, 3rd and 4th harmonics from the 0th drop to the last recorded drop event.

Temp-Humidity 85ºC/85%RH Sample II
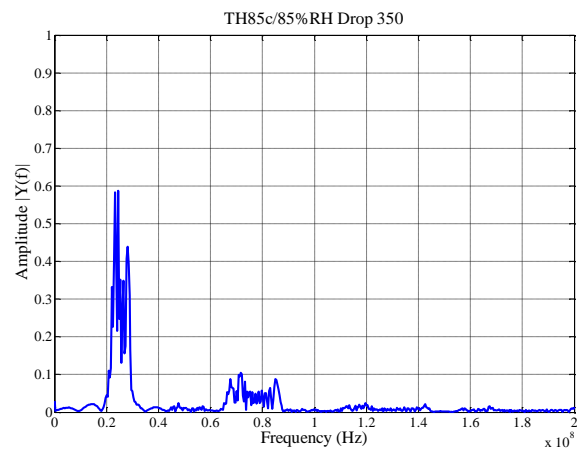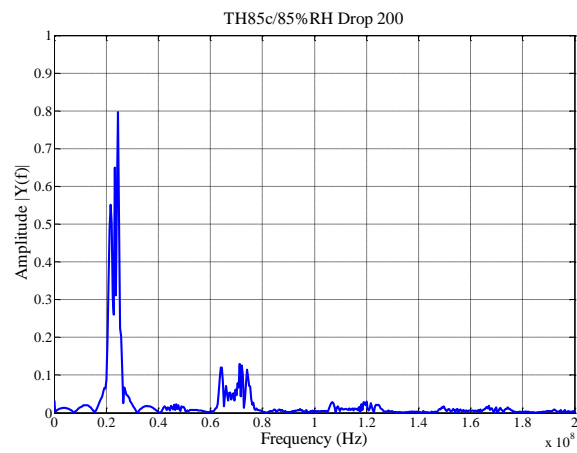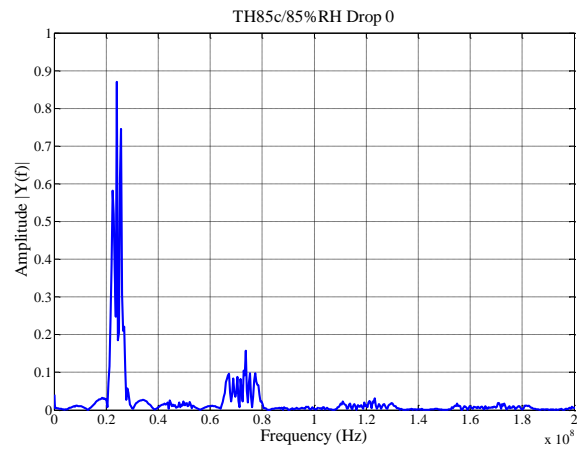
Figure 136:- FFT analysis at 0th, 200th and 350th drop for the second TH sample

Figure 136 shows the FFT plots for second 85°C/85%RH sample after 0,200 and 350 drops respectively. The peak amplitude reduces from 0.8698 at the 0th drop to 0.5869 at the 350th drop. Significant reductions can also be seen in the 2nd, 3rd and 4th harmonics from the 0th drop to the last recorded drop event.

Temp-Humidity 85°C/85%RH Sample III
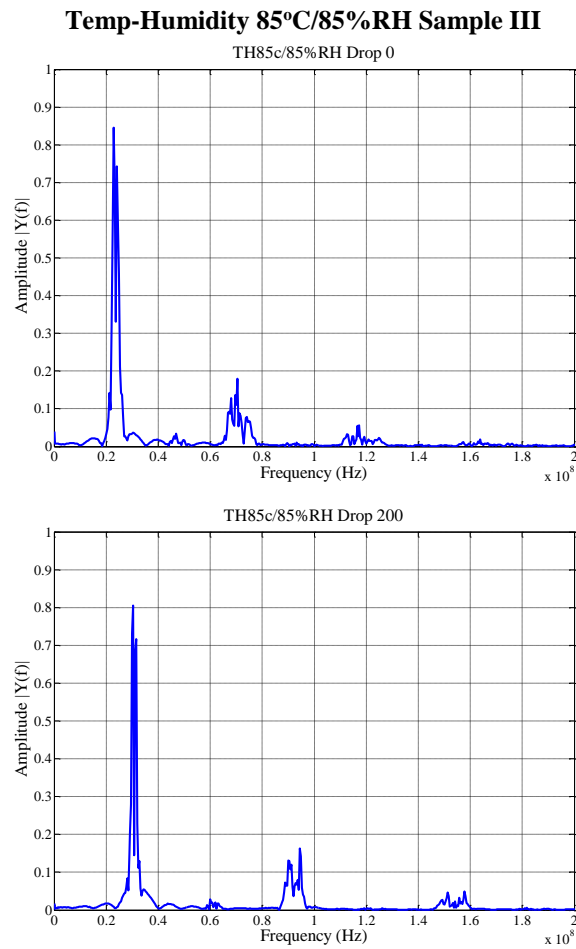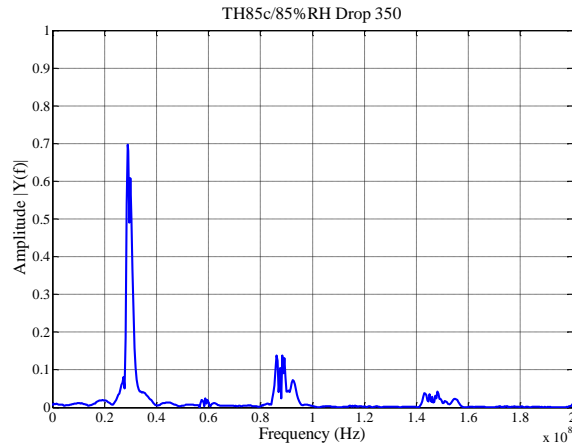
Figure 137:- FFT analysis at 0th, 200th and 350th drop for the third TH sample

Figure 137 shows the FFT plots for second 85°C/85%RH sample after 0,200 and 350 drops respectively. The peak amplitude reduces from 0.8455 at 0th drop to 0.6966 at the 350th drop. In Figure 138 the y-axis upper ends, peak amplitude, for the TH samples is lower than the upper ends for the pristine samples, Whereas the peak amplitude lower ends are almost the same for both pristine and TH samples. On comparing the FFT plots for 0th, 200th and 350th drop for pristine and 85°C/85%RH samples, it is clearly visible that the peak amplitude and other harmonics are affected more in the high temperature humidity condition especially during the first 50-100 drops.
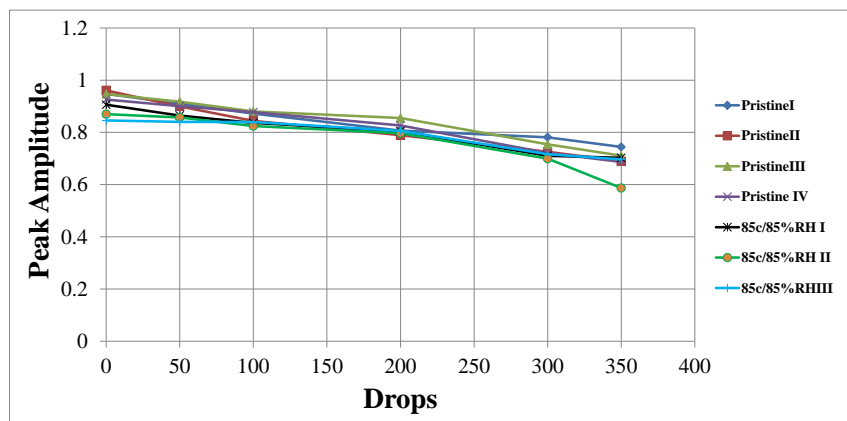
Figure 138:- Peak amplitude variation with respect to number of drops for all the samples
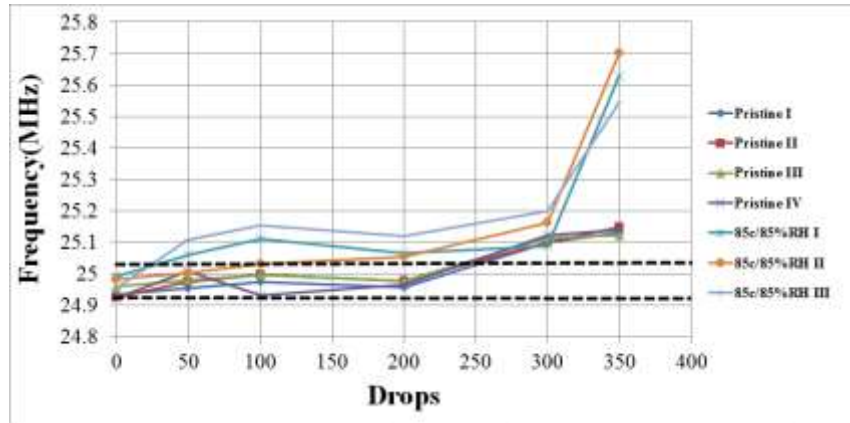
Figure 139:- Output Frequency Shift with respect to number of drops for all the samples

An increasing shift in output frequency was observed for all the samples over the period of 350 drops. Figure 139 shows the shift in frequency, much more prominent in the 85°C/85%RH samples. In the above figure the black dotted lines are the upper and the lower bounds on the output frequency [3]. Frequency for pristine samples remains within the bounds till the 250th drop mark, whereas the frequency shift in 85°C/85%RH samples happens much faster and moves out of frequency bounds as early as the 50th drop mark. Both peak amplitude degradation and shift in the output frequency point to the fact that 85°C/85%RH harsher of the two pre-conditions

Failure Analysis

Few studies have been conducted which explain MEMS failures related to type of material especially Silicon. Shea [2006] observed MEMS failure mechanisms and modes for conditions involving space, radiation, vacuum and thermal-vibration shocks. While on the other hand Fitzgerald [2009] described and validated a methodology for reliability prediction of single crystal Silicon. No prior study exists which shows failure modes for MEMS oscillators put to use in sequential harsh thermal humidity and high G environments.

SiT8103 MEMS oscillator has a stacked configuration with the resonator die on top of the oscillator die as shown in Figure 117. The two dies are adhered to each other by conductive epoxy which holds them together.

Table 21:- Failure Modes by Pre-conditions

Pre-Condition	Failure-Modes	Test Condition
Pristine, 85ºC/85%RH	Cracked epoxy layer	1500g
Pristine, 85ºC/85%RH	Cracked decoupling capacitor	1500g
Pristine	Cracked MEMS oscillator package	1500g
85ºC/85%RH	Cracked oscillator die	1500g

De-capping process, as described in previous sections, was conducted on all the samples in order to visualize the internal structure of the oscillator. For the failed samples De-capping process was useful to see the internal failure sites and modes. Scanning Electron Microscopy (SEM) has been used to identify the failure sites. Studies conducted in the past involving MEMS devices have shown that shock impact induced failure modes include fracture cause by stress exceeding the yield strength, stiction, micron size particles causing short circuit and packaging failures. Failure modes have been categorized into two sub sections namely primary and secondary. Primary failure modes focus on the internal failure sites i.e. within the SiT8103 oscillator whereas the secondary modes focus more on the exterior and are package based failures.

Primary Failure Modes

- Cracks in the conductive epoxy layer

- Cracks on the oscillator die

Secondary failure Modes

- Cracked MEMS oscillator package

- Cracks on decoupling capacitor

- Out-of-place and cracked decoupling capacitor
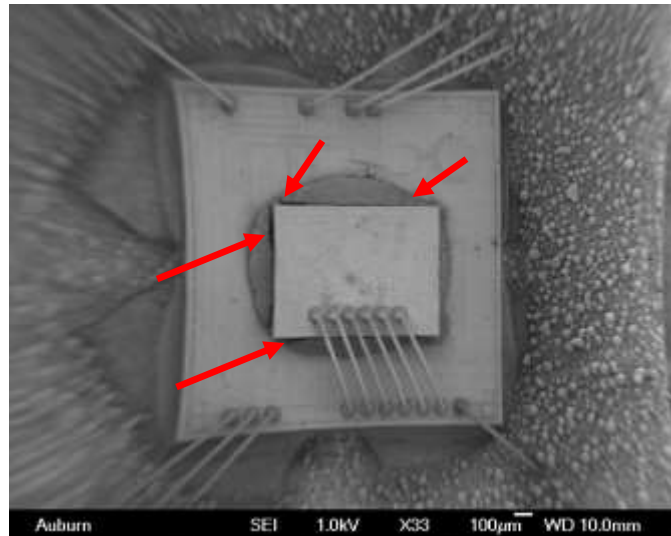
Figure 140:- Cracks in conductive epoxy layer for an 85ºC/85%RH sample
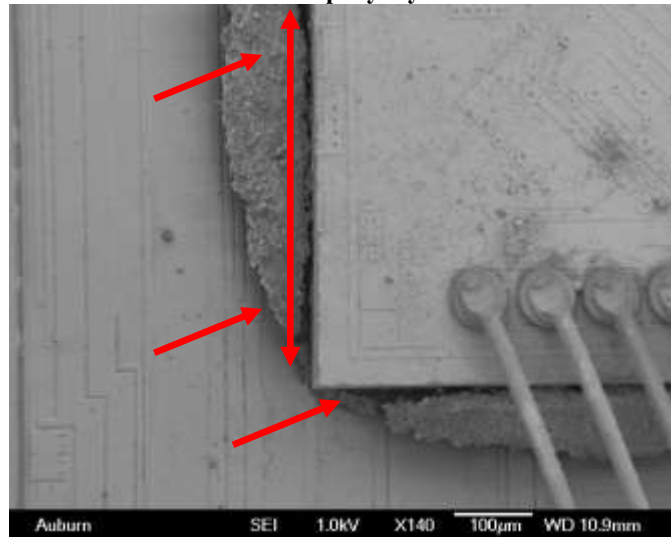
Figure 141:- Cracks in conductive epoxy layer for an 85ºC/85%RH sample
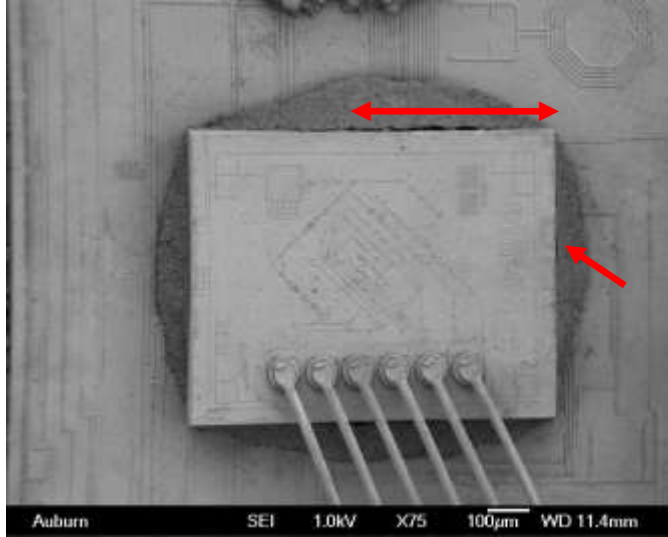
Figure 142:- Cracks in conductive epoxy layer for a pristine sample
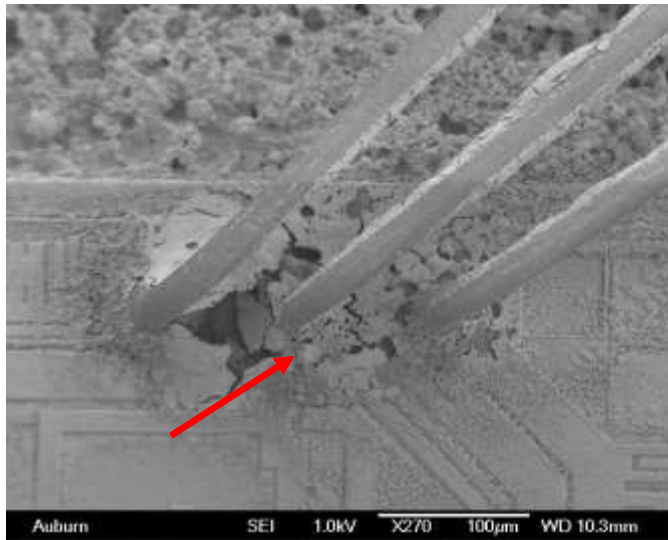
Figure 143:- Cracked site on the oscillator die for an 85ºC/85%RH sample
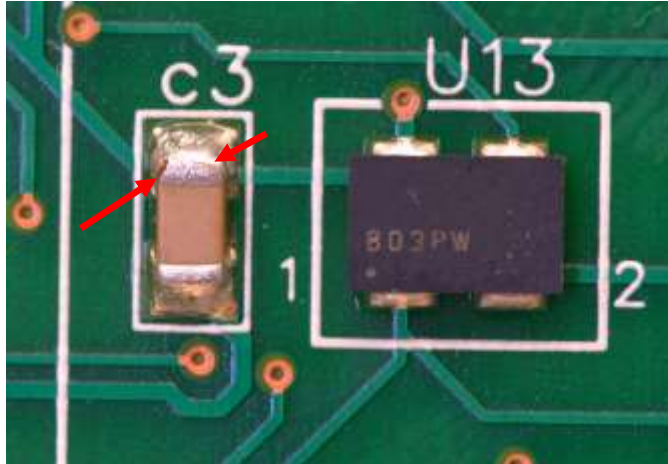
Figure 144:- Cracked decoupling capacitor, for a pristine case

Figure 145:- Cracked decoupling capacitor, for an 85ºC/85%RH case
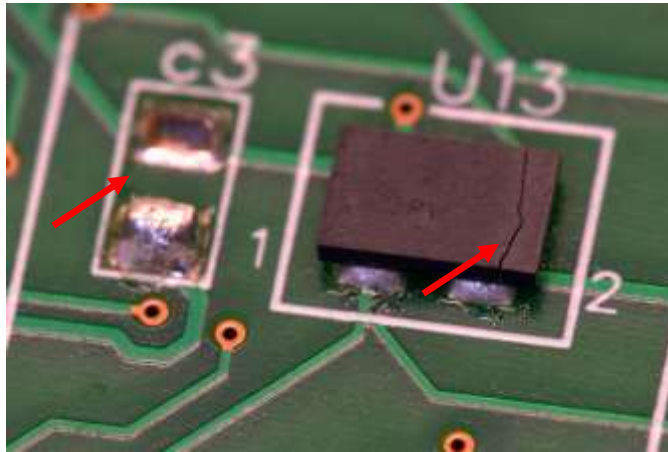
Figure 146:- Cracked MEMS oscillator package and displaced decoupling capacitor for a pristine case

Figure 140, Figure 141, Figure 142, Figure 143, show the primary failure modes and failure sites.

Figure 144, Figure 145, Figure 146 show the secondary failure modes and failure sites.

Principal Component Analysis (PCA)

A procedure that transforms a number of correlated variables to a smaller number of uncorrelated variables called principal components. Principal components are directions where the variance is most, i.e. the directions where data is most spread out. PCA computes the direction with the maximum variance for the data points. Then, all the data points can be easily represented on line

in that direction of maximum variance. This line is called the first principal component. In order to calculate the principal components, covariance matrix is calculated first from the data points. Then the Eigen values and Eigen vectors are calculated, Eigen vector corresponding to the largest Eigen value is the first principal component (PC). Similarly the other Eigen vectors correspond to the other principal components. The first PC is of the highest importance as it is able to represent the information most accurately. Minitab 17.0, statistical software was used to carry out the principal component analysis. For this study the four output parameters of SiT8103 were chosen as input components. Correlation matrix was also calculated in order to see how closely the four output parameters are related to each other. Figure 147 shows the correlation matrices for the first, second, third and fourth pristine samples respectively. It can be clearly seen from the above correlation matrices that there is a strong correlation between rise and fall times. Output frequency is also related strongly to both rise and fall times. Whereas as duty cycle shows significant correlation to the rise times in almost all cases but has the least correlation to fall times and output frequencies among all the variables.

Pristine		RiseTime	FallTime	Frequency	Duty Cycle
	RiseTime	1.000	0.767	0.766	0.646
	FallTime	0.767	1.000	0.676	0.495
	Frequency	0.766	0.676	1.000	0.251
	Duty Cycle	0.646	0.495	0.251	1.000
85°C/85%RH		RiseTime	FallTime	Frequency	Duty Cycle
	RiseTime	1.000	0.112	0.519	0.020
	FallTime	0.112	1.000	0.280	0.032
	Frequency	0.519	0.280	1.000	0.012
	Duty Cycle	0.020	0.032	0.012	1.000

Figure 147:- Representative Correlation matrix

Pristine		RiseTime	FallTime	Frequency	Duty Cycle
	RiseTime	1.000	0.661	0.691	0.525
	FallTime	0.661	1.000	0.479	0.282
	Frequency	0.691	0.479	1.000	0.123
	Duty Cycle	0.525	0.282	0.123	1.000
85°C/85%RH		RiseTime	FallTime	Frequency	Duty Cycle
	RiseTime	1.000	0.236	0.558	0.035
	FallTime	0.236	1.000	0.296	0.029
	Frequency	0.558	0.296	1.000	0.040
	Duty Cycle	0.035	0.029	0.040	1.000

Figure 148:- Representative Correlation matrix

Figure 147 and Figure 148 show correlation matrices for representative samples. For the pristine cases there is high correlation among rise time, fall time and frequency but this correlation goes down when compared to 85ºC/85%RH cases. Decreasing correlation indicates that the components are failing faster in temperature-humidity cases.

Scree Plot of Pristine_SampleI
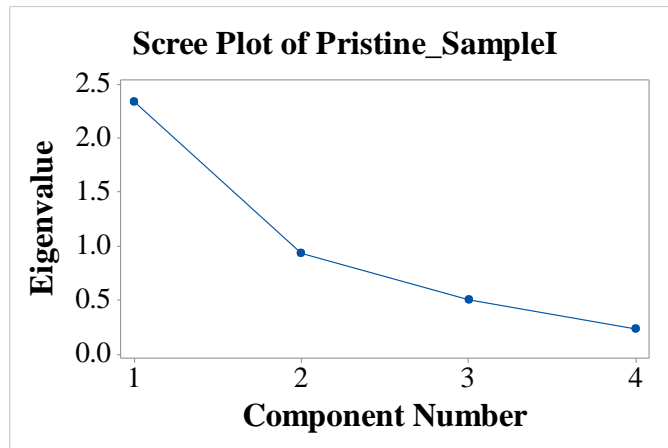
Figure 149:- Representative Scree plot for pristine sample

Scree Plot of TH85c/85%RH_SampleI
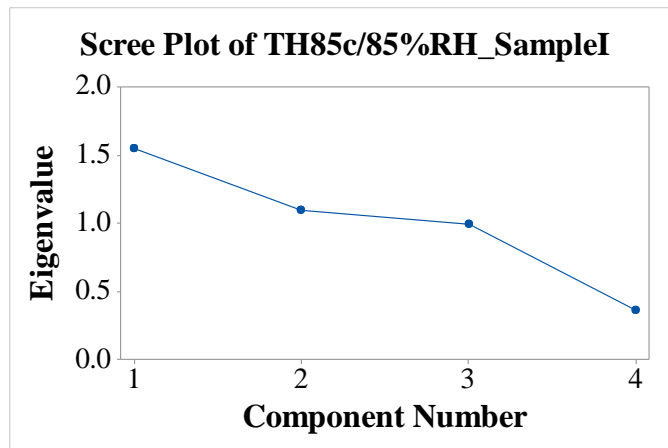
Figure 150:- Representative Scree plot for 85ºC/85%RH sample

Figure 149 shows the scree plots for the first, second, third and fourth pristine samples. It can be clearly seen that the first and second the principal components in all the cases explain most of the variability in the data. Figure 150 shows the scree plots for the first, second and third

temperature-humidity samples. It can be clearly seen that the first and the second principal components in all the cases explain most of the variability in the data.

5.5 SUMMARY AND CONCLUSIONS

In this study we present a methodology to analyze the behavior of a commercial MEMS based Silicon oscillator when exposed to harsh environmental operating conditions. The high performance oscillator was tested under high relative humidity and high temperature followed by subjection to high-G shock loading environments. This damage progression investigation monitored four output parameters for the SiT8103 oscillator and was successful in characterizing the overall behavior of the MEMS device. It was noted that the MEMS oscillator is more sensitive to temperature and humidity changes. The SiT8103 MEMS oscillators have plastic packaging and might not be hermetically sealed which is why sequential high temperature and humidity and high G cause much more deterioration as compared to just high G environment. Plastic packaging can be avoided and SiT8103 should be packaged more hermetically in order to achieve optimum performance in conditions involving humidity. Results from both the pristine and 85°C/85%RH samples show that these Silicon based oscillators deviate from the promised metrics. Key output parameters such as rise/fall time(s), output frequency and duty cycle show significant drift, more in 85°C/85%RH samples. For instance the 85°C/85%RH samples show duty cycle percentage to be around 47-49% whereas pristine samples have duty cycle percentage between 50-55%; this clearly indicates that the 85°C/85%RH samples are less responsive as a system. The SiT8103 are plastic packages and therefore not hermetically sealed, this makes water condense into small cracks and pores on the surface of Silicon and other materials. FFT analysis demonstrate that the 85°C/85%RH samples have less peak amplitudes and lower signal

energy of the output waveform as compared to pristine samples especially during the first 50-100 drops. Shift in output frequency was also observed for the all the samples, worst in temperature-humidity cases. On conducting the failure analysis, SEM images provide visual evidence of failure sites and modes which in turn indicates that for SiT8103 Silicon MEMS oscillator the most vulnerable or the area most prone to damage is the conductive epoxy region which attaches the resonator die to the oscillator die. Other evidences indicate that cracking of SiT8103 MEMS oscillator package is also possible along with cracking of the decoupling capacitor. PCA results show that there is more correlation among the output parameters in the pristine cases as compared to the temperature-humidity cases. The decreasing correlation in the 85°C/85%RH cases suggest that the components are failing faster in the temperature-humidity samples than the pristine cases and also points to the fact that there can be more of white noise present in the temperature-humidity data sets. In order to mitigate the effects of environmental loads on oscillator performance, the following potential solutions can be explored:

☐ Alternative packaging architecture to mitigate the effect of environmental loads.

☐ Explore the use of alternate attachment epoxies.

Chapter 6

Survivability of MEMS Accelerometer under Sequential Thermal and High-G Mechanical Shock Environments

Reliability data on MEMS accelerometers operating in harsh environments is scarce. Micro-electro-mechanical systems (MEMS) are used in a variety of military and automotive applications for sensing acceleration, translation, rotation, pressure and sound. This research work focuses on dual axis MEMS accelerometer reliability in harsh environments. Structurally an accelerometer behaves like a damped mass on a spring. Commercially there are three types of accelerometers namely piezoelectric, piezoresistive and capacitive depending on the components that go into the fabrication of the MEMS device. Previously, majority of concentration was focused on an effective internal design, performance enhancement of CMOS-MEMS accelerometers and packaging techniques Cheng [2002], Qiao [2009], Lou [2005], and Weigold [2001]. Studies have also been conducted to obtain an enhanced inertial mass SOI MEMS process using a high sensitivity accelerometer Jianbing [2013], Chen [2005]. There have been prior test(s) conducted on MEMS accelerometers, Jiang [2004], Cao [2011], Chun-Sun [2009], Lou [2009], Tanner [2000] and Yang [2010] but the availability of data on reliability degradation of such devices in harsh environments Brown [2003] is almost little to none which thereby generates the importance of this work and also makes way for a whole new path involving the reliability assessment techniques for MEMS devices. Concentration of our work is primarily on the reliability of this accelerometer upon sequential exposure to harsh environment(s) and drop-shock. Reliability of accelerometers in high G environments is unknown. The effects of these pre-conditions along with the drop test condition has been studied and analyzed. In this piece of research work, a test vehicle with a MEMS accelerometer, ADXL278 dual axis capacitive

accelerometer, has been tested under high/low temperature exposure followed by subjection to high-g and low-g shock loading environments. The test boards have been subjected to mechanical shocks using the method 2002.5, condition G, under the standard MIL-STD-883H test. The stress environment and the test condition used for this investigation are 1500g and 70g respectively where 70g is the full scale range output of ADXL278 in the drop direction with pulse duration set to 0.5millisecond. The deterioration of the accelerometer output has been characterized using the techniques of Mahalanobis distance and Confidence intervals. Scanning Electron Microscopy (SEM) has been used to study the different failure modes inside of the accelerometer, which were potted and polished and later de-capped. Furthermore, the non-destructive evaluations of the MEMS accelerometer have been demonstrated through X-rays and micro-CT scans. Consumer products such as automotive airbags, Collison prevention system and anti-braking systems make extensive use of Surface/Bulk micro machined MEMS accelerometers. Commercially there are three types of accelerometers namely piezoelectric, piezoresistive and capacitive depending on the components that go into the fabrication of the MEMS device. From Figure 151 , structurally an accelerometer behaves like a damped mass on a spring, where the proof mass is a rigid structure that does not bend but can move in the direction of applied force. The beam/spring/flexure is an elastic structure, generally made of single crystal silicon.
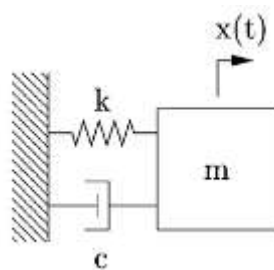
Figure 151: Spring Mass Damper

No prior reliability data exists for a dual axis MEMS accelerometer on exposure to harsh environments and then subjection to simultaneous shock events. The purpose of this investigation is to analyze the characteristics of a, commercially available, MEMS dual axis accelerometer and study the adverse effects. In this study, the MEMS board assemblies were subjected to five sets of different pre-conditions, elaborated later in the study, followed by sequential shock events till failure of the MEMS device. For the different types of thermal, temperature-humidity and shock pre-conditions, outcomes of the deterioration mechanisms in MEMS dual axis accelerometer have been reported. The MEMS board assemblies have been subjected to mechanical shocks using the method 2002.5, condition G, under the standard MIL-STD-883H test. The stress environment and the test condition used for this study are 1500g and 70g respectively, where 70g is the full scale range output of ADXL278 in the drop direction with pulse duration set to 0.5millisecond. The MEMS accelerometer used in this piece of research work was ADXL278, a dual axis high-g accelerometer manufactured by Analog devices. The output of the MEMS sensor has been captured using high speed data acquisition system. The drift in the output of the accelerometer with increasing number of drops has been quantified by computing the Mahalanobis distance. Failure analysis was conducted in order to see the internal degradation of accelerometer caused by the accrued harsh environmental conditions.

6.1 TEST VEHICLE

In this study, first the layout of the MEMS test board was designed using Free-PCB software, second the board was fabricated and lastly the MEMS components, i.e. ADLX278 and the required capacitors to complete the external circuitry, were assembled on it using the SMT line at

the CAVE3 Electronics Research Center. The dimensions of the test vehicle are 132mm x 77mm.The test board is a JEDEC standard double sided FR4 material PCB.

Figure 152: Layout of ADXL278, courtesy Analog devices
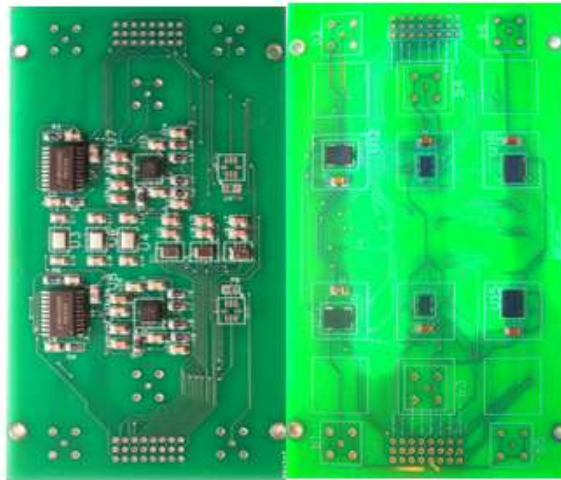
Figure 153: Bottom and top layer with all the MEMS devices mounted.

The printed circuit board pads were solder mask defined (SMD) with immersion finish. Figure 153 demonstrates the top and the bottom layer of the test board. This particular PCB has been designed for testing of Accelerometers, Gyroscopes, Pressure Sensors and Microphones but for this study we are only dealing with the testing of one type of accelerometer. Figure 152 depicts the layout and pin connections for the ADXL278.
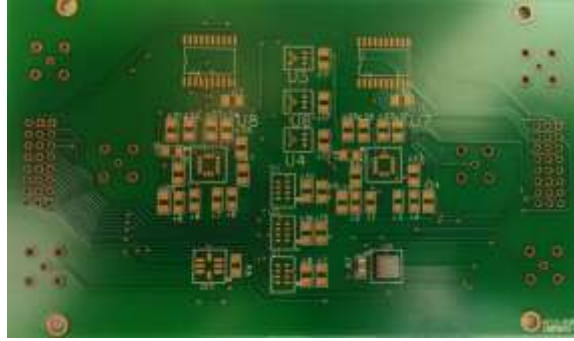
Figure 154:- Bottom Layer with ADXL278 and external capacitor

Table 22:- Pin Configurations

Pin No.	Mnemonic	Description
1	V_{DD3}	3.5 to 6V
2	Y_{out}	Y Output
3	COM	Common
4	ST	Self-Test
5	NC	Not Connected
6	X_{out}	X Output
7	V_{DD}	3.5 to 6V
8	V_{DD2}	3.5 to 6V
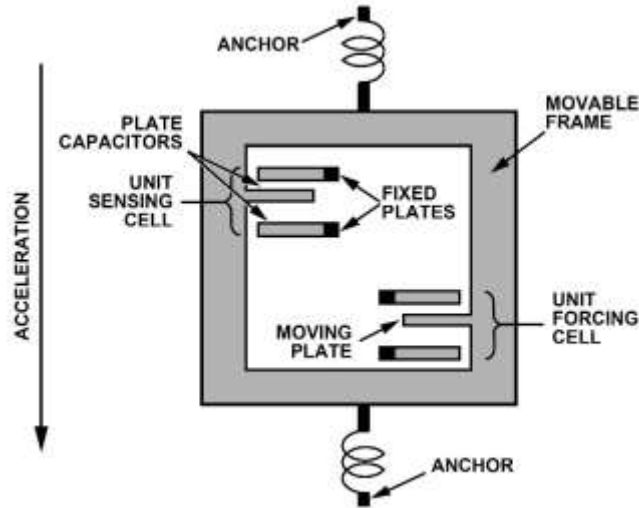
Figure 155:- Simplified View of Sensor (courtesy: - analog devices)

The ADXL278 is a low-power, dual axis accelerometer with signal conditioned voltage outputs on monolithic IC. This product measures acceleration with a full scale range of $\pm$ 70g/ $\pm$35g.This product can measure both dynamic (vibration) and static acceleration (gravity). The ADXL278 is a fourth generation surface-micro-machined *iMEMS* 8 terminal LCC package. The

169

dimensions of the MEMS sensor are 5mm x 5mm x 2mm. Table 22 represents the pin configurations of this 8 pin package. ADXL278 provides a fully differential sensor structure and circuit path. It uses electrical feedback with zero-force feedback for improved accuracy and stability. Figure 155 is a simplified view of the differential sensor element present inside the LCC package. Each cell is composed of fixed plates attached to the substrate and movable plates attached to the frame. Displacement of the frame changes the differential capacitance, which is measured by the on-chip circuitry. An application specific integrated circuit is attached to this differential sensor element which picks up the change in capacitance and converts it into a voltage output which is captured on the data acquisition system.

6.2 RELIABILITY TESTING AND TEST MATRIX

The testing of ADXL278 involves a sequential procedure which involves exposing the MEMS test board assembly to different environmental pre-conditions, as listed in , then subjecting it to the defined stress condition followed by the test condition and then finally analyzing data for computation of Mahalanobis distance and Confidence intervals.

Table 23: -Test Matrix

Pre-condition	Stress Condition	Drop Height	Test Condition	Drop Height
Pristine	1500g	12.5in	70g	4in
-40°C to 85°C	1500g	12.5in	70g	4in
-55°C to 125°C	1500g	12.5in	70g	4in
85°C/85% RH	1500g	12.5in	70g	4in

Table 24: - Reliability Testing Matrix with five sets of pre-conditions and the stress condition

Sets	Pre-Conditioning	Test Condition
Set-1	Pristine	MIL-STD-883H test. Shock pulse amplitudes have been ramped from 500 to 30,000g with pulse duration between 0.1 to 1 millisecond
Set-2	-40°C to 85°C with a 10 min dwell, 10 min ramp for 100 cycles	
Set-3	-55°C to 125°C with a 10 min dwell, 10 min ramp for 100 cycles	
Set-4	85°C/85RH for 500hrs	

Figure 156:- Block diagram of testing procedure

The test protocol for the testing of ADXL278 requires a stress environment of 1500g to be achieved on the Lansmont Drop Tower using a test and measurement shock accelerometer. Figure 157 demonstrates the 1500g shock pulse attained from a drop height of 12.5 in on the drop tower.
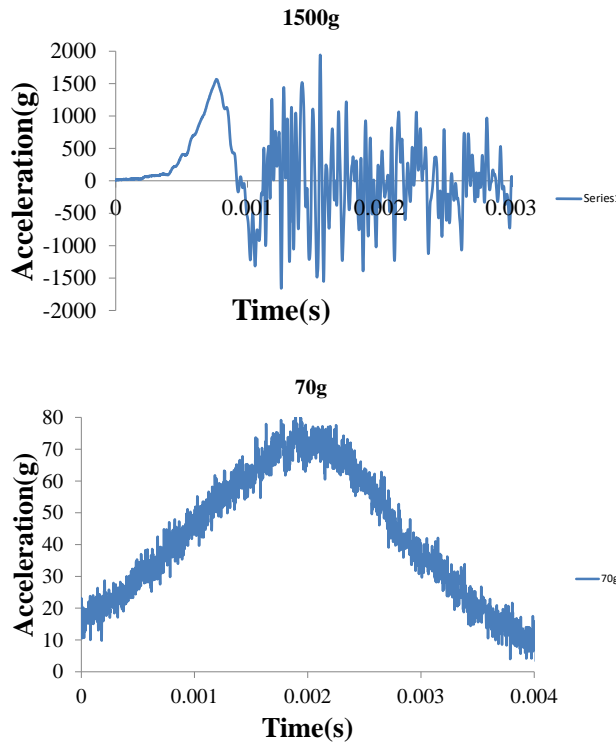
Figure 157:- 1500g Shock Pulse for Stress Condition and 70g Shock Pulse for Test Condition respectively

171

The MEMS accelerometer, ADXL278, was subjected to 1500g using the MIL-STD 883H test method 2002.5. All the drops were sequential and after an interval of every 10 drops, at the stress condition, ADXL278 was then subjected to 70g i.e. the drop height now being 4in. This was done in order to see the degradation in the output as 70g is the full scale range output of this accelerometer in the drop orientation. The sensor's mechanical structure provides a linear measurement range that is 8 times that of each axis' actual output range but the presence of a 400Hz low pass Bessel filter inside of the LCC package influences the response of accelerometer. The maximum acceleration that can be measured by this device in the pre-filtering phase is 560g which corresponds to 70g in the post-filtering phase, where 70g being the full scale output range in X axis.

6.3 EXPERIMENTAL TEST SETUP

MEMS test board assemblies were assembled on the SMT line present at CAVE3 facility. Figure 158 showcases the Stencil Printer, Pick and Place machine and the reflow oven. After the assembly phase these test boards were subjected to the various pre-conditions as discussed in table 3. The first set consists of pristine board assemblies; the second set consists of board assemblies being exposed to thermal cycling standard JESD22-A105C. In this set the test boards were subjected to temperature cycle of -40°C to 85°C with a 10 min dwell, 10 min ramp time for 100 cycles, Figure 9. The third set of pre-conditioning involved subjection of test boards to -55°C to 125°C with a 10 min dwell, 10 min ramp for 100 cycles. The fourth and the fifth set of pre-conditions were focused on the temperature-humidity environmental conditions. In these the test boards were subjected to 85°C/85%RH for 500 hours and 55°C/85%RH for 500 hours respectively.

Figure 158:- Semi-automatic SMT line at CAVE3 research center; Stencil Printer, Pick & Place machine and Reflow Oven respectively

Figure 8:- Thermal cycling chamber (left), Temperature-Humidity chamber (right)

The next step in the Experimental setup was the subjection of these test board assemblies to same shock profile. The shock profile used was MIL-STD-883H test with shock pulse amplitude at 1500g. After an interval of every 10 drops the drop height was reduced to 4in in order to subject the test board assemblies to a test condition of 70g. In the data evaluation phase the pristine data was regarded as the benchmark to which data from other pre-conditions was compared using the technique(s) of statistical pattern recognition.
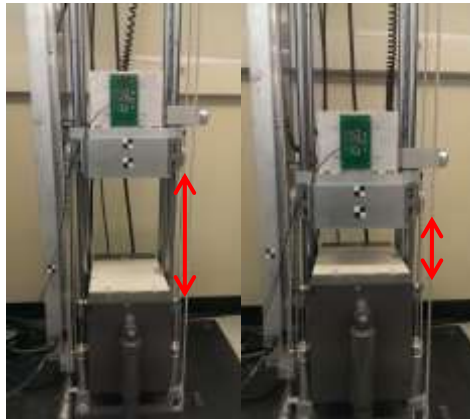
Figure 9:- 12.5in Drop Height (Left), 4in Drop Height (Right)

For instance the shock pulse from the first drop on the pristine test board assembly was compared to the shock pulse from first drop of another pre-condition being taken into account. Similarly all the drops from all the pre-conditions were compared to their respective pristine counterparts. Damage indicator analysis includes gaging of Mahalanobis distance and use of t-test to estimate the confidence intervals. Mahalanobis distance is a statistical approach that provides a relative measure of a data point's distance from a mean of the data set. For the purpose of this research work we have quantified the drift in the accelerometer's response from the mean-measured response of the data-set under identical conditions. Mathematically Mahalanobis distance is defined as:

$$D(x) = \sqrt{(x - \mu)^T S^{-1}(x - \mu)} \tag{1}$$

Where x is a multivariate vector

$$x = (x1, x2, x3 \dots x_N^T) \tag{2}$$

$$\mu = (\mu1, \mu2, \mu3 \dots \mu_N^T) \tag{3}$$

where μ is the mean-signal of pristine assemblies used to construct the reference configuration. Preconditioned board assemblies with MEMS sensors were mounted on the Lansmont drop tower and tested till failure under high-g shock load. Signals were analyzed in each case for drift of tested assemblies compared to the healthy configuration. The confidence values have been computed for the following hypothesis test:

$$
\begin{aligned}
H_0: & \quad \mu = \mu_0 \\
H_a: & \quad \mu \neq \mu_0
\end{aligned}
\tag{4}
$$

The confidence value (CV) represents the highest level of confidence at which we can reject the null-hypothesis and accept the alternate. The t-test assesses how different the means of two groups are from each other. This analysis involves acceptance or rejection of null hypothesis depending on the t-statistic. A two sample t-test assuming unequal variances was carried out on the collected data. For each shock excursion, the CV has been computed. As per the hypothesis, if the mean of a pristine shock pulse for a specific drop event is equal to the mean of a pre-conditioned (TC1 or TC2 or TH1 or TH2) shock pulse for a specific drop event then we accept the null and reject the alternate hypothesis. Similarly we accept the alternate and reject the null if they are not equal. Confidence values have been computed for the above hypothesis. These values represent the highest level of confidence at which we can reject the null-hypothesis and accept the alternate. This hypothesis depends on the t-test which assesses how different the means of are. Depending on the value of t-statistic we either accept or reject the null hypothesis.

6.4 EXPERIMENTAL RESULTS

Pristine Pre-Condition

For this section of the test protocol, the pristine test board assemblies have been subjected to high-g shocks till failure. The objective behind the conduction of drop test is to quantify the survivability of ADXL278, dual axis accelerometer, for use in electronics which may be subjected to inadvertent drops, forces or have abrupt changes in motion. Drop and shock standard MIL-STD-883H test method 2002.5 has been used and the board assemblies have been subjected to multiple facets of shocks under the above defined method. The board assemblies have been subjected to 1500g for an interval of 10 drops and then subjected to the test condition of 70g to capture the output response of ADXL278. **Figure 159** , Figure **160** Figure **161** show pristine responses. For each sample the acceleration peaks vs time have been plotted from the first to the last drop before failure.
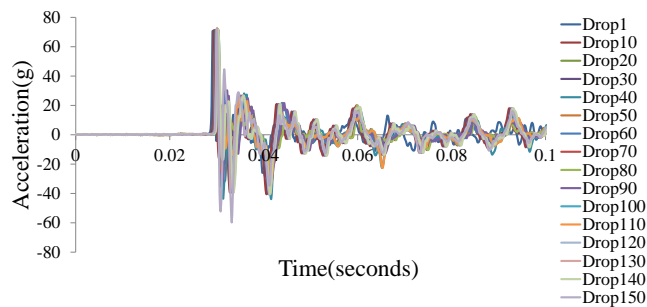
Figure 159:- Drop traces from sample I for a pristine ADXL278, all the drops are superimposed from first to the last drop before failure, total drops 150
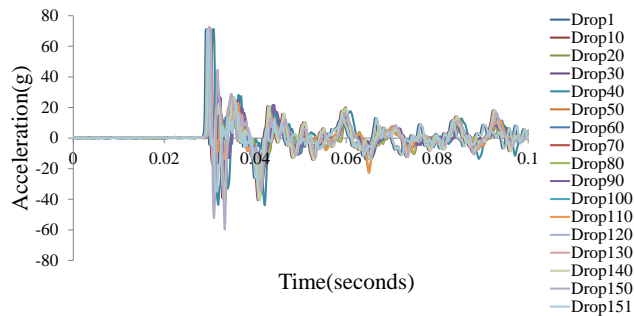
Figure 160:- Drop traces from sample II for a pristine ADXL278, all the drops are superimposed from first to the last drop before failure, total drops 151

176
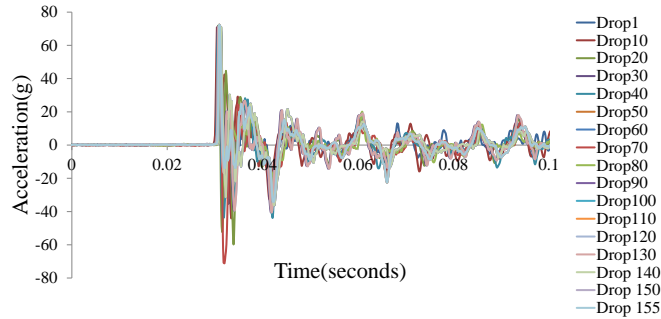
Figure 161:- Drop traces from sample III for a pristine ADXL278, all the drops are superimposed from first to the last drop before failure, total drops 155

Effect of Thermal Cycling (-40ºC to 85ºC)

In this section of the test protocol, the board assemblies were subjected to 100 cycles of thermal cycling from -40ºC to 85ºC with 10 min dwell and 10 min ramp time followed by exposure to high g-shocks till failure. The board assemblies have been subjected to 1500g for an interval of 10 drops and then subjected to the test condition of 70g to capture the output response of ADXL278, the stress condition and the test condition are imposed on to the board assemblies till failure occurs. **Figure 162,** Figure **163** and Figure **164** show the response from three thermal aged ADXL278 samples.
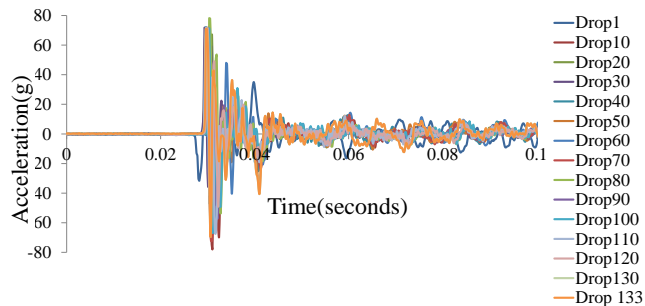
Figure 162:- Drop traces from sample I for a thermal aged ADXL278; all the drops are superimposed from first to the last drop before failure, total drops 133

177
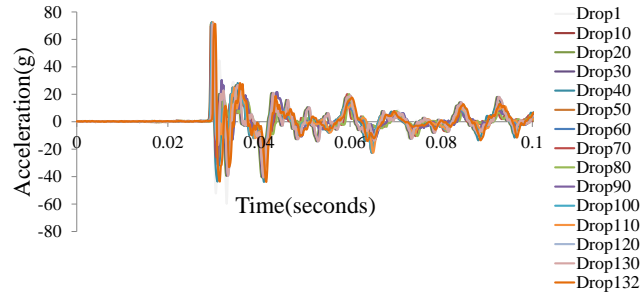
Figure 163:- Drop traces from sample II for a thermal aged ADXL278; all the drops are superimposed from first to the last drop before failure, total drops 132
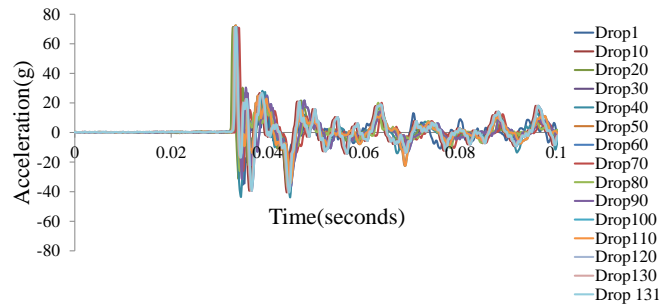
Figure 164:- Drop traces from sample III for a thermal aged ADXL278; all the drops are superimposed from first to the last drop before failure, total drops 131

Effect of Thermal Cycling (-55°C to 125°C)

In this section of the test protocol, the board assemblies were subjected to 100 cycles of thermal cycling from -55°C to 125°C with 10 min dwell and 10 min ramp time followed by exposure to high g-shocks till failure. The board assemblies have been subjected to 1500g for an interval of 10 drops and then subjected to the test condition of 70g to capture the output response of ADXL278, the stress condition and the test condition are imposed on to the board assemblies till failure occurs. Figure **165**, Figure **166** and Figure **167** show the response from three thermal aged ADXL278 samples.
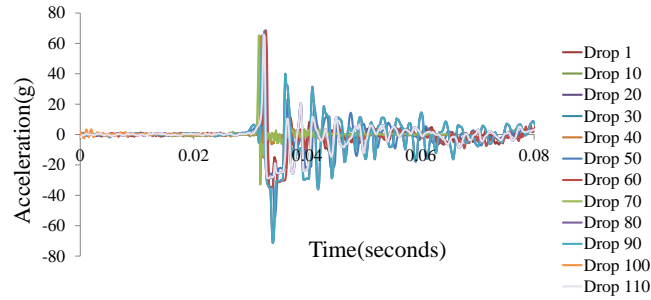
Figure 165:- Drop traces from sample I for a thermal aged ADXL278; all the drops are superimposed from first to the last drop before failure, total drops 110
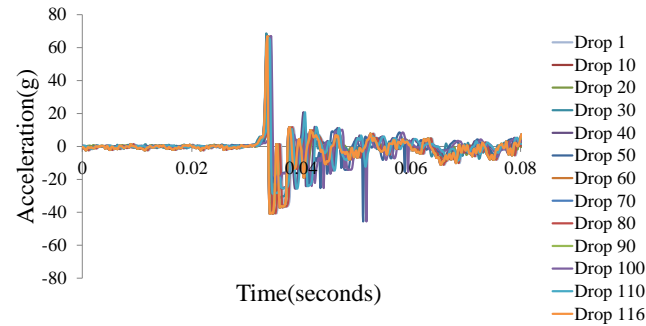
Figure 166:- Drop traces from sample II for a thermal aged ADXL278; all the drops are superimposed from first to the last drop before failure, total drops 116
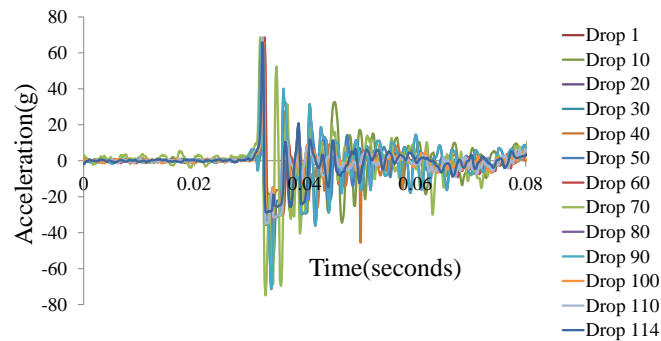
Figure 167:- Drop traces from sample III for a thermal aged ADXL278; all the drops are superimposed from first to the last drop before failure, total drops 114

Temperature-Humidity (85ºC/85%RH)

In this section of the test protocol, the board assemblies have been subjected to thermal humidity at 85ºC/85%RH for 500 hours followed by combined exposure of stress and the test conditions. A total of five ADXL278 samples were tested under the 85ºC/85%RH harsh environment but none of them were successfully able to output even a single acceleration peak. Further, non-

destructive methods such as micro-CT and X-ray were performed to study the failure modes but nothing conclusive has been reported. Scanning electron microscopy was also used to analyze the internal defects, if any. Although a specific failure mode and type has not been observed for this particular pre-condition, it can be argued that the internal complex circuitry of the ADXL278 might have taken a toll due the presence of high moisture content in the neighborhood specially keeping in mind that these packages are not fully hermetically sealed in reality.

COMPUTATION OF MAHALANOBIS DISTNANCE

For the computation of Mahalanobis Distance(s), the output of ADXL278 accelerometer, acceleration vs the time traces, were converted to frequency domain by performing a Fast Fourier analysis. Basic Fast Fourier Transform having a complexity of NlogN was conducted on the MEMS output data. This resulted in amplitude vs frequency plots for each sample from each pre-condition. Figure **168**, Figure **169** and Figure **170** show some sample FFT results of a Pristine ADXL278 accelerometer. Figure **171** and Figure **172** show sample FFT plots of thermal cycled ADXL278 accelerometer from -40°C to 85°C and -55°c to 125°C respectively. Similar FFT plots, for each sample from each pre-condition having undergone drops till failure, were generated. As mentioned before in this study the drift in the accelerometer response has been quantified by gaging the Mahalanobis Distance. A matlab routine was written to calculate the Mahalanobis Distance which compared the pristine assemblies, serving as baseline, with the other pre-conditions. The Fast Fourier results were used as inputs. As the full scale range output of ADXL278 is 70g, test condition, therefore only the test condition drops were compared i.e. every 10th drop from initial till failure.
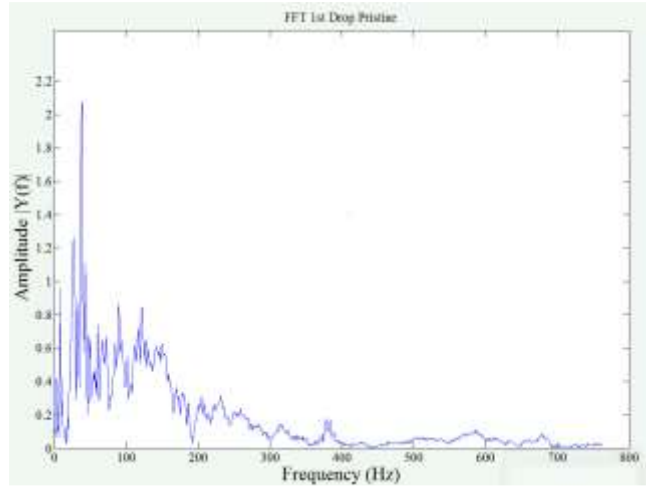
Figure 168:- Amplitude vs Frequency trace of a pristine sample after 1st drop
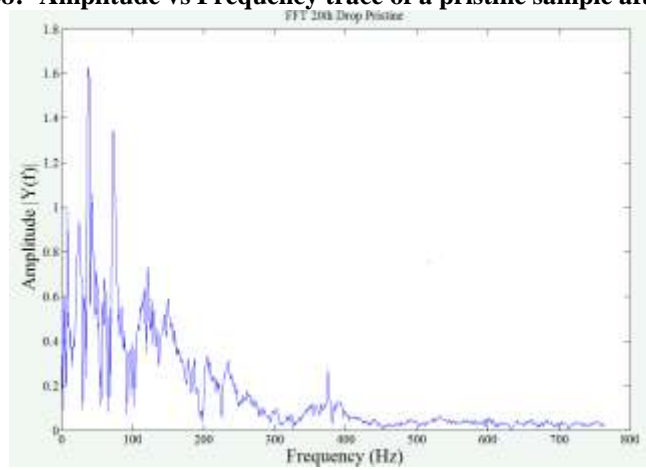
Figure 169:- Amplitude vs Frequency trace of a pristine sample after 20th drop
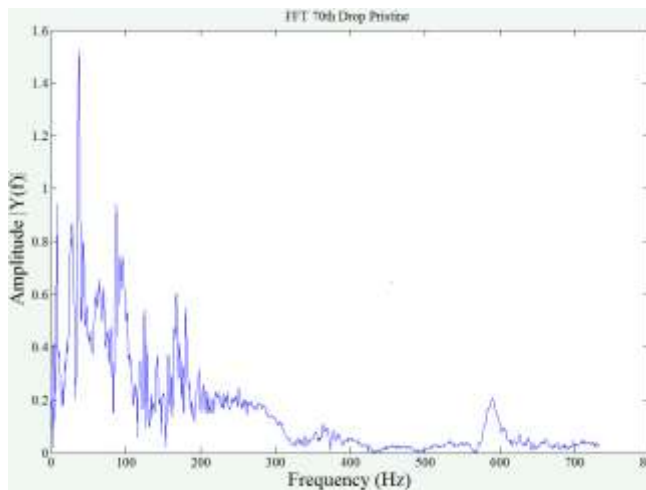
Figure 170:- Amplitude vs Frequency trace of a pristine sample after 70th drop

181
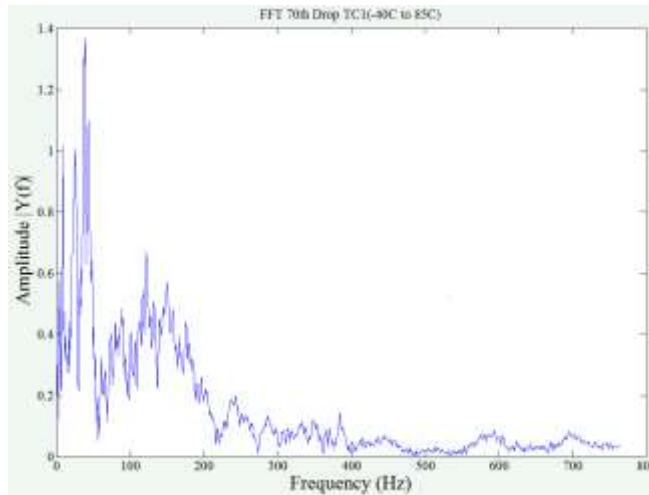
Figure 171:- Amplitude vs Frequency trace of a TC1, (-40ºC to 85ºC, 100 cycles) sample after 70th drop
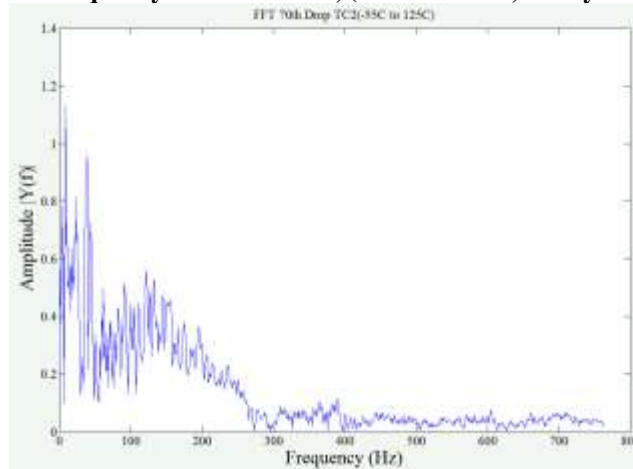
Figure 172:- Amplitude vs Frequency trace of a TC2, (-55ºC to 125ºC, 100 cycles) sample after 70th drop
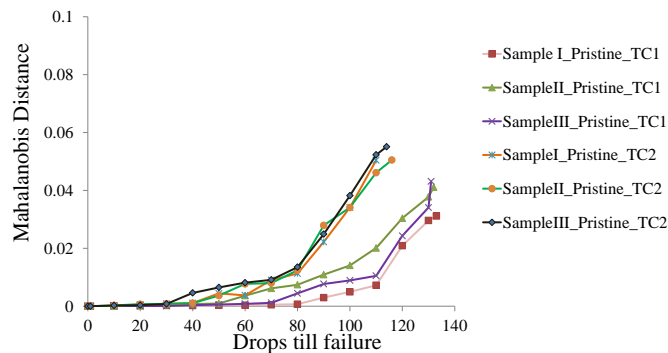
Figure 173:- Mahalanobis Distance trend vs the total number of drops to failure

The Mahalanobis Distances were calculated after the board assemblies completed the pre-condition and test-condition sets. In the plot, Figure **173**, it can be seen that the Mahalanobis Distances increase as the number of drops increase for each pre-condition. The TC2 (-55ºC to

125ºC, 100 cycles) samples have a bigger drift in the output as the TC1 (-45ºC to 85ºC, 100 cycles) samples. An increasing trend can be clearly observed in the Mahalanobis Distance vs the drops to failure curves, this depicts that the difference between the means for the damaged signal(s) and the pristine signal(s) increases with the number of drops. The increase in the Mahalanobis Distance indicates a drift of the ADXL278 response versus the number of shock events. All three TC2 and TC1 samples have been compared to the pristine assemblies. In the above plot the top three curves represent the drift in the TC2 samples and bottom three curves depict the drift in TC1 samples.

FAILURE ANALYSIS

The ADXL278 accelerometer consists of differential elements which are composed of anchors, folded spring and fixed capacitive plates. The folded spring and capacitive plates form an interdigitated structure, where the extended spring fingers are allowed to move between two capacitive plates. These capacitive plates are attached to the substrate while the movable fingers are attached to the frame. The frame in this case is movable and acts as the proof mass. After the subjection of MEMS test board assemblies to shock till failure, the MEMS device was separated from the PCB and potted using epoxy resin and hardener. The potted ADXL278 was then polished using a 240 grit size polishing paper. Figure **174** shows the potted and polished samples respectively. All this was performed to de-cap the accelerometer and see the internal failure sites and modes. Scanning Electron Microscopy (SEM) has been used to identify the failure sites.
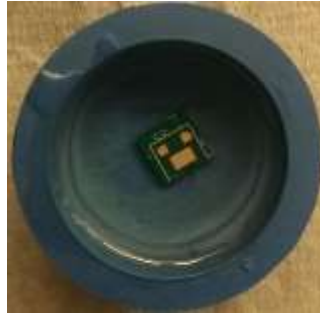
Figure 174: The above figure shows potted (above) and polished (below) ADXL278 samples

Over the years it has been found out that shock impact induced failure modes in conventional MEMS devices include fracture caused by stress exceeding the yield strength, Stiction of parts(permanent contact), micron size particles short circuiting a comb drive and packaging failures. Table 4 showcases the failure modes observed for ADXL278 by different test conditions.

Table 25:- Failure Mode by Pre-Conditions and Stress Condition

Pre-Conditioning	Failure Modes	Test Condition
Pristine	Stiction, capacitive plates in contact	MIL-STD-883H test. Shock pulse amplitudes have been ramped from 500 to 30,000g with pulse duration between 0.1 to 1 millisecond
-40°C to 85°C with a 10 min dwell, 10 min ramp for 100 cycles	Stiction, capacitive plates in contact	
-55°C to 125°C with a 10 min dwell, 10 min ramp for 100 cycles	Stiction, capacitive plates in contact	
85°C/85RH for 500hrs	Unknown	

Analysis of deterioration of MEMS accelerometer was further anatomized by the usage of Scanning Electron Microscopy. SEM images taken for ADXL278 show the most common failure mode, stiction, observed in almost all the pre-conditions. Figure 175 demonstrates the

failure sites in the ADXL278 accelerometer for a failed pristine pre-conditioned test board assembly which has undergone 155 drops. In Figure 176, it can be clearly seen that, a capacitive plate is missing from the differential cell element and there is a permanent contact between fingers of the movable beam and the fixed plate. In Figure 177 SEM image for accelerometer having undergone -55ºC to 125ºC (TC2) thermal cycling environment and then subjected to 116 drops (till failure) is presented. A permanent contact between two capacitive plates and also contact formation between the fingers of movable beam and fixed plates can clearly be seen.
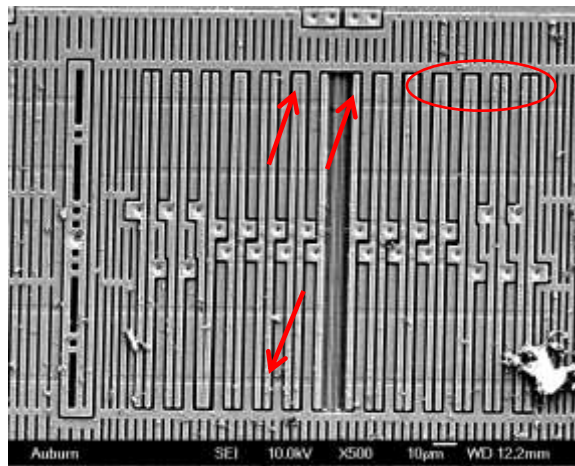
Figure 175: SEM image for a Pristine pre-conditioned ADXL278 after 155 drops
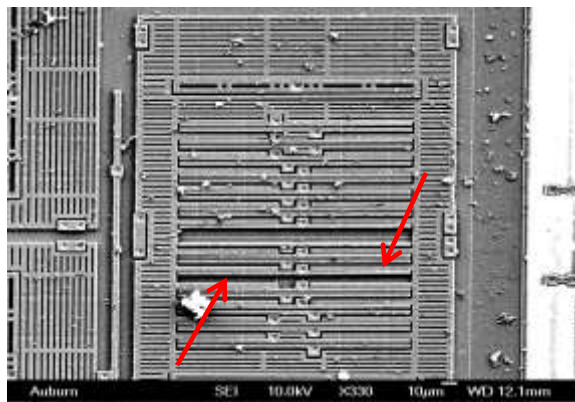
Figure 176: SEM image for a pristine pre-conditioned ADXL278 after 155 drops
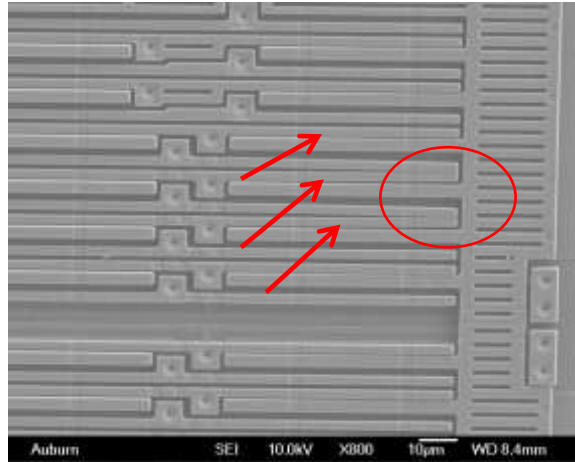
Figure 177: SEM image for thermal cycling,-55ºC to 125ºC for 100 cycles, pre-conditioned ADXL278 after 116 drops
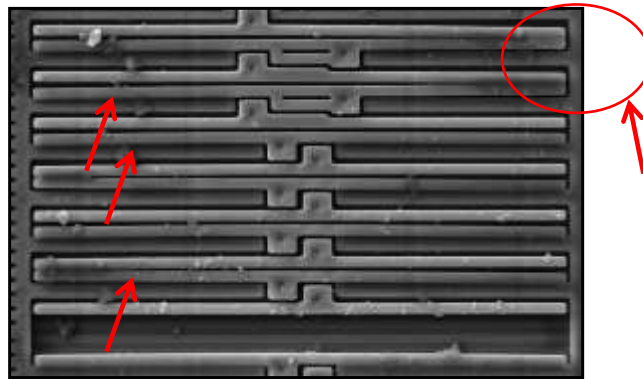
Figure 178: SEM image for thermal cyclingd,-40ºC to 85ºC for 100 cycles, pre-conditioned ADXL278 after 133 drops
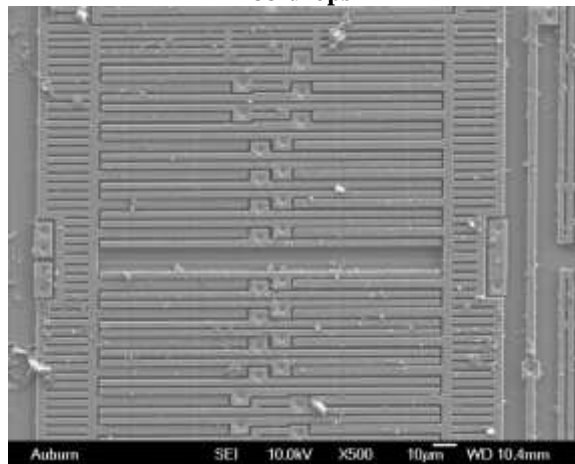
Figure 179: SEM image for an 85oC/85%RH pre-conditioned ADXL278

6.5 SUMMARY AND CONCLUSIONS

A methodology has been presented to study the drift in the output response of a MEMS accelerometer, ADXL278. This high-g dual-axis capacitive accelerometer has been tested under high/low temperature and high humidity exposure followed by subjection to high-g and low-g shock loading environments. The deterioration of the accelerometer output has been characterized using the techniques of Mahalanobis distance in conjunction with t-statistics for defect detection and estimation of confidence intervals. Later Scanning Electron Microscopy has been used to identify the dominant failure modes. The feasibility of the approach has been demonstrated for pristine test assemblies and the ones withdrawn from Thermal Cycling (TC1 and TC2), Temperature-Humidity followed by exposure to mechanical shock.

Chapter 7

Effect of Shallow Cycling on Flexible Power-Source Survivability under Bending Loads and Operating Temperatures Representative of Stresses of Daily Motion

Flexible electronic systems require the power system to be thin, robust and be able to handle the dynamic bending stress from the body. These applications indicate that the future flexible battery will be exposed to the direct mechanical and environmental stress. Electronics in portable products may be often not charged to full capacity and may not be discharged completely prior to re-charge cycle. Further, the shallow charge cycles may outnumber the deep-charge cycles in operation of the portable product. In this research study, the simultaneous effects of shallow cycling combined with and without bending loads along with different operating temperatures have been characterized for Li-Ion batteries. The charge and discharge rate was varied between 0.5C to 1C and the battery was charged to 75-percent capacity prior to discharge and re-charge cycle to evaluate the effect of shallow cycles. It was found that repeated shallow cycles resulted in no memory effect where the Li-Ion battery test samples did not develop "new-capacity". State-of-the-art Li-Ion batteries have been tested under multiple operating temperatures of 50°C and 25°C combined with distinct bending load of 15° which is imposed only during the discharge cycles in order to replicate real world applications. Efficiency, power, capacity and charge-discharge time have been analyzed for battery state assessment and survivability of Li-Ion batteries has been documented. Li-Ion batteries use a positive electrode cathode, a negative electrode anode and an electrolyte as a conductor. The cathode is generally comprised of a metal oxide and the anode is made of a carbon based material mostly graphite. When discharging the Lithium ion based power source the ions flow from anode to cathode while travelling through the electrolyte and separator interfaces, this direction is reversed when the battery is the charging

mode. Manufactures have tried introducing additives in order to achieve high energy and low cost but it has a trade off with the stability of the battery cells Survivability of thinner power sources such as flexible Li-Ion batteries when exposed to repeated shallow cycles at different operating temperatures along with mechanical bending load is relatively unknown. Operation in harsh environmental conditions can drastically affect the Li-Ion battery parameters such as capacity, efficiency, charge-discharge time and power. These parameters have been analyzed for battery state assessment and the observed damage progression has been reported. Li-Ion power sources have been the benchmark for portable electronics for some time now because of their high energy density and power density [6,18]. [10] Sasaki has showcased the presence of memory effect, more prevalent in Nickel-Metal Hydride batteries, in $LiFePO_4$ based Li-Ion batteries when exposed to partial charge-discharge and how it affects the state of charge. The storage capacity of Li-Ion batteries is also affected by memory affect. Operating temperature of Li-Ion batteries is also a concern as it can change the performance of the power source and thermal runaway reaction can easily cause the battery to explode, resulting in catastrophic failure when operating at high temperatures [14,16]. Techniques such as XRD and SEM have also been used before to study the effect of aging process of electrode's binder and electrolyte interface [15]. The authors observed formation of a binder layer at the surface of positive electrode. [19] Jin presented a protocol which reduces electrolyte interface resistances and also shows an improvement in capacity retention. Studies conducted previously as in [9] have demonstrated the effect of thermal stresses on Li-Ion battery electrodes and electrolyte. Present day portable technologies, demand for thinner flexible power sources and capability to tackle the stresses of daily motion. This requires thinner form flexible sources such as Li-Ion batteries to have stable characteristics which are not greatly affected by harsh environmental operating conditions such

as bending loads, shallow charge-discharge cycles and operating temperatures. Recently [1,2] investigated the effect of large bending loads of up to 150° on Li-Ion power sources and found that excessive bending loads can drastically affect the energy storage parameters such as capacity and efficiency of the power source. Modern day flexible electronic systems require the power system to be thin, robust and be able to handle the dynamic bending stress from the body. Current applications indicate that the future flexible battery will be exposed to the direct mechanical and environmental stress. Present and past studies have not yet fully accomplished how shallow cycling affects the performance of flexible Li-Ion based power sources since most of them are/were focused on improving capacity retention techniques by altering electrolyte salts or developing different material based cathode/anode. Deep cycling causes a lot of strain on the battery therefore it is important to investigate the after effects of shallow cycling and whether or not it is the go-to method for flexible Li-Ion power sources. Nowadays portable technology applications experience shallow charge-discharge cycles which may outnumber the deep-charge cycles in operation of the portable product and such devices are also subjected to daily stresses of motion, thus the importance of investigating simultaneous effects of shallow cycling combined with and without bending loads along with different ambient temperatures. This work is primarily focused on providing harsh environmental reliability data and survivability of Li-Ion batteries which the previous studies don't look into. In this study, a test methodology has been developed for thin form flexible Lithium-ion power sources subjected to repeated shallow cycles at different C rates namely 0.5C and 1C. The effects of bending load and ambient temperature have also been demonstrated. This test methodology makes use of a hardware-testbed [1,2] which is essentially a battery state assessment analyzer developed at CAVE3 electronics research center, Auburn University. The testbed comprises of programmable source meter and electronic

190

load, a multi-channel data acquisition system, LabVIEW user interface and a mechanical

bending actuator controlled via microcontroller. Li-Ion batteries have been tested at 1C and 0.5C

rates to charge and discharge during the lifecycle tests. In order to replicate real-world shallow

cycling different cut off voltages have been introduced into the test matrix. The life cycle tests

run continuously for 180 cycles which provides significant data points about parameters such as

capacity, efficiency and charge-discharge time and further to be able to predict time to failure.

The effects of shallow cycling at different C rates, different operating temperatures and

with/without bending have been characterized. A total of 8 flexible Li-Ion battery samples have

been tested at different test conditions which are mentioned and explained later in the study.

7.1 TEST VEHICLE

State-Of-The-Art Li-Ion batteries in pouch form have been used as flexible sources for this

investigation. The nominal rated capacity of these sources is 45mA-h. The dimensions of the Li-

Ion test samples are 43mm x 38mm x 0.5mm. The test vehicle can cater to the daily stresses of

motion such as bending and flexing. The anode of the test vehicle is comprised of graphite; the

cathode is made of $LiCoO_2$ while the electrolyte is a combination of Li based salts in an organic

solvent, Ether. Upon completion of the external circuitry the negative electrode (anode)

undergoes oxidation i.e. loses electrons and creates positive ions, similarly there is a reduction

reaction at the positive electrode (cathode). **Figure 180** demonstrates the ion flow in Li-Ion

batteries. Li-Ion samples used in this investigation consist of only one microcell. Each microcell

is further comprised of two one-sided anodes (graphite) and one two-sided cathode ($LiCoO_2$).

The nominal rated capacity of the test samples is 45mAh; **Figure 181** represents the Li-Ion test

sample used for this investigation. As per the battery manufacturer's specification sheet the ideal

temperature range(s) during the charging process is 0°C to 45°C and -20°C to 60°C during the discharging period. In Lithium-Ion batteries both the electrodes have the capability to intercalate (absorb) Li^+ ions. During the charging phase of flexible power source $LiCoO_2$ oxidizes i.e. loses electrons and in order to maintain the charge balance same number of Li^+ ions are released into the electrolyte. The electrolyte solution which is a mixture of solvents and Lithium salts is already rich in Li^+ ions; therefore the arriving Li^+ ions from the cathode replace the existing Li^+ ions which travel to the anode. The graphite based anode of the flexible power source intercalates the incoming Li^+ ions where are they are attached to the electrons lost by the cathode. This electrochemical reaction is reversible and the direction of Li^+ ions and electrons reverses during the discharging phase.

Figure 180:- Working of illustration Li-Ion Battery during charging and discharging processes

Figure 181:- Li-Ion test sample

7.2 EXPERIMENTAL TEST SETUP AND RELIABILTIY TEST MATRIX

The shallow charging/discharging investigation was conducted using a hardware-testbed which is essentially a battery state assessment analyzer developed at CAVE3 electronics research center, Auburn University. The battery state assessment analyzer is comprised of a programmable source meter and DC electronic load, a multi-channel data acquisition system, LabVIEW user interface and a mechanical bending actuator controlled via microcontroller. A National Instruments LabVIEW module was developed which essentially controls the number of cycles, cut off voltages, end of charge current and end of charge voltage. The user can also control the presence/absence of bending load during discharging via the module. **Figure 4** shows the schematic of test setup used for shallow cycling. The NI module is responsible for sending both the charging and discharging profile to the source meter and the DC load respectively.
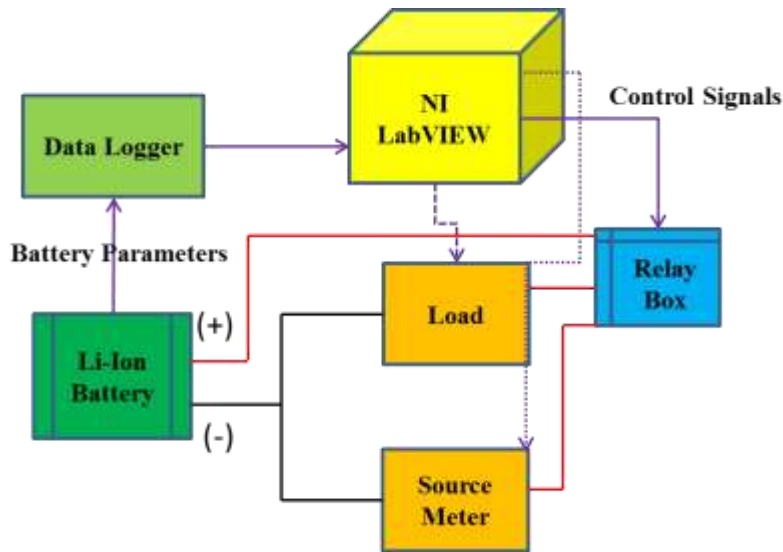
Figure 182:- Schematic of hardware-testbed

Further, the source meter and the load are connected to the battery via a relay box which switches between the two profiles. The LabVIEW test environment is makes use of GPIB interface to connect to the source meter, load and the multi-channel data logger. When monitoring the battery health at temperatures higher than room temperature a DELTA Design 5900 environmental chamber was used in addition to the above mentioned external devices. **Figure 183** represents the experimental test setup used for this study.

Figure 183:- Source meter, Electronic load, relay box and multichannel data acquisition system

Table 26 provides detail about the battery control parameters during the charging and discharging processes. In order to better understand the effects of shallow cycling it is divided in two groups namely Shallow-A and Shallow-B, with the only difference being the discharging cutoff voltages. Shallow-B is a much narrower cycle with discharge cutoff voltage at 3.75V whereas in Shallow-A the discharge cutoff was at 3.5V. For both Shallow-A and Shallow-B the charging cutoff voltage was kept same at 4.2V. The full depth cycle represents discharging the full specified voltage of 2.75V and then charging it to 4.2V. **Table 27** showcases the test matrix used for this investigation.

Table 26:- CONTROL PARAMTERS

Control Parameter	Value
Charging Cutoff Voltage	4.2V
Charging Cutoff Current	4mA
DischargingCutoff Voltage	3.5V, 3.75V
Charging Current Rate	1C,0.5C
Discharging Current rate	1C,0.5C
Charging Current	45mA,25mA
Discharging Current	45mA,25mA

The Li-Ion test samples were tested for cases with and without the stresses seen during daily motion at two different temperatures of 25°C and 50°C. A total of 8 flexible Li-Ion battery samples have been tested at different test conditions to simulate the stresses of daily motion.

Table 27:- RELIABILITY TEST MATRIX

Test Temp.	Bending(15°)	Rate	Cycle Type
25°C	NA	1C	Full
25°C	Applied	1C	Full
25°C	NA	0.5C	Shallow-A
25°C	NA	0.5C	Shallow-B
25°C	Applied	0.5C	Full
25°C	Applied	0.5C	Shallow-A
25°C	Applied	0.5C	Shallow-B
25°C	Applied	1C	Full
50°C	NA	1C	Full
50°C	Applied	1C	Full
50°C	NA	0.5C	Shallow-B
50°C	Applied	0.5C	Shallow-B

The effect of different C rates for repeated shallow cycles has been investigated which the previous and current studies have not examined. During the life-cycle tests battery output parameters such as capacity, efficiency and charge-discharge time have been analyzed and documented. Battery voltage and battery current have also been recorded using the multi-channel data logger. As mentioned in **Table 26** and **Table 27** two different charging/discharging rates have been used 1C and 0.5C. The repeated cyclic test has three steps where first one is constant current discharging at 1C/0.5C until the voltage dropped to 2.75V/3.75V/3.5V followed by a constant current 1C/0.5C charging profile until the voltage reaches 4.2V. Finally, constant

voltage charging at 4.2V is performed until the current narrows down to 4mA. **Figure 6** represents the charging/discharging voltages during one single cycle for Shallow-A, Shallow-B and Full-depth cases. The programmable mechanical actuator which is used for mimicking the daily stresses of motion is controlled via a commercial off the shelf microcontroller. The actuator is capable of providing bending loads from 15° to 180°. The microcontroller is programmed using ARM KEIL software where the bending frequency and bending angles can be pre-defined by the user. The bending loads are only subjected on the Li-Ion battery test samples during the discharge cycle and each discharge cycle accommodates for 10 bending cycles. Since wearable flexible electronics are repeatedly subjected to bending and flexing on a daily basis therefore it is the need of the hour to include it in our reliability test matrix. It has been previously established [1,2] that large bending loads of up to 150° can cause a permanent shift in the electric characteristic curves of the battery and also affect the battery output parameters. Effect of small bend angles of up to 15°, which is much more close to a real world application, is yet to be established especially when combined with repeated shallow cycles. **Figure 7** illustrates the mechanical actuator used in this investigation. Battery output parameters such capacity, efficiency, charge-discharge time and state-of-charge were evaluated by recording the in-situ electric characteristic curves for voltage and current.

197
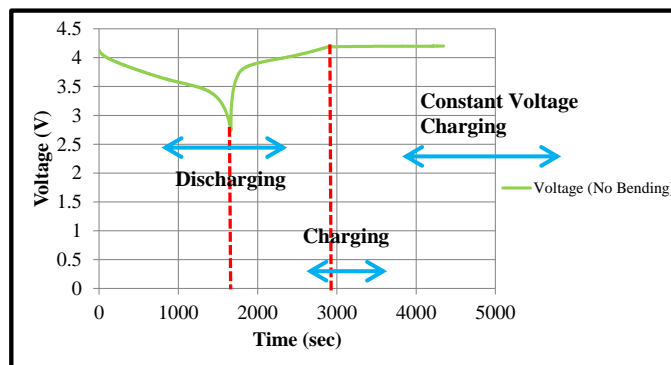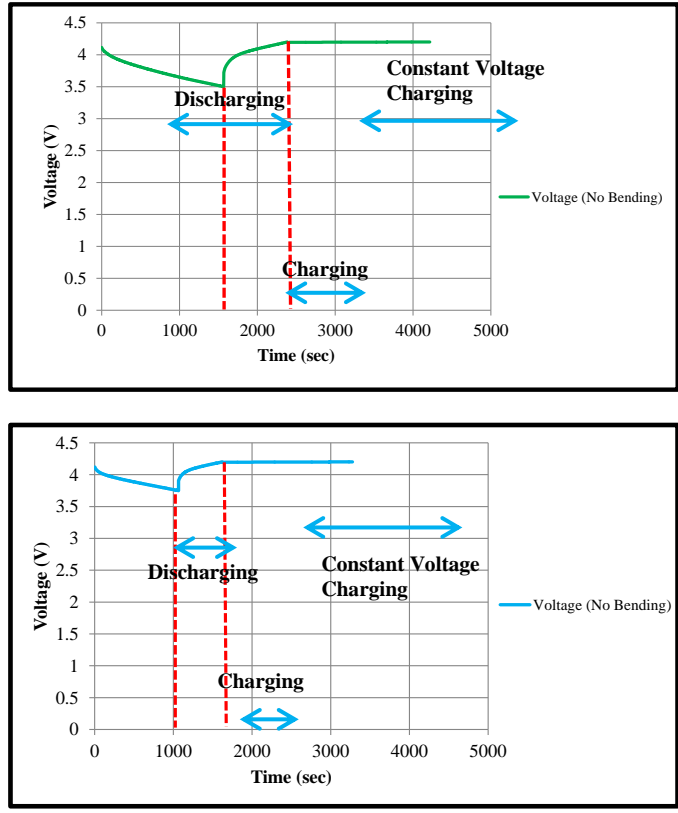
Figure 184:- Charging/discharging voltages for Full, Shallow-A and Shallow-B cases respectively
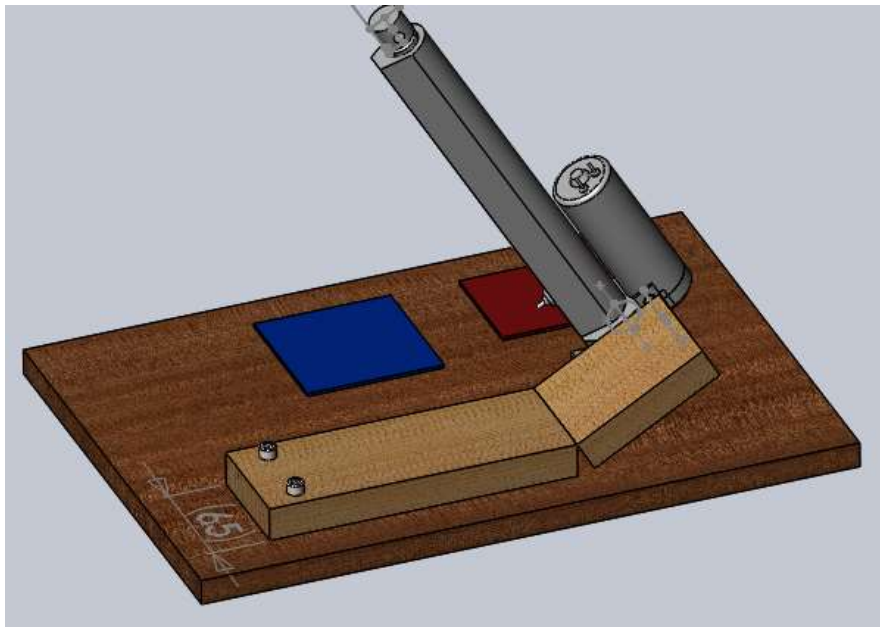
Figure 185:- Mechanical Bending Actuator controlled via MCU

7.3 Experimental Results

Effect of Shallow Cycling and Bending loads at 25°C

Shallow charging/discharging occurs when the state of a power source changes abruptly. This study focusses on how repeated shallow cycles especially during the discharge phase can affect the battery parameters. Nickel-based batteries have shown a significant amount of memory effect when exposed to shallow cycles. There is no reliability data available for Li-Ion based flexible batteries under shallow cycles; through this study we present reliability data which can be beneficial to battery designers and manufacturers. **Figure 186** and **Figure 187** show the charging-discharging current and voltage curves for a Li-Ion test sample at 25°C without bending at a C rate of 0.5 and Shallow-B case.
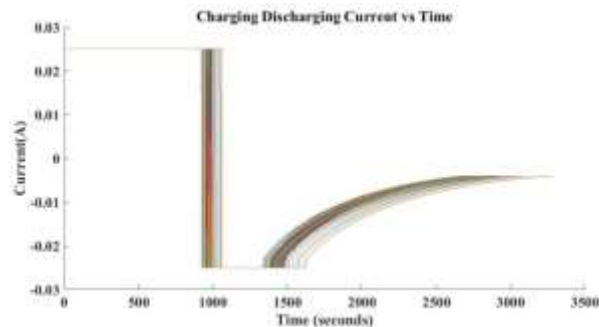
Figure 186:- Discharging-Charging Current
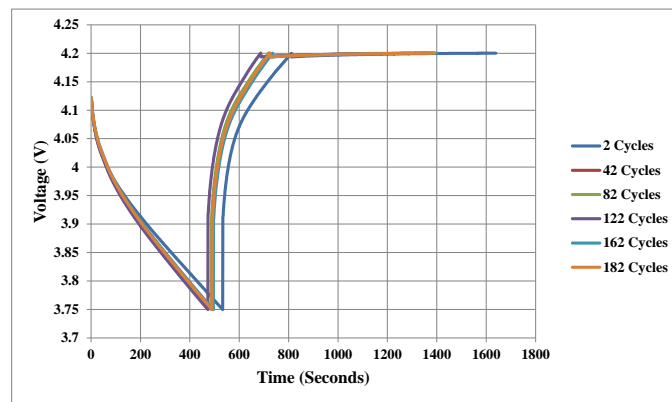
Figure 187:- Discharging-Charging Voltage

State of Charge (SOC) and Battery Capacity

Ratio of useable charge to the maximum charge of the battery is defined as SOC. As mentioned before Li-Ion transport results in charging and discharging of the power source, therefore when the SOC is at the highest possible level the anode has maximum concentration of Li-Ions and cathode has the minimum concentration. Similarly the SOC is lowest when the reverse happens. Before the start of each of the 182 cycles, state of charge for the cell should ideally be maximum and minimum at the end of discharge and then maximum at the end of cycle. This parameter is used to estimate the state of the battery after each cycle, and has been used to calculate the capacity of the flexible power sources. Battery capacity has been evaluated during Li-Ion transport from anode to cathode or when the discharge phase was in progress. Capacity is generally described in mAh and equals the multiple of discharge current, measurement interval and SOC. Discharge current was 0.025A for 0.5C and 0.05A for 1C test conditions. Data was recorded every 2 seconds. **Figure 188** and **Figure 189** demonstrate the battery capacities and SOC respectively at different test conditions.
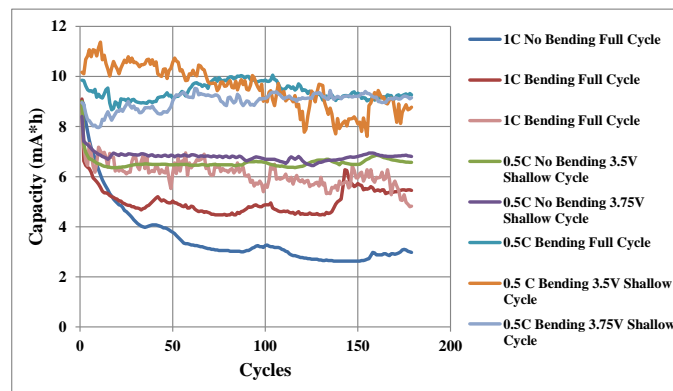
Figure 188:- Battery Capacities at different test conditions

It can be clearly seen that a low charge-discharge rate combined with shallow cycles result in higher capacity retention till the end of life cycle test. Ideally the SOC for flexible Li-Ion battery

should be 100-0-100 (%) after each cycle but this does not happen in real world applications. As seen from **Figure 189** the two test conditions which are the most close to the ideal pattern of 100-0-100 (%) for SOC, belong to the shallow life cycle tests. Performing shallow cycle's helps in better retention of battery capacity and the SOC remains as close to the ideal case as possible. Also, shallower the cycle the better the battery life and less prolonged effects of harsh environmental conditions on flexible Li-Ion power sources. **Figure 190** explains the battery capacity degradation (%) for different test conditions. High discharge rate of up to 1C without bending will cause the battery to degrade very fast and is the worst performing test conditions of all.
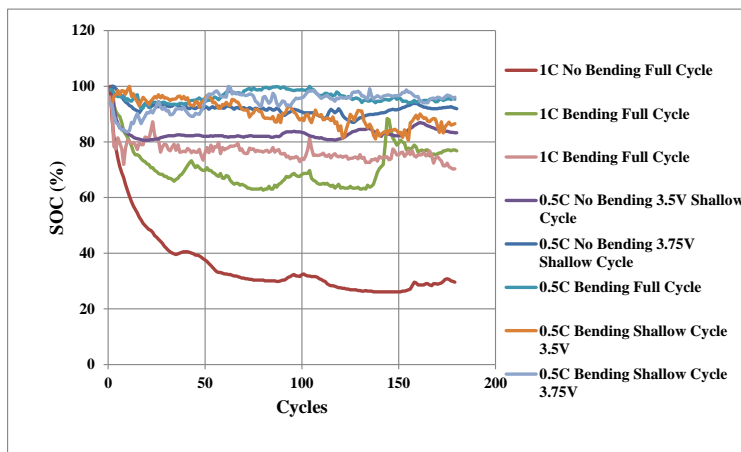
Figure 189:- SOC of the Battery at different test conditions

In previous study [1,2] it was demonstrated that bending loads of 150° with charge-discharge rate of 1C at 25°C can severely damage the battery and has a drastic impact on the capacity and efficiency.
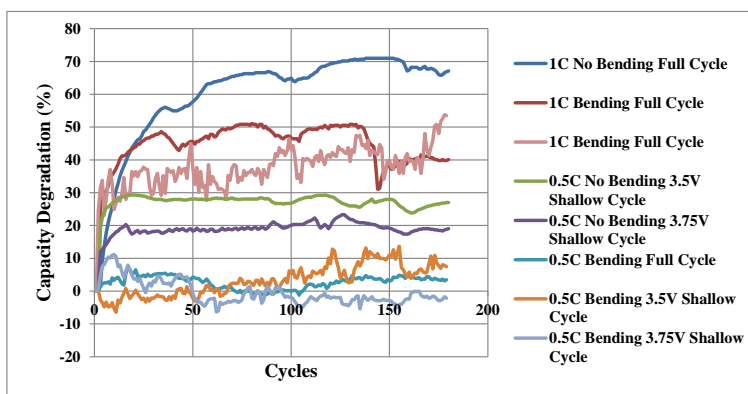
Figure 190:- Capacity degradation for various test conditions

Smaller bending loads of up to 15° on the flexible power sources seem to make the battery perform better as compared to no bending at all as seen in **Figure 188**. This result is prevalent irrespective of the ambient temperature since it can be later seen in 50°C test results too. Capacity degradation is change in the battery capacity from the first cycle to the end of life cycle test when exposed to repeated shallow/full charging-discharging profiles at various test conditions. The battery capacity is a function of the state-of-charge (SOC), measurement interval and the discharge current where time interval and discharge current are constants for each specific test condition. The state-of-charge, which is defined as the ratio of usable charge to the maximum charge produced by the battery, can adversely affect the resulting capacity of the power source. Increase/stability in the state-of-charge due to the presence of bending loads can be correlated to the fact that more/stable number of Li^+ ions are able to move through the electrolyte during the charging and discharging phases. Higher SOC combined with small bending loads of 15° and a lower discharge rate leads to better contact/interaction of the electrolyte and electrode interface, enhanced reaction kinetics and smaller electron/ion transport resistances.

It can be concluded from **Figure 188**, **Figure 189** and **Figure 190** that the decay rate of 1C test conditions at full-depth cycling is much higher than 0.5C at shallow cycling. Observing the

shallow cycling results in **Figure 190** the battery capacity degrades up until the first 10 cycles but then remains almost stable with capacity degradation around 40-percent; effect is present during partially discharge and then recharge at 25°C. As indicated in the results significant amount of capacity degradation, more than 200 percent, takes place at 1C with full-depth cycling. Monitoring the test parameters at low charge-discharge rate and shallow cycles can help improve the life of the flexible Li-Ion power sources used for life tests in this study.

Shallow Cycling effects on Battery efficiency

Efficiency of the battery is largely defined as the ratio of the power which is being discharged to the input power to the battery. For evaluating the power which is being discharged, at each recorded interval, voltage and current are multiplied and then integrated for each specific cycle.
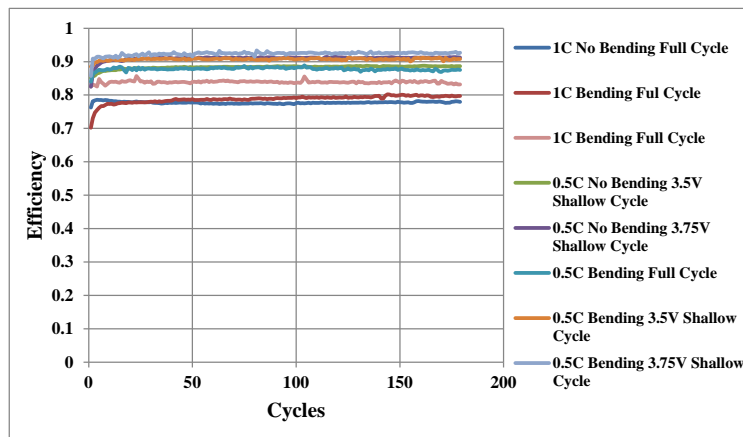
Figure 191:- Battery efficiency at different test conditions

This is done for all cycles till the end of the life cycle test. Battery efficiency results plotted in **Figure 191** demonstrate the effect of different test conditions. Shallow cycling at low charge-discharge rate result in significantly higher battery efficiencies with Shallow-B at 0.5C being the most productive condition of all 25°C test results. Bent state induced wrinkles and contours on the electrode surfaces can generate more active sites for acceptance of Li^+ ions [3] resulting in

lower capacity degradations, higher battery efficiencies (as shown in this study) and if combined with shallow cycling the results prove out to be much better.

Effect of Shallow Cycling and Bending loads at 50°C

Shallow charging/discharging occurs when the state of a power source changes abruptly. This study focusses on how repeated shallow cycles especially during the discharge phase can affect the battery parameters. **Figure 192** and **Figure 193** show the charging-discharging current and voltage curves for a Li-Ion test sample at 50°C without bending at a C rate of 0.5 and Shallow-B case.
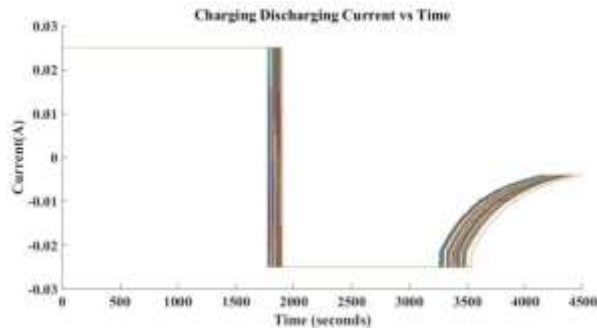
Figure 192:- Discharging-Charging Current

On comparing the voltage-current characteristic curves from the test conditions at 25°C and 50°C shown in **Figure 186, Figure 187, Figure 193** and **Figure 192** it can be clearly observed that higher ambient temperature will result in the shift of V-I curves even if the other test parameters such as discharge-charge rate, full-depth/shallow cycle and mechanical bending load(s) are all kept consistent.
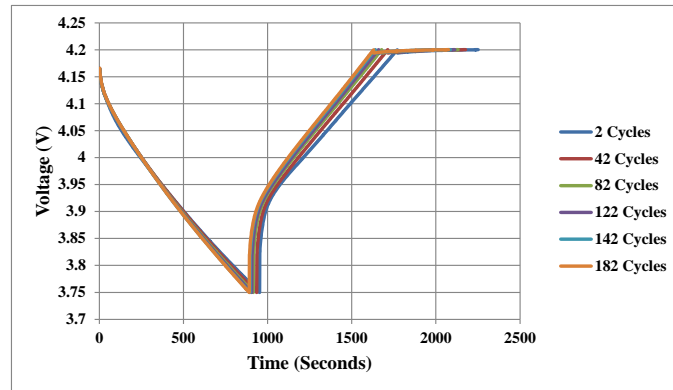
Figure 193:- Discharging-Charging Voltage

State of Charge (SOC) and Battery Capacity

Ratio of useable charge to the maximum charge of the battery is defined as SOC. This parameter is used to estimate the state of the battery after each cycle, and has been used to calculate the capacity of the flexible power sources. Battery capacity has been evaluated during Li-Ion transport from anode to cathode or when the discharge phase was in progress. Capacity is generally described in mAh and equals the multiple of discharge current, measurement interval and SOC. Discharge current was 0.025A for 0.5C and 0.05A for 1C test conditions. Data was recorded every 2 seconds. As explained before High SOC and bending loads enhance/maintain the battery life in terms of capacity, the following test results indicate that high operating temperature can also help the battery to maintain its capacity over the length of repeated cycling test . The operating temperature should not be extreme, 20°C-25°C more than the room temperature, since that results in the unlocking of oxygen atoms from the cathode. The presence of oxygen atoms at a high temperature in a flammable electrolyte can cause severe damage to the battery.
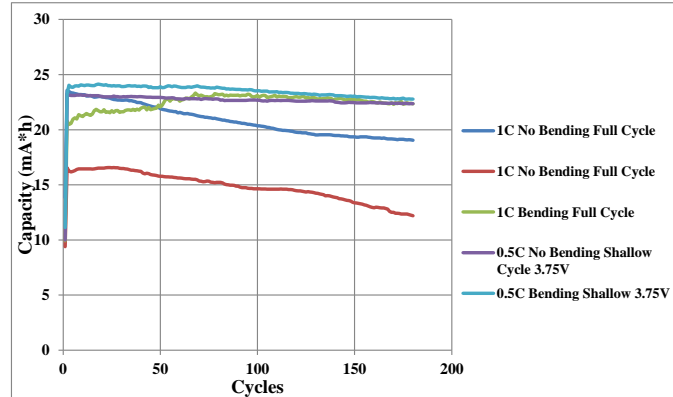
Figure 194:- Battery Capacity at different test conditions
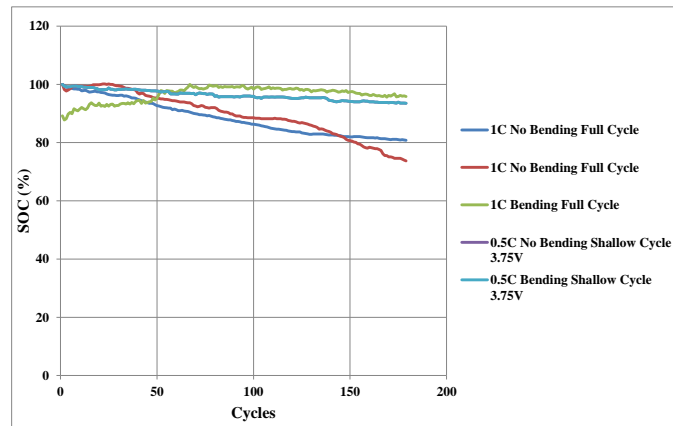
Figure 195:- SOC of the battery at different test conditions

Similar to the 25°C test results, the shallow cycle test condition at 0.5C operating at 50°C has the least decay rate when compared to full-depth cycle at the same temperature without any bending loads. It can be clearly seen from **Figure 194** that a low charge-discharge rate combined with shallow cycles result in higher capacity retention till the end of life cycle test. As mentioned before smaller bending loads of up to 15° on the flexible power sources seem to make the battery perform better as compared to no bending at all as seen in **Figure 188** , **Figure 194** and **Figure 195**.

206
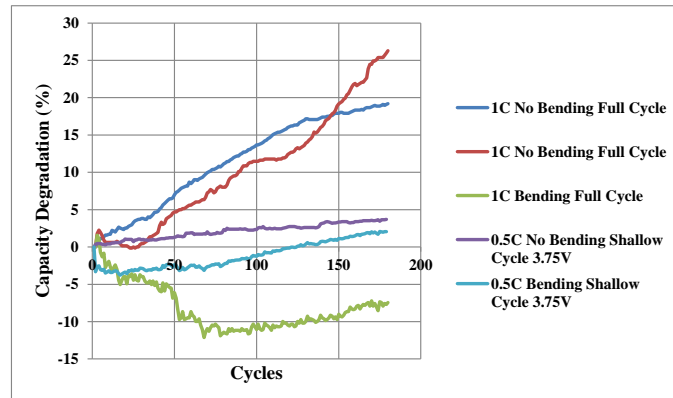
Figure 196:- Capacity degradation of Li-Ion flexible battery

It can be concluded from **Figure 194** and **Figure 195** that the decay rate of 1C test conditions at full-depth cycling is much higher than 0.5C at shallow cycling. As indicated in the results significant amount of capacity degradation, more than 30 percent, takes place at 1C with full-depth cycling. Capacity degradation is much less; compare **Figure 190** and **Figure 196**, at higher ambient temperature even when high charge-discharge rate, full-depth cycling and bending loads are present. For shallow cycling result at 50°C, the battery capacity increases after first two cycles due to high ambient temperature (this is common for both shallow and full cycling) but then remains almost stable with capacity degradation around 3-percent; effect is present during partially discharge and then recharge at 50°C.

Shallow Cycling effects on Battery efficiency

Efficiency of the battery is largely defined as the ratio of the power which is being discharged to the input power to the battery. For evaluating the power which is being discharged, at each recorded interval, voltage and current are multiplied and then integrated for each specific cycle. This is done for all cycles till the end of the life cycle test. Battery efficiency results plotted in **Figure 197** demonstrate the effect of different test conditions. Shallow cycling at low charge-

discharge rate result in significantly higher battery efficiencies with Shallow-B at 0.5C being the most productive condition of all, even better than the most efficient battery at 25°C.

Bent state induced wrinkles and contours on the electrode surfaces can generate more active sites for acceptance of Li^+ ions [3] resulting in lower capacity degradations, higher battery efficiencies (as shown in this study) and if combined with shallow cycling the results prove out to be much better. [1,2] showed one of the major failure modes caused by bending stress was the discharge voltage fluctuation due to the presence of large bending loads. **Figure 198** demonstrates the presence of voltage fluctuation even when a small bending load of 15° is used irrespective of the ambient temperature; however it does not yield a catastrophic failure but contrastingly seems to improve the battery capacity retention ability as shown in the above results. The crests in the voltage fluctuations represent the tension load and the troughs represent the compressive load during bending.
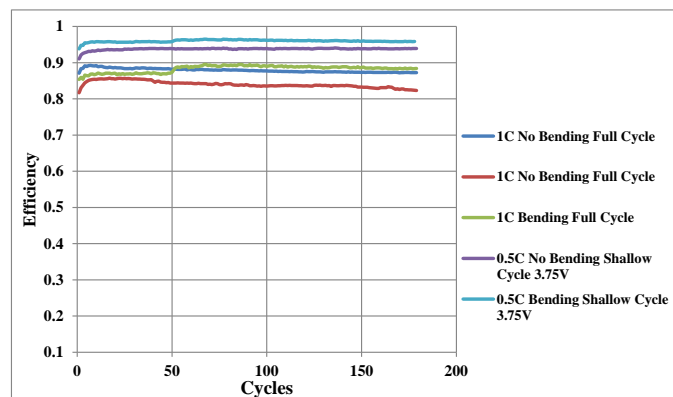
Figure 197:- Battery Efficiency at different test conditions

Voltage Fluctutations during discharging

Voltage fluctuations caused during the discharge phase while the bending load is active can be attributed to the fact that during bending the compression loads act as a catalyst for removal of more Li^+ ions and the tied electrons from the anode, therefore the trough in the voltage signal i.e.

208

the ionic mass removal rate is faster. While the tension loads during bending transfer back a few Li$^+$ ions from the electrolyte back to the anode, resulting in the crest in the voltage signal resulting in a faster ionic mass addition rate.
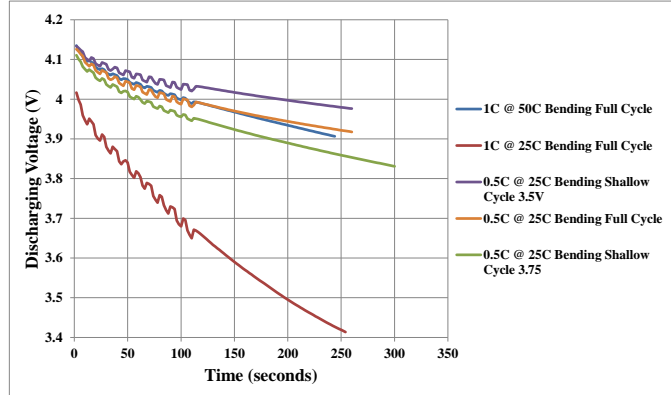
Figure 198:- Discharging voltage during small bending load of 15°

This back and forth process does not ideally cancel out each other and the effect of the bending loads is documented in this study when done over repeated cycles.

7.4 Regression Model

Present and previous studies concerning Li-Ion power sources are yet to establish a regression model for flexible Li-Ion power sources operating in harsh environmental conditions. A time-to-failure model has been established to start off with as shown in **Equation (1)** which is a generalized form of Arrhenius equation.

$$Cap.Deg\left(\%\right)=$$
$$\left(e^{\frac{A_1}{T}}\right).\left(rate^{A_2}\right).\left(bend^{A_3}\right).\left(cycletype^{A_4}\right).\left(Cycles^{A_5}\right) \quad (1)$$

The regression model is based on the following independent variables, operating temperature, charge/discharge rate, bending loads, full/shallow cycling, and number of cycles; and dependent

variable which is percent capacity degradation. **Equation (1)** can be simplified as a linear equation as shown in **Equation (2)**. For simplicity capacity degradation (%) has been termed as a variable y in **Equation (2)** and **Equation (3)**

$$Ln(y) =$$
$$\frac{A_1}{T} + A_2 Ln(rate) + A_3 Ln(bend) + A_4 Ln(cycletype) \qquad (2)$$
$$+ A_5 Ln(cycles)$$

For **Equation (3)** the natural log terms in **Equation (2)** have been named as x_1, x_2, x_3 and x_4 for simplicity.

$$Y = \frac{A_1}{T} + A_2 X_1 + A_3 X_2 + A_4 X_3 + A_5 X_4 \qquad (3)$$

The regression model has been captured in Error! Reference source not found.. The regression model has low VIF values for all the constants which reflect to the fact that there are no multicollinearity issues within the battery dataset.

Table 28:-REGRESSION MODEL VALUES

Term	Coef.	SE Coef.	P-Value	VIF
Constant	-16.69	2.37	0.000	1.00
A1	-0.0699	0.0083	0.000	1.41
A2	5.243	0.578	0.000	4.00
A3	-0.0899	0.0449	0.053	2.50
A4	0.248	0.578	0.002	4.16
A5	0.468	0.245	0.055	1.00

Table 29:-MODEL SUMMARY

S	R-square	R-square(adj.)	R-square(predicted)
0.33	94.79%	92.19%	84.37%

The ANOVA test results are shown in, where a zero P value from the test confirms the acceptability of the model.

Table 30:-ANOVA Test Results

Source	DF	SS	MS	F	P
Regression	5	21	4	36	0.000
Residual Error	10	1.15	0.11		
Total	15	22.16			

The resulting regression equation from the model has been shown in **Equation (4)**.

$$Cap.Deg(\%) = \left(e^{\frac{(-0.069)}{T}} \right).(rate^{(5.243)}).(bend^{(-0.089)})$$
$$.(cycletype^{(0.248)}).(cycles^{(0.468)})$$

(4)

7.5 SUMMARY AND CONCLUSIONS

In this study, a test methodology has been developed for thin form flexible Lithium-ion power sources subjected to repeated shallow cycles at different C rates namely 0.5C and 1C. The effects of bending load and ambient temperature have also been demonstrated. The life cycle tests have been analyzed for deterioration in battery parameters such as state of charge, capacity and efficiency. The effects of shallow cycling at different C rates, different operating temperatures and with/without bending have been characterized. Repeated cycling of the flexible power source result in a volumetric change of the electrode materials due to continuous ionic mass removal and deposition process; this also deteriorates the cathode/anode structures and the electrode-electrolyte interface. The after effects can be observed in the resulting battery capacities for the various test conditions. It can be concluded that the decay rate of 1C test conditions at full-depth cycling is much higher than 0.5C at shallow cycling. Observing the shallow cycling results, the battery capacity degrades up until the first 10 cycles but then remains almost stable with capacity

degradation around 40-percent; effect is present during partially discharge and then recharge at 25°C. Due to the repeated cycling tests a solid electrolyte interface (SEI) layer is formed over the anode and as the number of cycling increase the layer gets more and more thicker which results in formation of a barrier. As indicated in the results significant amount of capacity degradation, more than 200 percent, takes place at 1C with full-depth cycling. Monitoring the test parameters at low charge-discharge rate and shallow cycles can help improve the life of the flexible Li-Ion power sources used for life tests in this study. At 50°C as indicated in the results, significant amount of capacity degradation, more than 30 percent, takes place at 1C with full-depth cycling. Capacity degradation is much less at higher ambient temperature even when high charge-discharge rate, full-depth cycling and bending loads are present. Li batteries with solid state electrolyte's (SSE) need to have closer contact of Li-SSE interface which is usually applied as an external pressure during long-term cycling and better performance. This study shows that small bending loads applied to flexible Li power sources with ether based electrolytes perform better than those tested without the loads. For shallow cycling results at 50°C, the battery capacity increases after first two cycles due to high ambient temperature (this is common for both shallow and full cycling) but then remains almost stable with capacity degradation around 3-percent; effect is present during partially discharge and then recharge at 50°C. Bending results show the presence of voltage fluctuation even when a small bending load of 15° is used irrespective of the ambient temperature; however it does not yield a catastrophic failure but contrastingly seems to improve the battery capacity retention ability as shown in the results. Higher SOC combined with small bending loads of 15° and a lower discharge rate leads to better contact/interaction of the electrolyte and electrode interface, enhanced reaction kinetics and smaller electron/ion transport resistances.

Chapter 8

Flexible Li-Ion power sources operating at shallow discharge depths: Effect on Capacity and computation of regression based Capacity degradation model

Estimating the state of a system especially for lithium-ion battery has been an area of extensive research; where most of the remaining useful life (RUL) prediction techniques are highly dependent on usage of offline data. Development of a prognostics health management (PHM) framework for flexible electronics and flexible components is still in its nascent stages due to the novelty and understanding of the flexible regime. Little to no information exists on techniques which incorporate depth of discharge (DoD) and other varying test parameters such as varying load (across test conditions) and can then successfully evaluate the degradation in capacity and compute the remaining useful life for flexible lithium-ion power sources. Flexible electronic systems need to have a thin, robust power system that also has the capability to sustain dynamic stresses which are replicative of daily motions. Such applications can foresee the usage of flexible power sources in areas with both direct mechanical and environmental stresses. Current health monitoring techniques and test standards for rigid power sources which are used in portable electronics and electric vehicles (EVs) demonstrate robust and efficient RUL techniques with some of them considered as the benchmark in terms of model accuracy. With the current boom in internet of things (IoT), flexible power sources/flexible energy harvesting units will be the go to product of the industry for the next couple of decades. Therefore it is the need of the hour to develop PHM frameworks for such flexible lithium-ion based power sources. In this research study, 65mAh flexible lithium-ion batteries have been analyzed by cycling them through multiple full charge and shallow discharge cycles at distinct DoD operating conditions. Effects of simultaneous thermal stresses and repeated cyclic events have been studied on output

parameters such as efficiency, capacity and charge-discharge time. State-Of-the-art Li-Ion batteries have been tested under: multiple operating temperatures of 40°C and 25°C with different C-rates. In this study, capacity and "number of cycles" have been used as vectors to monitor the health of the power source and assess remaining useful life. Regression based modeling technique has been used to estimate the battery capacity deterioration in form of number of cycles to reach the end of life (EoL) which is about 80% of the original life.

Since the development of Li-ion chemistry, the regime of batteries has been highly governed by it due to its sheer potent combination of high energy density and high volumetric density. Almost all of the present day technologies such as EVs, portable electronics have this chemistry incorporated. Power sources based on Li-ion technology are also known to be highly efficient therefore allowing them to be used in energy harvesting applications, electric grid applications and can also be implemented in the Internet-of-things (IOT) network. This specific chemistry and its by-products are of great interest from both the academia and industry standpoint, in order to build an energy sustainable economy [Nitta 2015]. With the recent emergence of flexible Li-ion power sources the challenges associated with this chemistry have increased exponentially. Present and past studies have not yet fully accomplished how environmental stresses, both mechanical as well as electrical, can affect the performance of flexible Li-Ion based power sources. Majority of studies are/were focused on improving capacity retention techniques by altering electrolyte salts or developing different material based cathode/anode but mostly for the rigid batteries. Three major chemical processes which degrade Li-ion rigid batteries are: - electrolyte decomposition, transition metal dissolution and lithium plating. Not much attention has been paid towards the flexible side which can be the go-to product given how the industry is shifting towards flexible-hybrid electronics. Since the same chemistry is implemented in flexible

batteries it is yet to be fully established whether the above mentioned processes prevail within flexible batteries or is there introduction of new failure modes and sites due to the novelty of flexible technology and the types of stresses subjected on to the power sources. These are some important factors to consider since the areas of application for flexible batteries can vary vastly as opposed to their rigid counterparts. Recently [Lall 2018, Lall 2018] investigated the after effects of shallow discharge and bending loads of up to 15° on a 45mAh single cell flexible battery. The authors found out that low charge-discharge rate, shallow cycles and small bending loads can help retain the life of the flexible Li-Ion power sources. It was also established that capacity reduction is much less at higher operating temperature even when high charge-discharge rate and full-depth cycling were present. Another study conducted by [Lall 2017] demonstrated the effects of large bending loads of up to 150° on flexible Li-ion batteries and put forth that harsh bending loads can drastically affect the energy storage parameters such as capacity and efficiency of the power source thereby resulting in complete cracking of the electrodes and the outer pouch. In the study [Hu 2010], the authors were one of the few firsts to bring the flexible battery, to be used on a commercial scale, to limelight. The manufactured power sources were able to bend down to 6mm and had introduced paper as separator material for lowering the impedance. Application of a flexible and robust electrode to increase the Li storage capacity was demonstrated by [Deng 2017]. The authors showcased that by constructing a 3D macro-porous structure of molybdenum sulfide on carbon cloth, the volume expansion issues during the charging-discharging process can be reduced. The novelty of the flexible batteries regime is still being explored and enhanced by introduction of flexible hetero-structures for electrodes [Zhang 2017], development of halide ion based Co_3O_4 nano-sheets [Yao 2018] and prolusion of 3D graphene foam based nano-architecture to improve the performance of flexible Li-ion batteries

[Mo 2017]. All in all there is a significant amount of deficiency in understanding the behavior of these flexible power sources when put to accelerated life tests where the operating environments mimic their areas of applications. Also, no established capacity degradation models exist which can capture the true behavior of flexible power sources. In the present day modern applications such as portable electronics, shallow discharge cycles easily outnumber the deep discharge cycles in operation and while simultaneously being subjected to daily stresses of motion; thus the importance of investigating the effect of DoD with different operating parameters. This research work is focused on establishing the survivability and behavior of flexible Li-ion batteries under accelerated life conditions replicative of real world applications.

In this study, we show how ultra-thin flexible form factors behave when subjected to shallow discharge cycles-full charge cycles at different C rates of 0.5C and 1C. This test framework puts to use a battery state assessment analyzer (BSAA) [Lall 2017, Lall 2018, Lall 2018] developed at CAVE3 electronics research center, Auburn University. The BSAA has the ability to store the battery parameters such as voltage, current and resistance online and later computes the capacity, efficiency and power offline. BSAA has four major components: -

1. Programmable source meter
2. Electronic Load
3. Multi-Channel DAQ
4. LabVIEW user interface

The test samples (Li-ion power sources) have been tested and evaluated at 1C and 0.5C rates. Discharge during the lifecycle tests is characterized by the depth of discharge from a full charge

state whereas during the charging phase the batteries are charge to a full charge always. Therefore the charge state of a test was always defined by x to 100% where x is the DoD. Depth-of-discharge is synonymous with shallow cycling, a term often used in this study. In order to replicate real-world shallow cycling different discharge cut off voltages have been introduced within the test matrix. The accelerated tests run continuously for 130 cycles, where in each cycle voltage, current and resistance values are stored every 2 seconds, which provide significant amount of data points for offline evaluation of parameters such as capacity, efficiency and charge-discharge time and power. Later a regression based capacity degradation and a cycle to failure model has been developed. The effects of shallow cycling at different C rates have been characterized. A total of 10 flexible Li-ion power source samples have been tested at different test conditions which are mentioned and explained in detail later in the study.

8.1 TEST VEHICLE

State-Of-The-Art Li-ion pouch form shaped form factors have been used as flexible sources in this study. The nominal rated capacity of these sources is 65mA-h. The dimensions of the Li-ion test samples are 60mm x 35mm x 0.5mm as shown in Figure199. The test samples are commercially available and can cater to the daily stresses of motion such as bending and flexing. As widely known, that a Li-ion power source is comprised of a positive electrode cathode, a negative electrode anode and an electrolyte as a conductor. The cathode is composed of a metal oxide and the anode is made of a carbon based material mostly graphite. The test samples used in this investigation have a graphite based anode; the cathode is made of $LiMnNiCoO_2$ while the electrolyte is a combination of Li based salts in an organic solvent, Ether. When the power source is powered on the negative electrode (anode) undergoes oxidation i.e. loses electrons and

217

creates positive ions, similarly there is a reduction reaction at the positive electrode (cathode) this process occurs during the discharge phase and a similar event occurs but in reversed direction during the charging phase.

A layer by layer structure of the battery test sample is shown in   Figure 200. Li-Ion samples used in this investigation consist of only one microcell. Each microcell is further comprised of two one-sided anode (graphite) layers, one two-sided cathode ($LiCoO_2$) layers, two separators, one positive current collector and one negative current collector.

Figure199:- Test vehicle used for this investigation (left)

High resolution scanning electron microscopy images were obtained to visualize and study the internal structure of the Li-ion test samples. As seen in $LiMnO_2$ forms a α-$NaFeO_2$ structure more commonly known as the distorted rock salt structure. Energy dispersive X-ray analysis was done on the cathode to characterize the different elements which make up the electrode. Lithium being a light metal and X-ray florescent yield probability is low therefore it remains undetected.
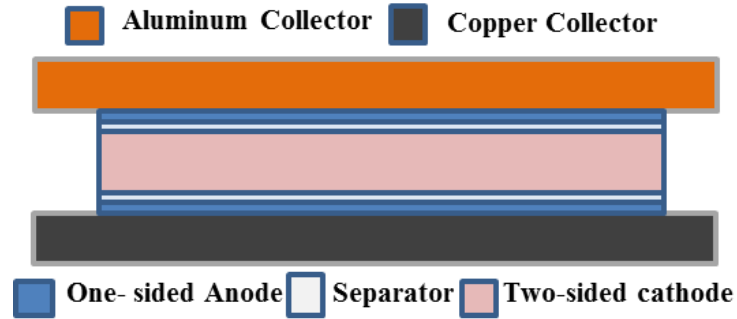
Figure 200: - Layer by layer configuration of the test sample
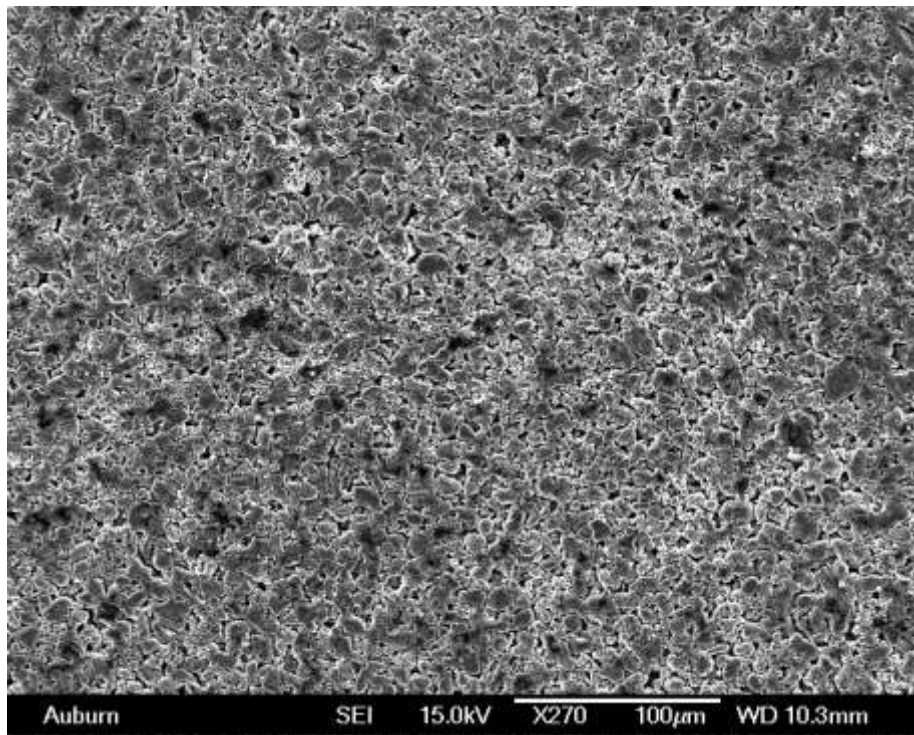
Figure 201: - SEM of cathode

The battery manufacturer specifies the temperature ranges during the charging process to be 0°C to 45°C and -20°C to 60°C during the discharging period. In most rechargeable power sources especially the Li-ion ones, both the electrodes have the capability to intercalate Li^+ ions. During the charging period $LiMnNiCoO_2$ oxidizes i.e. loses electrons and in turn same amount of Li^+ ions are released into the electrolyte. Mixture of solvents and Lithium salts, the electrolyte, is

already rich in Li^+ ions; therefore the arriving Li^+ ions from the cathode replace the existing Li^+ ions which in turn travel to the negative electrode. The graphite based anode absorbs the arriving Li^+ ions where are they get clumped to the electrons lost by the positive electrode. The direction of the Li^+ ions is reversed when in the discharging phase which makes this electrochemical reaction reversible in nature.

Figure 202: - x2000 zoomed in cathode SEM image and EDX analysis for elemental composition

Figure 203: - SEM image of Separator layer

Figure 204: - SEM image of Copper current collector

8.2 EXPERIMENTAL TEST SETUP AND RELIABILTIY TEST MATRIX

As mentioned before a battery state assessment analyzer (BSAA) was developed before undertaking this investigation. The depth-of-discharge or shallow discharging experiment was conducted using the same BSAA. The BSAA has the ability to store the battery parameters such as voltage, current and resistance online and later compute the capacity, efficiency and power offline. BSAA has four major components a programmable source meter and DC electronic load, a multi-channel data acquisition system, LabVIEW user interface. A LabVIEW test protocol was developed which can control the number of cycles, cut off voltages, end of charge current and end of charge voltage. The user can also control the presence/absence of bending load during discharging via the module, which was demonstrated in [Lall 2018]. Figure 205 shows the schematic of test setup used for depth-of-discharge testing. The developed National Instruments module is responsible for transmitting both the discharging and the charging profiles to the DC load and source meter respectively.

Figure 205: - Schematic of BSAA, [Lall 2018]

The test setup connections and other required components have been previously explained in detail in previous studies [Lall 2018] and will not be discussed in this study. Table 31 lists the battery control parameters which need to be maintained during the entirety of the test. A term, delta discharge, has been introduced which is used in this study to describe the depth-of-discharge being conducted. A total of five delta discharge variations have been studied. For the charging phase all the samples have been charged to a 100%, so whilst the discharging depths vary the Li-ion samples are always charged to a value of 4.2V, charging cutoff voltage. A total of 10 flexible Li-ion power source samples have been tested at different discharging depths, which are later discussed in detail in the results section. Table 32 and Table 33 show the reliability test matrices developed for the investigation of Li-ion power sources under varying depth of discharges with full charging. The effect of different C rates with different DoD has been investigated and using the same data sets a regression made capacity degradation model has been developed.

Table 31: - Battery Control Parameters

Control Parameter	Value
Charging Cutoff Voltage	4.2V
Charging Cutoff Current	4mA
Discharging Cutoff Voltage	A function of DoD
Charging Current Rate	1C,0.5C
Discharging Current rate	1C,0.5C
Charging Current	65mA,30mA
Discharging Current	65mA,30mA

Table 32: - Test matrix for 1C

Test Temp.	Delta discharge	Rate	Cutoff
25°C	30%	1C	3.75V
25°C	45%	1C	3.5V
25°C	60%	1C	3.3V
25°C	80%	1C	3V
25°C	100%	1C	2.75V

Table 33: - Test matrix for 0.5C

Test Temp.	Delta discharge	Rate	Cutoff
25°C	30%	0.5C	3.75V
25°C	45%	0.5C	3.5V
25°C	60%	0.5C	3.3V
25°C	80%	0.5C	3V
25°C	100%	0.5C	2.75V

During the accelerated life tests power source parameters such as capacity, efficiency charge-discharge time, state-of-charge and power have been evaluated and analyzed. As mentioned in Table 32 and Table 33 two different charging/discharging rates have been used 1C and 0.5C. Each cycle in the repeated cyclic tests evolves in has three different steps where in the first step constant current discharging at 1C/0.5C occurs until the voltage dropped to the operating DoD, succeeded by a constant current 1C/0.5C charging profile until the voltage reaches 4.2V. Finally, with constant voltage charging phase at 4.2V is until the current tapers to 4mA. Li-ion battery output parameters namely capacity, efficiency, charge-discharge time, state-of-charge and power were evaluated by recording the in-situ characteristic VI curves. In [Lall 2018] the effect of repeated mechanical bending on wearable flexible electronics along with 30% and 45% shallow

discharge cases was presented and it was shown how these operating parameters can affect the battery life and in some cases help retain the state-of-charge. In order to better understand the results from [Lall 2018] and cement the hypothesis similar tests need to be conducted on and the study needs to be expanded on to different flexible battery chemistries and flexible power sources of different dimensions.
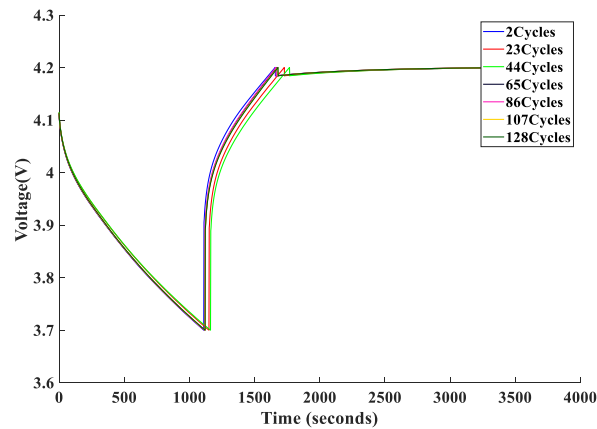
Figure 206: - Voltage characteristic curve during discharging and charging for a DoD of 30% from full charge
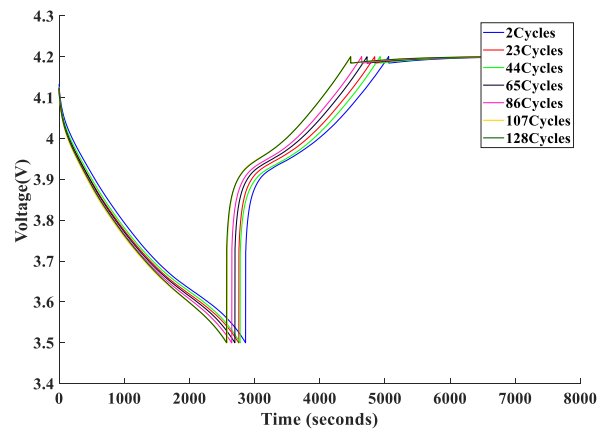
Figure 207: - Voltage characteristic curve during discharging and charging for a DoD of 45% from full charge
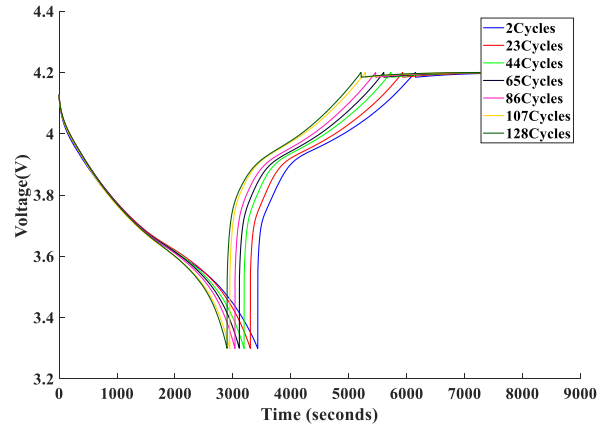
Figure 208: - Voltage characteristic curve during discharging and charging for a DoD of 60% from full charge
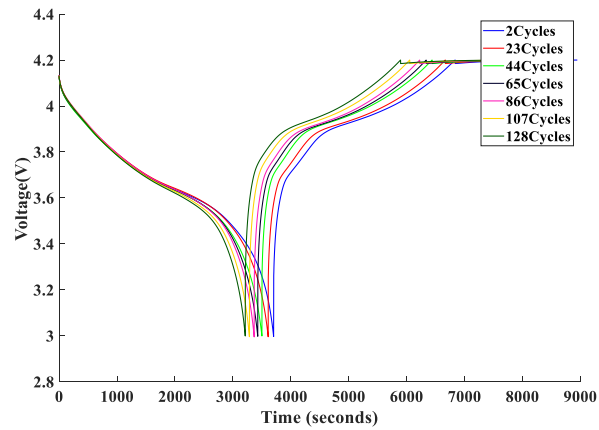
Figure 209: - Voltage characteristic curve during discharging and charging for a DoD of 80% from full charge
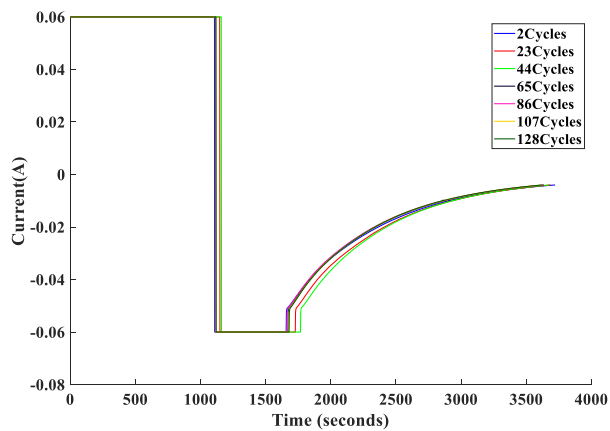
Figure 210: -Current characteristic curve during discharging and charging for a DoD of 30% from full charge

226
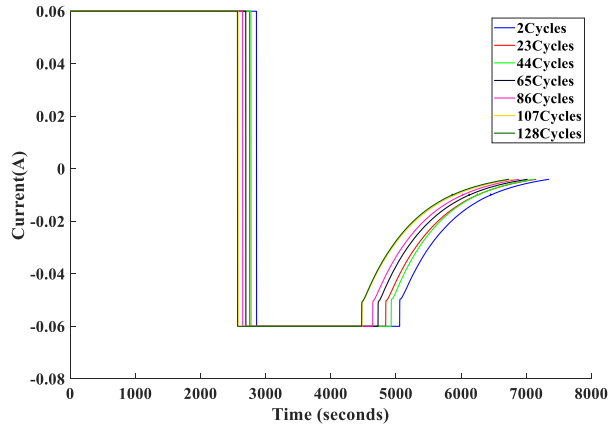
Figure 211: - Current characteristic curve during discharging and charging for a DoD of 45% from full charge
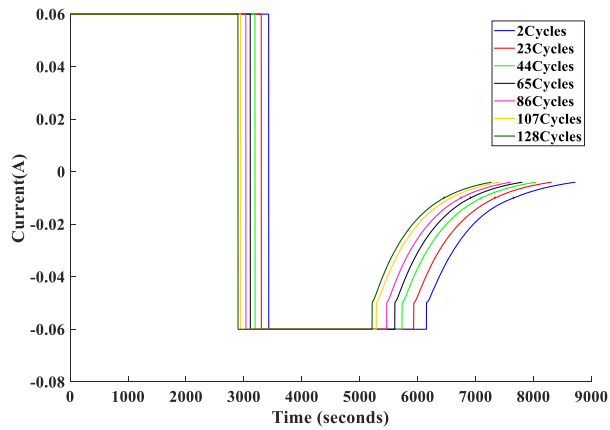
Figure 212: - Current characteristic curve during discharging and charging for a DoD of 60% from full charge
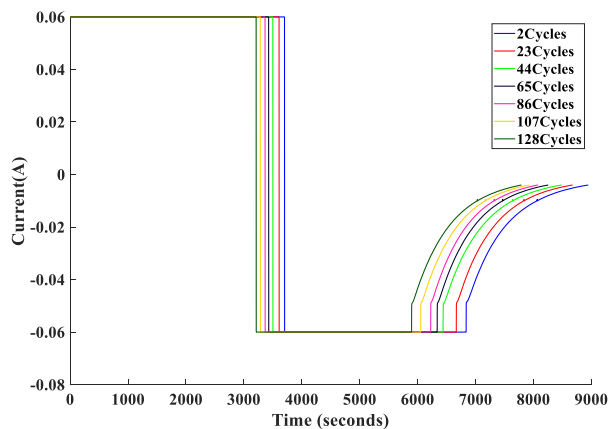
Figure 213: - Current characteristic curve during discharging and charging for a DoD of 80% from full charge

8.3 Experimental Results

Variation in depth-of-discharge occurs when the state of a power source changes inadvertently. The present study focusses on how accelerated shallow discharge-charge cycles can affect the battery parameters.
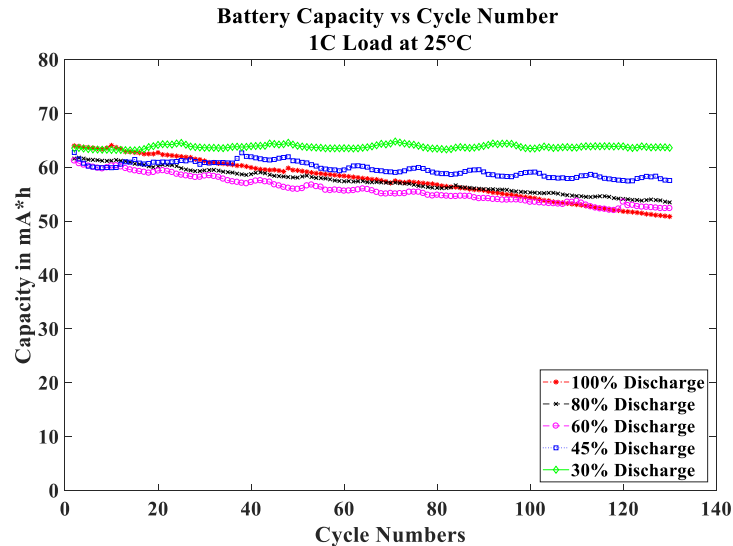
Figure 214: -Capacity vs the number of cycles as a function of the Depth-of-Discharge

There is no reliability data available for Li-ion based flexible batteries under shallow cycles; through this study and previous studies [Lall 2018, Lall 2018] we present reliability data which can be beneficial to battery designers and manufacturers.

Battery discharge capacity has units of mA-h and is defined by the product of discharge current, measurement interval and the state-of-charge. All the battery test samples were evaluated at a C-rate of 1C and 0.5C where the discharge current was set to 0.060A and 0.030A respectively. In-situ data for voltage, current and resistance was recorded every 2 seconds until the end of the accelerated life cycle test which is 130 cycles. Figure 214 shows the battery discharge capacity vs the number of cycles as a function of the depth-of-discharge. It can be clearly seen that the higher the amount of DoD the faster the capacity degrades and the lesser it is at the end of life

cycle test. This has to do with the fact that a shallow cycle would help preserve the electrodes from constantly expanding and contracting during the release-acceptance of Li-ions and also will aid in deterioration of the electrode-electrolyte interface. Figure 215 shows the normalized capacity curves as a function of the depth-of-discharge. A 100% discharge curve shows more deterioration in capacity as opposed to the 30% discharge sample.
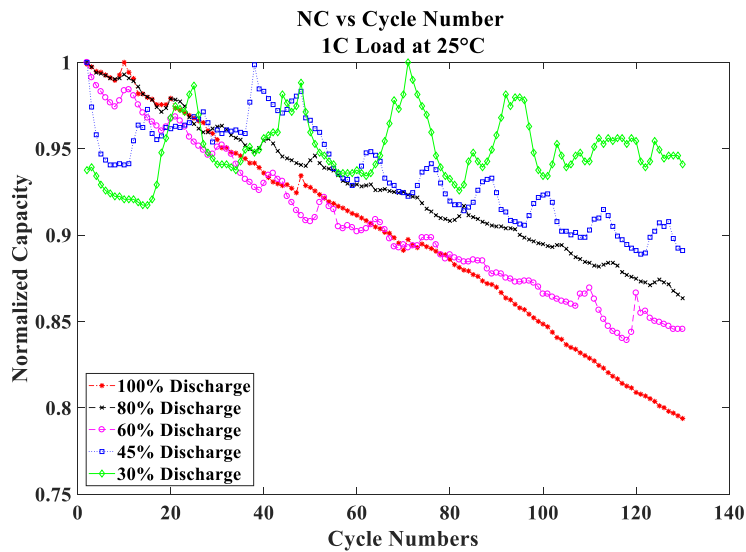
Figure 215: -Normalized capacity vs the number of cycles as a function of the Depth-of-Discharge
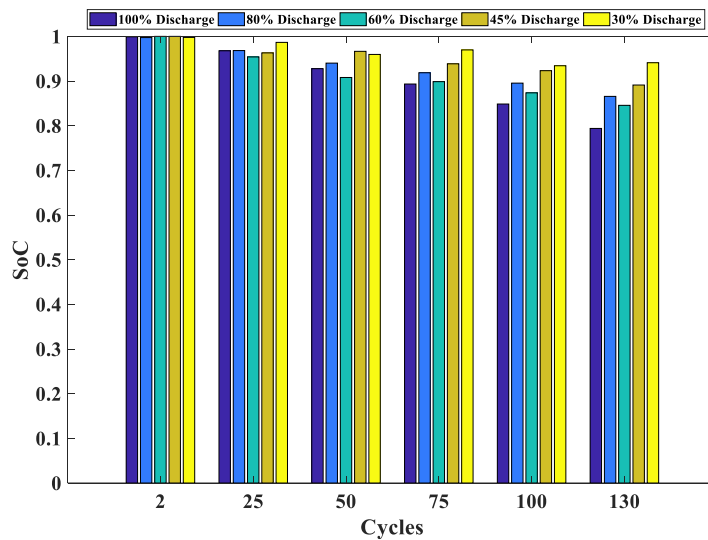
Figure 216: -State-of-Charge vs the number of cycles as a function of the Depth-of-Discharge

One of the most important and studied battery parameter is the state-of-charge. It is defined as the ratio of the useable charge to the maximum charge that can be stored within the power source. It is a known fact that Li-ion transport between the electrodes will result in charging and discharging of the power source; therefore when the anode has maximum concentration of Li-ions and cathode has the minimum concentration at that point the state-of-charge is at the highest possible level. Upon the completion of the circuit an internal redox reaction occurs enabling the anode to lose some electrons by creating cations, while the cathode gains a few electrons. Following the same trend the state-of-charge is at its lowest when the reverse reaction occurs. As mentioned before since the test samples are comprised of a single micro-cell; for an ideal case this cell should start with a full or a 100-percent state-of-charge at the start of a cycle and end with 100-percent SOC at end of each cycle. Figure 216 shows that all test samples start with the same SOC but as the accelerated life cycle test progresses the sample which was subjected to only 30% discharge is able to retain the maximum SOC at the end of the test. As mentioned before in all the test conditions the discharge during the lifecycle tests is characterized by the depth of discharge from a full charge state whereas during the charging phase the batteries are charge to a full 100% always. Therefore the charge state of a test was always defined by x to 100% where x is the DoD.
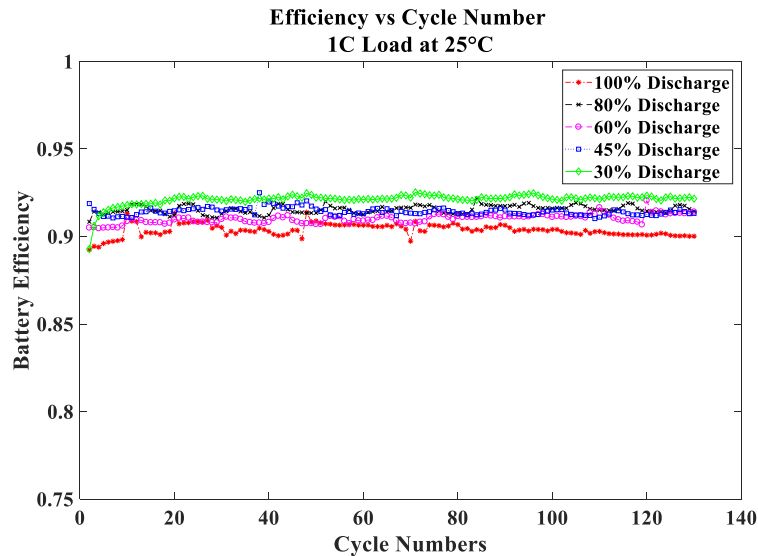
Figure 217: - Battery efficiency vs the number of cycles as a function of the Depth-of-Discharge

Battery efficiency is another key parameter in understanding the power source operation. Mathematically, the ratio of power discharged by the battery to the input power supplied to the battery determines how efficient the power source is. Figure 217 shows the battery efficiency curves as a function of different discharge profiles. It can be clearly seen that the 30% discharged sample turned out to be the most efficient. The online measurements recorded for voltage and current at each measurement interval are multiplied and then integrated for each specific cycle. The aforementioned process is carried out for all cycles till the end of the accelerated life cycle test. Figure 218 demonstrates the capacity degradation (%) for different DoD test conditions; degradation is an important variable in understanding the effects of operational stresses such as DoD on the Li-ion power source samples. Capacity degradation is defined as the change in the battery discharge capacity between two consecutive cycles until the end of the accelerated life cycle test when exposed to repeated charging-discharging profile. It should be noted that the 30% discharged sample only shows a capacity degradation of about 5% whereas a full discharged sample shows a capacity degradation of about 21%. Capacity degrades much faster

231

when doing repeated full discharge-full charge cycles as opposed to repeated shallow discharge-full charge cycles.
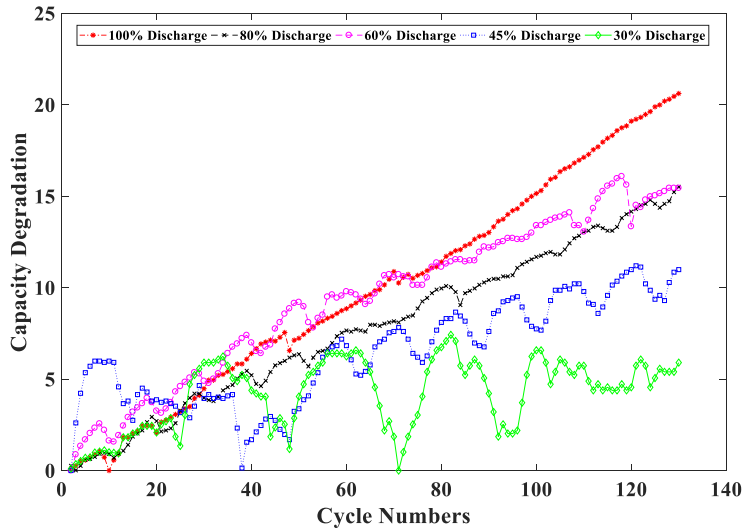
Figure 218: - Capacity Degradation as a function of the Depth-of-Discharge

Figure 219: - Capacity vs the number of cycles as a function of the Depth-of-Discharge
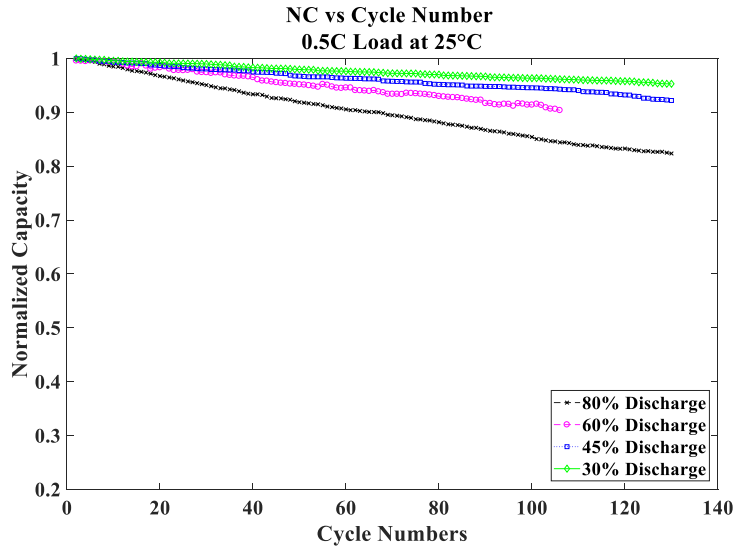
Figure 220: - Normalized capacity vs the number of cycles as a function of the Depth-of-Discharge
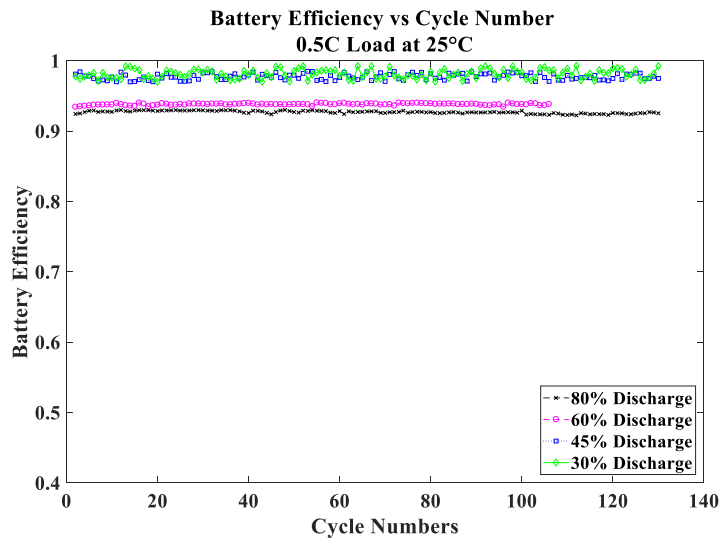
Figure 221: - Battery efficiency vs the number of cycles as a function of the Depth-of-Discharge

233

Capacity Degradation vs Cycle Number
0.5C Load at 25°C
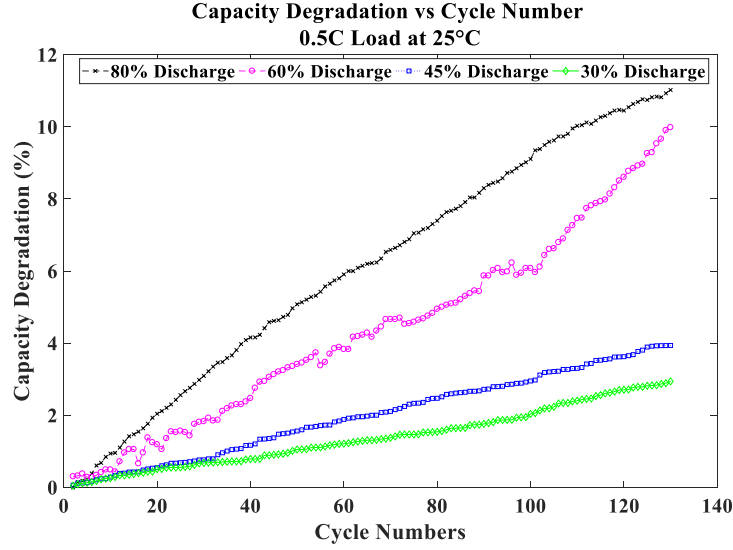
Figure 222: - Capacity Degradation as a function of the Depth-of-Discharge

8.4 Regression Model

Previously we had established a capacity degradation model [1, 2] for flexible Li-ion power sources. The model has been modified to predict the capacity degradation for different species of Li-Ion power sources. The presented model serves as the first to establish a capacity prediction baseline for flexible power sources operating in harsh environmental conditions. **Equation (1)** shows a generalized form of Arrhenius equation which is used as a starting point.

$$S* = \left(e^{\frac{A_1}{T\_kelvin}} \right) \cdot \left(ncycles\_num^{A_2} \right) \cdot \left(DoD^{A_3} \right) \cdot \left(current\_mA^{A_4} \right) \cdot \left(bend\_dv^{A_5} \right)$$

(1)

; Where S* is the defined as the capacity degradation in percent.

Table 34: - Model Parameters

Independent Variables	Dependent Variables
Operating Temperature	
No. of Cycles	Capacity Degradation (%)
Depth of Discharge	
Electronic Load	
Bending Load	

Table 34 lists all the important variables taken into consideration for the regression model and their roles.

Equation (1) can be simplified as a linear equation as shown in **Equation (2)**.

$$Ln(S*) = \frac{A_1}{T\_kelvin} + A_2 Ln(ncycles\_num) + A_3 Ln(DoD)$$
$$+ A_4 Ln(current\_mA) + A_5 Ln(bend\_dv)$$

(2)

For **Equation (3)** the natural log terms in **Equation (2)** have been named as x_1, x_2, x_3 and x_4 for simplicity.

$$S* = \frac{A_1}{T} + A_2 X_1 + A_3 X_2 + A_4 X_3 + A_5 X_4$$

(3)

The regression model has been captured in Table 35. The regression model has low VIF values for all the constants which reflect to the fact that there are no multicollinearity issues within the battery dataset.

Table 35:-REGRESSION MODEL VALUES

Term	Coef.	SE Coef.	T-Value	P-Value	VIF
Constant	-2.617	0.213	-12.31	0	
(1/T_kelvin)	25.17	1.51	16.66	0	1.25
current_mA	0.5426	0.0110	49.27	0	1.28
bend_dv	-0.5735	0.0140	-41.06	0	1.22
DoD	0.6986	0.0437	15.98	0	1.37
ncycles_num	0.4577	0.0131	35.04	0	1.01

Table 36:-MODEL SUMMARY

S	R-sq	R-sq(adj)	R-sq(pred)
0.3620	80.71%	80.64%	80.50%

The ANOVA test results are shown in   Table 37 where a zero P value from the test confirms the acceptability of the model.

Table 37:-ANOVA Test Results

Source	DF	SS	MS	F	P
Regression	5	727.32	145	1109	0.000
Residual Error	1326	173.81	0.131		
Total	1331	901.13			

The resulting regression equation from the model has been shown in **Equation (4)**.

$$S* = A.\left(e^{\frac{25.17}{T\_kelvin}} \right).\left(ncycles\_num \right)^{0.4577}.\left(DoD \right)^{0.6986}$$

$$.\left(current\_mA \right)^{0.5426}.\left(bend\_dv \right)^{-0.5735} \quad (4)$$

8.5 SUMMARY AND CONCLUSIONS

In this study we present the effects of repeated shallow discharge-full charge on Li-ion based ultra-thin flexible form factors. Effects of simultaneous environmental stresses and repeated cyclic events have been studied on output parameters such as efficiency, capacity and charge-discharge time. The effect of Depth-of-discharge has been studied on Li-ion test samples, which showcase that performing shallow cycling, can help retain the battery samples life and SOC. A volumetric change within the electrode materials due to repeated cycling occurs which is governed by a continuous ionic mass removal and deposition process; this in turn makes the cathode/anode structures and also the electrode-electrolyte interface, progressively worse. Shallow cycling results show that this deteriorating process can be controlled by performing shallow discharging in conjunction with full charging. A regression model has been presented which takes into account the operating variables such operating temperature, mechanical stresses, electronic load and depth of discharge. The model is responsible for computing the capacity degradation for different battery chemistries and is able to capture the overall trend in battery capacity over increasing charging-discharging cycles.

Chapter 9

Effect of calendar aging and thermal cycling on ultra-thin flexible Li-Ion power sources: Capacity fade and effect on microstructure

The capacity of a power source, dependent on electrode materials and cell design, degrades during its life as a function of time is also highly influenced by the operating and storage environments. Calendar aging is a term often used to describe long term storage at elevated temperatures. Effect of such storage environments on the health of ultra-thin flexible li-ion batteries is relatively unknown but needs to be studied as it is replicative of shelf life the power sources see between fabrication and in-field usage. Also, health monitoring techniques which can successfully predict remaining useful life for flexible lithium-ion power sources have yet to be fully studied. It is well known that cyclic aging can deteriorate the health of a power source ultimately resulting in capacity fade over its lifetime. Now, whether or not calendar aging and varying thermal loads (during storage) have an effect on the working of flexible li-ion battery is yet to be established. With the current state-of-the-art moving towards flexible electronics and flexible components, it is therefore of the utmost importance to establish test protocols, test standards, prognostic health management frameworks and test methodologies for flexible power sources which will be implemented as energy harvesting units in such electronic assemblies. In this research study, flexible lithium-ion batteries have been analyzed for effects of long term calendar aging and varying thermal loads by subjecting the test samples to: 1) unpowered aging at 50°C ranging from 10 days-120 days 2) unpowered exposure to thermal cyclic environment, 10°C-50°C, ranging from 50 loops to 550 loops. After the pre-conditional exposure the power sources were cycled through multiple full charge and full discharge cycles at ambient operating temperature under a constant C-rate. Output parameters such as efficiency, capacity and charge-

discharge time have been studied for battery degradation. SEM and EDX techniques have also been utilized to study the effects on cathode microstructure and report if any visual evidence for film formation, electrolyte decomposition and/or lithium plating is observed.

Effect of aging on Li-ion batteries has been a major source of concern since the electrochemical system is being used in almost all of the portable electronics, automotive and other applications. Applications such as stand-alone power sources and EVs require long life therefore it is of the utmost importance to understand and analyze the side-reactions that can lead to either capacity or power loss. Two variations of aging can occur: calendar (storage) aging and cyclic (repeated usage) aging. It has been observed that while calendar aging occurs due to side reactions which result from thermodynamic instability of the surrounding materials, cyclic aging generates dynamic instability effects such as volumetric changes [Broussely 2005]. Strong capacity fading has been reported and extensively studied for rigid Li-ion batteries when stored or cycled between 60°C and 100°C; deterioration of active materials has been frequently pointed out as the major source of this fading. Issues with SEI and interface degradation have also been highlighted on the electrodes [Bodenes 2013, Yabuuchi 2005, Ramadass 2002, Ma 2006]. With the recent emergence of flexible Li-ion power sources the challenges associated with this chemistry have increased exponentially. Present and past studies have not yet fully accomplished how environmental stresses, both mechanical as well as electrical, can affect the performance of ultra-thin flexible Li-Ion based power sources. Three major chemical processes which degrade Li-ion rigid batteries are: - electrolyte decomposition, transition metal dissolution and lithium plating. Not much attention has been paid towards the flexible side which can be the go-to product given how the industry is shifting towards flexible-hybrid electronics. Recent studies like [Nair 2017] have tried to develop a novel thermal induced free radical polymerization technique to be able to

produce highly robust and thermally stable solid polymer membranes to be used as separators in aging resistant Li-ion power sources. Another study [Blake 2017] established an approach to 3D print Li-ion battery electrolytes using a dry phase inversion method in order to enhance their thermal stability. All in all long-term storage effects and the effects of varying thermal stresses on ultra-thin flexible Li-ion batteries has not been studied. Since, mostly the same Li-ion chemistry is implemented in flexible batteries as opposed to rigid form factors, it is yet to be fully established whether the above mentioned degradation processes prevail within flexible batteries or is there introduction of new failure modes and sites due to the novelty of flexible technology and the types of stresses subjected on to the power sources. These are some important factors to consider since the areas of application for flexible batteries can vary vastly as opposed to their rigid counterparts. Recently [Lall 2018, Lall 2018] investigated the after effects of shallow discharge and bending loads of up to 15° on a 45mAh single cell flexible battery. The authors found out that low charge-discharge rate, shallow cycles and small bending loads can help retain the life of the flexible Li-Ion power sources. It was also established that capacity reduction is much less at higher operating temperature even when high charge-discharge rate and full-depth cycling were present. Another study conducted by [Lall 2017] demonstrated the effects of large bending loads of up to 150° on flexible Li-ion batteries and put forth that harsh bending loads can drastically affect the energy storage parameters such as capacity and efficiency of the power source thereby resulting in complete cracking of the electrodes and the outer pouch. In the study [Hu 2010], the authors were one of the few firsts to bring the flexible battery, to be used on a commercial scale, to limelight. The manufactured power sources were able to bend down to 6mm and had introduced paper as separator material for lowering the impedance. Application of a flexible and robust electrode to increase the Li storage capacity was

demonstrated by [Deng 2017]. The authors showcased that by constructing a 3D macro-porous structure of molybdenum sulfide on carbon cloth, the volume expansion issues during the charging-discharging process can be reduced. The novelty of the flexible batteries regime is still being explored and enhanced by introduction of flexible hetero-structures for electrodes [Zhang 2017], development of halide ion based Co_3O_4 nano-sheets [Yao 2018] and prolusion of 3D graphene foam based nano-architecture to improve the performance of flexible Li-ion batteries [Mo 2017]. All in all there is a significant amount of deficiency in understanding the behavior of these flexible power sources when put to accelerated life tests where the operating environments mimic their areas of applications. This research work is focused on establishing the survivability and behavior of flexible Li-ion batteries under accelerated life conditions replicative of real world applications.

In this study, we show how ultra-thin flexible form factors behave 1) when stored at elevated temperatures 2) exposed to varying thermal loads and then put to test under an accelerated discharge-charge cycles at different C rates of 0.5C and 1C. This test framework puts to use a battery state assessment analyzer (BSAA) [Lall 2017, Lall 2018, Lall 2018] developed at CAVE3 electronics research center, Auburn University. The BSAA has the ability to store the battery parameters such as voltage, current and resistance online and later computes the capacity, efficiency and power offline. BSAA has four major components: -

5. Programmable source meter

6. Electronic Load

7. Multi-Channel DAQ

8. LabVIEW user interface

The test samples (Li-ion power sources) have been tested and evaluated at 1C rate. Li-ion test samples were investigated under full discharge and charge cycles during the lifecycle tests are characterized by the storage and thermal cyclic pre-conditions. The accelerated tests run continuously for 130 cycles, where in each cycle voltage, current and resistance values are stored every 2 seconds, which provide significant amount of data points for offline evaluation of parameters such as capacity, efficiency and charge-discharge time and power. The effects of shallow cycling at different C rates have been characterized. A total of 12 flexible Li-ion power source samples have been tested at different test pre-conditions (storage/thermal cycling) which are mentioned and explained in detail later in the study.

9.1 TEST VEHICLE

State-Of-The-Art Li-ion pouch form shaped form factors have been used as flexible sources in this study. The nominal rated capacity of these sources is 60mA-h. The dimensions of the Li-ion test samples are 60mm x 35mm x 0.5mm as shown in Figure199. The test samples are commercially available and can cater to the daily stresses of motion such as bending and flexing. As widely known, a Li-ion power source is comprised of a positive electrode cathode, a negative electrode anode and an electrolyte as a conductor. The cathode is composed of a metal oxide and the anode is made of a carbon based material mostly graphite. The test samples used in this investigation have a   graphite based anode; the cathode is made of $LiMnNiCoO_2$ while the electrolyte is a combination of Li based salts in an organic solvent, Ether. When the power source is powered on the negative electrode (anode) undergoes oxidation i.e. loses electrons and creates positive ions, similarly there is a reduction reaction at the positive electrode (cathode) this process occurs during the discharge phase and a similar event occurs but in reversed

direction during the charging phase. Li-Ion samples used in this investigation consist of only one microcell. Each microcell is further comprised of two one-sided anode (graphite) layers, one two-sided cathode ($LiMnNiCoO_2$) layers, two separators, one positive current collector and one negative current collector.

Figure223:- Test vehicle used for this investigation (left)

High resolution scanning electron microscopy images were obtained to visualize and study the internal structure of the Li-ion test samples. As seen in Figure **225** $LiMnO_2$ forms a α-$NaFeO_2$ structure more commonly known as the distorted rock salt structure. Energy dispersive X-ray analysis was done on the cathode to characterize the different elements which make up the electrode. Lithium being a light metal and X-ray florescent yield probability is low therefore it remains undetected. The battery manufacturer specifies the temperature ranges during the charging process to be 0°C to 45°C and -20°C to 60°C during the discharging period.
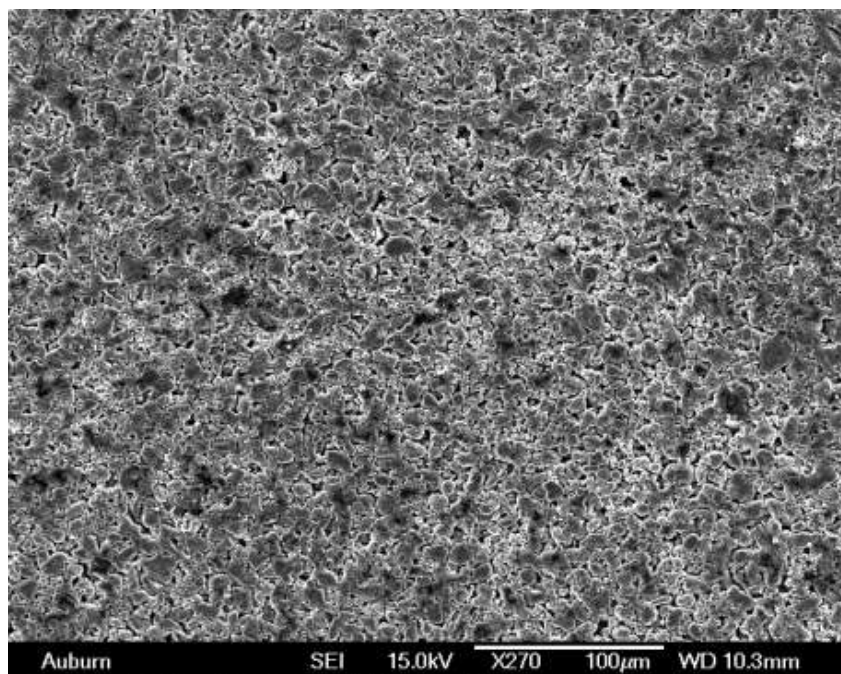
Figure 224: - SEM of cathode

In most rechargeable power sources especially the Li-ion ones, both the electrodes have the capability to intercalate Li^+ ions. During the charging period $LiMnNiCoO_2$ oxidizes i.e. loses electrons and in turn same amount of Li^+ ions are released into the electrolyte. Mixture of solvents and Lithium salts, the electrolyte, is already rich in Li^+ ions; therefore the arriving Li^+ ions from the cathode replace the existing Li^+ ions which in turn travel to the negative electrode. The graphite based anode absorbs the arriving Li^+ ions where are they get clumped to the electrons lost by the positive electrode. The direction of the Li^+ ions is reversed when in the discharging phase which makes this electrochemical reaction reversible in nature.

Figure 225: - x2000 zoomed in cathode SEM image and EDX analysis for elemental composition

In [Lall 2018] the effect of repeated mechanical bending on wearable flexible electronics along with 30% and 45% shallow discharge cases was presented and it was shown how these operating parameters can affect the battery life and in some cases help retain the state-of-charge. In order to better understand the results from [Lall 2018] and explore the effects of aging and thermal cycling on flexible batteries tests need to be conducted on and the study needs to be expanded which can replicate the environments as seen by such batteries in modern day applications.
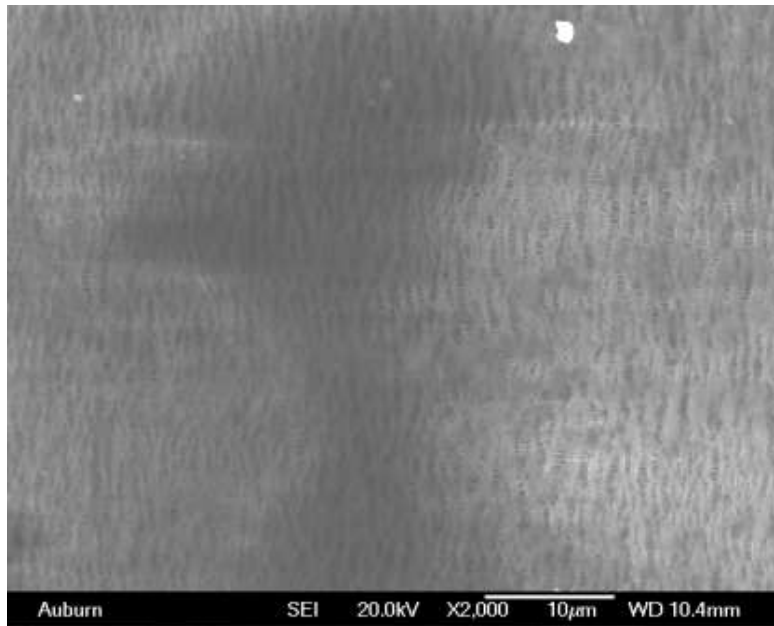
Figure 226: - SEM image of Separator layer
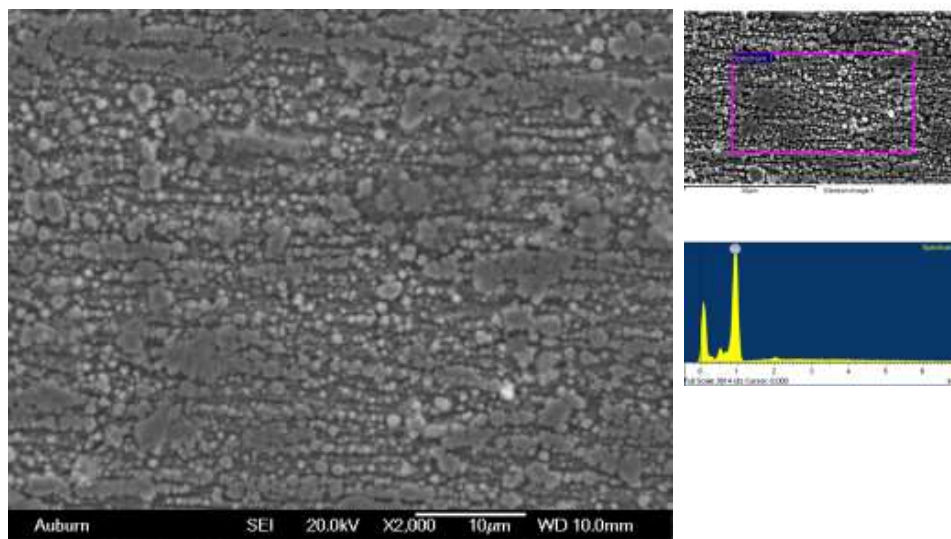
Figure 227: - SEM image of Copper current collector

9.2 EXPERIMENTAL TEST SETUP AND RELIABILTIY TEST MATRIX

As mentioned before a battery state assessment analyzer (BSAA) was developed before undertaking this investigation. The repeated charging-discharging experiment was conducted using the same BSAA. The BSAA has the ability to store the battery parameters such as voltage, current and resistance online and later compute the capacity, efficiency and power offline. BSAA

has four major components a programmable source meter and DC electronic load, a multi-channel data acquisition system, LabVIEW user interface. A LabVIEW test protocol was developed which can control the number of cycles, cut off voltages, end of charge current and end of charge voltage. The user can also control the presence/absence of bending load during discharging via the module, which was demonstrated in [Lall 2018]. Figure 205 shows the schematic of test setup used for depth-of-discharge testing. The developed National Instruments module is responsible for transmitting both the discharging and the charging profiles to the DC load and source meter respectively. The test setup connections and other required components have been previously explained in detail in previous studies [Lall 2018] and will not be discussed in this study.
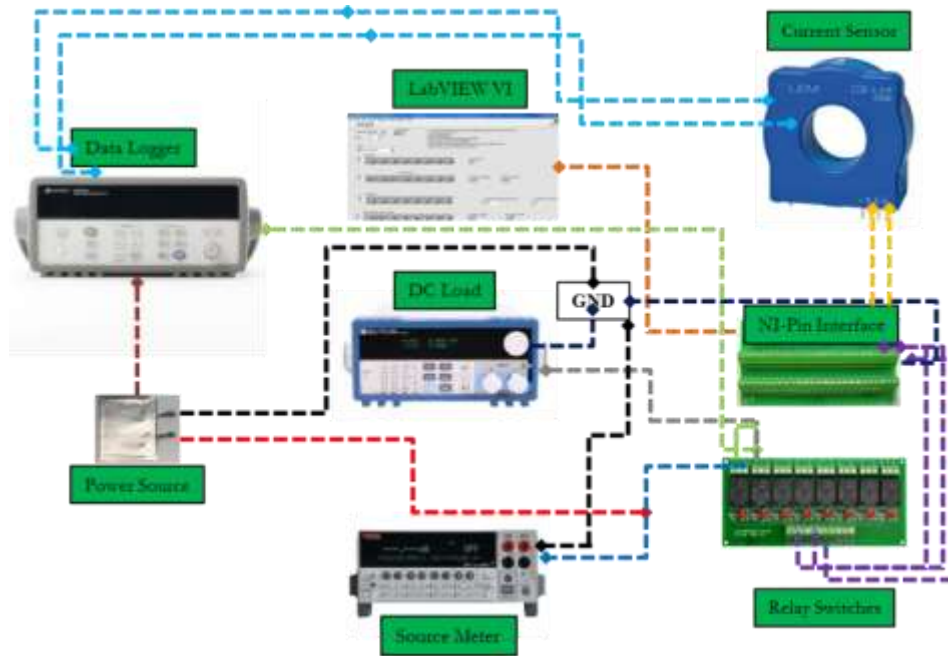
Figure 228: - Schematic of BSAA, [Lall 2018]

Table 31 lists the battery control parameters which need to be maintained during the entirety of the test. This study is categorized into two parts, where the first part looks into the effects of long term calendar aging followed by experimentation at accelerated life conditions for flexible Li-ion

247

batteries. A total of six samples have been used for part a. In part b, another set of six samples was investigated to analyze the effects of varying thermal stresses under storage followed by experimentation at accelerated life conditions for flexible Li-ion batteries. Table **32** and Table **33** show the reliability test matrices developed for the investigation of Li-ion power sources under aging and thermal cyclic pre-conditions. The effect of storage conditions under a constant temperature and under varying thermal loads has been investigated and later the effects of pre-conditions and operating environments have been analyzed on the cathode microstructures.

Table 38: - Battery Control Parameters

Control Parameter	Value
Charging Cutoff Voltage	4.2V
Charging Cutoff Current	4mA
Discharging Cutoff Voltage	2.7V
Charging Current Rate	1C,0.5C
Discharging Current rate	1C,0.5C
Charging Current	60mA,30mA
Discharging Current	60mA,30mA

Table 39: - Test matrix for Aging

Aging Duration	Test Temp.	Aging Temp	Rate	Cutoff
10Days	25°C	50°C	1C	2.75V
25Days	25°C	50°C	1C	2.75V
40Days	25°C	50°C	1C	2.75V
66Days	25°C	50°C	1C	2.75V
90Days	25°C	50°C	1C	2.75V
115Days	25°C	50°C	1C	2.75V

Table 40: - Test matrix for Thermal Cycling

Thermal Cycling	Test Temp.	TC Profile	Rate	Cutoff
50Loops	25°C	10°C-50°C	1C	2.75V
140Loops	25°C	10°C-50°C	1C	2.75V
230Loops	25°C	10°C-50°C	1C	2.75V
345Loops	25°C	10°C-50°C	1C	2.75V
440Loops	25°C	10°C-50°C	1C	2.75V
550Loops	25°C	10°C-50°C	1C	2.75V

During the accelerated life tests power source parameters such as capacity, efficiency charge-discharge time, state-of-charge and power have been evaluated and analyzed. As mentioned in Table 32 and Table 33 two different pre-conditioning environments have been test for. After that the test samples are put to test under repeated discharging-charging cycles, where each cycle in the repeated cyclic tests evolves in three different steps; first step starts with a constant current discharging at 1C until the voltage drops to the cut-off voltage of 2.75V, then it is succeeded by a constant current 1C charging profile until the voltage reaches 4.2V.

Figure 229: - Aging oven for calendar storage of Li-ion test samples

Figure 230: - Thermal Cycling chamber for varying thermal stresses test on Li-ion batteries

Finally, the constant voltage charging phase occurs at 4.2V until the current tapers to 4mA. Li-ion battery output parameters namely capacity, efficiency, charge-discharge time, state-of-charge and power were evaluated by recording the in-situ characteristic VI curves.
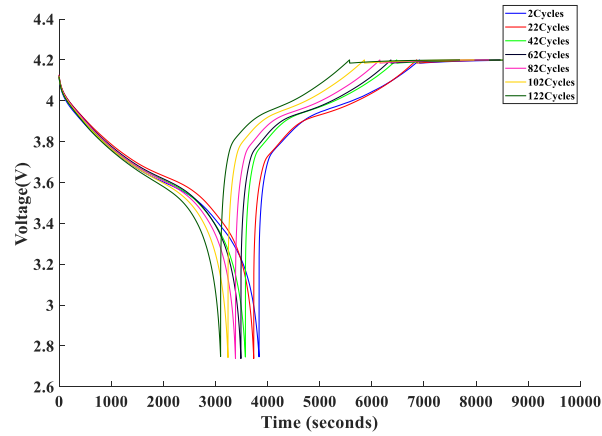
Figure 231: - Voltage characteristic curve after 10 aging days at 50°C
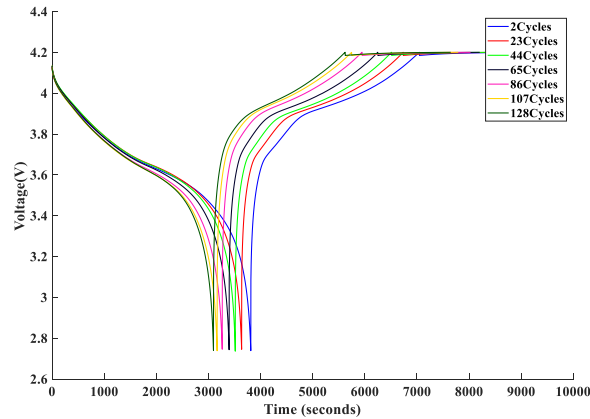
Figure 232: - Voltage characteristic curve after 50 TC Loops at 10°- 50°C
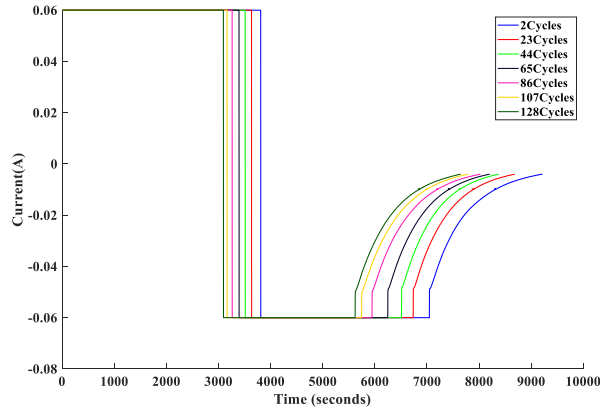
Figure 233: - Current characteristic curve after 50 TC Loops at 10°- 50°C
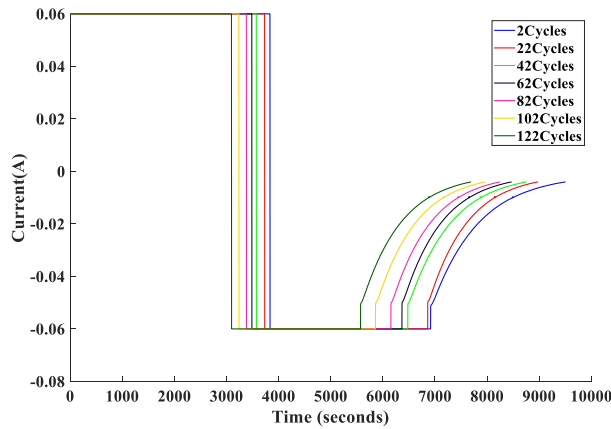
Figure 234: - Current characteristic curve after 10 aging days at 10°C

9.3 Experimental Results

The importance of calendar aging and varying thermal stresses can be explained when contemplating the areas of applications which make use of flexible, wearable technologies. The present study focusses on how stored pre-conditional environment affect the battery parameters. There is no reliability data available for Li-ion based flexible batteries under shallow cycles; through this study and previous studies [Lall 2018, Lall 2018] we present reliability data which can be beneficial to battery designers and manufacturers.

251

I.   Effect of Aging
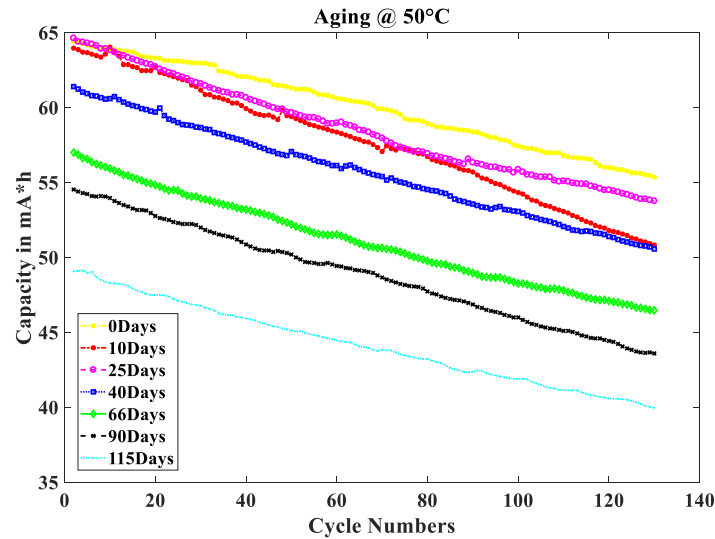
Figure 235: - Capacity vs the number of cycles of repeated lifecycle test after long term calendar aging

Battery discharge capacity has units of mA-h and is defined by the product of discharge current, measurement interval and the state-of-charge. All the battery test samples were evaluated at a C-rate of 1C where the discharge current was set to 0.060A.

Online data was recorded every 2 seconds till the end of the accelerated life cycle test which is 130 cycles. Figure 235 shows the battery discharge capacity vs the number of cycles as a function of aging days. It can be seen that up until 115 days of calendar aging the battery discharge capacity tends to decrease. Figure **236** demonstrates the normalized capacity of the battery test samples, normalizing the data helps in getting a better visualization of the discharge capacity as all the curves originate from one starting point and it also has the advantage of being dimensionless.
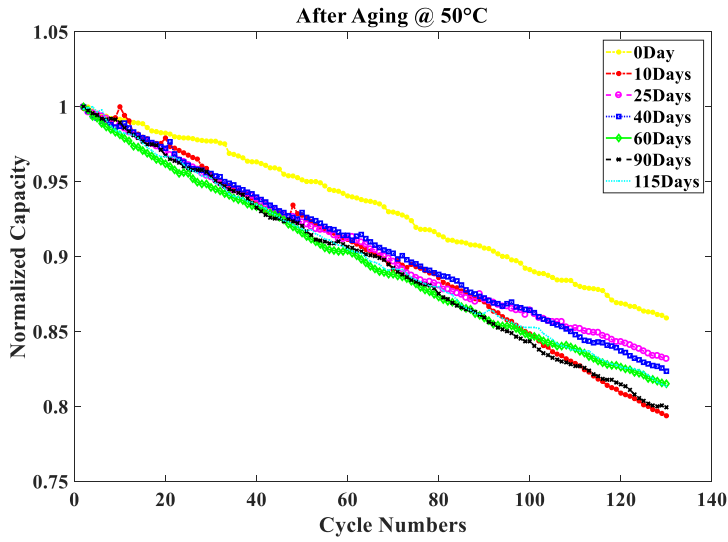
Figure 236: -Normalized capacity vs the number of cycles of repeated lifecycle test after long term calendar aging
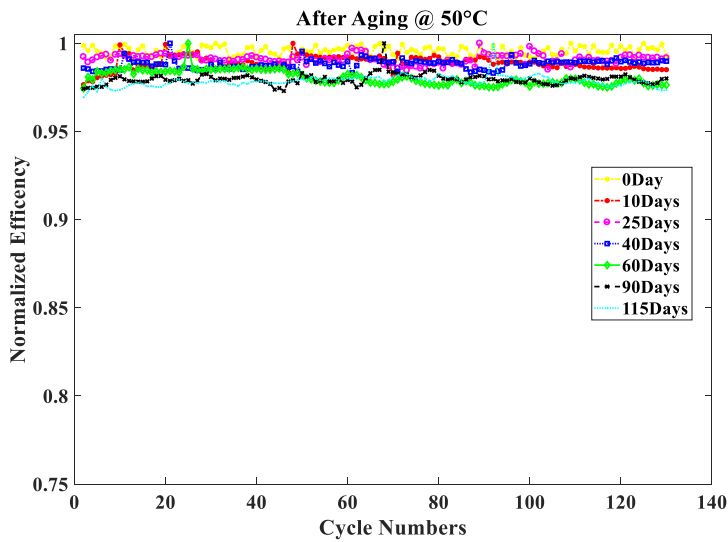
Figure 237: - Battery efficiency after long term calendar aging

After Aging @ 50°C

Legend: 0Days, 10Days, 25Days, 40Days, 66Days, 90Days, 115Days
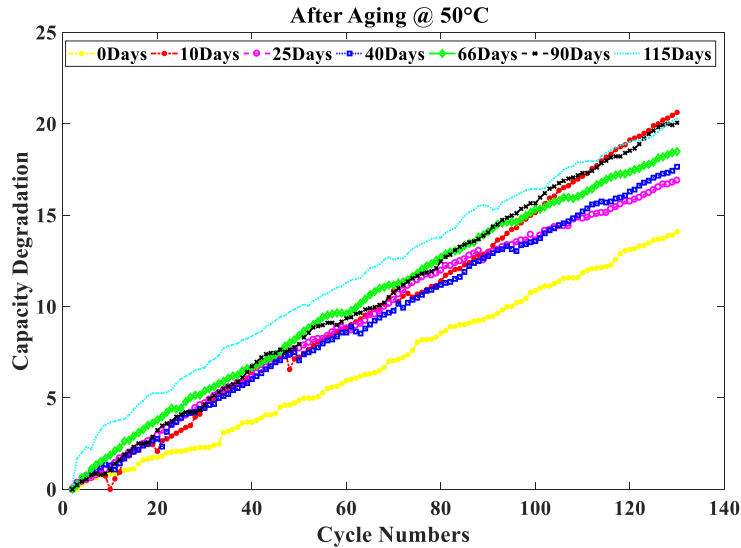
Figure 238: -Capacity degradation with respect to number of cycles after long term calendar aging

Battery efficiency is another key parameter in understanding the power source operation. Mathematically, the ratio of power discharged by the battery to the input power supplied to the battery determines how efficient the power source is. The online measurements recorded for voltage and current at each measurement interval are multiplied and then integrated for each specific cycle. The aforementioned process is carried out for all cycles till the end of the accelerated life cycle test. Figure **237** demonstrates the computed power source efficiencies for different aging days. It can be observed that the 66 days aged sample which had the least battery capacity to start off with is also the least efficient sample from the entire data set. Figure **238** demonstrates the capacity degradation (%) for different calendar aging conditions; degradation is an important variable in understanding the effects of storage and operational stresses on the Li-ion power source samples. Capacity degradation is defined as the change in the battery discharge capacity between two consecutive cycles until the end of the accelerated life cycle test when exposed to repeated charging-discharging profile after long term storage at elevated temperatures.

254

II. Effect of Thermal Cycling
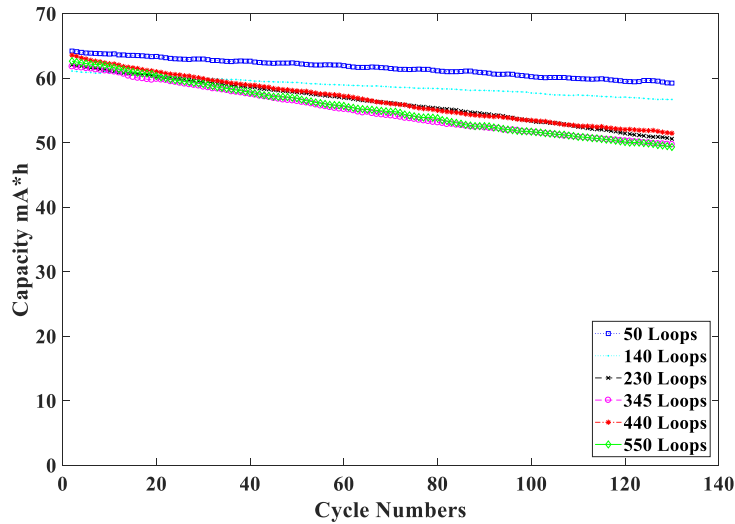
Figure 239: - Capacity vs the number of cycles of repeated lifecycle test after long term thermal cyclic storage
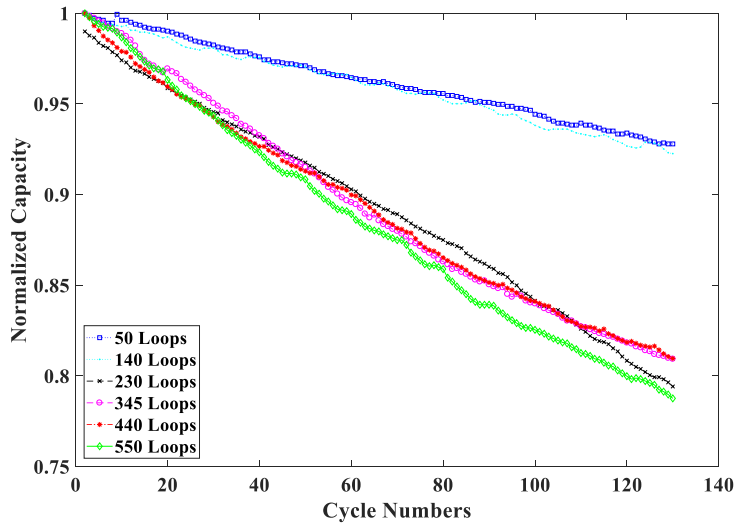
Figure 240: -Normalized capacity vs the number of cycles of repeated lifecycle test after long term thermal cyclic storage

The importance of varying thermal stresses can be explained when contemplating the areas of applications which make use of flexible, wearable technologies. Often times in our daily routine the portable electronic devices can experience sudden temperature changes.
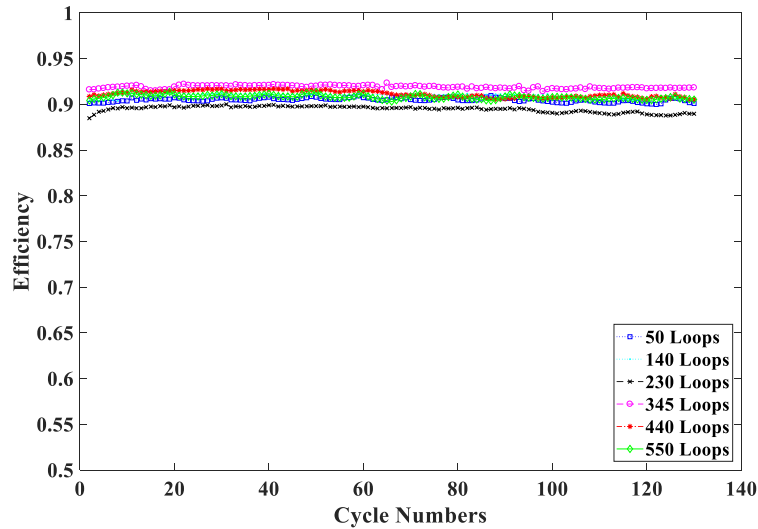
Figure 241: -Battery efficiency after long term thermal cyclic storage

For the sake of consumer electronics and portable devices the battery test samples have been subjected to thermal variations between 10°C-50°C. The present study focusses on how stored pre-conditional environment affect the battery parameters. Figure **239** shows the battery discharge capacity vs number of cycles as a function of thermal cycling loops. There is a significant decay in the slope of the discharge capacity after 140 loops. It can be better visualized in Figure **240** where the normalized capacity data shows reduction in the discharge capacity as the exposure to thermal cycling loops increases. Figure **242** also agrees with the computed results, where the capacity degradation is most in the test sample exposed to 550 loops, about 22%; whereas the degradation is only about 7% in the battery test samples exposed to 50 and 150 loops.
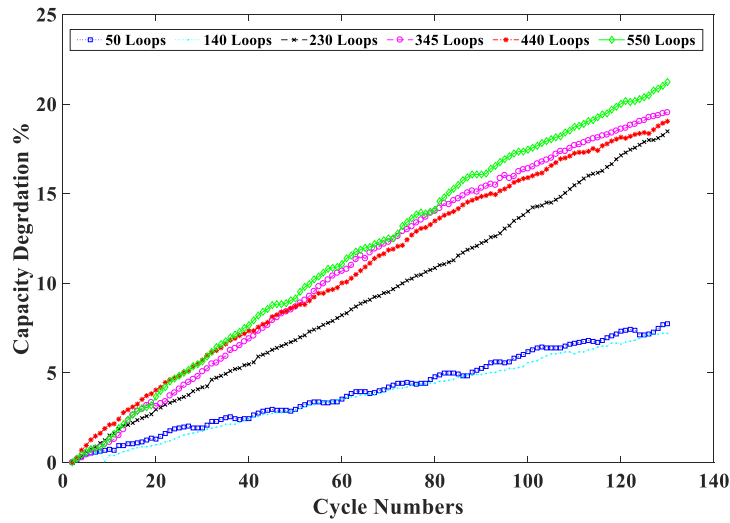
Figure 242: Capacity degradation vs the number of cycles of repeated lifecycle test after long term thermal cyclic storage
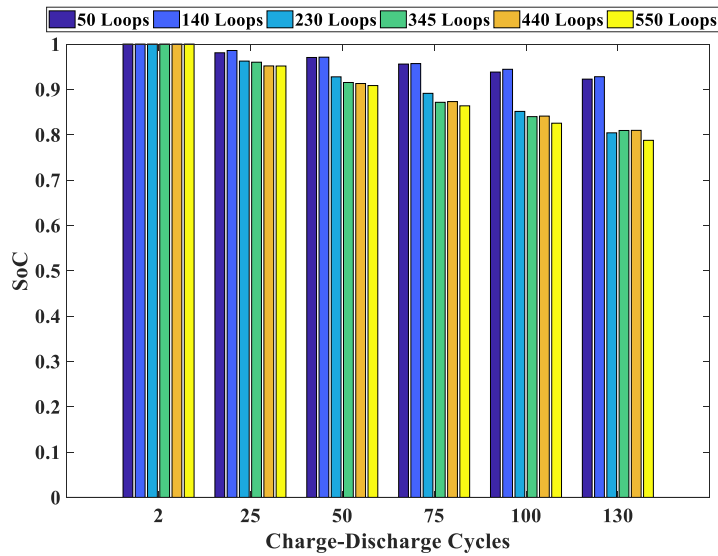
Figure 243: -State-of-Charge evolution as a function of thermal cycling loops

One of the most important and studied battery parameter is the state-of-charge. It is defined as the ratio of the useable charge to the maximum charge that can be stored within the power source.

It is a known fact that Li-ion transport between the electrodes will result in charging and discharging of the power source; therefore when the anode has maximum concentration of Li-

ions and cathode has the minimum concentration at that point the state-of-charge is at the highest possible level. Upon the completion of the circuit an internal redox reaction occurs enabling the anode to lose some electrons by creating cations, while the cathode gains a few electrons. Following the same trend the state-of-charge is at its lowest when the reverse reaction occurs. As mentioned before since the test samples are comprised of a single micro-cell; for an ideal case this cell should start with a full or a 100-percent state-of-charge at the start of a cycle and end with 100-percent SOC at end of each cycle. Figure **243** shows the evolution of state-of-charge for different thermal cyclic storage conditions. At the end of the 2nd cycle all the samples have similar state-of-charge but after the completion of accelerated life cycle test it can be seen that the sample exposed to 550 loops of thermal cyclic environment between 10°C-50°C has the least amount of SOC available.

III.   Effect on cathode microstructure

As mentioned before, high resolution scanning electron microscopy images were obtained to visualize and study the internal structure of the Li-ion test samples. As seen in Figure **225**, Figure **244** and Figure **245** $LiMnO_2$ forms a α-NaFeO$_2$ structure more commonly known as the distorted rock salt structure. Energy dispersive X-ray analysis was done on the cathode to characterize the different elements which make up the electrode, shown in Figure **225**. Lithium being a light metal and X-ray florescent yield probability is low therefore it remains undetected.

258
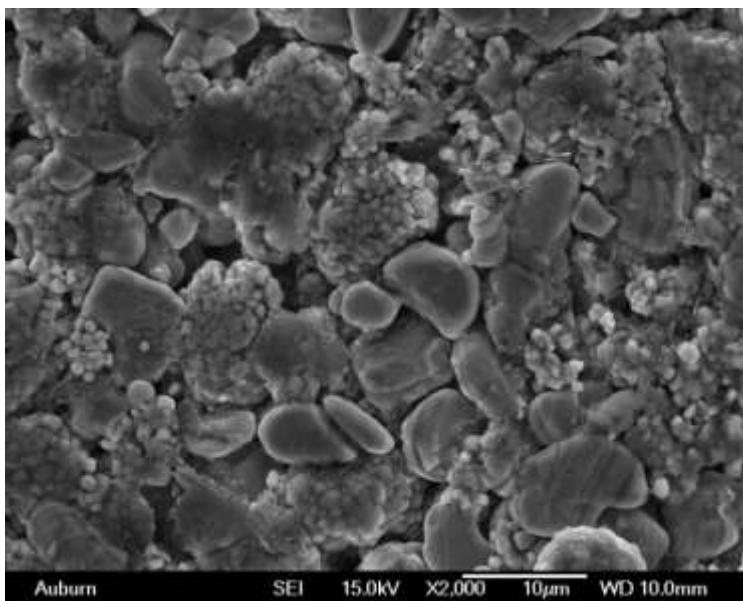
Figure 244: -Cathode microstructure after 130 repeated cycles of the accelerated life cycle tests
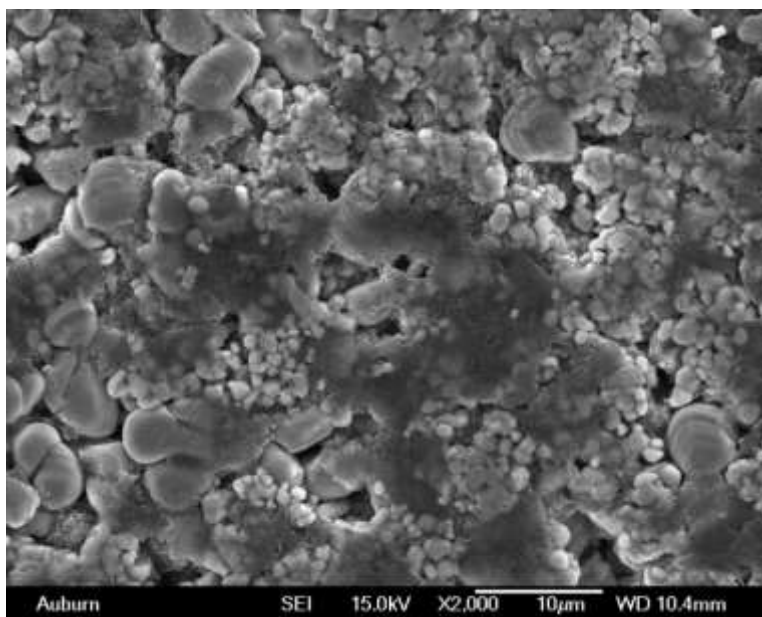
Figure 245: -Cathode microstructure after 90 days of calendar aging at 50°C plus 130 repeated cycles of the accelerated life cycle tests

SEM images show the formation of a thin film over the cathode as the aging time increases. Figure 244 and Figure 245 show the contrasting difference between the formations of the thin layer. While after 130 repeated discharging-charging cycles of the accelerated life cycle tests there is a small presence of the thin film/layer, on the other hand the thin layer is much more wide spread and prevalent within the battery sample which has been exposed to 90 days of calendar aging and also undergone 130 repeated discharging-charging cycles of the accelerated life cycle tests. The presence of the thin film over the cathode reduces the area for acceptance and release of Li-ions during the charging and discharging process, which thereby acts as a catalyst for faster decay in the battery discharge capacity.

9.4 SUMMARY AND CONCLUSIONS

In study we present a test methodology for ultra-thin flexible form factors based on Li-ion technology. The successive effects of calendar aging-thermal cycling followed by accelerated life testing have been reported. The Li-ion test samples have been investigated for storage effects at 50°C ranging from 10 days-120 days and exposure to varying thermal stresses from 10°C-50°C, ranging from 50 loops to 550 loops. After the pre-conditional exposure the power sources were cycled through multiple full charge and full discharge cycles at ambient operating temperature under a constant C-rate. Battery discharge capacity tends to decrease with the increase in the aging days up-to 115 days. The presence of the thin film over the cathode reduces the area for acceptance and release of Li-ions during the charging and discharging process, which thereby acts as a catalyst for faster decay in the battery discharge capacity. Interestingly this leads to lower starting discharge capacities at 0th cycle when comparing the aged samples.

A much more firm trend is observed for the thermal cyclic environment, where the test samples show a decreasing trend in the discharge capacity all the way from 50 loops to 550 loops. Also, on comparing the capacity degradation from the two pre-conditions; overall capacity degradation is similar in both the cases, about 20%. The lower end of the two test matrices i.e. 10 days of calendar aging and 50 loops of thermal cycling show that aging results in much more capacity degradation, about 15%, as opposed to thermal cycling where the capacity degrades to only about by 7%.

REFERENCES

[1] Z. Szucs, G. Nagy, S. Hodossy, M. Rencz and A. Poppe, "Vibration combined high Temperature Cycle Tests for capacitive MEMS accelerometers," *2007 13th International Workshop on Thermal Investigation of ICs and Systems (THERMINIC)*, Budapest, 2007, pp. 215-219.

[2] E. Yilmaz and D. Bindel, "Temperature Sensitivity and Shape Optimization of Solid-State Wave Gyroscopes," in *IEEE Sensors Journal*, vol. 16, no. 16, pp. 6213-6221, Aug.15, 2016.

[3] Xuemeng Chen *et al*., "A micromachined gyroscope with piezoresistance for both high performance Coriolis-effect detection and torsional vibration monitoring," *The 13th International Conference on Solid-State Sensors, Actuators and Microsystems, 2005. Digest of Technical Papers. TRANSDUCERS '05.*, 2005, pp. 117-120 Vol. 1.

[4] Z. Hou *et al*., "Effect of parasitic resistance on a MEMS vibratory gyroscopes due to temperature fluctuations," *2011 6th IEEE International Conference on Nano/Micro Engineered and Molecular Systems*, Kaohsiung, 2011, pp. 293-296.

[5] M. I. Ferguson, D. Keymeulen, C. Peay, K. Yee and D. L. Li, "Effect of Temperature on MEMS Vibratory Rate Gyroscope," *2005 IEEE Aerospace Conference*, Big Sky, MT, 2005, pp. 1-6.

[6] Wu Y, Xi X, Tao Y, Wu X, Wu X. A Study of the Temperature Characteristics of Vibration Mode Axes for Vibratory Cylinder Gyroscopes. *Sensors (Basel, Switzerland)*. 2011

[7] Lall, P.; Abrol, A.S.; Simpson, L.; Glover, J.,   Survivability of MEMS accelerometer under sequential thermal and high-g mechanical shock environments, InterPACKICNMM 2015

[8] P. Lall, A. S. Abrol, L. Simpson and J. Glover, "A study on damage progression in MEMS based Silicon oscillators subjected to high-g harsh environments," *2016 15th IEEE Intersociety Conference on Thermal and Thermomechanical Phenomena in Electronic Systems (ITherm)*, Las Vegas, NV, 2016, pp. 546-559.

[9] ST microelectronics, LPY510AL analog rate gyroscope, Technical Data Sheet, DOC ID 15805, rev 2

[10] Analog Devices, Gyro Mechanical Performance: The most important parameter, Technical Article, MS-2158, 2011

[11] Analog Devices, Voltage References, Tutorial , MT-087, 2009

[12] Lall, P.; Abrol, A.S.; Simpson, L.; Glover, J., Reliability of MEMS devices under multiple environments, Thermal and Thermomechanical Phenomena in Electronic Systems (ITHERM), pp.1313-1321,2014

[13] Brown, T.G.; Harsh military environments and Microelectromechanical systems, Sensors, Proceedings of IEEE, Vol.2, pp, 753-760, 2003

[14]N.Marsi, B.Majlis, A.Hamzah, F.Yasin,"High Reliability of MEMS Packaged Capacitive Pressure Sensor Employing 3C-SiC for High Temperature," *2nd International Conference on Sustainable Energy Engineering and Application (ICSEEA)*, 2015, pp. 471-479.

[15] Z.Chen, W.Du, F.Zhao, "Silicon Carbide MEMS capacitive sensor for harsh environment," *ASME Proceedings: Micro-and Nano-Systems Engineering and Packaging*, pp. 1-5, 2013.

[16] J.Yang "A harsh environment wireless pressure sensing solution utilizing high temperature electronics," *Sensors, 2013, Basel*

[17] Daniel J. Fonseca and Miguel Sequera, "On MEMS Reliability and Failure Mechanisms," International Journal of Quality, Statistics, and Reliability, vol. 2011.

[18] P. Lall, A. S. Abrol, J. Suhling, L. Simpson, J. Glover and D. Locker, "Effect of simultaneous high temperature and vibration on MEMS based vibratory gyroscope," *2017 16th IEEE Intersociety Conference on Thermal and Thermomechanical Phenomena in Electronic Systems (ITherm)*, Orlando, FL, 2017, pp. 1214-1228

[19] Pedersen, C., Jespersen, S. T., Jacobsen, K. W., Krog, J. P., Christensen, C., & Thomsen, E. V. (2004). Highly reliable O-ring packaging concept for MEMS pressure sensors. *Sensors and Actuators A: Physical*, *115*(2), 617-627.

[20] Lall, P.; Abrol, A.S.; Simpson, L.; Glover, J., Survivability of MEMS accelerometer under sequential thermal and high-g mechanical shock environments, InterPACKICNMM 2015

[21] P. Lall, A. S. Abrol, L. Simpson and J. Glover, "A study on damage progression in MEMS based Silicon oscillators subjected to high-g harsh environments," *2016 15th IEEE Intersociety Conference on Thermal and Thermomechanical Phenomena in Electronic Systems (ITherm)*, Las Vegas, NV, 2016, pp. 546-559.

[22] NXP Semiconductors, MPL3115A2 Precision Pressure Sensor with Altimetry, Technical Data Sheet, rev 6

[23] Krondorfer, Rudolf, Yeong K. Kim, Jaeok Kim, Claes-Gøran Gustafson, and Timothy C. Lommasson. "Finite element simulation of package stress in transfer molded MEMS pressure sensors." *Microelectronics Reliability* 44, no. 12 (2004): 1995-2002.

[24] Lin, Liwei, and Weijie Yun. "MEMS pressure sensors for aerospace applications." In *Aerospace Conference, 1998 IEEE*, vol. 1, pp. 429-436. IEEE, 1998.

[25] Lall, P.; Abrol, A.S.; Simpson, L.; Glover, J., Reliability of MEMS devices under multiple environments, Thermal and Thermomechanical Phenomena in Electronic Systems (ITHERM), pp.1313-1321,2014

[26] Brown, T.G.; Harsh military environments and Microelectromechanical systems, Sensors, Proceedings of IEEE, Vol.2, pp, 753-760, 2003

[27] Bowei Li, G. Q. Zhang, D. G. Yang, Fengze Hou and Yang Hai, "The effect of diaphragm on performance of MEMS pressure sensor packaging," *2010 11th International Conference on Electronic Packaging Technology & High Density Packaging*, Xi'an, 2010, pp. 601-606.

[28] M. Broas *et al*., "Galvanic corrosion of silicon-based thin films: A case study of a MEMS microphone," *2015 IEEE 65th Electronic Components and Technology Conference (ECTC)*, 2015, pp. 453-459.

[29] J. Li *et al*., "Reliability assessment of a MEMS microphone under shock impact loading," *2013 14th International Conference on Thermal, Mechanical and Multi-Physics Simulation and Experiments in Microelectronics and Microsystems (EuroSimE)*, Wroclaw, 2013, pp. 1-6.

[30] W. Fang and Q. Huang, "A study of the mechanical reliability of a MEMS microphone," *Proceedings of the 20th IEEE International Symposium on the Physical and Failure Analysis of Integrated Circuits (IPFA)*, Suzhou, 2013, pp. 716-719.

[31] Fonseca, D.; Sequera, M., "On MEMS reliability and failure mechanisms" *2011 International Journal of Quality, Statistics and Reliability,* 2011

[32] P. Lall, A. S. Abrol, L. Simpson and J. Glover, "Effect of Simultaneous High temperature and vibration on MEMS based vibratory gyroscope" *2017*, InterPACK

[33] NTI-Audio, Reverberation Time RT60, 2017

[34] Lall, P.; Abrol, A.S.; Simpson, L.; Glover, J., Survivability of MEMS accelerometer under sequential thermal and high-g mechanical shock environments, InterPACKICNMM 2015

[35] P. Lall, A. S. Abrol, L. Simpson and J. Glover, "A study on damage progression in MEMS based Silicon oscillators subjected to high-g harsh environments," *2016 15th IEEE Intersociety Conference on Thermal and Thermomechanical Phenomena in Electronic Systems (ITherm)*, Las Vegas, NV, 2016, pp. 546-559.

[36] ST microelectronics, Best practices in manufacturing process of MEMS microphones, Application Note, AN4428

[37] ST microelectronics, Tutorial for MEMS microphones Application Note, AN4426

[38] Analog Devices, ADMP401, Technical data sheet, Rev E

[39] Lall, P.; Abrol, A.S.; Simpson, L.; Glover, J., Reliability of MEMS devices under multiple environments, Thermal and Thermomechanical Phenomena in Electronic Systems (ITHERM), pp.1313-1321,2014

[40] Brown, T.G.; Harsh military environments and Microelectromechanical systems, Sensors, Proceedings of IEEE, Vol.2, pp, 753-760, 2003

[41] Lall, P.; Abrol, A.S.; Simpson, L.; Glover, J., Survivability of MEMS accelerometer under sequential thermal and high-g mechanical shock environments, InterPACKICNMM 2015

[42] Lall, P.; Abrol, A.S.; Simpson, L.; Glover, J., Reliability of MEMS devices under multiple environments, Thermal and Thermomechanical Phenomena in Electronic Systems (ITHERM), pp.1313-1321,2014

[43] Silicon Time Corporation, SiT8103 high performance 1-110 MHz oscillator, Technical Support Document, Rise and Fall time selection for SiT8103, SiT8003 and SiT9003 September 2011

[44] Silicon Time Corporation, SiT8103 high performance 1-110 MHz oscillator, Technical Data Sheet, 2011

[45] Silicon Time Corporation, SiT8103 high performance 1-110 MHz oscillator, Technical Support Document, Resilience and Reliability of Silicon MEMS Oscillator, 2015

[46] Azevedo, R.G.; Jones, D.G.; Jog, A.V.; Jamshidi, B.; Myers, D.R.; Li Chen; Xiao-An Fu; Mehregany, M.; Wijesundara, M.B.J.; Pisano,A.P., A SiC MEMS resonant sensor for harsh environment applications, Sensors Journal, IEEE, Vol.7, pp.568-576, 2007

[47] Azevedo, R.G.; Myers, D.R.; Pisano, A.P., Temperature-insensitive silicon carbide resonant micro-extensometers, Solid-State Sensors, actuators and microsystems conference, Transducers,pp.268-271,2009

[48] Azevedo, R.G.; Jingchun Zhang; Jones, D.G.; Myers, D.R., Jog, A.V.; Jamshidi, B.;Wijesundara, M.B.J.; Maboudin, Roya; Pisano A.P., Silicon Carbide coated MEMS strain sensor for harsh environment applications, MEMS, IEEE 20th International Conference, pp.643-646, 2007

[49] Bo Sun, J.C., Zeng,S.K., Sudy on MEMS board-level package reliability under high-G impact, Proceedings of the Annual Conference of the Prognostics and health Management Society,pp.1-6, 2011

[50] Srikar, V.T., Senturia, S.D., The Reliability of Microelectromechanical Systems (MEMS) in Shock Environments, journal of Microelectromechanical Systems, Vol.11, No.3, pp.206-214, June2002

[51] Knobloch, A.J.; Ahmad, F.R.; Sexton, Dan W.; Vernooy, David W., Remote Driven and Read MEMS sensors for harsh Environments, Sensors, Vol.13, pp.14175-14188, 2013

[52] Tanner, D.M., Walraven, J.A., Helgesen, K., Irwin, L.W., Brown, F., Smith, N.F., Masters, N., MEMS reliability in shock environments, International Reliability Physics Symposium, pp.129-138, 2000.

[53] Brown, T.G.; Harsh military environments and Microelectromechanical systems, Sensors, Proceedings of IEEE, Vol.2, pp, 753-760, 2003

[54] Alsaleem, F.M., Younis, M.I., Ibrahim, M.I., A study for the effect of PCB motion on the dynamics of MEMS devices under mechanical shock, Volume 18, issue 3, pp.597-609, June 2009

[55] Shea, H., Reliability of MEMS for space applications. Proceedings, SPIE, 2006

[56] Fitzgerald, A., Pierce, D., Huigens, B., White, C., A general methodology to predict the reliability of Single crystal Silicon MEMS device, IEEE, Volume 18, 2009

[57]   Bo Sun, J. C., Zeng, S.K., Study on MEMS board-level package reliability under high-G impact, Proceedings of the Annual Conference of the Prognostics and Health Management Society, pp. 1-6, 2011

[58]   Srikar, V.T., Senturia, S.D., The Reliability of Microelectromechanical Systems (MEMS) in Shock Environments, journal of Microelectromechanical Systems, Vol. 11, No. 3, pp. 206-214, June 2002

[59]   Chen, T.D.; Kelly, T.W.; Collins, D.; Berthold, B.; Brosnihan, T.J.; Denison, T.; Kuang, J.; O'Kane, M.; Weigold,J.W.; Bain, D.; The next generation integrated MEMS and CMOS process on SOI wafers for overdamped accelerometers, Solid-State Sensors,Actuators and Microsystems, Vol.2, pp.1122-1125, 2005

[60]   Weigold, J.W.; Najafi, K.; Pang, S.W.; Design and fabrication of submicrometer, single crystal Si accelerometer, Microelectromechanical Systems, Vol.10, Issue 4,

[61]   Lou,W.,Song,R.,Liu,Y.,Liu,X.,Li,W.,Lin,W., A novel multi-direction high shock reliability test on MEMS devices,Nano/Micro Engineered and molecular systems,pp.261-264,2009

[62]   Tanner,D.M.,Walraven,J.A.,Helgesen,K.,Irwin,L.W.,Brown,F.,Smith,N.F.,Masters,N.,M EMS   reliability   in   shock   environments,   Reliability   Physics symposium,2000.Proceedings.38th Annual 2000 IEEE international, pp.129-138

[63]   Yang,C.,Zhang,B.,Chen,D.,Lin,L.,Drop-shock dynamic analysis of   MEMS/package system,MEMS 2010 IEEE 23rd International conference,pp.520-523,2010

[64]   Analog Devices, ADXL278 high g dual axis accelerometer, Technical Data Sheet Rev B, 2010

[65]   Brown, T.G.; Harsh military environments and Microelectromechanical systems (MEMS), Sensors, Proceedings of IEEE, Vol.2, pp.753-760, 2003

[66]   Huang,Y.,Vasan,A.S.S.,Doraiswami,R.,Osterman,M.,Pecht,M.,   MEMS   reliability review,volume 12, issue 2, Devices and Materials reliability ,IEEE transactions,pp.482-493,2012

[67]   Sundaram,S.,Tormen,M.,Timotijevic,B.,Lockhart,R.,Overstolz,T.,Stanley.R.P.,Shea.H.R. ,Vibration and shock reliability of MEMS: modeling and experimental validation, March 2011

[68]   Jue Li; Broas, M.; Makkonen, J.; Mattila, T.T.; Hokka, J.; Paulasto-Krockel, M.; Shock Impact Reliability and Failure Analysis of a Three-Axis MEMS Gyroscope, Microelectromechanical Systems, Vol.23, Issue 2, pp.347-355, 2014

[69]   Jiang Yu-Qi; Cheng Ying-Jun; Xu Wei; Zhang Kim; Li Xin-xin; Luo Le; Dynamic response of a plastic encapsulated high-g MEMS accelerometer, High Density and Microsystem Design and Packaging and Component Failure Analysis, pp.353-358, 2004

[70]   Chen Yang; Bin Zhang; Dajing Chen; Liwei Lin; Drop-shock dynamic analysis of MEMS/package system, Micro Electro Mechanical Systems(MEMS), pp. 520-523, 2010

[71]   Lall, P.; Iyengar, D.; Shantaram, S.; Panchagade, D.; Suhling, J.; Development of survivability envelopes for SnAg leadfree packaging architectures under shock and vibration, Thermal and Thermomechanical Phenomena in Electronic Systems(ITHERM), pp.822-835, 2008

[72]   Xiong,X.,Wu,Y.L.,Jone,W.B.,Material fatigue and reliability of MEMS accelerometers, Defect and fault tolerance of VLSI systems,pp.314-322,2008

[73]   Alsaleem,F.M.,Younis,M.I.,Ibrahim,M.I., A study for the effect of the PCB motion on the dynamics of MEMS devices under mechanical shock,Volume 18, issue 3, pp. 597-609, June 2009

[74]   Solder-Joint Reliability in Electronics under Shock and Vibration using Explicit Finite Element Sub-modeling, Lall, P., Gupte, S., Choudary, P., Suhling, J., IEEE Transactions on Electronic Packaging Manufacturing, Volume 30, No 1, pp.74-83, January 2007

[75]   Lall, P.; Zhang, H., "Test Protocol for Assessment of Flexible Power Sources in Foldable Wearable Electronics under Stresses of Daily Motion during Operation," *2017 IEEE 67th Electronic Components and Technology Conference (ECTC)*, Orlando, FL, 2017, pp. 804-814

[76]   Lall, P.; Zhang, H., "Prognostication of remaining useful-life for flexible batteries in foldable wearable electronics," *2016 IEEE International Conference on Prognostics and Health Management (ICPHM)*, Ottawa, ON, 2016, pp. 1-10.

[77]   Wang, J., Jin, D., Zhou, R., Li, X., Liu, X., Shen, C., Xie, K., Li, B., Kang, F. & Wei, B. "Highly Flexible Graphene/Mn_3O_4 Nanocomposite Membrane as Advanced Anodes for Li-Ion Batteries" ACS NANO 2016, 10, 6227-6234

[78]   Ning, G., Haran, B. & Popov, B. N. *Capacity fade study of lithium-ion batteries cycled at high discharge rates*. J. Power Sources **117**, 160–169 (2003)

[79]   Wu, B. et al. "Interfacial behaviors between lithium ions conductors and electrode materials in various battery systems," *Journal of Materials Chemistry, 2016*

[80]   B. Scrosati and J.Garche, "Lithium batteries: Status, prospects and future." Journal of Power Sources 195.9 (2010): 2419-2430

[81]   Leng, F., Tan, C. M., & Pecht, M. (2015), Effect of Temperature on the Aging rate of Li-Ion Battery Operating above Room Temperature. Scientific Reports, 5, 12967.

[82]   B. Scrosati, F. Croce, and S. Panero, "Progress in lithium polymer battery R&D." Journal of Power Sources 100.1 (2001): 93-100
[83]   F. Ruijan, M. Xiao, and S. Choe. "Modeling, validation and analysis of mechanical stress generation and dimension changes of a pouch type high power Li-Ion battery." Journal of Power Sources 224 (2013): 211-224

[84]   T. Sasaki, Y. Ukyo, and P. Novak. " Memory effect in lithium-ion battery." Nature Materials 12, 569-575 (2013)

[85]   P. Balbuena and Y.Wang." Lithium-ion batteries." Solid Electrolyte Phase, London

[86]   B. Saha, and K. Goebel. "Modeling of Li-ion battery capacity depletion in a particle filtering framework." Proceedings of the annual conference of the prognostics and health management society. 2009

[87]   B. Saha, K. Goebel, S. Poll and J. Christophersen, "Prognostics Methods for Battery Health Monitoring Using a Bayesian Framework," in *IEEE Transactions on Instrumentation and Measurement*, vol. 58, no. 2, pp. 291-296, Feb. 2009

[88]   Williard, N., Wei, H., Hendricks, C. and Pecht, M. *Lessons learned from the 787 dreamliner issue on lithium-ion battery reliability*. Energies **6**, 4682–4695

[89]   Bodenes, L. et al. *Lithium secondary batteries working at very high temperature: Capacity fade and understanding of aging mechanisms*. J. Power Sources **236**,   265–275 (2013)

[90]   Feng, L., Cher Ming, T., Rachid, Y. & Minh Duc, L. *A practical framework of electrical based online state-of- charge estimation of lithium ion batteries*. J. Power Sources **255**, 423–430 (2014)

[91]   V. Sangwan, R. Kumar and A. K. Rathore, "State-of-charge estimation for li-ion battery using extended Kalman filter (EKF) and central difference Kalman filter (CDKF)," *2017 IEEE Industry Applications Society Annual Meeting*, Cincinnati, OH, USA, 2017, pp. 1-6

[92]   J. D. MacKenzie and C. Ho, "Perspectives on Energy Storage for Flexible Electronic Systems," in *Proceedings of the IEEE*, vol. 103, no. 4, pp. 535-553, April 2015

[93]   S. Jin., J. Li., C. Daniel., D. Mohanty., S. Nagpure. & D.Wood "The state of understanding of the lithium-ion-battery graphite solid electrolyte and its relationship to formation cycling" Carbon, vol. 105,pp. 52-76, Aug. 2016